

10/12/1995
10-32
36112

AN ACOUSTIC CHARGE TRANSPORT IMAGER FOR HIGH DEFINITION TELEVISION APPLICATIONS

NASA Grant #NAGW-2753

**W.D. Hunt and K.F. Brennan
School of Electrical and Computer Engineering**

and

**C.J. Summers
Georgia Tech Research Institute**

**Georgia Institute of Technology
Atlanta, Georgia 30332-0250**

Second Semiannual Report for FY 1995

**A COMPREHENSIVE ANALYSIS OF THE PHYSICAL PROPERTIES OF
ADVANCED GaAs/AlGaAs JUNCTIONS**

**A Thesis
Presented to
The Academic Faculty**

by

Hicham M. Menkara

**In Partial Fulfillment
of the Requirements For The Degree
of Doctor of Philosophy in Physics**

**Georgia Institute of Technology
June 1996**

**A COMPREHENSIVE ANALYSIS OF THE PHYSICAL PROPERTIES OF
ADVANCED GaAs/AlGaAs JUNCTIONS**

Approved:

Dr. Christopher J. Summers, Chairman

Dr. Brent K. Wagner

Dr. Rajarshi Roy

Dr. Henry S. Valk

Date Approved by Chairman _____

To Emilie, for her incredible charm, wit, and sense of humor.

ACKNOWLEDGMENTS

I would like to first acknowledge my thesis advisor, Dr. C. J. Summers, for his constant guidance, patience, and assistance throughout the course of this Ph.D. work. I would also like to thank Dr. Tuyen Tran, Dr. Brent Wagner, Dr. Rudy Benz, Dr. Bob Bicknell-Tassisus, and Dr. Mason Gross for their valuable guidance and the many thoughtful discussions we've had throughout the years. I wish to also extend my thanks to Profs. H.S. Valk, R. Roy, and E.W. Thomas for serving on my thesis committee. In addition, I would also like to thank Mr. S. Halpern and Mr. Mike Harris for the help and effort they put into processing and fabricating the devices that were used in my studies.

I would specially like to thank my family and relatives for their constant support and patience which greatly helped me through the many years it took to finish my research.

Finally, I would like to thank the Quantum Microstructures Branch at the Georgia Tech Research Institute for the use of their facilities and equipment. This work was supported through programs sponsored by the Georgia Tech Research Institute (GTRI), the Advanced Research Projects Agency (ARPA), and the National Aeronautics and Space Administration (NASA).

TABLE OF CONTENTS

ACKNOWLEDGMENTS	iv
TABLE OF CONTENTS	v
LIST OF TABLES	ix
LIST OF ILLUSTRATIONS	x
SUMMARY	xii
I. INTRODUCTION	1
1.1 Introduction.....	1
1.2 APDs in Receivers	4
1.3 APDs in Imaging Systems	5
1.4 Background and History of Semiconductor Junctions used in APDs	5
1.4.1 Common Semiconductor Materials	5
1.4.2 Comparison of Semiconductor Junctions used in APDs.....	6
1.4.2.1 PN/PIN Junctions	6
1.4.2.2 Doped/Undoped MQW Junctions	7
ACKNOWLEDGMENTS	IV
ACKNOWLEDGMENTS	IV
ACKNOWLEDGMENTS	IV

ACKNOWLEDGMENTS.....	IV
4.4 Modeling Capabilities	63
ACKNOWLEDGMENTS.....	IV
ACKNOWLEDGMENTS.....	IV
ACKNOWLEDGMENTS.....	IV
PUBLICATIONS	133
PRESENTATION	133
ACKNOWLEDGMENTS.....	IV
VITA.....	148

LIST OF TABLES

Table 4-1	Summary of APD characterization capabilities	58
Table 5-1	Measured quantum efficiencies as a function of doping for a GaAs PIN	89
Table A-1	Default bandgap narrowing values	134
Table A-2	Default Recombination Parameters for AlGaAs	134
Table A-3	Impact ionization coefficients for GaAs	135
Table A-4	Default Concentration-dependent mobilities for GaAs	136

LIST OF ILLUSTRATIONS

Figure 1-1 (a) Schematic of a PIN photodiode under reverse bias, (b) electric field profile.....	8
Figure 1-2: Band diagram of a MQW structure under electron injection.....	9
Figure 2-1: Band-to-band tunneling process in a reversed biased pn junction	22
Figure 2-2 One-dimensional step junction.....	25
Figure 2-3 Step junction.....	25
Figure 2-4 Initial hole (a) and electron (b) carrier concentrations across the junction	25
Figure 2-5 Depletion region electrostatics	27
Figure 2-6 Energy band diagram for a PN junction at thermal equilibrium	28
Figure 3-1 Conduction/valence band diagrams for an unbiased PIN APD.....	38
Figure 3-2 Electric field profile for an unbiased PIN APD	39
Figure 3-3 Simulated dark and light IV plots for a PIN APD under reverse bias	41
Figure 3-4 Spectral output (zero reflection) for a 3 μm GaAs PIN (1 μm /1 μm /1 μm) APD	42
Figure 3-5 Photogeneration rate in a 3 μm GaAs PIN under 400, 632, & 850 nm illumination..	43
Figure 3-6 Electric field profile for an undoped 9-wells MQW APD under no bias	45
Figure 3-7 Conduction/valence band diagrams for an unbiased, undoped MQW APD	46
Figure 3-8 Difference in built-in e-field profile between a PIN and an undoped MQW	47
Figure 3-9 Electric field profile for a doped 9-wells MQW APD under no bias.....	50
Figure 3-10 Conduction/valence band diagrams for an unbiased, doped MQW APD	51
Figure 3-11 Electric field profile at zero bias for a doped 9-wells MQW APD where $p=1.2n$	52
Figure 3-12 Conduction/valence band plot for an unbiased, doped MQW APD where $p=1.2n$	53
Figure 3-13 Electric field profile at $V = -20$ V for a doped 9-wells MQW APD where $p=1.2n$	54

Figure 3-14	Band diagram at $V = -20$ V for an unbiased, doped MQW APD where $p=1.2n$	55
Figure 4-1	Cross Section of a MQW APD	57
Figure 4-2	Experimental Set-up for IV, CV & Noise Measurements	60
Figure 4-3	Vacuum Chamber used for Low Temperature Measurements.....	60
Figure 4-4	Experimental Set-Up for Lifetime Response Measurements of APDs	62
Figure 5-1	Dark IV Plots for the PIN and the doped-well MQW APD.....	68
Figure 5-2	CV plots for PIN and a doped MQW APDs	69
Figure 5-3	Carrier concentration profile vs depletion width for the PIN APD	70
Figure 5-4	Carrier concentration profile vs depletion width for the doped MQW APD.....	71
Figure 5-5	Gain vs. the ratio of reverse bias to breakdown voltage for the (a)MQW APD and (b)PIN APD	74
Figure 5-6	Plot used for determining gain per stage for a doped MQW APD	75
Figure 5-7	Dark current reduction as a result of surface treatment by sodium sulfide.....	78
Figure 5-8	Excess noise factor $F(M)$ vs. M for constant k' , from McIntyre's equation.....	83
Figure 5-9	Excess noise factors for both (a)the doped MQW APD, and (b)the PIN APD. Dashed lines correspond to McIntyre theoretical curves for $k=1,2,5,10$, and 50	85
Figure 5-10	Optical absorption coefficients for different materials at 77 K and 300 K.....	87
Figure 5-11	Spectral response measurement of an MBE grown PIN APD	91
Figure 5-12	Theoretical quantum efficiency plot (zero reflection) for a $3\text{ }\mu\text{m}$ GaAs PIN ($1\mu\text{m}/1\mu\text{m}/1\mu\text{m}$) APD where $p^+ = n^+ = 3 \times 10^{18}\text{ cm}^{-3}$	92
Figure 5-13	Theoretical plots showing possible improvement in quantum efficiency for a PIN APD through the introduction of a thin ($0.02\text{ }\mu\text{m}$) top p^{++} layer (all doping concentrations given are in cm^{-3})	93
Figure 5-14	Oscilloscope trace for a pulse response of a doped $2.5\text{ }\mu\text{m}$ MQW APD under no bias.....	99

Figure 5-15 Oscilloscope trace for a pulse response of a doped 2.5 μm MQW APD under low bias	100
Figure 5-16 Oscilloscope trace for a pulse response of a doped 2.5 μm MQW APD near breakdown	101
Figure 5-17 Depletion width plot showing the increase in the depletion region with applied bias for a largely undepleted doped MQW APD (2.5 μm).....	104
Figure 5-18 Oscilloscope trace for a pulse response of an undoped 2.5 μm PIN APD at zero bias	105
Figure 5-19 IV characteristics of tunneling breakdown	107
Figure 5-20 Measured gain as a function of temperature (in K) for a doped MQW APD	108
Figure 5-21 Experimental data and fits for a doped-well MQW APD.....	110
Figure 5-22 Intrinsic carrier densities of Ge, Si, and GaAs as a function of temperature	112
Figure 5-23 Experimental CV as a function of temperature for a doped-well MQW APD.....	116
Figure 5-24 Comparison of theoretical light IV data obtained for same APD MQW structure where the doping mismatch in the wells was varied between 0% and 100%.....	119
Figure 5-25 Theoretical electric field profiles of the same MQW APD structures with different doping imbalance in the wells ($V = -20\text{ V}$)	120
Figure 5-26 Calculated doping profiles versus depletion width using theoretical CV data obtained from AC analysis on similar MQW APDs with different doping imbalance in wells.....	121
Figure 5-27 Theoretical band diagrams of the same MQW APD structures with different doping imbalance in the wells ($V = -20\text{ V}$)	122
Figure 5-28 Calculated doping profile versus depletion width using experimental CV data from four 10-period doped-well MQW APDs.....	124
Figure 5-29 Experimental light IV curves obtained for all four 10-period doped-well MQW APDs for the same incident photon flux (electron injection).....	127

SUMMARY

The multiple quantum well (MQW) structure was first proposed in 1980 as a method to enhance the electron-hole ionization ratio in photodiodes beyond that typically found in bulk materials. Later in 1982, the doped MQW was introduced in order to further improve the electron ionization rate over that of holes. The desire for high performance optical detectors has resulted in several proposed MQW structures using different material systems in an attempt to optimize their gain, noise, and bandwidth characteristics.

In this work, a detailed experimental investigation and analysis were performed of the physical properties of advanced semiconductor junctions. The analysis includes a study of (1) the difference in the structure-induced multiplication gain between doped GaAs/AlGaAs MQW and PIN junctions, (2) the effect of variations in the doping profiles on the properties of doped MQW structures, (3) the effect of surface treatments on the dark current and gain characteristics, (4) the spectral and time response limitations of the structures, and (5) a complete modeling of the junction physics for the different structure types. All of these investigations were performed by conducting experimental measurements and theoretical simulations on new avalanche photodiode (APD) structures with built-in intrinsic (PIN), doped and undoped MQW structures.

In order to properly interpret the experimental data provided by the measurements, one needs to understand the correlation between such data and the physical parameters used in designing the structures. To accurately determine such a correlation usually requires the ability to grow and fabricate a large sample of structures produced under very similar conditions. Unfortunately, this is not very practical or even possible during

material growth and fabrication. Therefore, developing theoretical models which accurately predict the relationships between the input and the output parameters is essential to understanding the physics behind the data.

Most of the experimental data will be presented and analyzed for the first time in the GaAs/AlGaAs material system. The experimental results were compared to theoretical models, and were used to demonstrate, for the first time, the impact of the doping imbalance throughout the structure on the optical and electrical characteristics of a doped MQW structure. These models accurately predicted most of the external behavior displayed by these structures during experimental testing. In addition, various surface treatment techniques which enabled a dramatic reduction in the reverse bias dark current by as much as a factor of 1000 will be discussed. Furthermore, a new technique will be presented for improving the quantum efficiencies of these structures, and its effectiveness was verified through theoretical models.

CHAPTER I

INTRODUCTION

1.1 Introduction

Extensive studies have been performed on MQW junctions and structures because of their potential applications as avalanche photodetectors in optical communications and imaging systems.¹ The role of the avalanche photodiode is to provide for the conversion of an optical signal into charge. Knowledge of junction physics, and the various carrier generation/recombination mechanisms, is crucial for effectively optimizing the conversion process and increasing the structure's quantum efficiency. In addition, the recent interest in the use of APDs in imaging systems has necessitated the development of semiconductor junctions with low dark currents and high gains for low light applications. Because of the high frame rate and high pixel density requirements in new imaging applications, it is necessary to provide some front-end gain in the imager to allow operation under reasonable light conditions. Understanding the electron/hole impact ionization process, as well as diffusion and surface leakage effects, is needed to help maintain low dark currents and high gains for such applications. In addition, the APD must be capable of operating with low power, and low noise. Knowledge of the effects of various doping configurations and electric field profiles, as well as the excess noise resulting from the avalanche process, are needed to help maintain low operating bias and minimize the noise output.

To understand and quantify the physics of the different junctions, it is necessary to develop the structures into devices that could be studied on the macroscopic level and under different testing conditions. The various APD structures that have been developed for such a purpose include volume-doped wells/barriers multiple quantum well (MQW), delta-doped MQW, conventional PIN structures, and doped i-region PIN APD's. One way to quantify the gain and noise properties of an APD involves the measurement of the ratio of the impact ionization coefficients of electrons and holes. The ionization coefficient (measured in units of cm^{-1}) represents the inverse of the average distance traveled by a carrier between two consecutive ionizing collisions. In the majority of compound semiconductor materials, the electron ionization coefficient (α) is comparable to that of holes (β) and are both greater than zero. An ideal device where the hole-ionization coefficient (β) is equal to zero would have no multiplication noise and a performance similar to that of a photomultiplier tube (PMT) (gain $\sim 10^5$) where multiplication takes place with just one type of carriers. In bulk GaAs materials, k ($=\alpha/\beta$) is equal to about 1.67. In bulk Silicon, k approaches a value of 20, but still does not compare to the single-carrier multiplication characteristics of PMT. Despite the advantages of PMTs, these photodetectors tend to be cumbersome, have low quantum efficiencies, and operate at very high voltages (1,000-10,000 V). On the other hand, APDs are small, rugged, have relatively low-cost, and low operating voltages (10-100 V), as well as high quantum efficiencies. The desire for high performance optical detectors has resulted in several

proposed MQW APD structures using different material systems in an attempt to optimize their gain, noise, and bandwidth characteristics.

In theory, the value of k in a MQW structure is much higher than that typically found in bulk materials since it is possible to design a structure which selectively enhances the energy of one carrier over another. In order to design such a structure, as well as optimize the other properties of a photodetector such as gain, quantum efficiency and time response, one needs to understand the various physical mechanisms that take place inside the semiconductor structures. In addition, the impact of various growth conditions on the structure's behavior must be understood in order to consistently grow devices with similar optical and electrical properties.

Different experimental techniques including current-voltage (IV), capacitance-voltage (CV), gain, excess noise, spectral and pulse response measurements were used to extract information on the various optical and energy band related processes and mechanisms that control the performance of these structures. Gain studies, for example, provide insights into carrier multiplication via impact excitation of confined electrons out of the narrow-gap semiconductor layers. Similarly, noise studies allow the measure of the ratio of the impact ionization ratio of electrons to that of holes, which is determined by various structure parameters such as well/barrier widths and the doping concentrations in the wells. CV data is used to determine the carrier concentration profile versus depth throughout the structure, while spectral response provides insights about the structures' quantum efficiency and its sensitivity to various electromagnetic wavelengths. Finally, time response and device bandwidth measurements provide information on the carrier transit

time in the electric field region, carrier diffusion time in the undepleted absorption region, as well as carrier trapping at the heterojunction interfaces.

1.2 APDs in Receivers

One common application of the avalanche photodiode structure involves using the device as an optical receiver in communication systems. The increasing requirements of high bit rate fiber communication networks require the development of suitable high performance optoelectronic components. The photodetector (APD) is used at the receiving end of the fiber to convert the optical signal into an electrical current which can be processed to recover the original data. For low bit rate and short range applications such as a local area network (LAN), the device performance requirements are only moderately stringent. For high bit rate, long distance applications and bulk data transmission (high resolution graphics/sound, high definition television), the device performance requirements become far more demanding in terms of speed, size, reliability, etc.

High speed electronics have made it possible to encode/decode data at continuously faster rates. The recent development of state of the art narrow linewidth lasers and low dispersion optical fibers has made it possible to transmit light at high bit rates for longer distances with minimum degradation in signal quality. With these developments, the limiting factors in fiber optical systems seems to be determined by the receiver sensitivity and speed performance. This provides considerable incentive to study

and develop high performance optical detectors that are designed to handle such stringent requirements.

1.3 APDs in Imaging Systems

Another related application of APDs is in the development of imaging systems to be used both in the visible and non-visible portions of the spectrum. While fiber optic communications are usually limited to the 1.3-1.55 μm spectral range, imaging systems can be developed using a wide range of materials to operate in a variety of optical ranges depending on the application in question. The role of the APD in such a system is to capture the optical images and to amplify the signal using its built-in gain properties. One such system is currently under development by the Georgia Tech Research Institute to be used in a high definition television (HDTV) imaging system. This system uses a 1920 x 1080 imaging array of superlattice GaAs/AlGaAs APDs as an image capture mechanism operating at wavelengths below 1 μm .

1.4 Background and History of Semiconductor Junctions used in APDs

1.4.1 Common Semiconductor Materials

Silicon APDs are one of the most widely used photodetector devices in the spectral range below 1.1 μm . Extensive research has been conducted in this area and the behavior of Si junctions is fairly well understood^{2,3,4}. Unfortunately, these devices are not very useful for fiber optic communication because of the high signal dispersion and attenuation at these wavelengths. Dispersion in fibers is zero around 1.3 μm , and

attenuation is minimized near 1.5 μm thereby requiring the use of semiconductor materials that will operate more efficiently at these wavelengths. Ge APDs have been developed to operate at these wavelengths, but they were found to have high dark currents and equal electron and hole impact ionization rates which limits their gain/noise properties. For that reason, recent work has been focused largely on lattice-matched III-V materials with adjustable energy gaps that can be customized to optimally operate at a wide range of wavelengths throughout the visible and near infrared part of the spectrum. Such material systems include ternary alloys such as $\text{Al}_x\text{Ga}_{1-x}\text{As}$ and quaternary alloys such as $\text{In}_x\text{Ga}_{1-x}\text{As}_y\text{P}_{1-y}$ where x and y are the mole fractions of the group III and V elements⁵. The complex MQW structures require a great degree of doping control as well as high interface quality during material growth. The progress realized in GaAs/AlGaAs growth by molecular beam epitaxy (MBE) during the past fifteen years makes this material system an ideal candidate for MQW structures.

1.4.2 Comparison of Semiconductor Junctions used in APDs

1.4.2.1 PN/PIN Junctions

Some of the first semiconductor junctions that were developed to be used as photodetectors were the PN/PIN structures. The PIN “APD” was first proposed by Read⁶ in 1958 and it operates in a manner similar to a PIN “photodiode”, with the exception that the primary photocurrent caused by the photoelectric effect is amplified within the same device. An APD-based receiver is more sensitive than a PIN photodiode-based receiver, provided the APD has sufficient bandwidth for the application⁷. However, an APD’s

bandwidth is significantly less than that of an equivalent PIN photodiode. In addition, as previously mentioned, there is excess noise associated with the avalanche multiplication process. This can limit the maximum useful gain of the APD to the point where the APD noise becomes comparable to the first stage amplifier noise⁷. In addition, the presence of high dark currents usually presents a limiting factor preventing the further increase in a device's photocurrent gain beyond avalanche breakdown. The PN/PIN junctions are simple to analyze using a one-dimensional approximation which simplifies the equations of state to a single spatial variable and enables closed-form solutions of the differential equations. A typical PIN structure is shown in Figure 1-1, and is composed of a highly doped p^+ layer, followed by an intrinsic layer and a highly doped n^+ layer. Electron or hole injection is accomplished by shining light on the p^+ or n^+ regions, respectively. Single-carrier injection can be obtained by designing the thickness of the contact region to be small enough to allow diffusion of carriers to the high field region, and yet large enough to prevent direct absorption of light in that region. In GaAs, the ideal contact region is generally between 1 and 3 μm depending upon the wavelength of the incident light.⁸

1.4.2.2 Doped/Undoped MQW Junctions

The MQW structure (Figure 1-2) was first proposed in 1980 by Chin et al.⁹ and Capasso et al.¹⁰ (1982) as a method to enhance the electron-hole ionization ratio beyond that in bulk materials. Later in 1982, Blauvelt¹¹ proposed the doped MQW structure which incorporates built-in field layers in the avalanche region in an attempt to further increase k . Since then, various new ideas have been proposed to help increase (or decrease) k . These proposals are all based on one or more of the following principles:

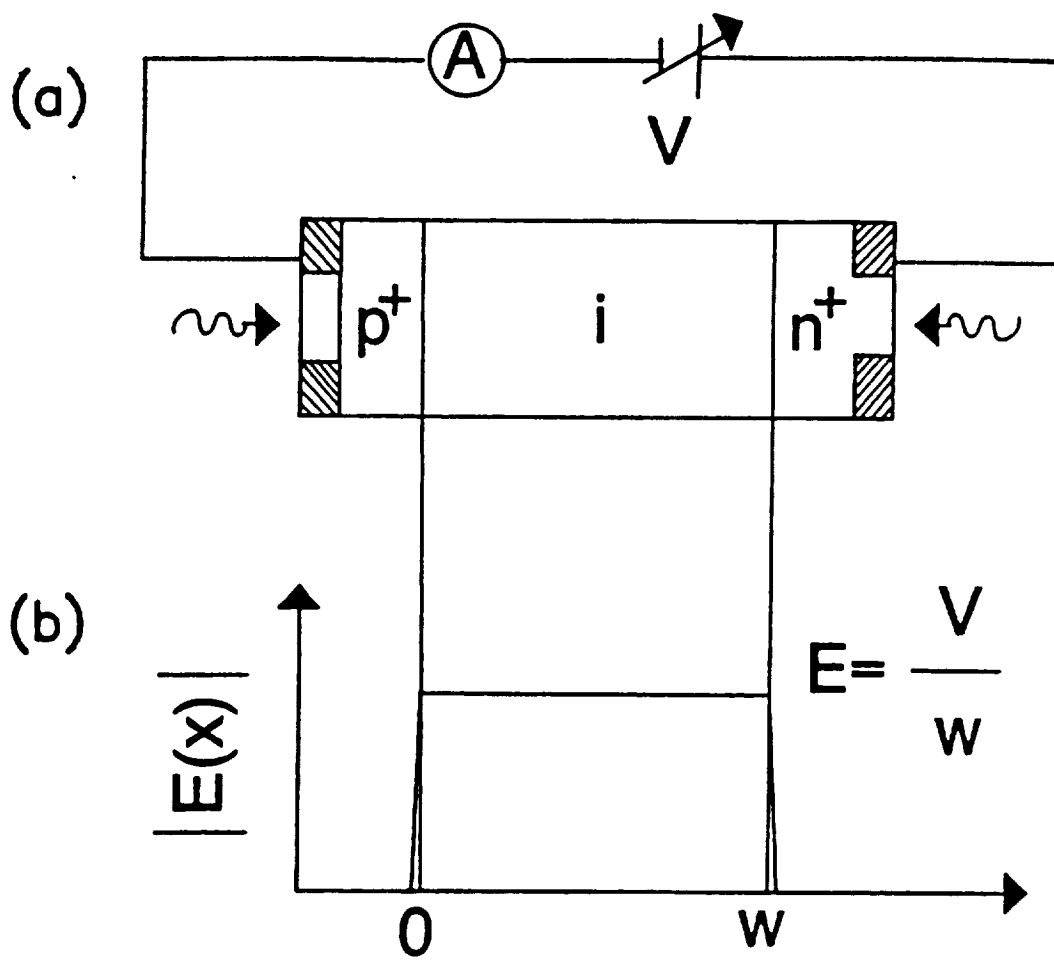


Figure 1-1: (a) Schematic of a PIN photodiode under reverse bias, (b) electric field profile

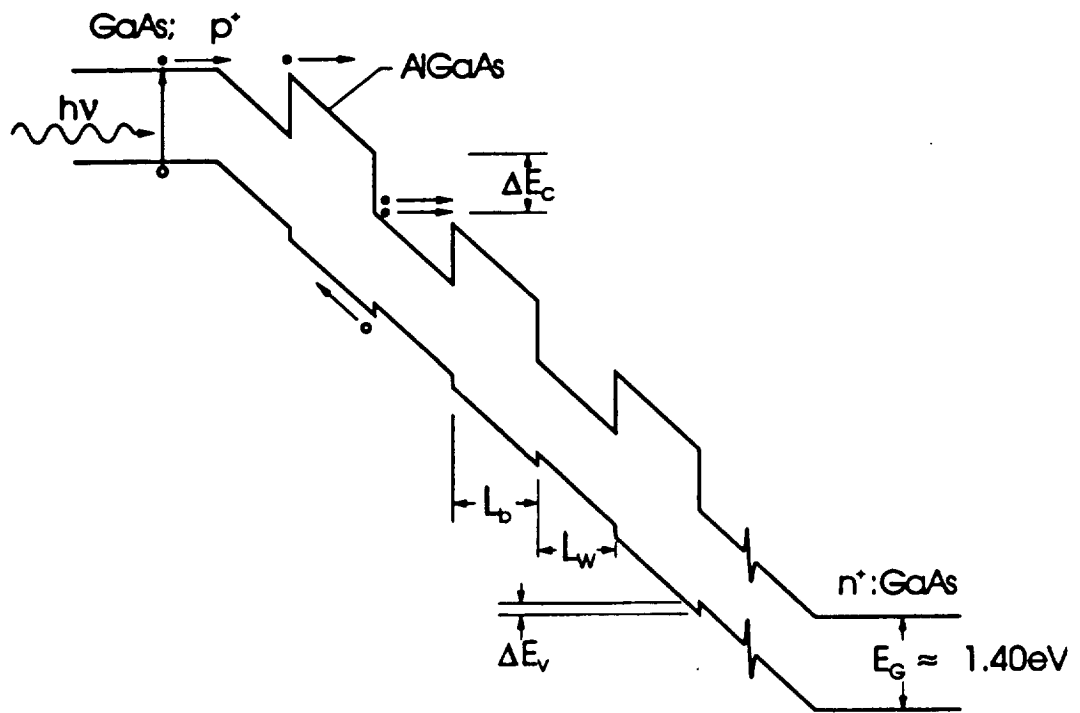


Figure 1-2: Band diagram of a MQW structure under electron injection

- The elimination of the “feed-back” process by confining the carriers in potential wells formed between two heterojunctions¹².
- The utilization of the difference in the ionization energies and the quasi-electric fields between the electrons and holes. These differences are incorporated into the material by gradually changing the energy gap and creating a “graded-gap APD”¹³.
- The utilization of the asymmetries between the conduction and valence band offsets present in composite III-V semiconductors (i.e, MQW, “staircase” APDs, etc.)^{14,15,16}
- The utilization of periodic doping layers in the MQW structure (PN heterojunction, doped-barrier MQW, doped-well MQW, delta-doping)^{17,18}

In 1982, Capasso conducted experimental measurements on a GaAs/Al_{0.45}Ga_{0.55}As MQW structure where he observed a value of α three times larger than that in bulk GaAs. He explained the results by suggesting that the conduction band discontinuity helps to contribute to the total ionization energy of electrons by reducing the impact ionization threshold energy by a value equal to ΔE_c . On the other hand, the much smaller valence band discontinuity (ΔE_v) does not significantly reduce the impact ionization threshold energy of holes. This results, according to Capasso, in increasing the value of α while keeping that of β relatively unchanged with respect to that found in bulk GaAs. However, as Aristin⁸ pointed out, according to the conservation of energy principle, there is no reason for the electron ionization coefficient to be increased over any given period since the total gain of energy is zero. This has to be true since the energy gain at the AlGaAs/GaAs interface is offset by an equal loss at the GaAs/AlGaAs interface.

Therefore, from a conservation of energy perspective, it would seem as if an overall gain of energy is only possible in structures where the energy gap is continuously graded¹³.

In 1987, Brennan et al.¹⁹ were the first to explain the origin of the observable increase in the electron impact ionization coefficient α_{MQW} in the MQW structure. Using a simplified analytical expression of $\alpha(E)$, they have shown that, by replacing the square potential wells by a series of Fourier functions $V(z)$, the final expression for α_{MQW} is always higher than that found in bulk GaAs materials. Such an increase is the result of the exponential dependence of α on the periodic electric field in the MQW structure. Therefore, even though the science itself is not yet very well understood, it became clear that the artificially enhanced ionization process inherent in MQW structures holds the key for designing optoelectronic devices with properties that could be optimized for a given application.

REFERENCES

- [1] F. Capasso, *Semiconductors and Semimetals*, edited by R. K. Willardson and A. C. Beer (Academic, New York, 1985), Vol. 22, part D, p.2
- [2] J. Gower, *Optical Communication Systems*, Prentice/Hall, London, 1984
- [3] P. P. Webb, R.J. McIntyre, and J. Conradi, "Properties of avalanche photodiodes", *RCA Review* 35, 234 (1974).
- [4] S.M. Sze, *Physics of Semiconductor Devices*, 2nd ed., Wiley, 1981.
- [5] Y. Suematsu, K. Iga and K. Kishino, *GaInAsP Alloy Semiconductors*, Ch. 14, ed. T. Pearsall, Wiley, 1982.
- [6] W. T. Read, Jr., "A proposed high-frequency, negative resistance diode", *Bell System Technical Journal* 401, March, 1958.
- [7] J. C. Campbell, in "Optoelectronics Technology and Lightwave Communications Systems," edited by Chinlon Lin (1989), Ch. 14.
- [8] P. Aristin, "Fabrication et Caracterization de Photodiodes a Avalanche a Puits Quantiques Multiples", Ph.D. thesis, January 1992.
- [9] R. Chin, N. Holonyak, G. E. Stillman, J. Y. Tsang, and K. Hess, *Appl. Phys. Lett.* 16, 467 (1980).
- [10] F. Capasso, W. T. Tsang, A. L. Hutchinson, and P. G. Williams, *Appl. Phys. Lett.* 40, 38 (1982).
- [11] H. Blauvelt, S. Margalit, and A. Yariv, *Electron. Lett.* 18, 375 (1982).
- [12] J. D. Gordon, R. E. Nahory, M. A. Pollack, and J. M. Warlock, *Electron. Lett.* 15, 518 (1979).
- [13] F. Capasso, W. T. Tsang, A. L. Hutchinson, and P. W. Foy, *Conf. Ser. - Inst. Phys.*, 63, 473 (1982).
- [14] R. Chin, N. Jr. Holonyak, G. E. Stillman, J. T. Tang, and K. Hess, *Electron. Lett.* 16, 467 (1980).

-
- [15] F. Capasso, W. T. Tsang, A. L. Hutchinson, and G. F. Williams, Tach. Dig.-Inst. Electron Devices Meet., 1981, Washington, DC, 284 (1981)
 - [16] F. Capasso, W. T. Tsang, and G. F. Williams, IEEE Trans. Electron Dev. ED-30, 381 (1983)
 - [17] H. Blauvelt, S. Margalit, and A. Yariv, Electron. Lett. 18, 375 (1982)
 - [18] K. Brennan, IEEE Trans. Electron Dev. ED-34, 1658 (1987)
 - [19] K. Brennan, K. Hess, F. Capasso, Appl. Phys. Lett. 50, 1897 (1987)

CHAPTER II.....	12
2.1 <u>INTRODUCTION</u>	12
2.2 <u>BASIC SEMICONDUCTOR EQUATIONS</u>	12
2.2.1 <u>Poisson and continuity equations</u>	12
2.2.2 <u>Position-dependent current density equations</u>	13
2.3 <u>CARRIER STATISTICS</u>	15
2.3.1 <u>Boltzman Statistics</u>	15
2.3.2 <u>Fermi-Dirac Statistics</u>	17
2.3.3 <u>Carrier Recombination Statistics</u>	18
2.3.4 <u>Carrier Generation</u>	19
2.3.5 <u>Carrier Mobility Modeling</u>	22
2.4 <u>PN/PIN JUNCTION EQUILIBRIUM ELECTROSTATICS</u>	23
2.4.1 <u>Built-in Potential Calculation</u>	29
2.4.2 <u>Depletion Region Calculation</u>	29
2.4.3 <u>Junction Capacitance</u>	31
2.4.4 <u>Multiplication and Ionization Coefficients</u>	32
2.5 <u>NUMERICAL METHODS</u>	33

CHAPTER II

THEORETICAL MODELING AND PHYSICS OF SEMICONDUCTOR JUNCTIONS

2.1 Introduction

The modeling of the various semiconductor junctions and APD devices was conducted using Silvaco's AtlasII® device modeling framework which works by solving the basic Poisson and continuity equations for electrons and holes. Poisson's equations describe variations in the electrostatic potential and how they relate to local charge densities while the continuity equations represent the effect of carrier transport and the recombination/generation processes on the material charge densities.

2.2 Basic Semiconductor Equations

2.2.1 Poisson and Continuity Equations

The electrical properties of semiconductor junctions can be described by the following Poisson's equation :

$$\text{div}(\epsilon \nabla \psi) = -q(p - n + N_D^+ - N_A^-) - \rho_F \quad [2-1]$$

as well as the following carrier continuity equations for both electrons and holes :

$$\begin{aligned}\frac{\partial n}{\partial x} &= \frac{1}{q} \nabla \bar{J}_n - U_n \\ \frac{\partial p}{\partial x} &= \frac{1}{q} \nabla \bar{J}_p - U_p\end{aligned}\tag{2-2}$$

where ψ is the intrinsic Fermi potential, N_D^+ and N_A^- represent the donor and acceptor ionized impurity concentrations, ρ_F is the fixed charge density, U_n and U_p are the net electron and hole recombination rates, respectively.

The modeling program solves the above three partial differential equations for the electrostatic potential, ψ , and for the electrons and hole concentrations, n and p , respectively.

2.2.2 Position-dependent Current Density Equations

The electron and hole current density equations can be written in terms of carrier concentrations, n and p , carrier mobilities, μ_n and μ_p , and the quasi-Fermi potentials for electrons and holes, ϕ_n and ϕ_p :

$$\begin{aligned}\bar{J}_n &= -\mu_n n \nabla \phi_n \\ \bar{J}_p &= -\mu_p p \nabla \phi_p\end{aligned}\tag{2-3}$$

where,

$$\begin{aligned}\phi_n &= -\frac{1}{q} E_{FN} \\ \phi_p &= -\frac{1}{q} E_{FP}\end{aligned}\tag{2-4}$$

and the Fermi energies are expressed as:

$$\begin{aligned} E_{FN} &= E_c + kT \ln \frac{n}{N_c} + kT \ln \gamma_n \\ E_{FP} &= E_v - kT \ln \frac{p}{N_v} + kT \ln \gamma_p \end{aligned} \quad [2-5]$$

The last terms in the above two equations are due to the influence of Fermi-Dirac statistics and are given later by equations [2-18] and [2-19] in section 2.3.2. In the case of Boltzman's statistics (see section 2.3.1), $\gamma_n = \gamma_p = 1$. In multi-layered heterojunction structures such as the ones used in MQW APDs, the energy band diagram is not uniform. The position-dependent conduction and valence band energies can therefore be written as:

$$\begin{aligned} E_c &= q(\psi_0 - \psi) - \chi \\ E_v &= q(\psi_0 - \psi) - \chi - E_g \end{aligned} \quad [2-6]$$

where,

χ is the position-dependent electron affinity, E_g is the position-dependent bandgap, and ψ_0 is some reference potential which can be selected in the form:

$$\psi_0 = \frac{\chi_r}{q} + \frac{kT}{q} \ln \frac{N_{cr}}{n_{ir}} = \frac{\chi_r + E_g}{q} - \frac{kT}{q} \ln \frac{N_{vr}}{n_{ir}} \quad [2-7]$$

where n_{ir} is the intrinsic carrier concentration of the arbitrarily selected reference material, and r is an index indicating that all of the parameters are taken from the reference material.

Consequently, by combining equations [2-3]-[2-7] with [2-18] and [2-19] the following position-dependent drift-diffusion current densities can be obtained:

$$\begin{aligned}\bar{J}_n &= kT\mu_n \nabla n - q\mu_n n \nabla \left(\psi + \frac{kT}{q} \ln \gamma_n + \frac{\chi}{q} + \frac{kT}{q} \ln \frac{N_c}{n_{ir}} \right) \\ \bar{J}_p &= -kT\mu_p \nabla n - q\mu_p p \nabla \left(\psi - \frac{kT}{q} \ln \gamma_p + \frac{\chi + E_g}{q} - \frac{kT}{q} \ln \frac{N_v}{n_{ir}} \right)\end{aligned}\quad [2-8]$$

2.3 Carrier Statistics

The electron and hole concentration densities can be defined using Fermi-Dirac distributions and a parabolic density of states giving :

$$\begin{aligned}n &= N_c F_{1/2} \left\{ \frac{1}{kT} [E_{Fn} - E_C] \right\} \\ p &= N_v F_{1/2} \left\{ \frac{1}{kT} [E_V - E_{Fp}] \right\}\end{aligned}\quad [2-9]$$

where N_v and N_c are the effective densities of states in the valence and conduction bands, E_v and E_C are the valence and conduction bands energies, and $E_{Fn} = -q\phi_n$ and $E_{Fp} = -p\phi_p$ are the electron and hole Fermi energies. The Fermi-Dirac integral of order one-half is defined as :

$$F_{1/2}(\eta_F) = \frac{2}{\sqrt{\pi}} \int_0^{\infty} \left[\frac{\eta^{1/2}}{1 + \exp(\eta - \eta_F)} \right] d\eta \quad [2-10]$$

2.3.1 Boltzman Statistics

For the range of operation of most semiconductor devices, the electron and hole concentration equations can be simplified using Boltzmann statistics as follows :

$$\begin{aligned}
n &\approx N_c \exp\left\{\frac{1}{kT}[E_{Fn} - E_c]\right\} = n_i \exp\left[\frac{q}{kT}(\psi - \phi_n)\right] \\
p &\approx N_v \exp\left\{\frac{1}{kT}[E_v - E_{Fp}]\right\} = n_i \exp\left[\frac{q}{kT}(\phi_p - \psi)\right]
\end{aligned}
\tag{2-11}$$

In the case when band-gap narrowing can be neglected, the intrinsic carrier concentration is expressed by :

$$n_i(T) = \sqrt{N_c N_v} \exp(-E_g / 2kT) \tag{2-12}$$

The band-gap and effective density of states have the following temperature dependencies according to Sze²⁰:

$$E_g(T) = E_g(0) - \frac{\alpha T^2}{T + \beta} = E_g(300) + \alpha \left[\frac{300^2}{300 + \beta} - \frac{T^2}{T + \beta} \right] \tag{2-13}$$

$$N_c(T) = 2 \left(\frac{2\pi m_{de} kT}{h^2} \right)^{3/2} = \left(\frac{T}{300} \right)^{3/2} N_c(300) \tag{2-14}$$

$$N_v(T) = 2 \left(\frac{2\pi m_{dv} kT}{h^2} \right)^{3/2} = \left(\frac{T}{300} \right)^{3/2} N_v(300) \tag{2-15}$$

m_{de} and m_{dv} are the density-of-state effective masses of the valence and conduction bands, respectively.

The intrinsic Fermi potential is given by :

$$-q\psi_i = E_c - \frac{E_g}{2} - \frac{kT}{2} \ln \frac{N_c}{N_v} \tag{2-16}$$

Under Boltzman statistics, the correlation between the mobilities and diffusivities in Equation [2-4] is given by the following Einstein's relationships :

$$\begin{aligned} D_n &= \frac{kT}{q} \mu_n \\ D_p &= \frac{kT}{q} \mu_p \end{aligned} \quad [2-17]$$

2.3.2 Fermi-Dirac Statistics

The AtlasII modeling program uses both Boltzman and Fermi-Dirac statistics. The form of the density of states equations can be adjusted by introducing degeneracy factors γ_n and γ_p given as :

$$\gamma_n = F_{1/2} \left\{ \frac{1}{kT} [E_{Fn} - E_C] \right\} \exp \left[-\frac{1}{kT} (E_{Fn} - E_C) \right] \quad [2-18]$$

$$\gamma_p = F_{1/2} \left\{ \frac{1}{kT} [E_V - E_{Fp}] \right\} \exp \left[-\frac{1}{kT} (E_V - E_{Fp}) \right] \quad [2-19]$$

and the density of states equations can be rewritten as :

$$n = N_c \gamma_n \exp \left(\frac{E_{Fn} - E_C}{kT} \right) \quad [2-20]$$

$$p = N_v \gamma_p \exp \left(\frac{E_V - E_{Fp}}{kT} \right) \quad [2-21]$$

When Fermi-Dirac statistics are used, Einstein's relationships must be modified as follows

:

$$D_n = \frac{\left(\frac{kT}{q} \mu_n\right) F_{1/2} \left\{ \frac{q}{kT} [E_{F_n} - E_c] \right\}}{F_{-1/2} \left\{ \frac{q}{kT} [E_{F_n} - E_c] \right\}} \quad [2-22]$$

$$D_p = \frac{\left(\frac{kT}{q} \mu_p\right) F_{1/2} \left\{ \frac{q}{kT} [E_v - E_{F_p}] \right\}}{F_{-1/2} \left\{ \frac{q}{kT} [E_v - E_{F_p}] \right\}}$$

2.3.3 Carrier Recombination Statistics

The modeling program supports the following three recombination mechanisms :

a) Shockley-Read-Hall:

$$U_{SRH} = \frac{pn - n_{ie}^2}{\tau_p \left[n + n_{ie} \exp\left(\frac{E_t - E_i}{kT}\right) \right] + \tau_n \left[p + n_{ie} \exp\left(\frac{E_i - E_t}{kT}\right) \right]} \quad [2-23]$$

b) Auger: $U_{Auger} = c_n (pn^2 - nn_{ie}^2) + c_p (np^2 - pn_{ie}^2) \quad [2-24]$

c) Optical Recombination:

$$U_{optical} = C_{opt} (pn - n_{ie}^2) \quad [2-25]$$

where E_i is the intrinsic Fermi energy, E_t is the trap energy level, and n_{ie} is the effective intrinsic concentration. C_{opt} , c_n , and c_p are material recombination parameters for the GaAs/AlGaAs systems. The electron and hole lifetime parameters, τ_n and τ_p used in Equation [2-19] can be functions of the impurity concentrations as follows²¹ :

$$\tau_n(x,y) = \frac{\tau_{n0}}{1 + N(x,y) / N_{SRH-n}} \quad [2-26]$$

$$\tau_p(x,y) = \frac{\tau_{p0}}{1 + N(x,y) / N_{SRH-p}} \quad [2-27]$$

where $N(x,y)$ is the localized total impurity concentration. N_{SRH-n} , N_{SRH-p} , τ_{p0} , and τ_{n0} are material parameters.

2.3.4 Carrier Generation

In addition to photogeneration of electron-hole pairs, the model can be modified to incorporate other carrier generation mechanisms such as impact ionization and generation due to band-to-band tunneling using the models presented in the following two sections.

2.3.4.1 Impact Ionization

Avalanche multiplication due to impact ionization is the most important process during junction breakdown. Under the effect of an electric field, a carrier (electron or hole) acquires sufficient energy that, upon impact with the lattice, an electron-hole pair (e-h) is produced. These new carriers are accelerated by the field and can themselves acquire high-energy, causing more e-h pairs to be created. If insufficient energy is transferred to the lattice, impact ionization does not occur, and the energy is lost, usually by heating. In addition, carriers can lose energy through non-ionizing scattering events before acquiring sufficient energy to ionize. The scattering rate can be different for electrons and holes.

The electron-hole generation rate due to impact ionization in the field region was modeled according to Selberherr²² as follows :

$$G = \alpha_n \frac{|J_n|}{q} + \alpha_p \frac{|J_p|}{q} \quad [2-28]$$

where α_n and α_p are the electron and hole ionization rates which can be expressed as a function of the electric field as :

$$\alpha_n = \alpha_n^\infty \cdot \exp \left[- \left(\frac{E_n^{crit}}{E} \right)^{\beta_n} \right] \quad [2-29]$$

$$\alpha_p = \alpha_p^\infty \cdot \exp \left[- \left(\frac{E_p^{crit}}{E} \right)^{\beta_p} \right] \quad [2-30]$$

where E is the component of the electric field in the current flow direction. All other impact ionization parameters are material dependent and are given in Appendix A for the AlGaAs material system.

2.3.4.2 Band-to-Band Tunneling

In the presence of a high electric field, electrons can tunnel from the valence band to the conduction band in a reverse-biased junction. The criteria for tunneling are met in a high-field junction where the depletion width is small, and the potential barrier (in a MQW structure) is very thin. This process is shown for a p-n junction in Figure 2-1 where the conduction band edge on the n-side (E_{cn}) drops below the valence band edge on the p-side

(E_{vp}), providing empty energy states for the electrons to tunnel into. Tunneling will increase the electron generation rate yielding larger reverse currents. The quantum mechanical tunneling transmission probability is given by²³:

$$T_t = \left[1 + \frac{E_0^2 \sinh^2 \kappa W}{4E(E_0 - E)} \right]^{-1} \quad [2-31]$$

where E_0 and W are the barrier height and thickness, E is the energy of the carrier, and:

$$\kappa \equiv \sqrt{\frac{2m(E_0 - E)}{\hbar^2}} \quad [2-32]$$

The tunneling current density is given by²⁴ :

$$J_t = \frac{\sqrt{2m^*} q^3 \xi V}{4\pi^2 \hbar^2 E_g^{1/2}} \exp\left(-\frac{4\sqrt{2m^*} E_g^{3/2}}{3q\xi\hbar}\right) \quad [2-33]$$

where V is the applied voltage, m^* is the effective mass, E_g is the bandgap, and ξ is the junction electric field. The resulting tunneling generation rate can be expressed by the Klaasen model as:

$$G_{bbt} = A_{bbt} E^\gamma \exp\left(-\frac{B_{bbt}}{E}\right) \quad [2-34]$$

where E is the electric field magnitude, A_{bbt} , B_{bbt} , and γ are material constants.

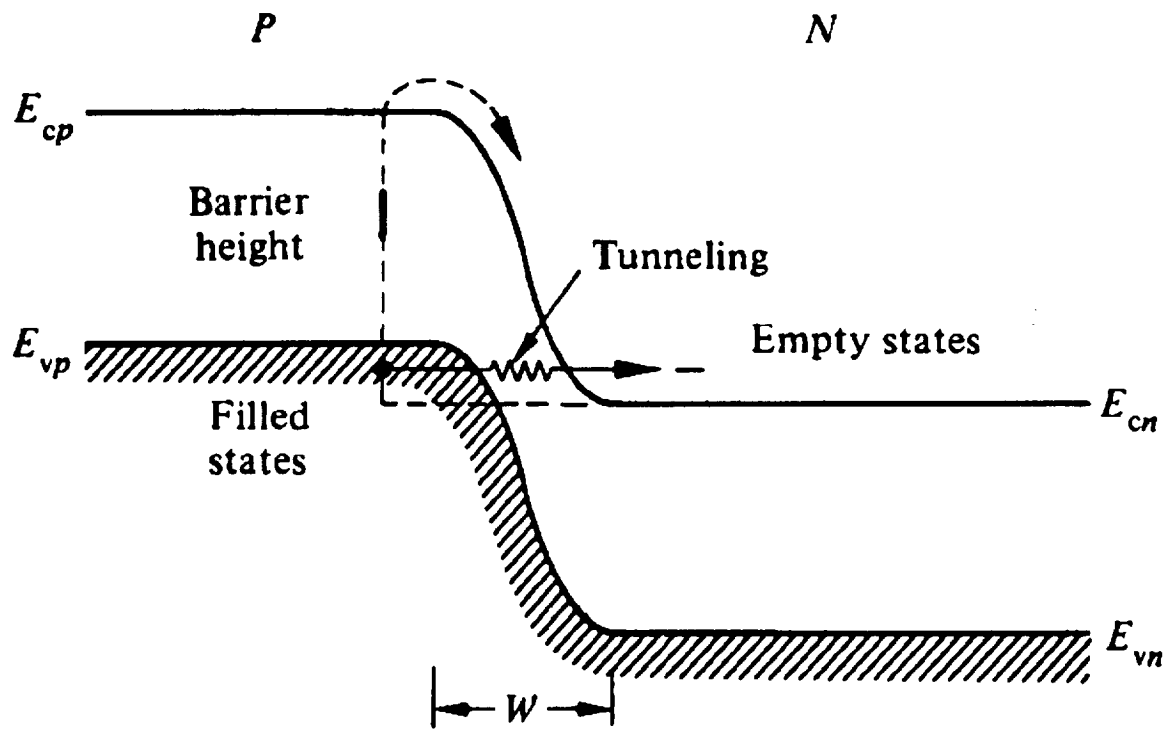


Figure 2-1: Band-to-band tunneling process in a reversed biased pn junction²⁵

2.3.5 Carrier Mobility Modeling

Throughout the junction, carriers are accelerated by the local electric field, but lose some momentum due to various scattering mechanisms. These scattering processes are a result of impurities, lattice vibrations (phonons), other carriers, surfaces, and other material imperfections. The macroscopic mobility parameters used in the current densities equation [2-3] express the effects of these microscopic phenomena. These mobilities are functions of the local electric field, the lattice temperature, the doping concentration, etc. At low enough fields, the mobility has a characteristic low-field value usually denoted by μ_0 . This is a result of the fact that carriers are almost in equilibrium with the lattice. The value of μ_0 is impacted by phonon and by impurity scattering. When the temperature of the lattice increases, phonon scattering increases, and the value of μ_0 decreases. Similarly, when the doping concentration increases, impurity scattering increases which causes μ_0 to decrease as well. On the other hand for high fields, the carrier mobility declines. This is because carriers with high energies can take part in a wider range of scattering processes. The mobility models used in our simulation are both doping- and field-dependent. The analytical mobility functions and data are provided in section A.5 of Appendix A.

2.4 PN/PIN junction equilibrium electrostatics

Figure 2-2 shows a one-dimensional step pn junction which will be used for the purpose of the analysis. In order to obtain a closed-form solution for such a junction, the following assumptions must be made²⁵:

- a) The device is one-dimensional (see Figure 2-2)

- b) At $x=0$, there is an abrupt metallurgical junction.
- c) The p and n layers are uniformly doped with a step junction from N_A to N_D (Figure 2-3)
- d) The p and n contacts are perfect ohmic contacts and are far separated from the junction.

Under equilibrium conditions, the “hypothetical” p and n initial carrier concentrations can be depicted as shown in Figure 2-4. Because of the concentration imbalance between the two sides of the junction, the carriers would begin to diffuse in order to make their distribution more homogeneous throughout the material. Therefore, the holes will tend to diffuse from the p- to the n-side and the electrons from the n- to the p-side leaving behind ionized acceptor (N_A^-) and donor (N_D^+) atoms. As a result, a net charge density (see Figure 2-5(b)) will be created by the reduction of the majority carrier concentrations.

The net charge density leads to the creation of an electric field and a built-in potential difference across the junction which inhibit further diffusion of the majority carriers. From Gauss’s law, the electric field can be determined as follows:

$$\xi(x) = \frac{1}{K_s \epsilon_0} \int_{-\infty}^x \rho(x) dx, \quad (V / cm) \quad [2-35]$$

where,

K_s = relative semiconductor dielectric constant

$\epsilon_0 = 8.854 \times 10^{-14}$, (farad/cm)

$\rho(x) = q(p - n + N_D - N_A)$, (coulombs/cm³)

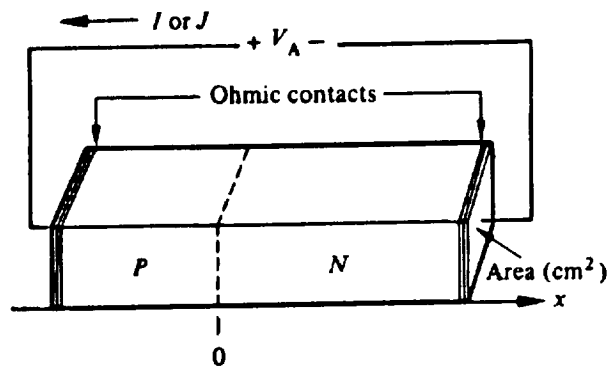


Figure 2-2: One-dimensional step junction²⁵

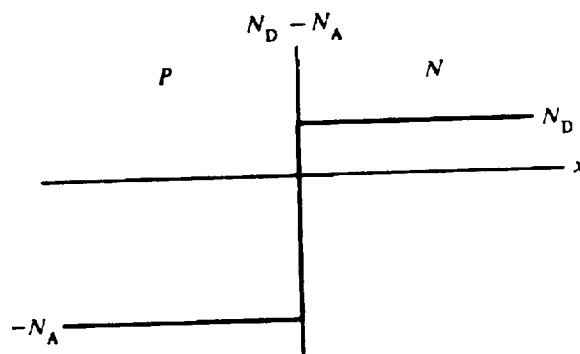


Figure 2-3: Step junction²⁵

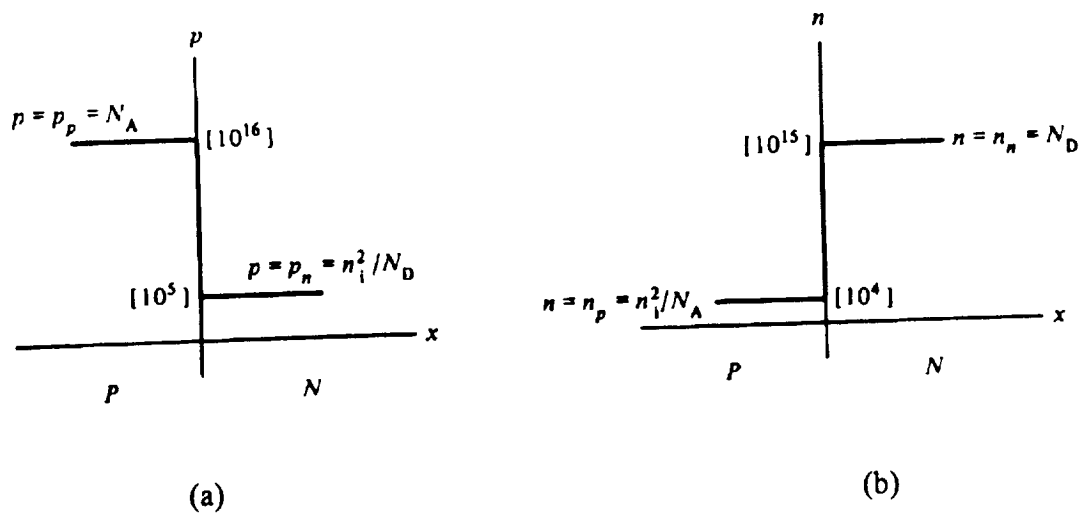


Figure 2-4: Initial hole (a) and electron (b) carrier concentrations across the junction²⁵

i.e, $\rho(x)$ is the imbalance between the charge carriers and the ions. Therefore, the electric field can be obtained through a graphical integration of Figure 2-5(b) which results in the profile shown in Figure 2-5(c). Subsequently, the potential gradient within the depletion region and across the device can be calculated from electromagnetic field theory as follows :

$$V(x) = - \int_{-\infty}^x \xi(x) dx \quad [2-36]$$

where the potential reference was chosen such that $V(-\infty)=0$. The potential diagram is shown in Figure 2-5(d). Therefore, there exists a built-in potential V_{bi} across the depletion region at equilibrium which results in energy band bending between the two sides of the junction and an energy difference equal to qV_{bi} as seen in Figure 2-6.

The net charge density can be derived from the energy band diagram using:

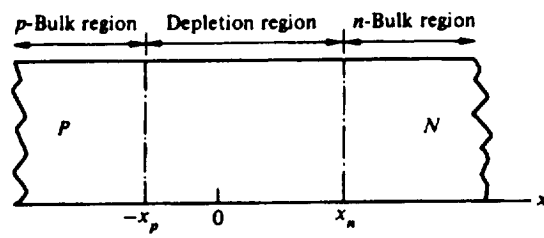
$$\frac{d\xi}{dx} = \frac{\rho}{K_s \epsilon_0} \quad [2-37]$$

and,

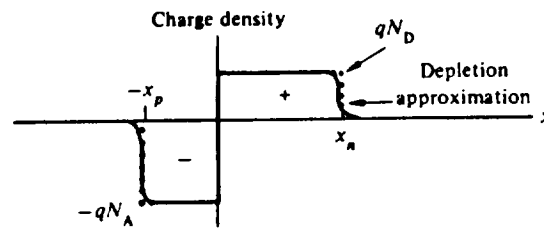
$$\xi = \left(\frac{1}{q} \right) \left(\frac{dE_i}{dx} \right) \quad [2-38]$$

which yields,

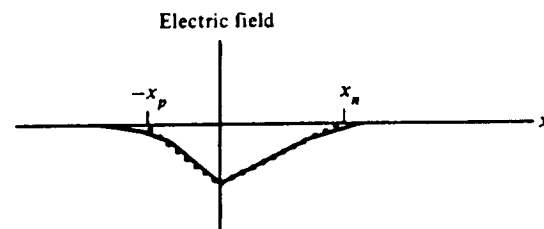
$$\rho = \left(\frac{K_s \epsilon_0}{q} \right) \left(\frac{d^2 E_i}{dx^2} \right) \quad [2-39]$$



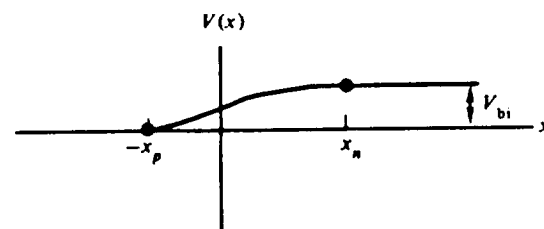
(a)



(b)



(c)



(d)

Figure 2-5 : Depletion region electrostatics²⁵

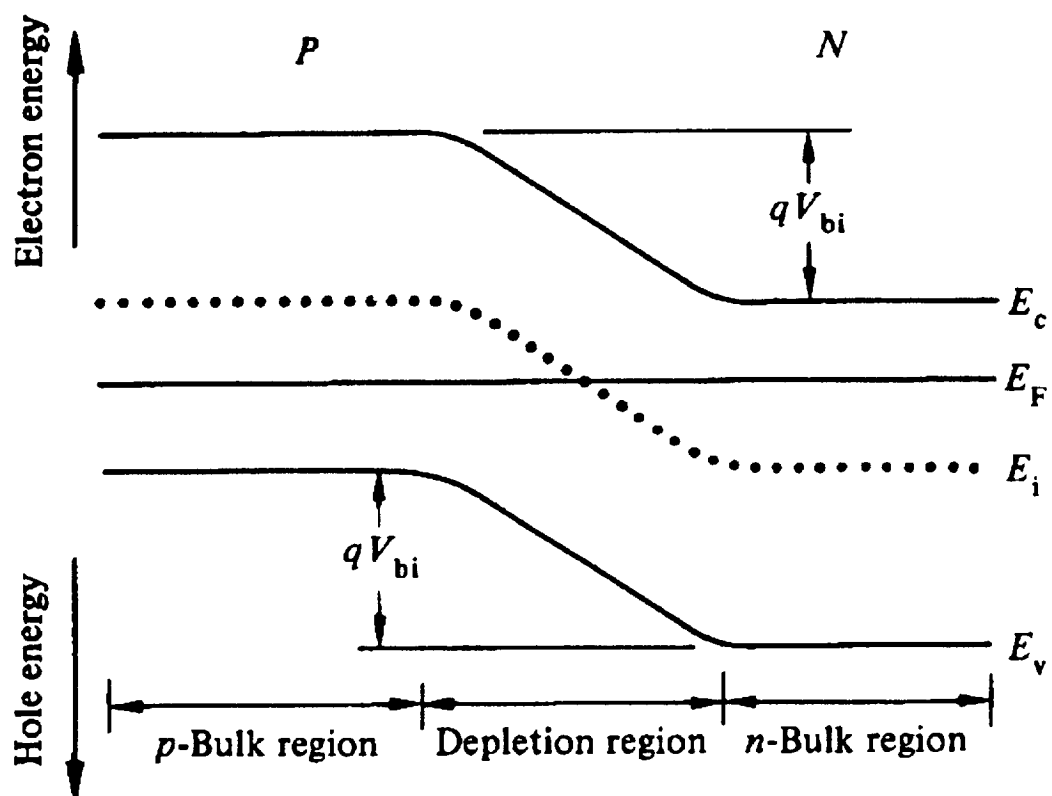


Figure 2-6: Energy band diagram for a pn junction at thermal equilibrium

2.4.1 Built-in Potential Calculation

In order to derive an expression for the built-in potential, V_{bi} , we will need to analyze the junction at thermal equilibrium with no applied bias and no net current flowing across the junction:

$$J_N = 0 = J_{N|drift} + J_{N|diffusion} = q\mu_n \xi + qD_N \frac{dn}{dx} \quad [2-40]$$

which yields,

$$\xi = -\left(\frac{D_N}{\mu_n}\right)\left(\frac{1}{n}\right)\left(\frac{dn}{dx}\right) = -\left(\frac{kT}{q}\right)\left(\frac{1}{n}\right)\left(\frac{dn}{dx}\right) \quad [2-41]$$

The built-in voltage can therefore be calculated from equation [2-18] :

$$V_{bi} = \frac{kT}{q} \int_{-\infty}^{+\infty} \left(\frac{1}{n}\right)\left(\frac{dn}{dx}\right) dx = \frac{kT}{q} \int_{n(-\infty)}^{n(+\infty)} \frac{dn}{n} \quad [2-42]$$

with,

$$n_p = n(-\infty) = n_i^2 / N_A \quad [2-43]$$

$$n_n = n(+\infty) = N_D \quad [2-44]$$

which yields,

$$V_{bi} = \frac{kT}{q} \ln \left[\frac{N_D N_A}{n_i^2} \right] \quad [2-45]$$

2.4.2 Depletion Region Calculation

In general, Poisson's equation [2-1] is not easily solved in "closed form" for most junctions because p and n are in turn functions of the unknowns variables V and x . In order to obtain an explicit solution of V as a function of x , one must make a set of

assumptions which is referred to as the depletion approximation. This approximation assumes that the mobile carrier concentrations (n and p) are small compared to the donor and acceptor levels in the depletion region, and that charge neutrality exists elsewhere in the region :

1. $N_A \gg n_p$ or p_p , i.e, $\rho = -qN_A$ for $-x_p \leq x \leq 0$.
2. $N_D \gg n_n$ or p_n , i.e, $\rho = qN_D$ for $0 \leq x \leq x_n$.
3. $\rho = 0$ for $x > x_n$ and $x < -x_p$.

The depletion approximation reduces Poisson's equation to :

$$\frac{d\xi}{dx} = \frac{qN_D}{K_s\epsilon_0} \quad \text{for } 0 \leq x \leq x_n \quad [2-46]$$

and,
$$\frac{d\xi}{dx} = \frac{qN_D}{K_s\epsilon_0} \quad \text{for } -x_p \leq x \leq 0 \quad [2-47]$$

The above equations can be solved for the electric field keeping in mind that the field is zero in the bulk regions and at the edges of the depletion region. This results in the following p- and n-side depletion region approximations of the electric field:

$$\xi(x) = \frac{-qN_A}{K_s\epsilon_0} (x_p + x), \quad \text{for } -x_p \leq x \leq 0 \quad [2-48]$$

and,

$$\xi(x) = \frac{-qN_D}{K_s\epsilon_0} (x_n - x), \quad \text{for } 0 \leq x \leq x_n \quad [2-49]$$

Since the electric field must be continuous at $x=0$, the above two equations can be reduced to :

$$N_A x_p = N_D x_n \quad [2-50]$$

which states that the areas in Figure 2-5(b) are equal and that the total negative charge must equal the total positive charge throughout the junction. Using Equation [2-36], we can derive the expressions for the potentials at both sides of the junction which are given by:

$$V(x) = \frac{qN_A}{2K_s\epsilon_0}(x_p + x)^2 \quad \text{for } -x_p \leq x \leq 0 \quad [2-51]$$

and,
$$V(x) = \frac{-qN_D}{2K_s\epsilon_0}(x_n - x)^2 + V_{bi} \quad \text{for } 0 \leq x \leq x_n \quad [2-52]$$

The depletion layer width can now be calculated by making use of the boundary condition for the potential function, i.e, $V(0^-)=V(0^+)$, and with the aid of Equation [2-50], we have:

$$x_n = \left[\frac{2K_s\epsilon_0 V_{bi}}{q} \frac{N_A}{N_D(N_A + N_D)} \right]^{1/2} \quad [2-53]$$

$$x_p = \left[\frac{2K_s\epsilon_0 V_{bi}}{q} \frac{N_D}{N_A(N_A + N_D)} \right]^{1/2} \quad [2-54]$$

and,
$$W = x_p + x_n = \left[\frac{2K_s\epsilon_0 V_{bi}}{q} \frac{(N_A + N_D)}{N_A N_D} \right]^{1/2} \quad [2-55]$$

which is valid for a two-sided abrupt junction. In the case of a one-sided junction (p^+n or pn^+), Equation [2-55] reduces to:

$$W = \left[\frac{2K_s\epsilon_0 V_{bi}}{qN_B} \right]^{1/2} \quad [2-56]$$

where $N_B=N_D$ or N_A depending on whether $N_A \gg N_D$ or vice versa. The previous equations give the depletion width under built-in bias. In the case of externally applied voltage, V_{bi} is replaced by $(V_{bi}-V_A)$ where V_A is the applied bias in volts and is positive for forward bias and negative for reverse bias.

2.4.3 Junction Capacitance

The junction capacitance of the structure can be approximated by that of a parallel plate capacitance given by:

$$C_J = \frac{K_s \epsilon_0 A}{W} \quad [2-57]$$

where C_J is a function of the applied bias and is decreased under reverse bias due to the increase in the value of the depletion width W . The above relationship can be used to accurately determine the depletion width of a junction with a known capacitance. Experimentally, the capacitance of a junction can be measured as a function of bias using a capacitance meter such as the HP4277A LCZ unit that was used in our experiments. Equation [2-56] can then be used to determine the doping profile N_B as a function of depletion width W assuming a one-sided depletion approximation.

2.4.4 Multiplication and Ionization Coefficients

As was mentioned in Chapter I, the electric field profile in a pin photodiode is constant throughout the intrinsic region. The values for the electron and hole impact ionization coefficients, α and β , can be calculated using the multiplication parameters as follows:

$$\alpha(E) = \frac{1}{w} \frac{M_n(V) - 1}{M_n(V) - M_p(V)} \ln \left(\frac{M_n(V)}{M_p(V)} \right) \quad [2-58]$$

$$\beta(E) = \frac{1}{w} \frac{M_p(V) - 1}{M_p(V) - M_n(V)} \ln \left(\frac{M_p(V)}{M_n(V)} \right) \quad [2-59]$$

where M_n and M_p are the electron and hole multiplication gains and are given by:

$$M(V) = \frac{I_{ph}(V) - I_D(V)}{I_{ph0}} \quad [2-60]$$

where,

$I_{ph}(V)$ = photocurrent at the applied voltage V

$I_D(V)$ = dark current at the applied voltage V

I_{ph0} = photocurrent at no applied bias (unity gain)

2.5 Numerical Methods

Based on the previously described theories, the modeling program uses different numerical methods for calculating the solutions to semiconductor device problems. Device operation is simulated using a set of anywhere from one to six coupled, non-linear, partial differential equations. The program produces numerical solutions to these equations by calculating the values of unknowns on a series of mesh points within the device structure. The original continuous model is converted to a discrete non-linear algebraic system that behaves approximately in the same manner. The non-linear algebraic system of equations is solved using an iterative procedure that refines consecutive estimates of the original guess. The iterative process continues until each successive correction is small enough to meet convergence criteria, or until it becomes apparent that the procedure is not going to converge.

For each model, there are basically three types of solution techniques: (a) decoupled (Gummel), (b) fully coupled (Newton) and (c) Block. The decoupled technique such as the Gummel method will solve for each unknown in turn while keeping the other

variables constant. The fully coupled techniques such as the Newton's method solve the total system of unknowns together. The Block method is a combination of the two. In other words, it will solve some equations fully coupled, while others are de-coupled. In general, the Gummel method is useful when the system of equations has linear convergence and is weakly coupled. The Newton method is useful in the case of quadratic convergence and when the system of equations is strongly coupled. The Block method has the advantage of faster simulation time over that of Newton, but is not as good as the Gummel in providing initial guesses to the solutions.

A good initial guess for the variables to be evaluated is crucial for obtaining convergence. When no previous solutions exist, the initial guess is usually calculated from the supplied structure parameters. For example, the initial guess (at zero bias) for potential and carrier concentrations can be made using the specified doping profile, etc. During bias ramps such as the ones used in our IV and CV calculations, the initial guess for any bias point is obtained by an extrapolation of the two previous results. The extrapolation method for the initial guess will generally give good results when the variables measured (such as the current in IV) have linear characteristics. However, problems may arise when the variable's behavior becomes highly nonlinear or change quickly such as is the case near breakdown or threshold. This will normally require repeated simulations to determine the threshold point at which the voltage steps must be reduced to allow proper convergence.²⁶

-
- [20] S.M. Sze, "Physics of Semiconductor Devices", Wiley, 1981.
- [21] D.J. Roulson, N.D. Arora, and S.G. Chamberlain, "Modeling and Measurement of Minority-Carrier Lifetime versus Doping in Diffused Layers of n^+ -p Silicon Diodes", IEEE Trans. on Electron Devices, ED-29, pp. 284-291. Feb., 1982.
- [22] S. Selberherr, "Analysis and Simulation of Semiconductor Devices", Springer-Verlag, Wien-New York. 1984.
- [23] L.J. Schiff, "Quantum Mechanics", 2nd ed., McGraw-Hill, New York, 1955.

-
- [24] J.L. Moll, "Physics of Semiconductors", McGraw-Hill, New York, 1964.
- [25] G.W. Neudeck, R.F. Pierret, "Modular Series on Solid State Devices: The PN Junction Diode", Vol.II, Addison-Wesley, 1983.

3.2 Simulation results for a doped/undoped MQW structure

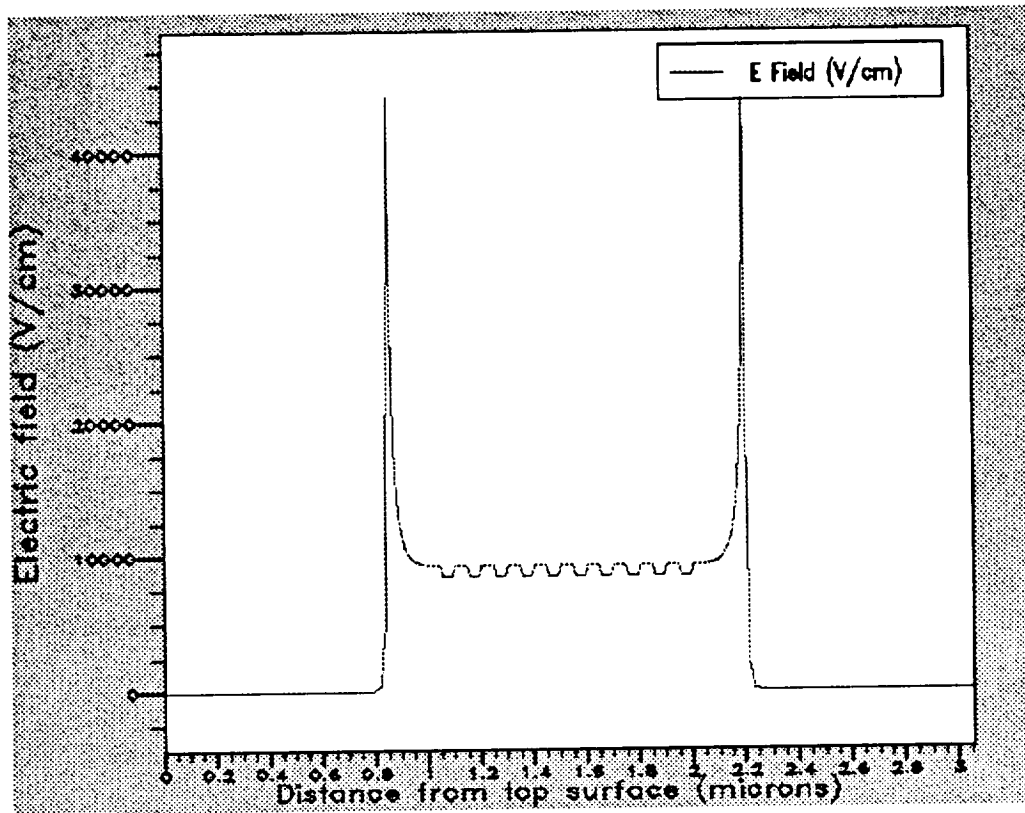


Figure 3-1: Electric field profile for an undoped 9-wells MQW APD under no bias

MQW_und_symm.out

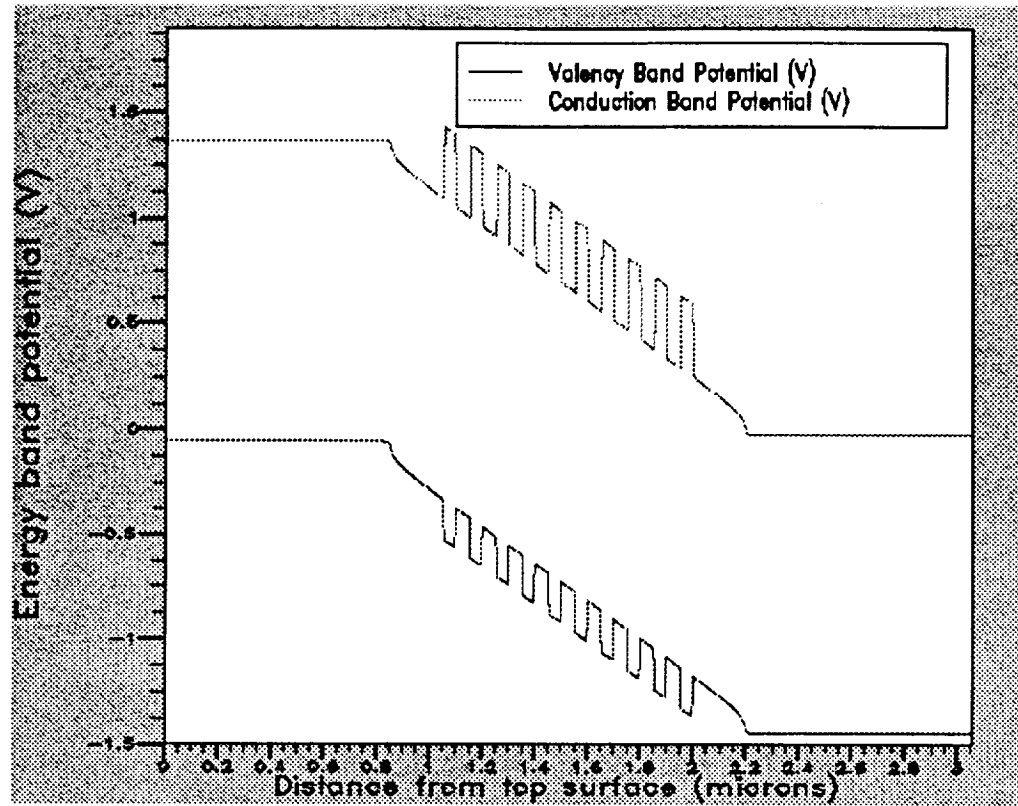


Figure 3-2: Conduction/valence band diagrams for an unbiased, undoped MQW APD

MQW_und_symm.out

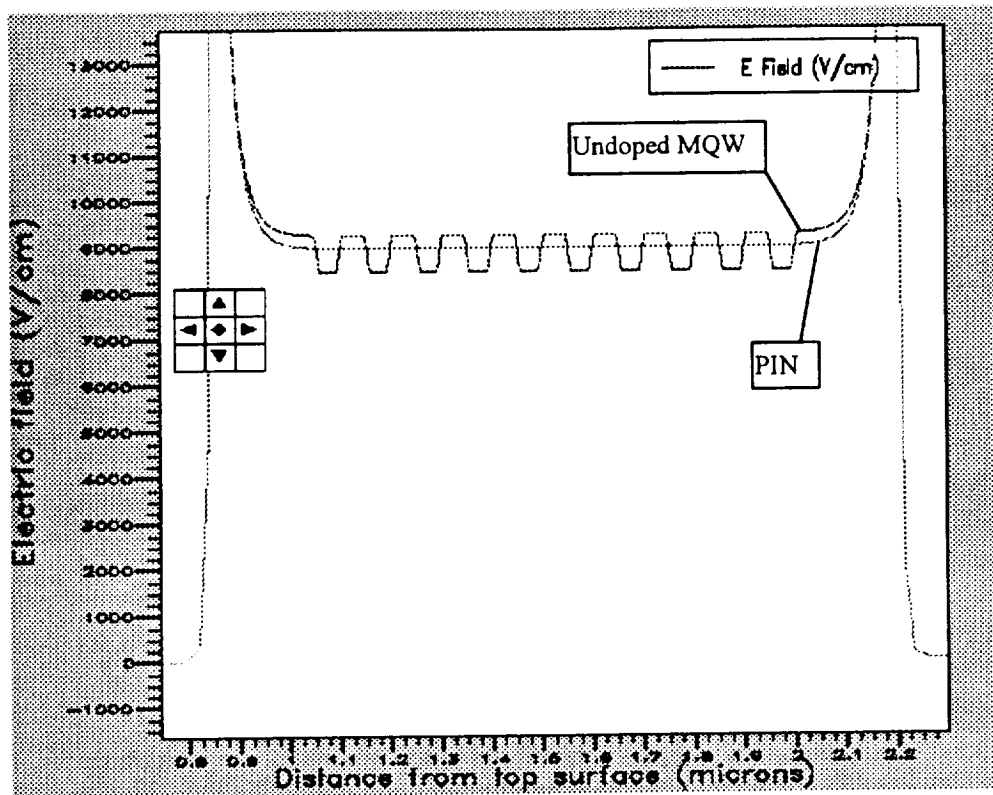


Figure 3-3: Difference in built-in e-field profile between a PIN and an undoped MQW

PINd1.out/ MQW_und_symm.out

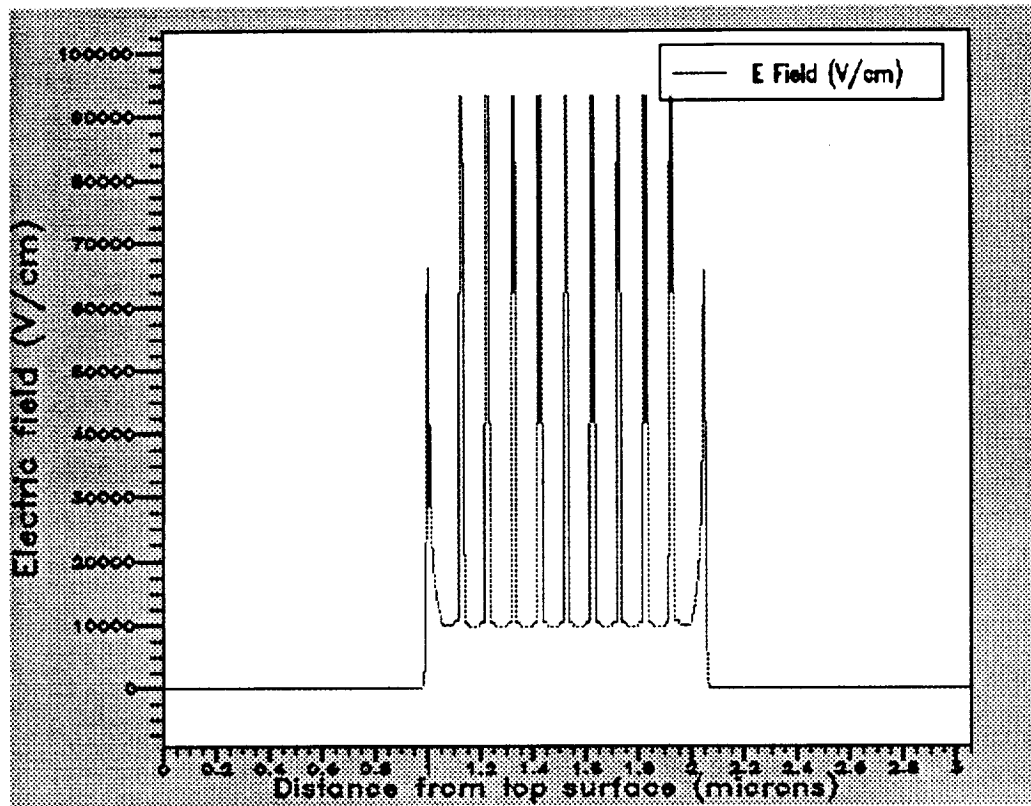


Figure 3- 4: Electric field profile for a doped 9-wells MQW APD under no bias

MQWspec2a0.out/MQWTVspec2a.in

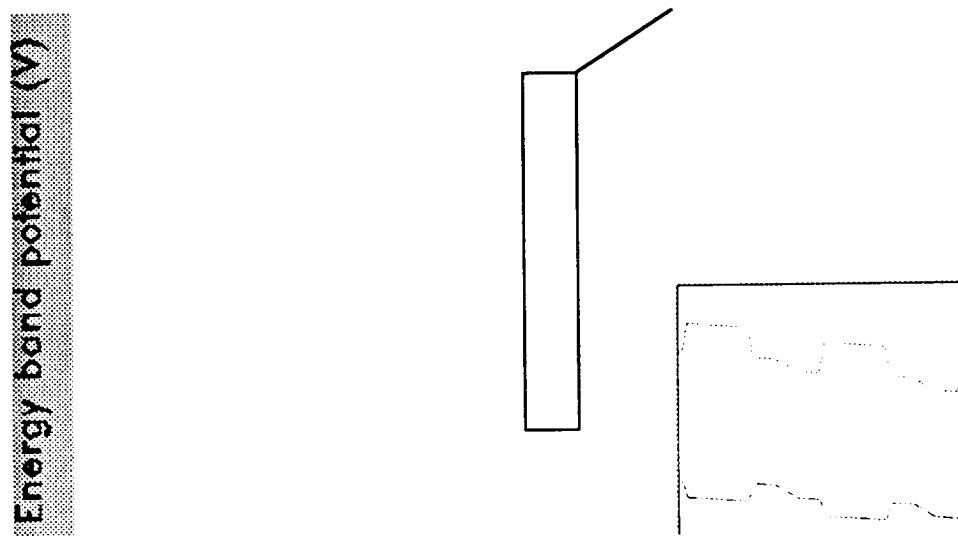


Figure 3- 5: Conduction/valence band diagrams for an unbiased, doped MQW APD

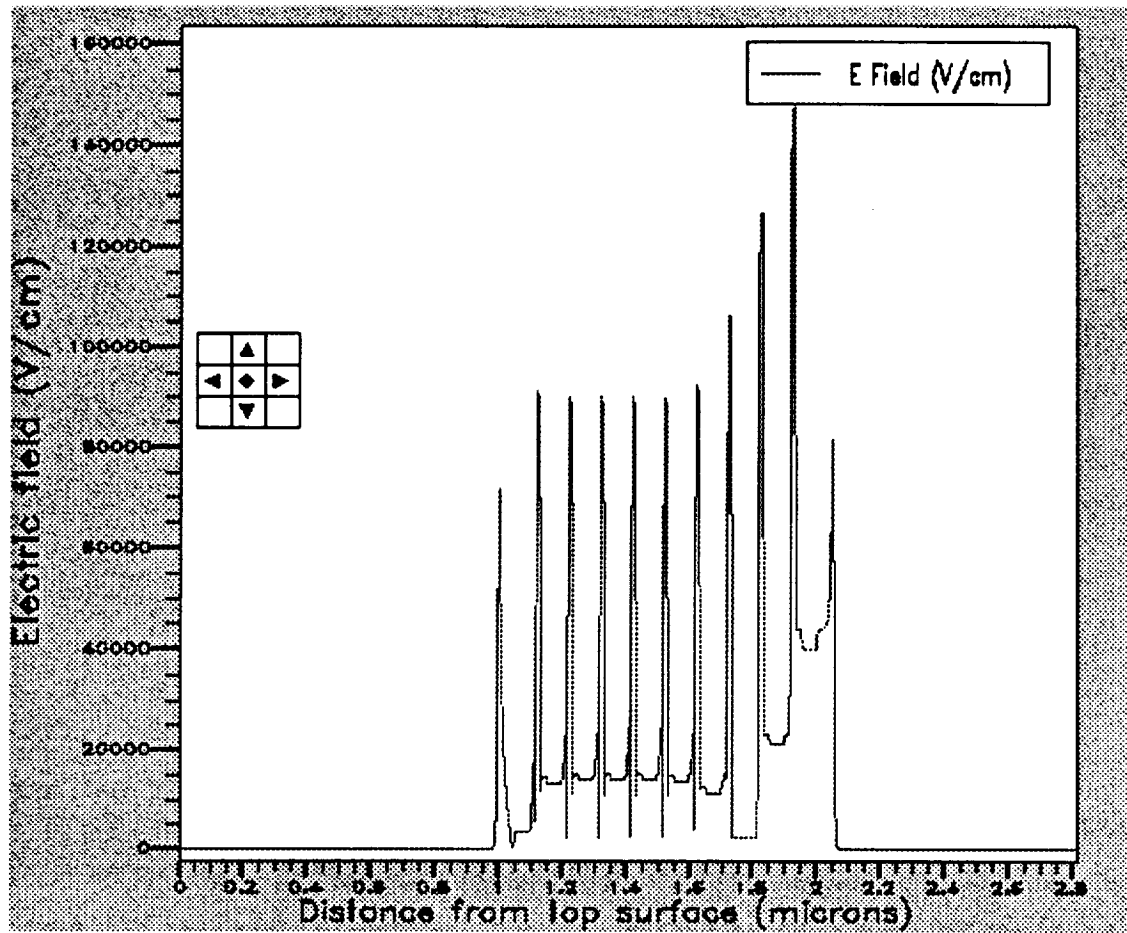


Figure 3- 6: Zero bias lectric field profile for a doped 9-wells MQW APD where $p=1.2n$
 MQWIVh5a2.out/MQWIV7s2aa.in

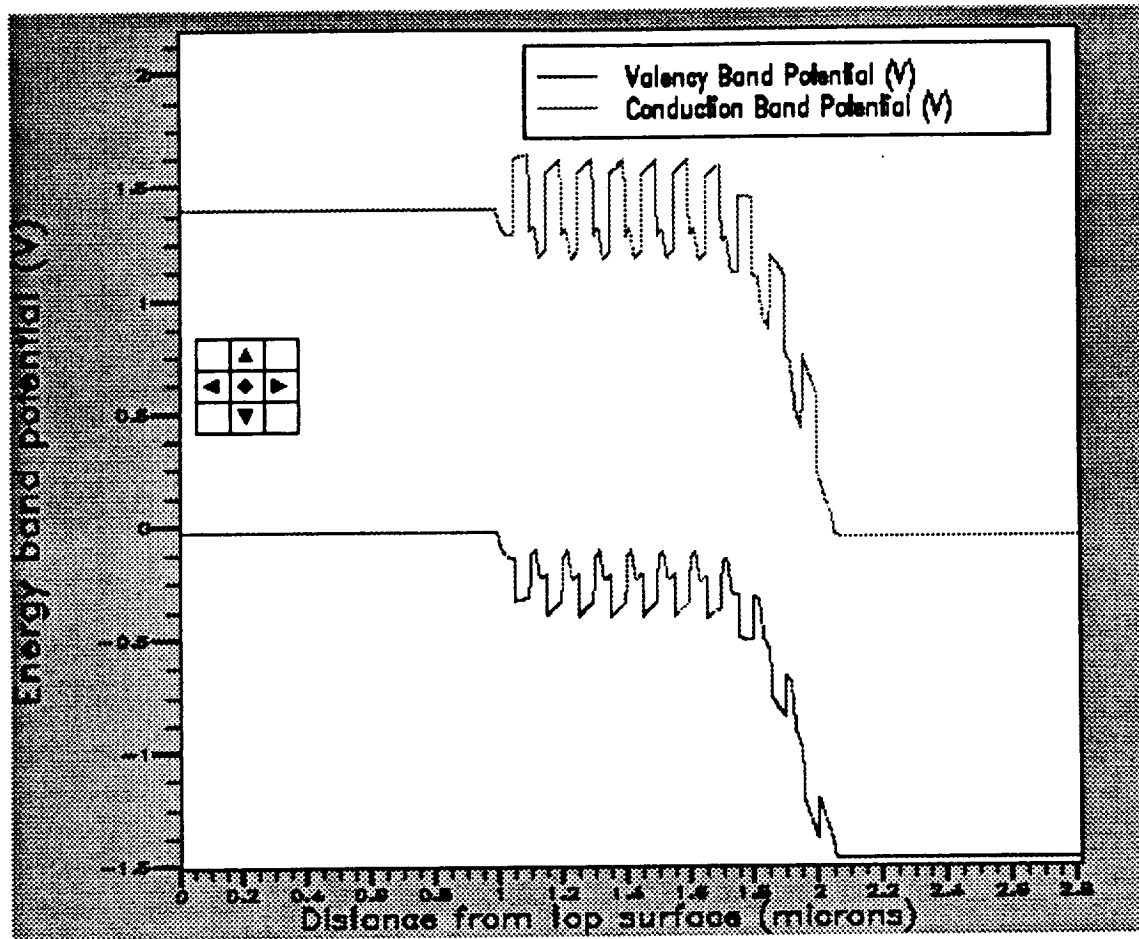
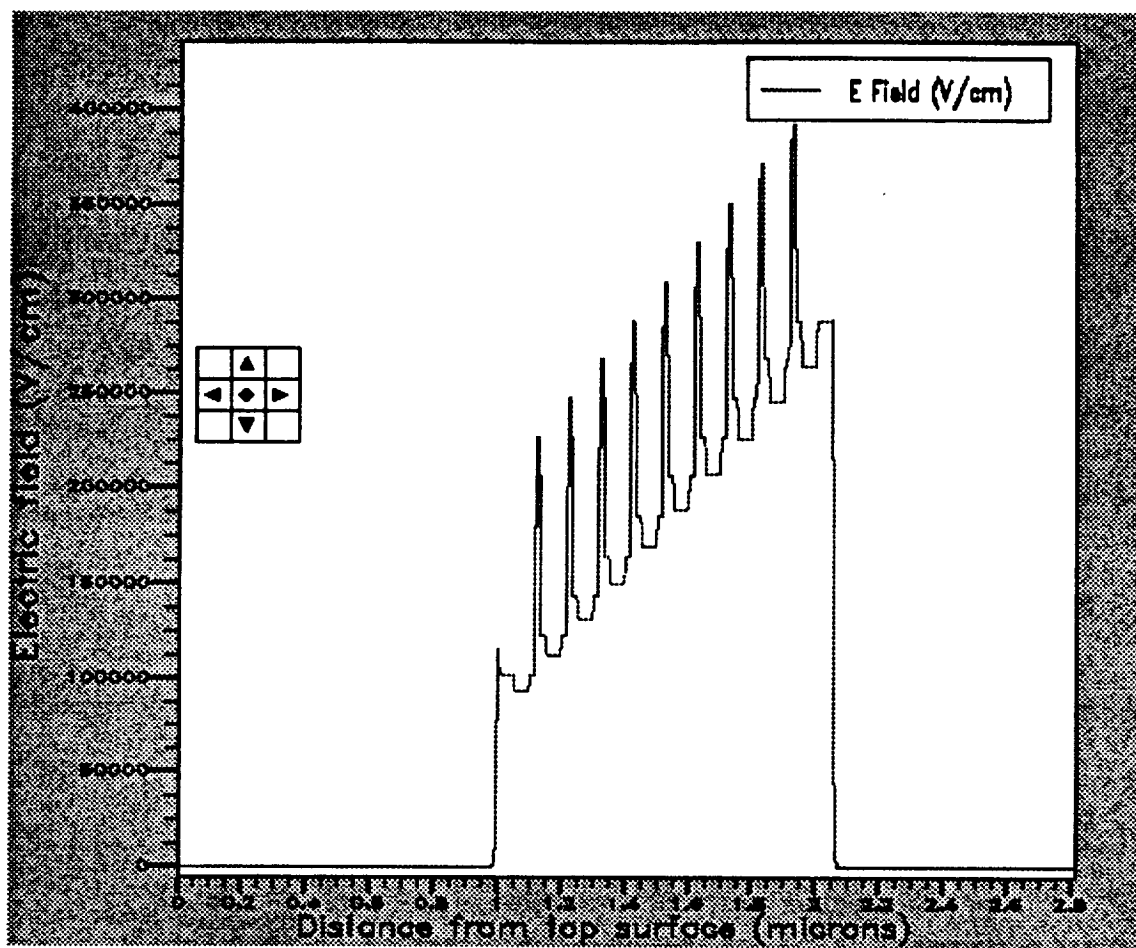
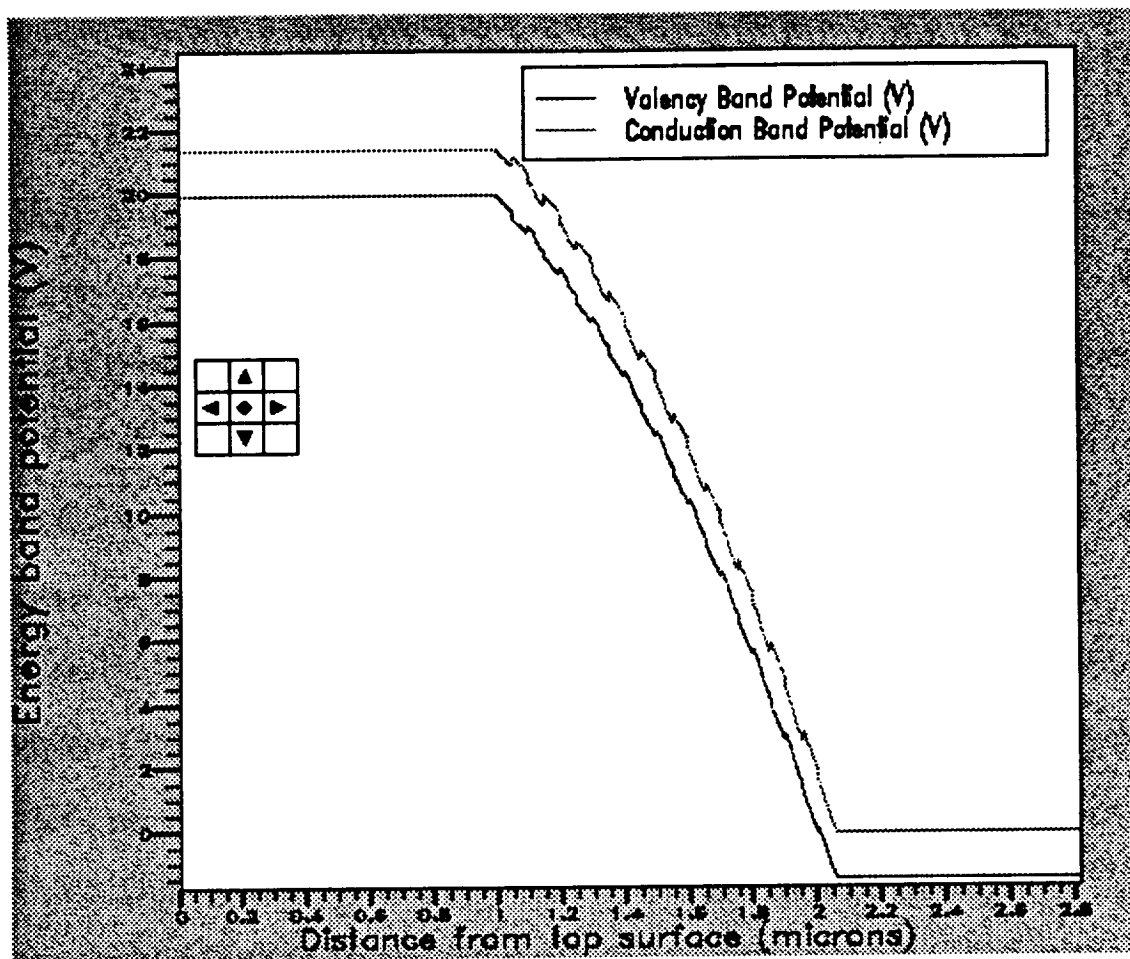


Figure 3- 7: Conduction/valence band diagrams for an unbiased, doped MQW APD where $p=1.2n$
 MQWIVh5a2.out/MQWIV7s2aa.in



MQWIVh20a2.out



3.3 Simulation results for an undoped MQW structure

Figures 3-6 and 3-7 shows the simulated electric field profile and the energy band diagram for a 9-well/10-barrier undoped MQW APD. The cap and bottom GaAs layers were 0.85 μm thick and were doped at $1 \times 10^{18} \text{ cm}^{-3}$. The $\text{Al}_{0.42} \text{Ga}_{0.58} \text{As}$ barriers and the GaAs wells were 500 \AA each and were separated from the top and bottom layers by 0.2 μm thick intrinsic GaAs layers. The structure was designed to be symmetric with respect to a plane at 1.525 μm from either surface. This resulted in a symmetric electric field profile with a peak value at zero bias of around 45 kV/cm at the two doped/undoped GaAs interfaces. The field in the GaAs wells is uniform across the structure and has a value of about 9.3 kV/cm. The magnitude of the field in the AlGaAs barriers is lower at 8.5 kV/cm as a result of the higher dielectric constant of the material as can be seen from Equation [A-7] in Appendix A.

The diagram in Figure 3-7 shows the zero-bias valence/conduction band diagram of the structure. Since the built-in voltage is determined by N_A , N_D , and n_i , it is equal to about 1.375 V as is the case for the PIN structure. Since the built-in bias is equal to the spatial integral of the electric field across the junction, one would expect the electric field magnitude to be slightly higher in the GaAs wells than that in the intrinsic region of a PIN APD, and lower in the AlGaAs barriers. This is shown schematically in Figure 3-8. This behavior helps to explain why the avalanche breakdown voltage in a MQW APD tends to be slightly lower than that of a conventional PIN with the same dimensions. This is because the higher field magnitude in the GaAs wells tends to induce the impact

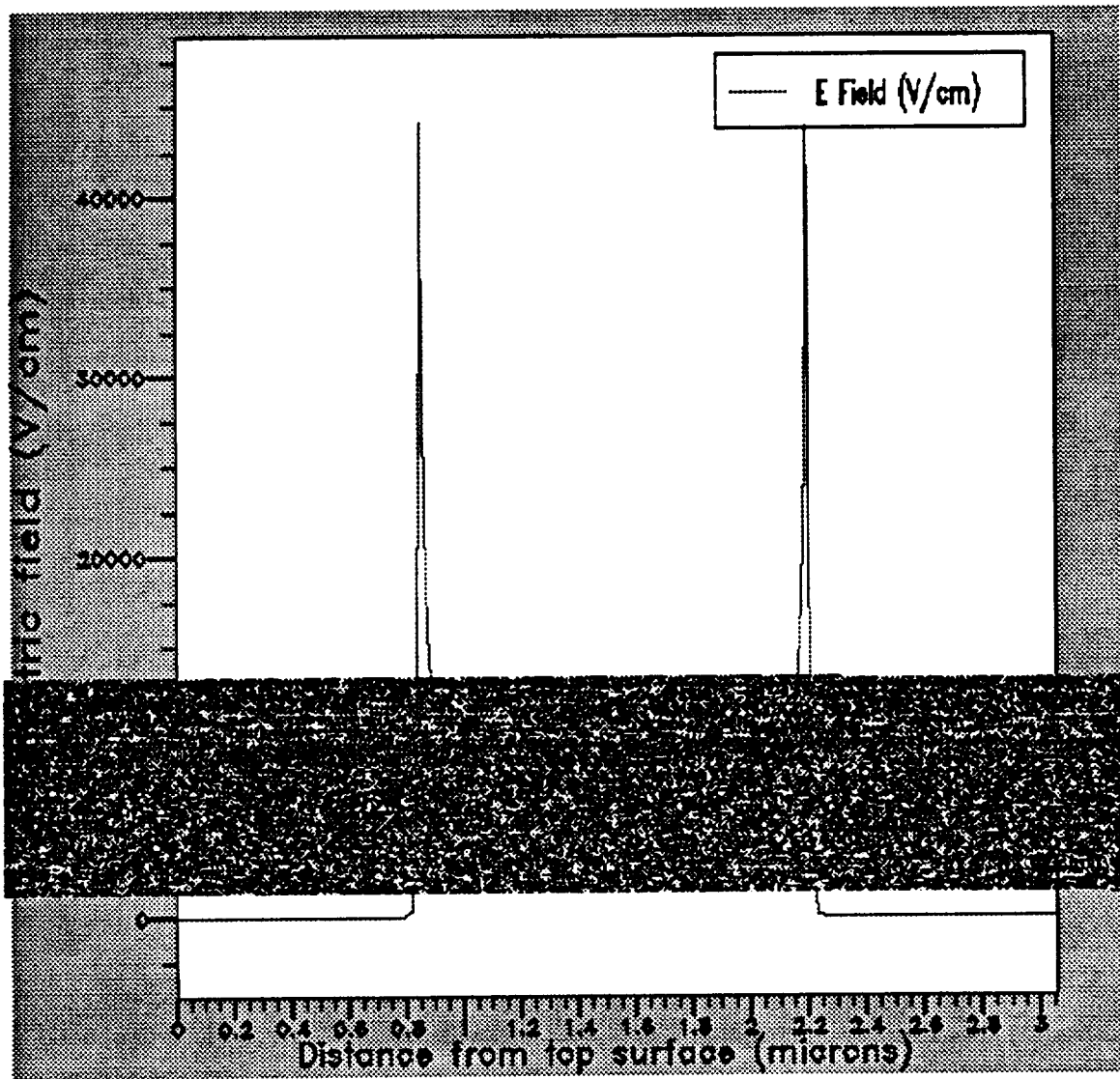


Figure 3-6: Electric field profile for an undoped 9-wells MQW APD under no bias

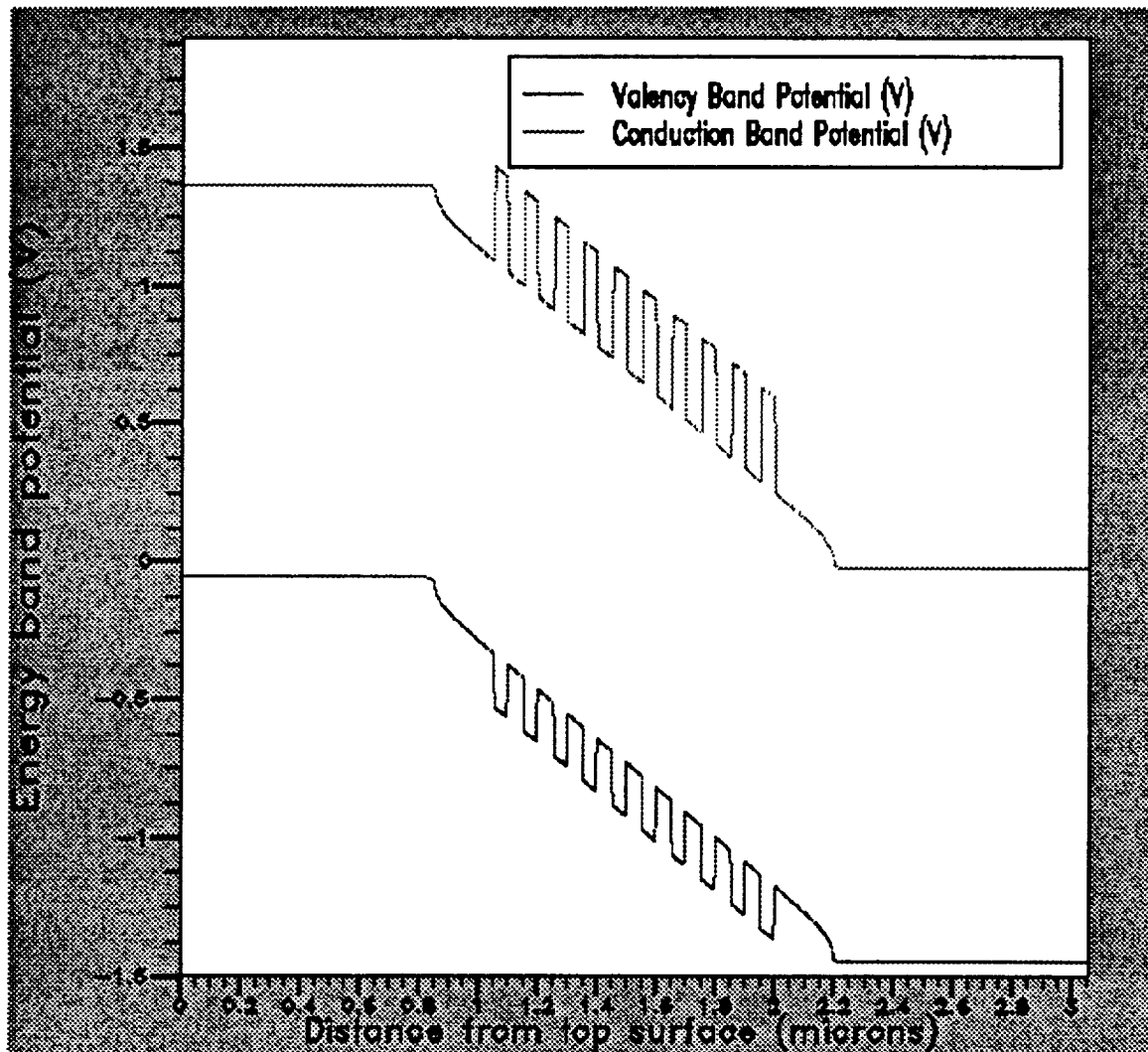


Figure 3-7: Conduction/valence band diagrams for an unbiased, undoped MQW APD

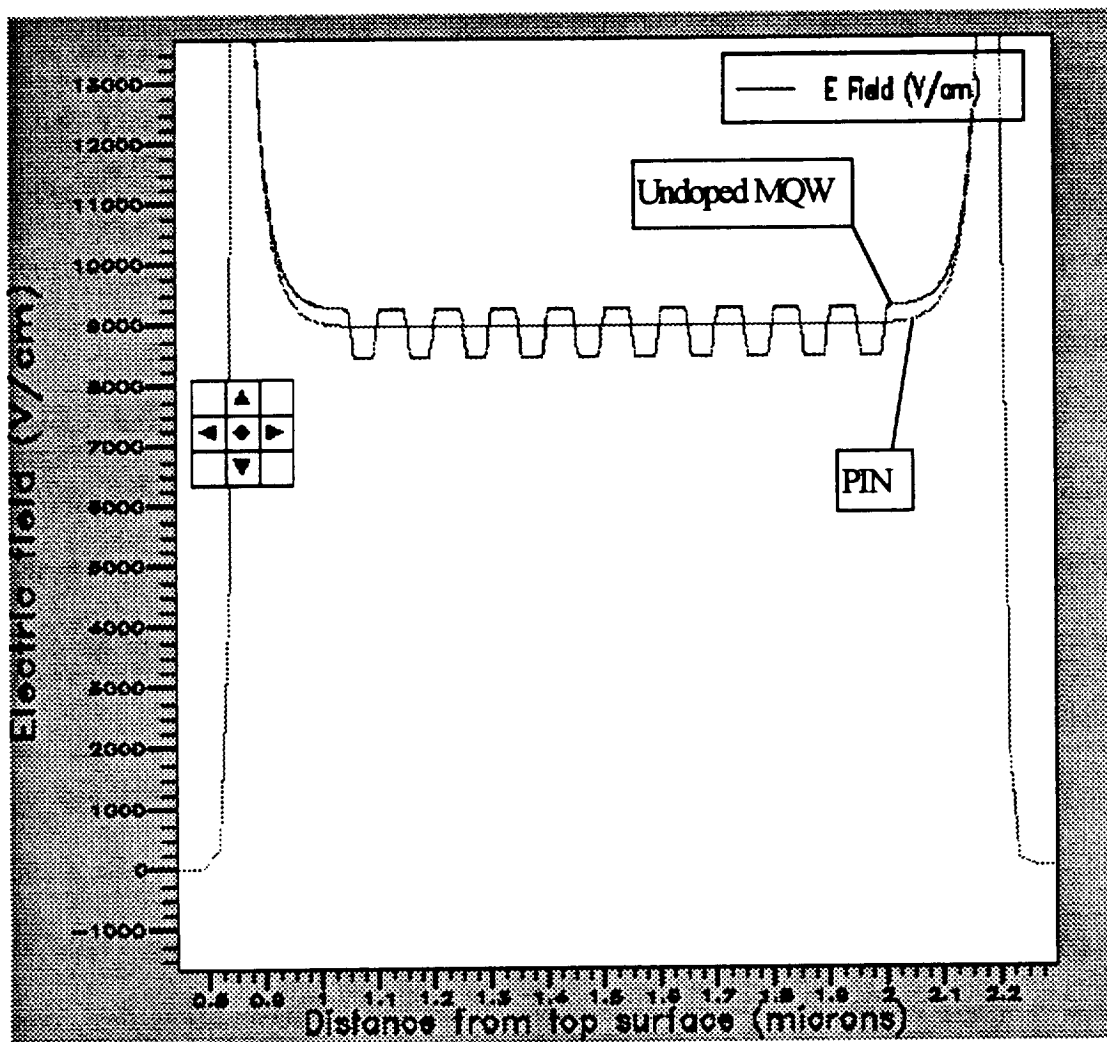


Figure 3-8: Difference in built-in e-field profile between a PIN and an undoped MQW

ionization process at a lower applied bias than would be possible if the MQW structure was not present.

3.4 Simulation results for a doped MQW structure

Figures 3-9 and 3-10 show the electric field and energy band diagrams for a doped-wells MQW structure at zero bias. The top p^+ and bottom n^+ layers were heavily doped at $3 \times 10^{18} \text{ cm}^{-3}$. All nine wells are doped with 50 Å wide p and n layers at $1.5 \times 10^{18} \text{ cm}^{-3}$. This creates localized high field regions throughout the structure with a peak value of around 95 kV/cm at zero bias as shown in Figure 3-9.

Figure 3-10 shows the corresponding band diagram where the effect of well doping on the band structure is outlined. The additional energy drop per well as a result of this particular doping configuration is equal to about 0.06 eV. It is possible to further enhance the energy gain by increasing the doping density as well as the widths of the p and n doping layers.

Figure 3-11 shows the field profile at a reverse bias of 4 V for the same doped-well APD previously described with the exception that the doping in the GaAs wells is such that $p = 1.8 \times 10^{18} \text{ cm}^{-3}$ and $n = 1.5 \times 10^{18} \text{ cm}^{-3}$. The doping imbalance in the wells ruins the symmetry in the electric field profile and results in undepleted MQW stages throughout the structure as shown in the band diagram in Figure 3-12. The undepleted or “inactive” stages are low-field regions which present highly resistive barriers to the flow of electrons and holes across the device. Furthermore, the AlGaAs barriers tend to reduce the internal quantum efficiency of the APD by preventing the injection of diffused electrons (when $p > n$) and holes (when $n > p$) into the avalanche region. These issues will be discussed in

more details in the following chapter. By increasing the applied reverse bias across the structure, the “inactive” stages are slowly depleted of carriers, but the non-symmetry characteristic of the field profile is nevertheless preserved as shown in Figure 3-13 for the same structure at -20 V. In the case where $p > n$, the field magnitude gradually increases from left to right. The reverse is true in the case where $n > p$. As seen in Figure 3-13, the magnitude of the field throughout the avalanche region varies by almost a factor of four at reverse bias of 20V. As a result, certain regions of the structure would reach breakdown field sooner than others, and the device’s breakdown voltage is substantially lowered. Once the device reaches breakdown voltage, the structure becomes increasingly conductive. If the doping imbalance is too high, some regions of the junction will never become depleted. Further depletion of these regions will then be limited by the avalanching mechanisms leading to breakdown. However, if the doping imbalance is small, the device will deplete fully with increasing bias. Figure 3-14 shows the band diagram of such a structure where the MQW region is shown to be fully depleted at -20 V in the case where $p=1.2n$.

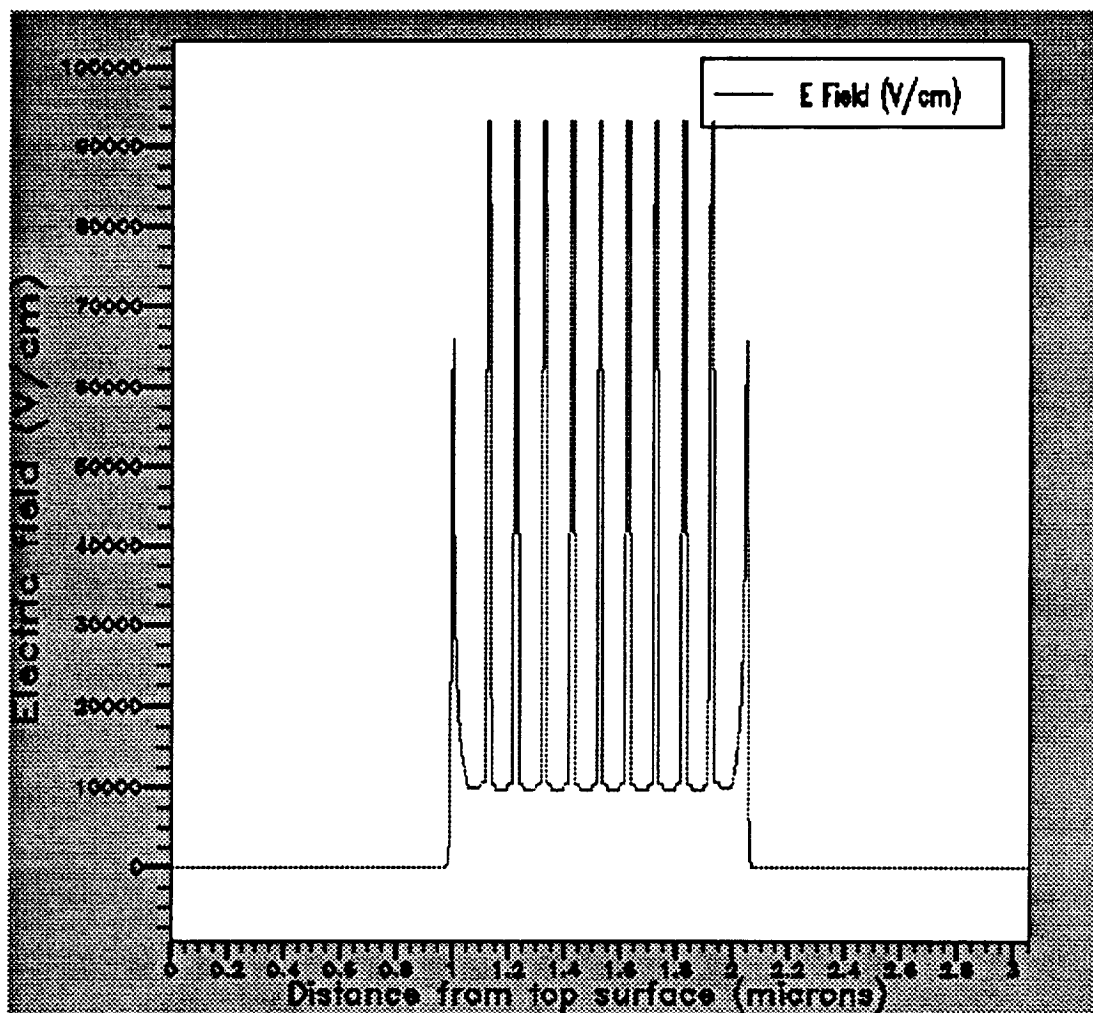


Figure 3-9: Electric field profile for a doped 9-well MQW APD under zero bias

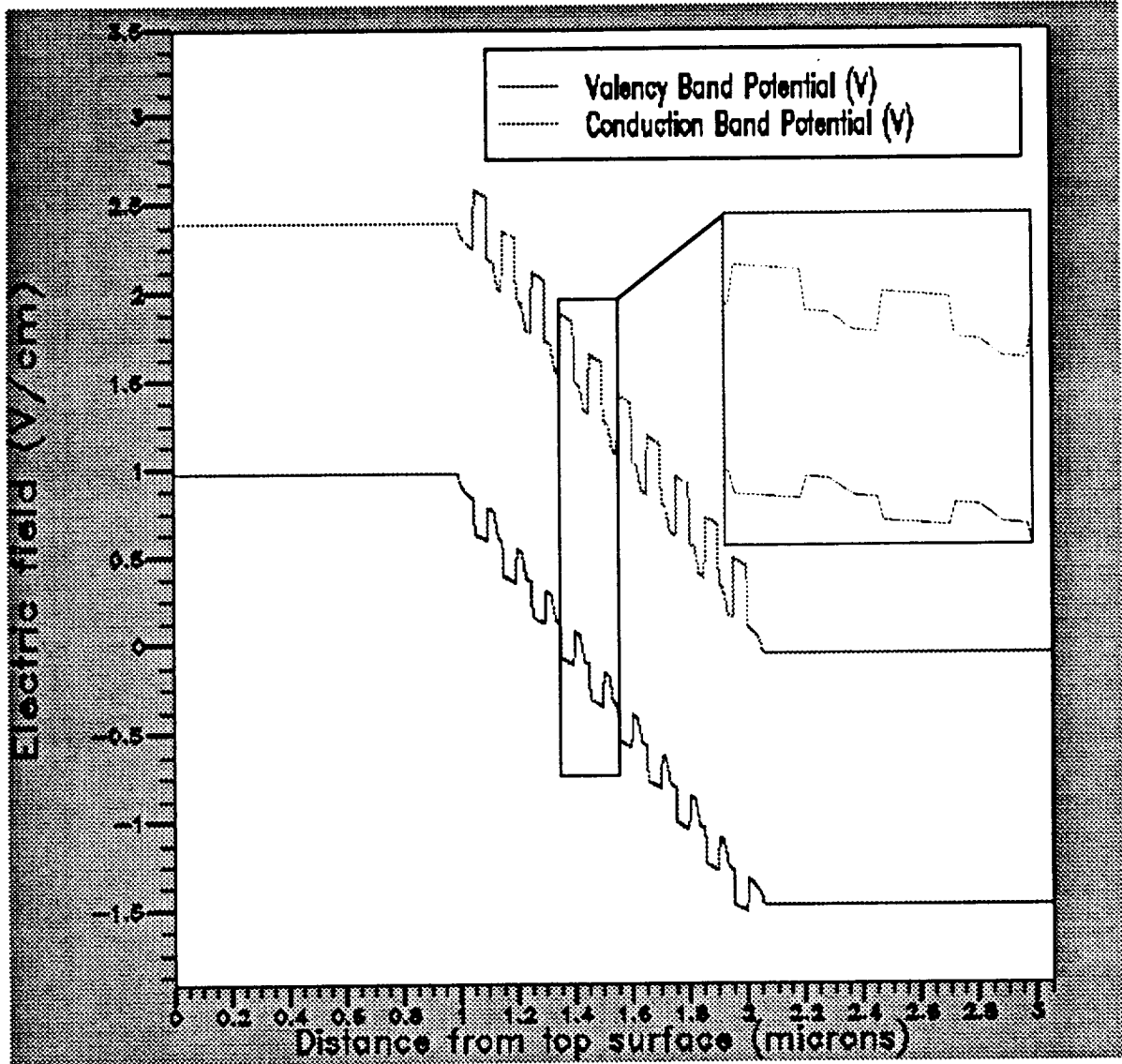


Figure 3-10: Conduction/valence band diagrams for an unbiased, doped MQW APD

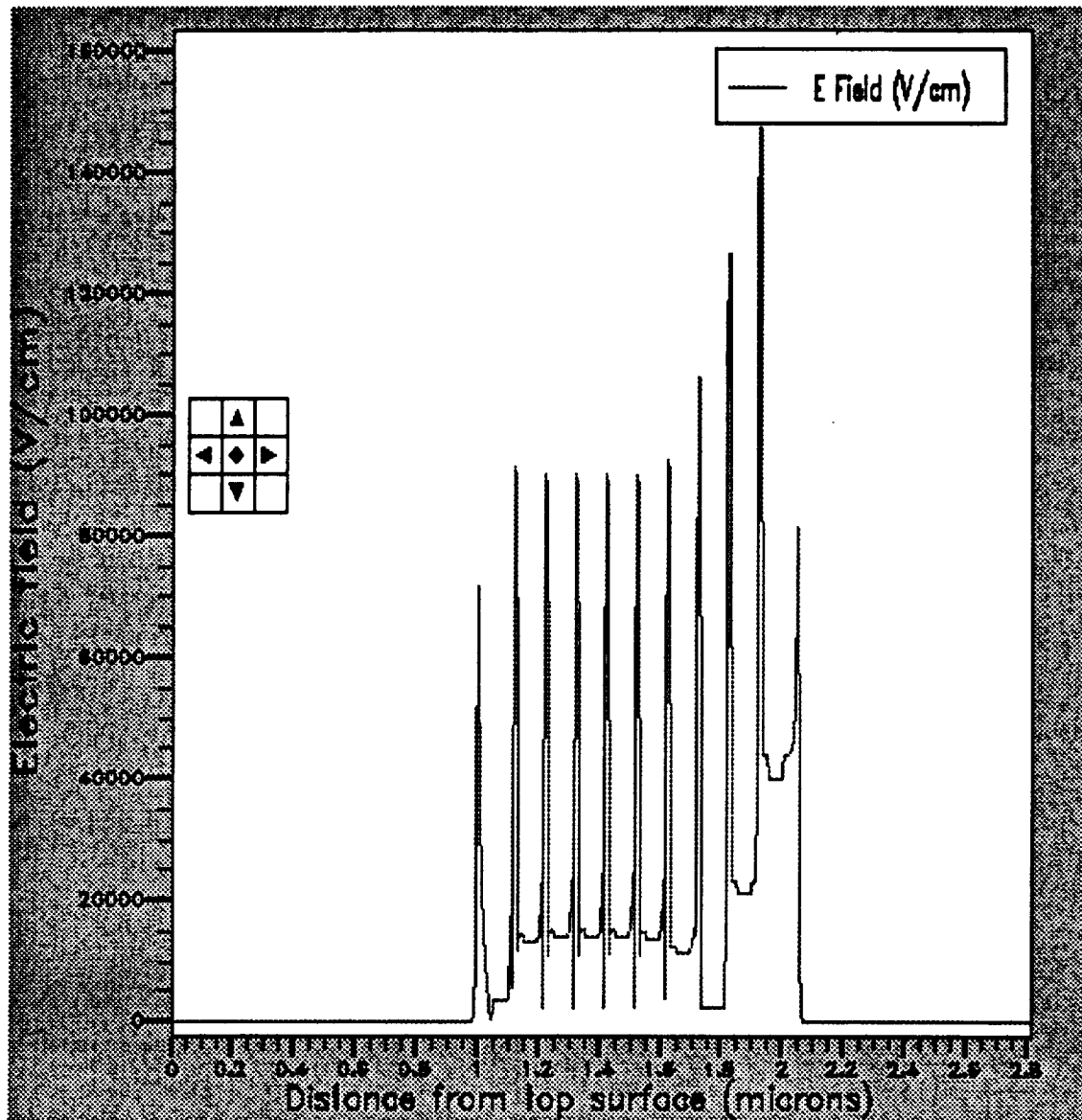


Figure 3-11: Electric field profile at zero bias for a doped 9-well MQW APD where $p=1.2n$

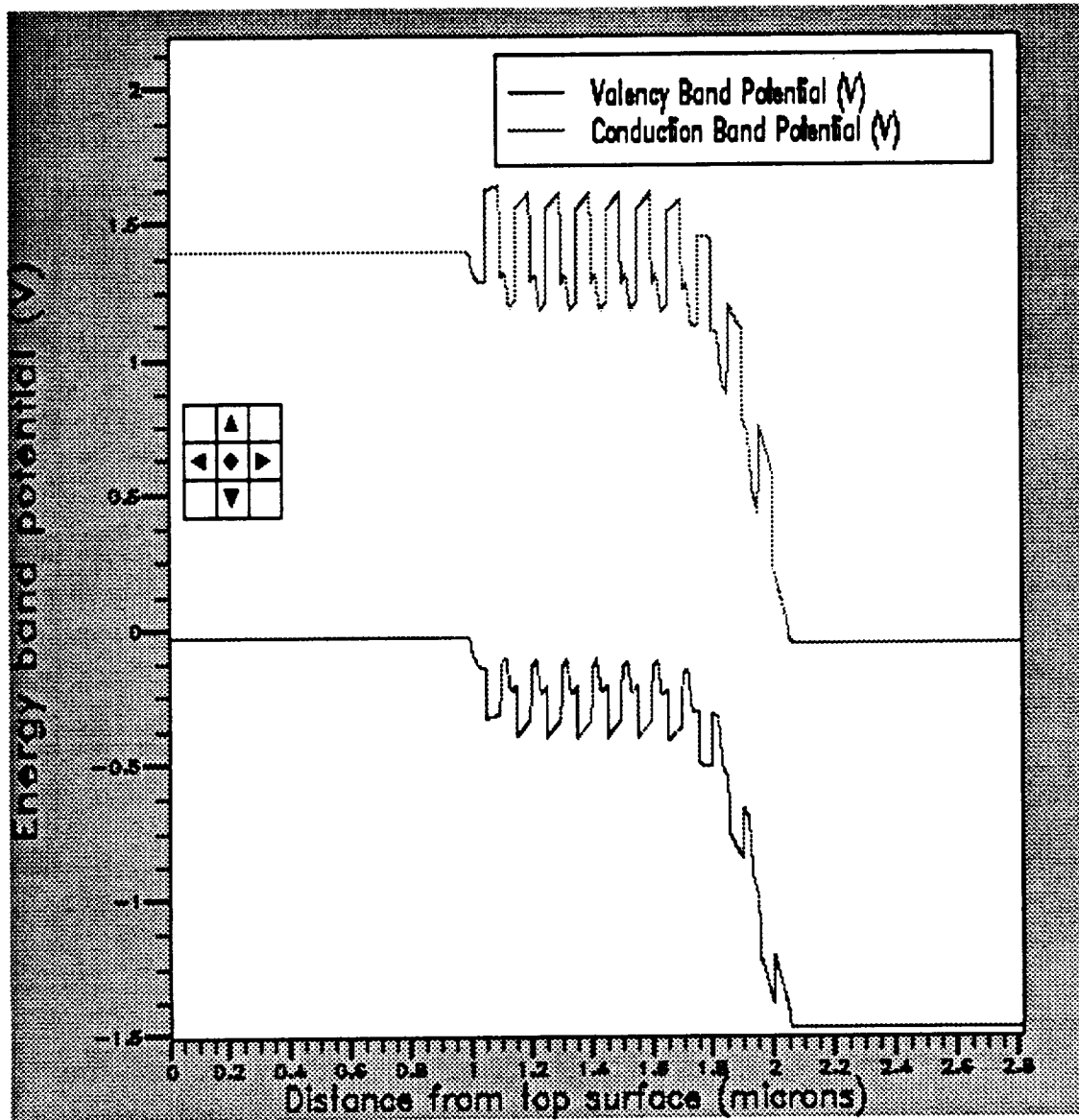


Figure 3-12: Conduction/valence band plot for an unbiased, doped MQW APD where $p=1.2n$

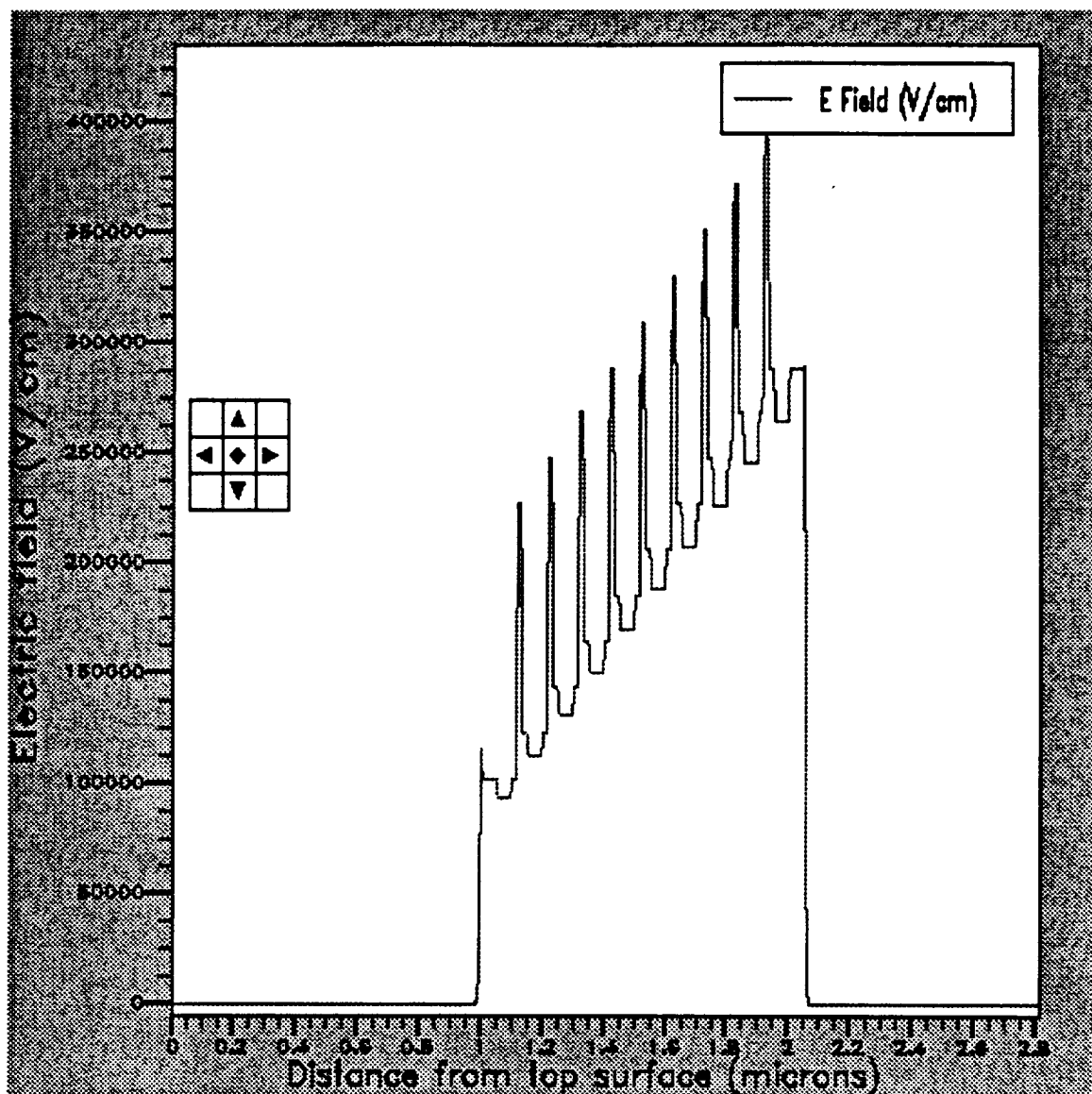


Figure 3-13: Electric field profile at $V = -20$ V for a doped 9-well MQW APD where $p=1.2n$.

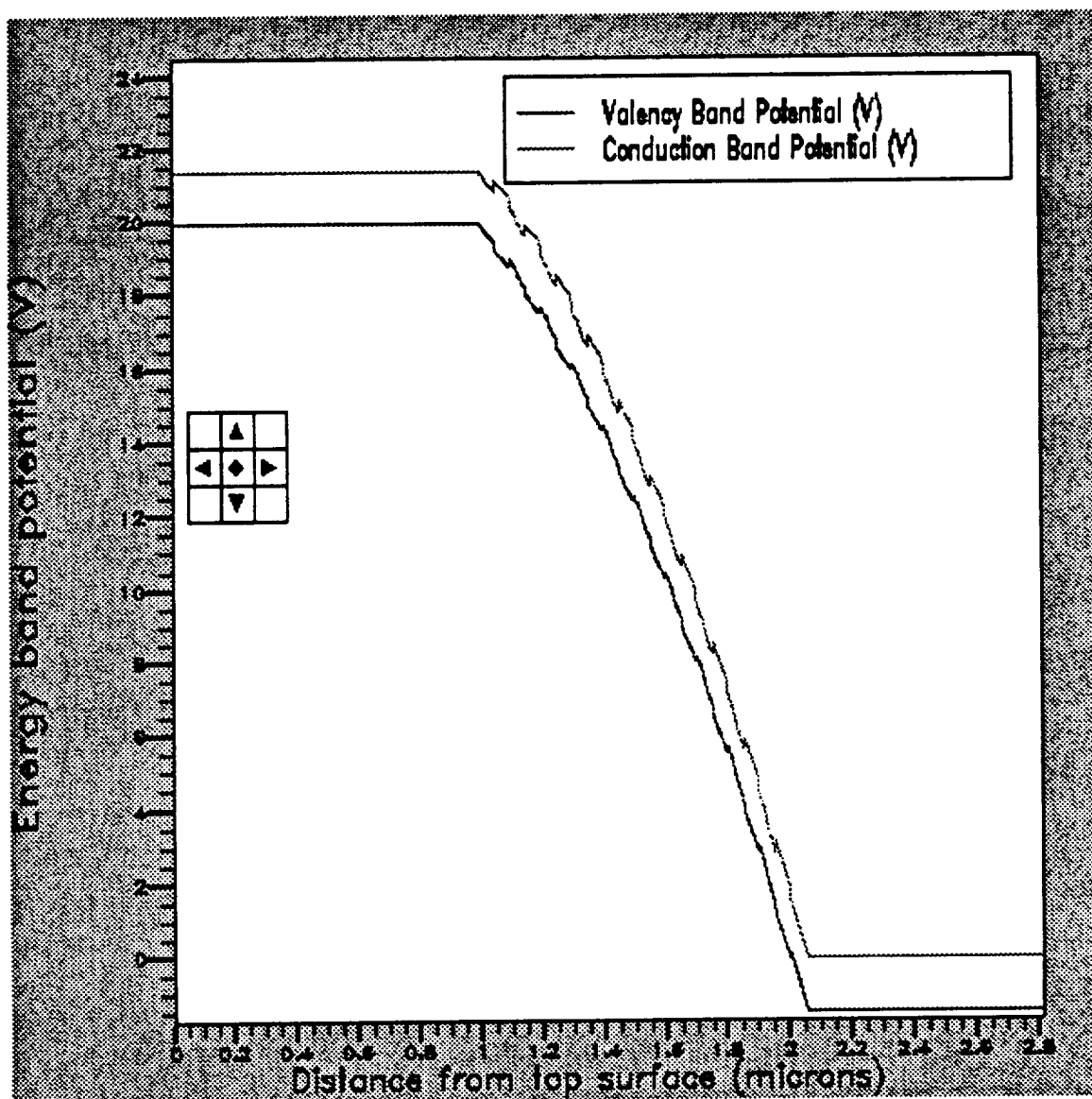


Figure 3-14: Band diagram at $V = -20$ V for a doped MQW APD where $p=1.2n$

Presentation:

- [1] Menkara, H. M., Wagner, B. K., Summers, C. J.
Effect of variations in the doping profiles on the properties of doped multiple quantum well avalanche photodiodes. First International Workshop on Materials for Optoelectronics, Sheffield Hallam University, Sheffield, U.K, August 1995.

Publications:

- [1] Menkara, H. M., Wagner, B. K., Summers, C. J., "Gain properties of doped GaAs/AlGaAs multiple quantum well avalanche photodiode structures", *Appl. Phys. Lett.*, Vol. 66, no. 14, pp. 1764-1766 April 1995.
- [2] Yun, I., Menkara, H. M., Wang, Y., Oguzman, I. H., Kolnik, J., Brennan, K.F., May, G. S., Summers, C. J., Wagner, B. K., "Reliability assessment of multiple quantum well avalanche photodiodes", *1995 IEEE International Reliability Physics Proceedings*. 33rd Annual, p. 200-204.
- [3] Menkara, H. M., Wagner, B. K., Summers, C. J., "Effect of variations in the doping profiles on the properties of doped multiple quantum well avalanche photodiodes", to be published in *Optical Materials*.
- [4] Yun, I., Menkara, H. M., Wang, Y., Oguzman, I. H., Kolnik, J., Brennan, K.F., May, G. S., Summers, C. J., Wagner, B. K., "The effect of manufacturing process sequence on the reliability of GaAs multiple quantum well avalanche photodiodes", to be published.

- [¹] F. Capasso, *Semiconductors and Semimetals*, edited by R. K. Willardson and A. C. Beer (Academic, New York, 1985), Vol. 22, part D, p.2
- [¹] J. Gower, *Optical Communication Systems*, Prentice/Hall, London, 1984
- [¹] P. P. Webb, R.J. McIntyre, and J. Conradi, "Properties of avalanche photodiodes", *RCA Review* 35, 234 (1974).
- [¹] S.M. Sze, *Physics of Semiconductor Devices*, 2nd ed., Wiley, 1981.
- [¹] Y. Suematsu, K. Iga and K. Kishino, *GaInAsP Alloy Semiconductors*, Ch. 14, ed. T. Pearsall, Wiley, 1982.
- [¹] W. T. Read, Jr., "A proposed high-frequency, negative resistance diode", *Bell System Technical Journal* 401, March, 1958.
- [¹] J. C. Campbell, in "Optoelectronics Technology and Lightwave Communications Systems," edited by Chinlon Lin (1989), Ch. 14.
- [¹] P. Aristin, "Fabrication et Caracterization de Photodiodes a Avalanche a Puits Quantiques Multiples", Ph.D. thesis, January 1992.
- [¹] R. Chin, N. Holoniak, G. E. Stillman, J. Y. Tsang, and K. Hess, *Appl. Phys. Lett.* 16, 467 (1980).
- [¹] F. Capasso, W. T. Tsang, A. L. Hutchinson, and P. G. Williams, *Appl. Phys. Lett.* 40, 38 (1982).
- [¹] H. Blauvelt, S. Margalit, and A. Yariv, *Electron. Lett.* 18, 375 (1982).
- [¹] J. D. Gordon, R. E. Nahory, M. A. Pollack, and J. M. Warlock, *Electron. Lett.* 15, 518 (1979).
- [¹] F. Capasso, W. T. Tsang, A. L. Hutchinson, and P. W. Foy, *Conf. Ser. - Inst. Phys.*, 63, 473 (1982).
- [¹] R. Chin, N. Jr. Holonyak, G. E. Stillman, J. T. Tang, and K. Hess, *Electron. Lett.* 16, 467 (1980).
- [¹] F. Capasso, W. T. Tsang, A. L. Hutchinson, and G. F. Williams, *Tech. Dig.-Inst. Electron Devices Meet.*, 1981, Washington, DC, 284 (1981)
- [¹] F. Capasso, W. T. Tsang, and G. F. Williams, *IEEE Trans. Electron Dev.* ED-30, 381 (1983)
- [¹] H. Blauvelt, S. Margalit, and A. Yariv, *Electron. Lett.* 18, 375 (1982)

[¹] K. Brennan, IEEE Trans. Electron Dev. ED-34, 1658 (1987)

[¹] K. Brennan, K. Hess, F. Capasso, Appl. Phys. Lett. 50, 1897 (1987)

VITA

Hicham Menkara was born in Lebanon on August 31, 1968. He received his Bachelor degree (Magna Cum Laude) in Engineering Physics from the University of Toledo, Ohio in 1989. He then joined the Georgia Institute of Technology where he received an M.S. in Physics in 1990 and an M.S. in Electrical Engineering in 1993. He expects to receive an M.S. in Management from Georgia Tech in September 1996.

CHAPTER III.....	35
<u>3.1 INTRODUCTION</u>	35
<u>3.2 SIMULATION RESULTS FOR A PIN STRUCTURE.....</u>	37
<u>3.2.1 INTERNAL PHYSICAL PROPERTIES.....</u>	37
<u>3.2.2 EXTERNAL PROPERTIES.....</u>	40

CHAPTER III

THEORETICAL RESULTS

3.1 Introduction

In this chapter, we will present some of the theoretical results that were obtained using the Atlas 2-D device simulation framework. Different models were developed for the various APD structures using the parameters given in Appendix A for the GaAs/AlGaAs material systems. Some examples of the algorithms that were used for the simulations are listed in Appendix B. In order to simulate devices with non-uniform band structures (i.e., MQWs), the drift-diffusion model with position dependent band structure was used. Unlike the hydrodynamic model²⁶, the drift-diffusion model neglects “non-local” transport effects such as velocity overshoot and energy-dependent impact ionization. Velocity overshoot occurs when carriers enter a high-field region where the field magnitude exceeds its threshold value. This will cause the carriers to accelerate to a higher velocity before relaxing to their equilibrium transport condition. Ignoring these effects may have significant impact on submicron structures, but the consequences are minor for large devices. It is important to note, however, that the purpose behind our modeling was mainly to understand the effect of variations in structure parameters on device performance and not to determine exact values of the output variables. In all models, Newton's two-carrier method was used for solving Poisson's and the continuity

equations. Impact ionization was modeled according to Selberherr(ref), and CV solutions were obtained through small signal ac analysis at 1 MHz and with a small signal bias of 0.03 V. Light IV characteristics were modeled using a 1 mW/cm² monochromatic light source operating at 632.8 nm, and spectral response simulations were performed with a 1 W/cm² broadband light source ranging from 200 to over 900 nm.

In order to simplify our models, reduce the number of degrees of freedom, and decrease program execution times, the following assumptions were made regarding the simulated structures:

- All structures were assumed to have rectangular geometries having a cross sectional area of 75 μm^2 . Therefore, a plane junction approximation was used, and a 1-D cartesian coordinate solution to Poisson's equations was applied.
- Only SRH and Auger recombination mechanisms were considered. Optical and surface recombinations were neglected.
- The presence of defect/trap centers in bulk materials and at interfaces was neglected.
- The top (p+) and bottom (n+) regions are uniformly and equally doped.
- The p and n contacts are perfect ohmic contacts.
- Doping imbalance in the MQWs is constant throughout an entire structure.
- Bandgap narrowing effects in AlGaAs are similar to those in GaAs.

3.2 Simulation Results for a PIN Structure

We first tested the accuracy of our model by examining the results for the internal and external properties of a simple 3 μm thick GaAs PIN structure where the top (p+) and bottom (n+) layers were uniformly doped at $1 \times 10^{18} \text{ cm}^{-3}$.

3.2.1 Internal Physical Properties

Figure 3-1 shows the energy band diagram at zero bias where the energy gap at 300 K is about 1.43 eV. The built-in voltage is shown to be equal to approximately 1.375 V. This can be easily verified using equation [2-45] with $N_A = N_D = 1 \times 10^{18} \text{ cm}^{-3}$, $n_i = 1.79 \times 10^6 \text{ cm}^{-3}$, and $kT/q = 0.02586 \text{ V}$. The effects of bandgap narrowing due to heavy doping is also shown in Figure 3-1. These effects were included in the model as spatial variations in the intrinsic carrier concentration²⁷:

$$n_{ie}(x, y) = n_i \exp \left\{ \frac{9 \times 10^{-3} q}{2kT} \left[\ln \frac{N(x, y)}{10^{17}} + \sqrt{\left(\ln \frac{N(x, y)}{10^{17}} \right)^2 + \frac{1}{2}} \right] \right\} \quad [3-1]$$

This spatial dependence of n_{ie} results in an adjustment to the electric field profile as shown by the presence of the two interface peaks in Figure 3-2.

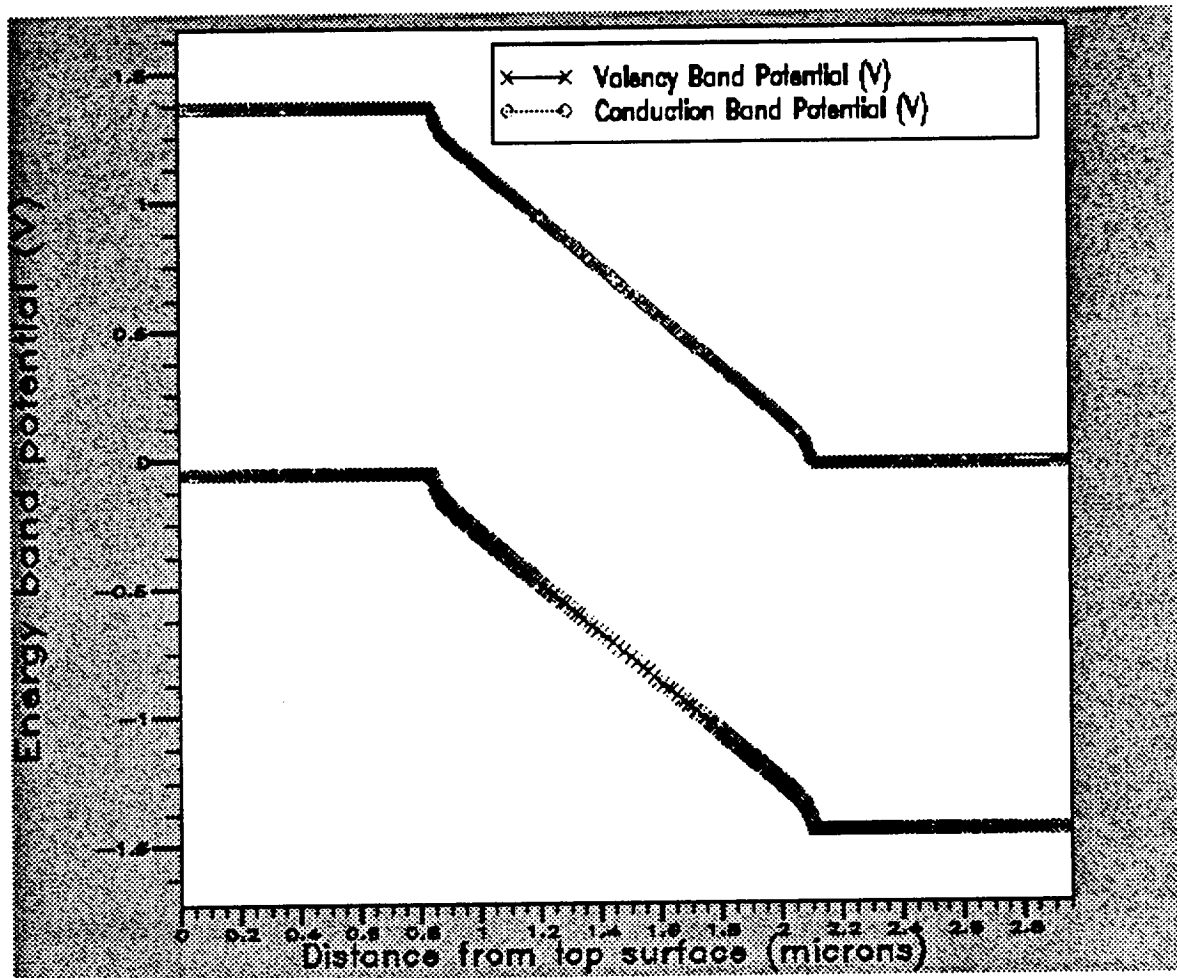


Figure 3-1: Conduction/valence band diagrams for an unbiased PIN APD

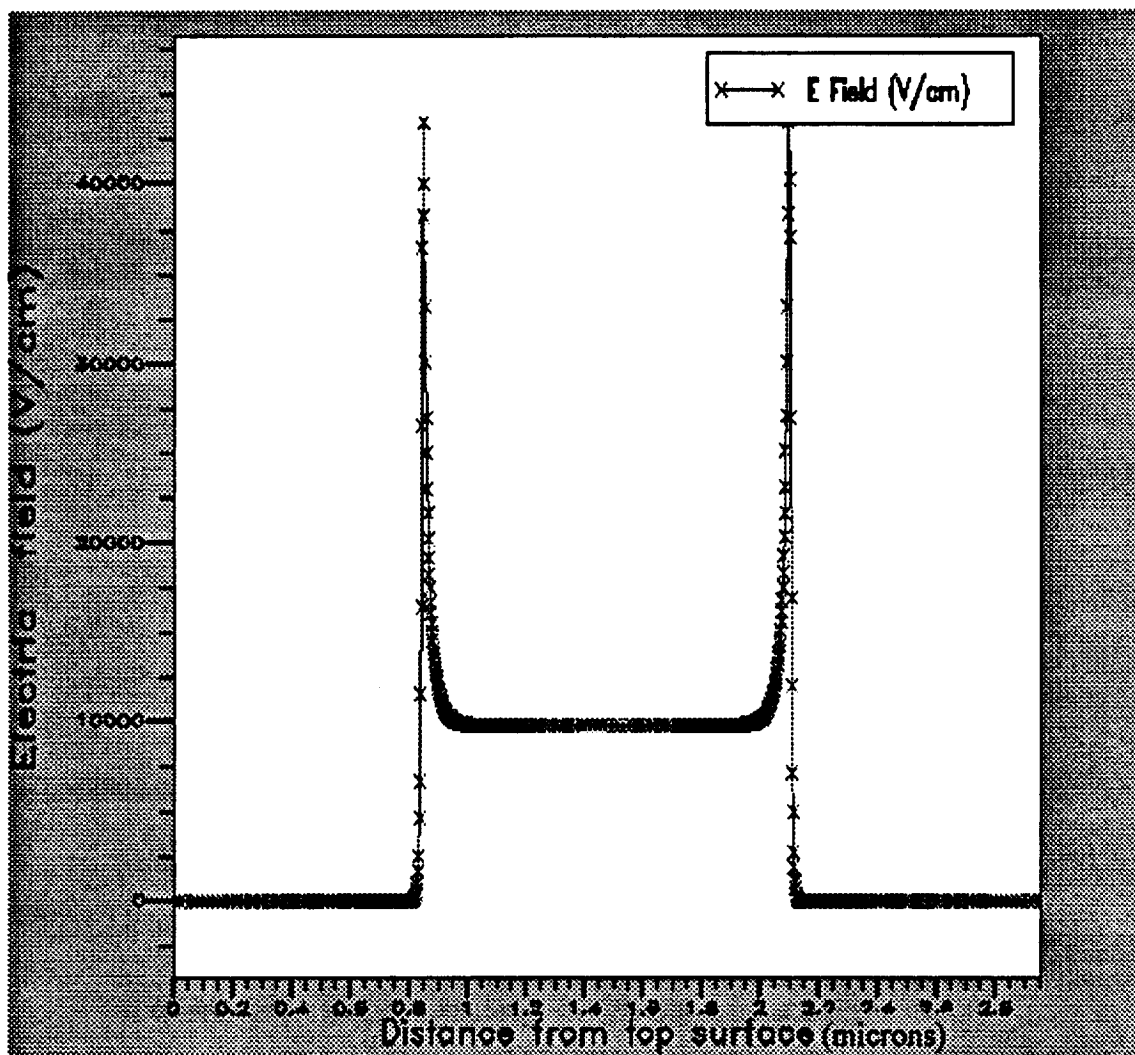


Figure 3-2: Electric field profile for an unbiased PIN APD

3.2.2 External Properties

Figure 3-3 shows the simulated dark and light IV characteristics for a PIN APD with a 1 μm intrinsic GaAs region. The distributed contact resistance for both the p and n contacts was set to $1 \times 10^4 \Omega \cdot \text{cm}^2$. The device shows a gain of about 4 at a reverse bias of 38 V.

Figure 3-4 shows the simulation results for the spectral output of the same PIN structure under constant power illumination compared to the output that would be expected if no recombination processes were present. The spectral response drops sharply around 0.9 μm due to the absorption properties of the material. This long-wavelength cutoff is determined by the GaAs energy gap which is about 1.43 eV ($\sim 867 \text{ nm}$) at room temperature. The spectral response data can be used to determine the external quantum efficiency of the structure as will be shown in the following chapter.

Figure 3-5 shows the photogeneration rate in a 3 μm GaAs PIN APD under 400, 632, & 850 nm illumination. At a wavelength of 400 nm, most of the photogenerated carriers are created near the top surface within the first 0.2 μm . At the HeNe wavelength of 632 nm, most of the incident light is absorbed in the p^+ GaAs layer before reaching the avalanche region. As the wavelength increases toward the near-infrared part of the spectrum, carrier photogeneration in the depletion region becomes increasingly important, and the light absorption capacity of the structure is reduced as was demonstrated by the spectral output of Figure 3-4.

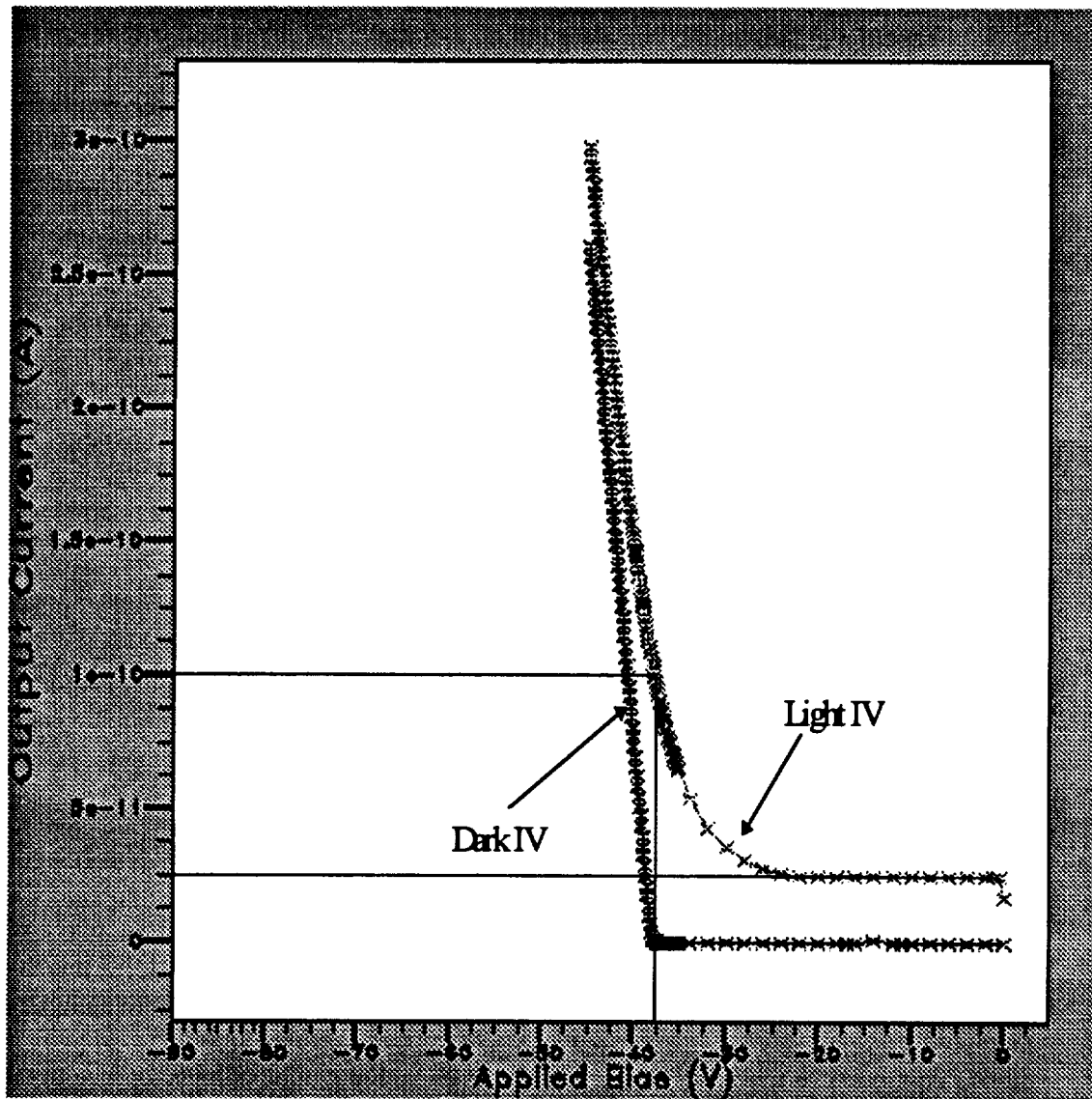


Figure 3-3: Simulated dark and light IV plots for a PIN APD under reverse bias

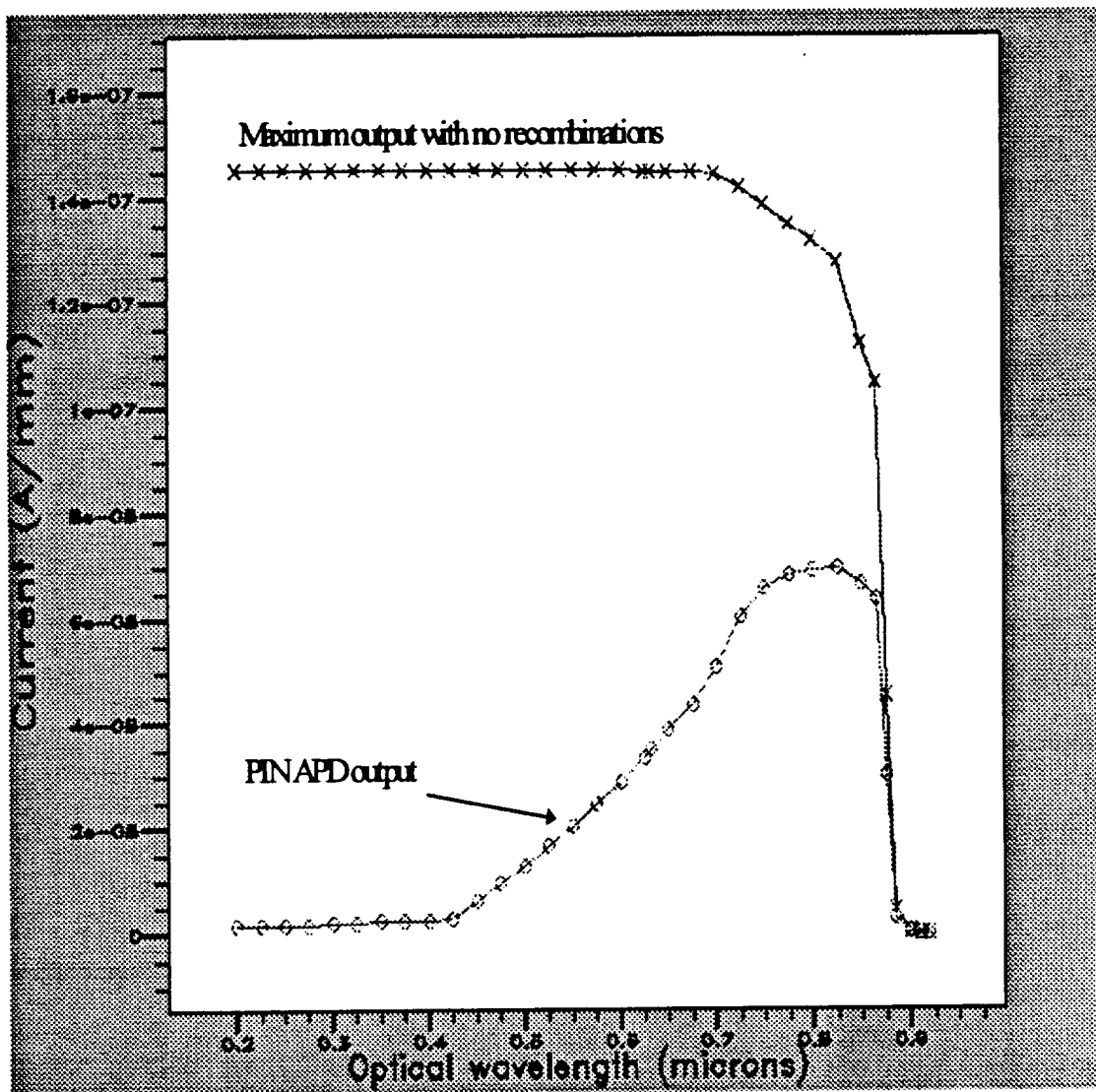


Figure 3-4: Spectral output (zero reflection) for a 3 μm GaAs PIN (1 μm /1 μm /1 μm) APD

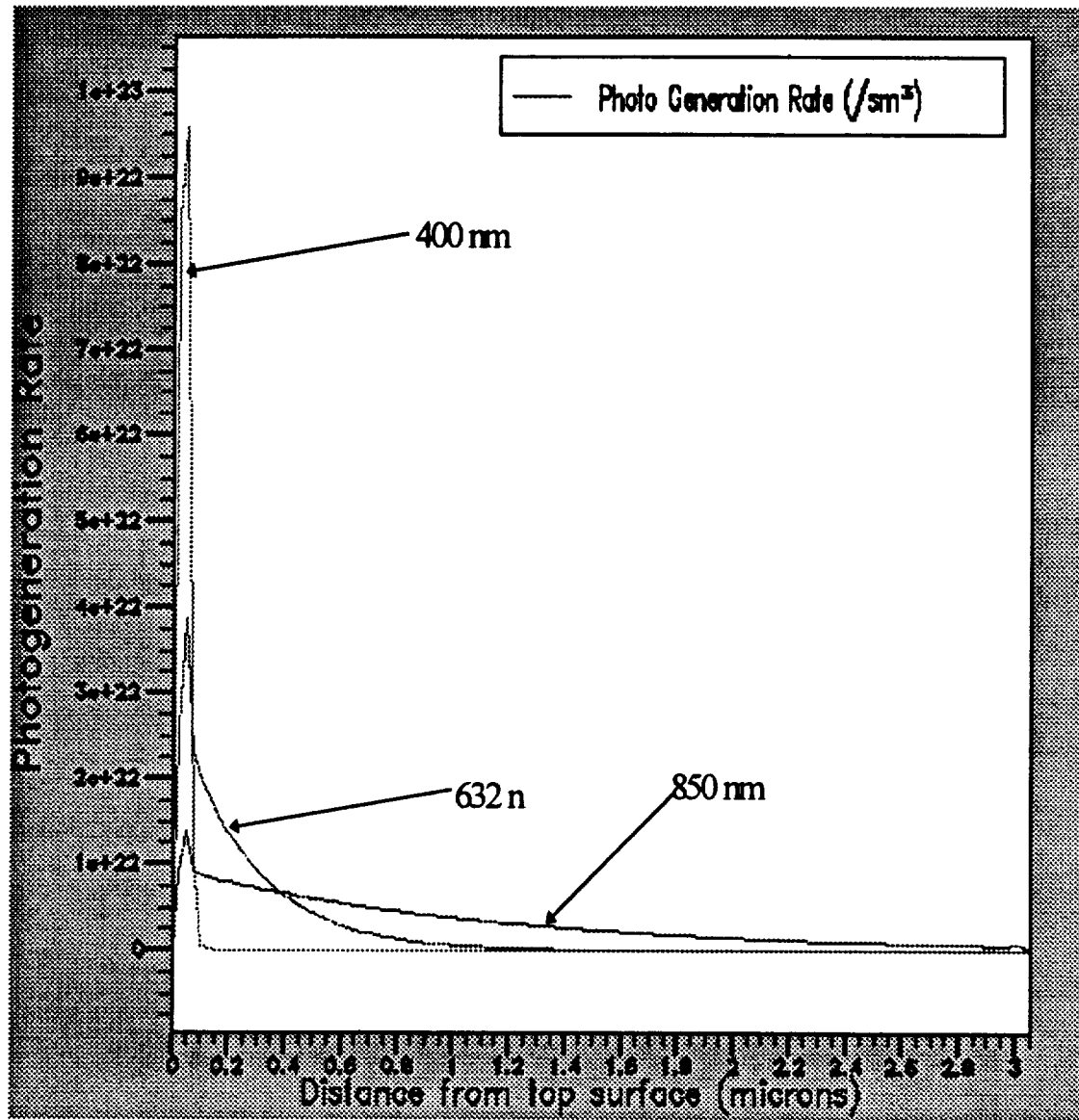


Figure 3-5: Photogeneration rate in a 3 μm GaAs PIN under 400, 632, & 850 nm illumination

-
- [26] Silvaco International, ATLAS User's Manual, Device Simulation Software, version 4.0, June 1995.
- [27] J.W. Slotboom, "The PN Product in Silicon", Solid State Electronics 20, pp. 279-283. 1977.

CHAPTER IV	56
4.1 DESCRIPTION OF STRUCTURES	56
4.2 SUMMARY OF CAPABILITIES OF THE APD CHARACTERIZATION LAB	58
4.3 EXPERIMENTAL TECHNIQUES	59
4.3.1 Spectral response measurements	59
4.3.2 Current as a function of reverse bias (IV)	59
4.3.3 Capacitance as a function of reverse bias (CV)	61
4.3.4 Noise measurements	61
4.3.5 Transient Response Measurements	61
4.4 MODELING CAPABILITIES	63

CHAPTER IV

EXPERIMENTAL APPARATUS

4.1 Description of Structures

All of the APD structures were grown by molecular beam epitaxy (MBE) in a Varian Gen II system and were fabricated using standard photolithographic techniques. Figure 4-1 shows a cross section of an experimental MQW APD where contact rings were used to provide a uniform electric field across the entire device. The MQW region in all tested devices consisted of 10 to 30 sets of alternating layers of GaAs (500 Å) and $\text{Al}_{0.42}\text{Ga}_{0.58}\text{As}$ (500Å) with 1000 Å periods. All APDs were composed of a 1 mm Be-doped ($3 \times 10^{18} \text{ cm}^{-3}$) p^+ top layer, and a 1.5 mm Si-doped ($3 \times 10^{18} \text{ cm}^{-3}$) n^+ back layer. In the doped-well MQW devices, high electric fields were achieved in the narrow bandgap GaAs wells of the avalanche region through the introduction of thin (50-150 Å) and highly doped (0.5×10^{18} - $1.5 \times 10^{18} \text{ cm}^{-3}$) p^+ and n^+ layers. The doped-barrier MQW structures were similar with the exception that the doping layers were in the AlGaAs barriers. In the undoped MQW structures, no doping was incorporated in the avalanche region, and in the conventional APD design (PIN), the MQW region was replaced by a 1 to 2.5 mm intrinsic GaAs layer. Pure electron injection was achieved by focusing a 632.8 nm HeNe laser inside the circular p-contact ring using a microscope objective.

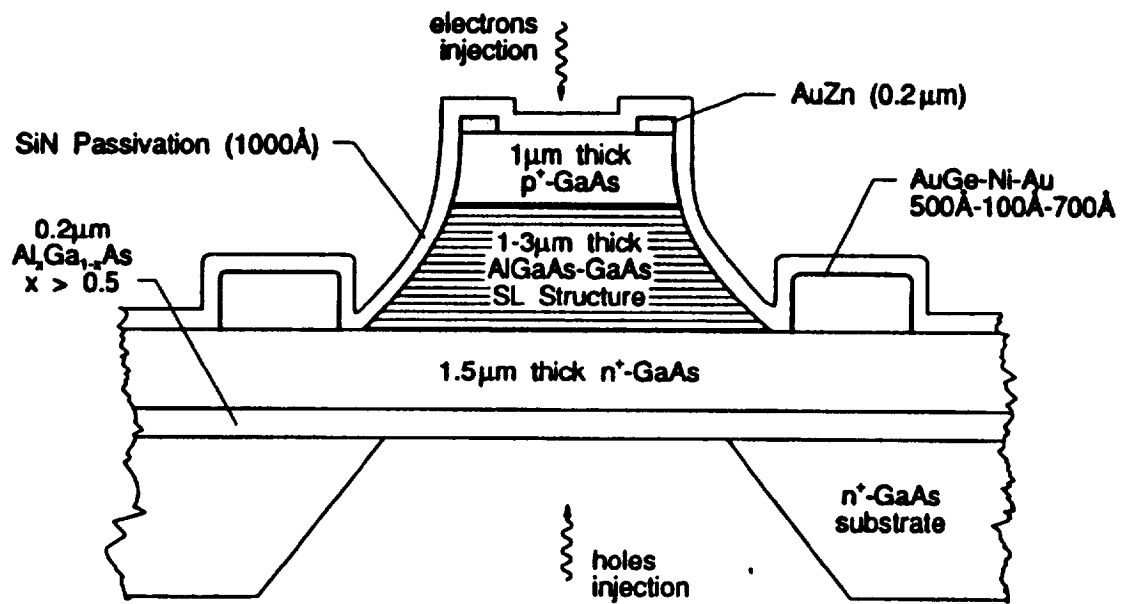


Figure 4-1: Cross Section of a MQW APD

4.2 Summary of Capabilities of the APD Characterization Lab

The purpose of this lab is to measure the various optical and electrical properties that determine the output performance of the avalanche photodiode (APD) structures that are grown and fabricated at the Quantum Microstructures Lab at GTRI. Various computer automated experiments have been developed to study and optimize the different parameters of the APDs in order to determine their gain, noise level, breakdown voltage, spectral response, and speed. A brief description of some of those experiments and the information they provide about the photodiode is presented in the table below.

Table 4-1: Summary of APD characterization capabilities

Experiment	Description	Information Provided
Spectral Response	Responsivity as a function of wavelength and gain	Sensitivity of photodiode throughout the optical spectrum
I-V response	Diode current output as a function of applied bias (10 K - 373 K)	Photodiode gain and variations with incident light intensities
C-V response	Diode capacitance as a function of applied bias (10 K - 373 K)	Profile of the carrier concentrations vs depletion width in doped APD's
Noise measurement	Noise level as a function of laser power density (10 K - 373 K)	Excess noise factor at various diode gains and temperatures
Transient Response	APD response to a high power 50 ps laser pulse	APD bandwidth limitations and heterojunction interface quality

In the following few sections, brief descriptions and illustrative diagrams will be provided to explain the operating principles behind each one of the above experiments.

4.3 Experimental Techniques

4.3.1 Spectral Response Measurements

The spectral response measurements were conducted using a $\frac{1}{2}$ m Jarrell-Ash spectrometer and a broadband light source placed near the entrance slit. The light component at the exit of the spectrometer was then focused on the top p-region of the photodiode. The output current of the APD was then measured as a function of wavelength between 300 and 900 nm and adjusted for the variations in the lamp's optical spectrum supplied by the manufacturer. By measuring the incident light power and neglecting surface reflection, the spectral data can be used to get an estimate of the external quantum efficiency of the device.

4.3.2 Current as a Function of Reverse Bias (IV)

IV measurements are conducted using a computer-controlled Keithley Source-Measure Unit (SMU) which provides the applied voltage and reads the corresponding output current of the photodiode. Both dark and light IV measurements are conducted and the data is then used to calculate the multiplication gain of the device as a function of applied bias. Either electron- or hole-injections can be achieved by focusing the HeNe laser beam inside the p-contact ring at the top, or the bottom n-layer as shown in Figure 4-1. The operating temperature can be varied between 80 to 400 K by mounting the structures inside a Joule-Thomson cooling system supplied by MMR Technologies. A

schematic of the optical set-up used to mount and test the APDs is shown in Figure 4-2.

The vacuum chamber used for low temperature measurements is shown in Figure 4-3.

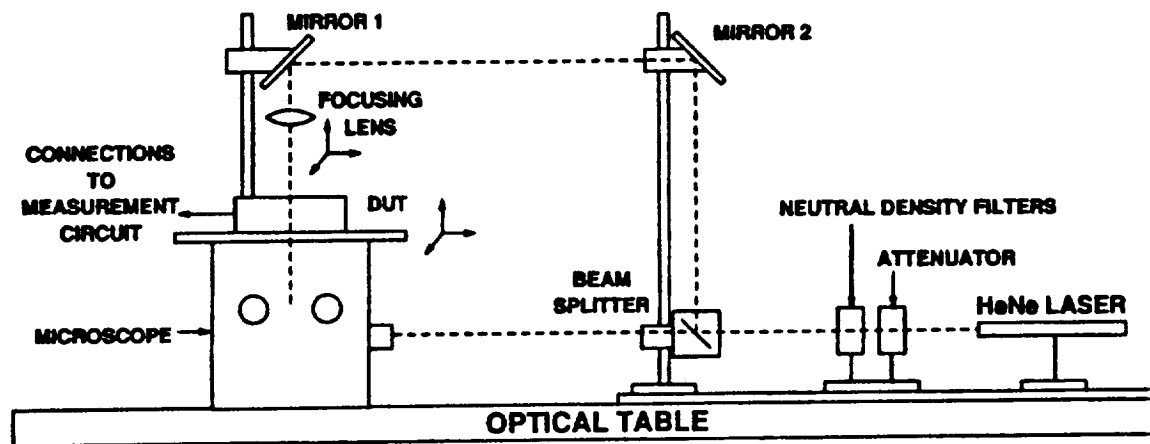


Figure 4-2: Experimental Set-up for IV, CV & Noise Measurements

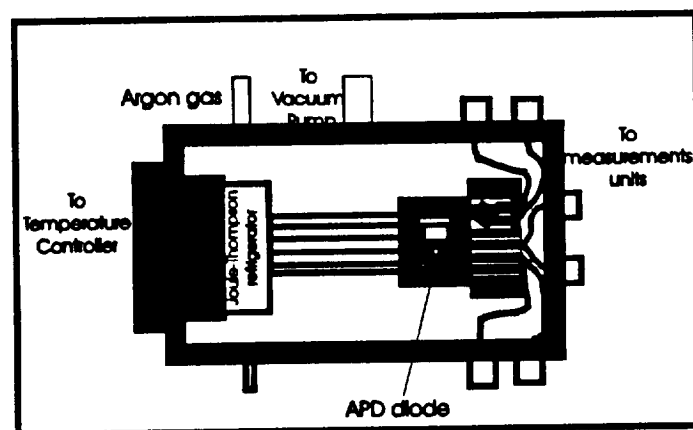


Figure 4-3: Vacuum Chamber used for Low Temperature Measurements

4.3.3 Capacitance as a Function of Reverse Bias (CV)

CV Measurements were made using a computer-controlled HP4277A LCZ meter which can be interfaced with the same experimental set-up shown in Figure 4-2 and Figure 4-3. The CV data is then used to calculate the doping concentrations and the depletion width profiles of the structures as was explained in Chapter II.

4.3.4 Noise Measurements

Excess noise measurements are made using an HP8568B Spectrum Analyzer controlled through an IEEE interface. The APD noise output is measured for a constant value of the gain or reverse bias, and is normalized to the noise value corresponding to a unity gain. The calculated excess noise factor, $F(M)$, is defined as the “excess” output noise resulting from impact ionization processes. It can be measured using either electron or hole injection, $F_e(M)$ or $F_p(M)$. The excess noise factor is then plotted as a function of structure gain and the data is compared to McIntyre theoretical curves to determine the electron/hole impact ionization ratio.

4.3.5 Transient Response Measurements

Time response measurements were conducted using a high-power Hamamatsu laser pulser (PLP-03) operating at ~820 nm with a pulsewidth around 50 picoseconds. The APD output pulse is detected using a Tek11801 digital oscilloscope w/ a 50 MHz SD-32 sampling head. The corresponding set-up is shown in Figure 4-4. Transient

response measurements are used to determine transit and diffusion times as well as the effect of carrier trappings on overall device bandwidth.

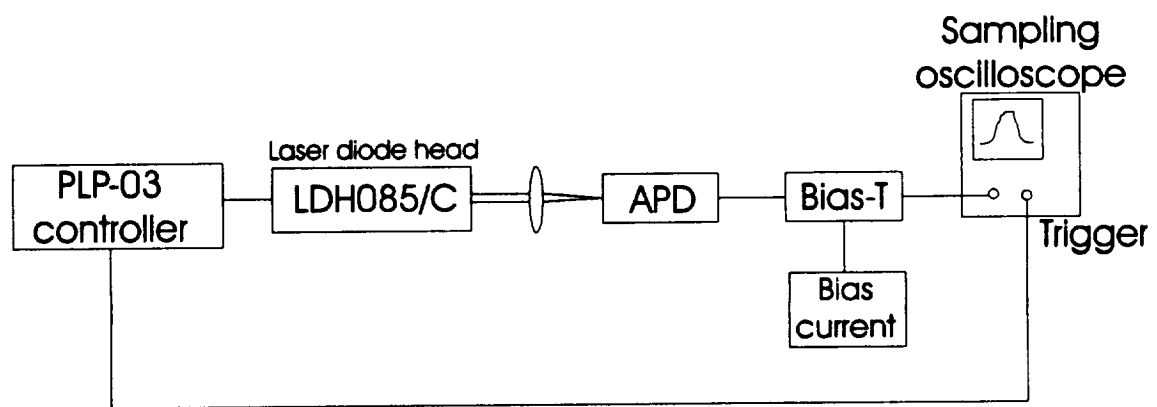


Figure 4-4: Experimental Set-Up for Lifetime Response Measurements of APDs

4.4 Modeling Capabilities

Silvaco's device simulation software uses powerful numerical techniques to solve for the various microscopic and macroscopic properties of heterojunction devices. The following is an overview of the general capabilities of ATLAS which includes the following tools and extensions:

- **ATLAS:** Supplies general capabilities that are accessible by all device simulation products.
- **S-PISCES:** Simulates silicon devices.
- **BLAZE:** Simulates devices fabricated using arbitrary semiconductors (including II-VI, III-V, and IV-IV materials), and heterojunction devices.
- **GIGA:** Adds the ability to perform nonisothermal calculations that include the effects of lattice heating and heat sinks.
- **TFT:** Allows the simulation of polycrystalline- and amorphous-based devices
- **LUMINOUS:** Provides capabilities to model optoelectronic devices, including sophisticated ray-tracing
- **LASER:** Allows the simulation of heterostructure lasers by self-consistent solution of the Helmholtz equation for the optical field.
- **MIXEDMODE:** Offers circuit simulation capabilities that employ numerical physically-based devices as well as compact analytical models
- **DEVICE3D:** Provides capabilities for three-dimensional device simulation
- **INTERCONNECT3D:** Provides capabilities for three-dimensional parasitic extraction.

- **THERMAL3D:** Provides capabilities for three-dimensional thermal analysis.

Using the above tools and packages, one can design programs where the material parameters and device structure are defined in the input deck. ATLAS is then used to provide a comprehensive set of physical models including -but not limited to- the following:

- DC, AC small-signal and full time dependency analysis.
- Drift-diffusion transport models.
- Advanced mobility models.
- Graded and abrupt heterojunctions.
- Ohmic, Schottky, and insulating contacts.
- SRH, radiative, Auger, and surface recombination.
- Local and non-local impact ionization.
- Band-to-band and Fowler-Nordheim tunneling.
- Optoelectronic interactions with general ray tracing.
- General electronic circuit environment.

ATLAS supports a large number of semiconductor materials and compounds such as Si, GaAs, AlGaAs, ZnS, as well as various metals and insulators such as aluminum, gold, SiN, SiO₂, vacuum, and air.

CHAPTER V

EXPERIMENTAL RESULTS AND COMPARISON WITH THEORY

5.1 Gain/Noise Properties of Doped MQW Junctions

5.1.1 Introduction

In this section, a detailed characterization has been made of the external properties of both the PIN and the MQW structures. Comparison of the gain properties at low voltages between the MQW and conventional APDs showed a direct experimental confirmation of a structure-induced carrier multiplication due to interband impact ionization. Similar studies of the bias dependence of the excess noise characteristics show that the low-voltage gain is primarily due to electron ionization in the MQW-APDs, and to both electron and hole ionization in the conventional APDs. For the doped MQW APDs, the average gain per stage was calculated by comparing gain data with depletion width and carrier profile measurements, and was found to vary from 1.03 at low bias to 1.09 near avalanche breakdown. These results are in good agreement with theoretical models developed by Brennan²⁸ for similar derivatives of the doped MQW APD.

5.1.2 Gain Enhancement

As was previously mentioned, superlattice multiplication APDs are designed to outperform bulk multiplication APDs by artificially enhanced ionization through the introduction of multiple quantum well layers. This behavior is attributed to the large difference in the conduction and valence-band edge discontinuities at the AlGaAs/GaAs

interface. To better understand these characteristics, consider once again the energy band diagram shown in Figure 1-2. When a “hot electron” enters from the AlGaAs barrier layer into a GaAs well, it abruptly gains an energy equal to the conduction band gap discontinuity, ΔE_c . The effect is that the electron “sees” an ionization energy reduced by ΔE_c with respect to the threshold energy in bulk GaAs ($E_{th}=2.0$ eV).²⁹ Since the impact ionization rate α increases exponentially with decreasing E_{th} , a large increase in the effective α compared to that in bulk GaAs is expected. When the electron enters the next barrier layer, the threshold energy in the AlGaAs material is increased by ΔE_c therefore decreasing the value of α in the AlGaAs. However, since $\alpha_{GaAs} \gg \alpha_{AlGaAs}$, the exponential dependence on the threshold energy results in an increase in the overall average α given by:

$$\alpha_{avg} = (\alpha_{GaAs} + \alpha_{AlGaAs}) / (L_{GaAs} + L_{AlGaAs}) \quad [5-1]$$

where L represents the layer thicknesses.

In contrast, the ionization rate for holes, β , is not increased substantially due to the smaller valence-band discontinuity. This results in a net enhancement in the α/β ratio.³⁰

The APD devices were characterized under both light and dark conditions using current-voltage (I-V), capacitance-voltage (C-V), and noise measurements. Gain curves were calculated from the reverse bias I-V measurements performed as a function of photon flux. Carrier concentrations and depletion width profiles were determined from the C-V data using a one-sided junction approximation.

The I-V measurements were taken in the dark and under HeNe laser illumination using the experimental apparatus described in section 4.3.2. In order to ensure pure electron injection, the laser beam was focused through a microscope objective at the center of the 75 μm diameter opening in the upper p-contact ring. Breakdown voltages, V_B , were measured to be about 27 V for the doped MQW APD and 63 V for the conventional APD with corresponding dark currents, measured at 20% of the breakdown voltages, of about 10 pA and 100 pA, respectively. The dark current IV plots are shown in Figure 5-1 where the low breakdown voltage characteristics of the doped MQW APD is demonstrated. This is a result of the high doping present in the junction which helps increase the electric field magnitude closer to its critical avalanche value.

The C-V measurements were performed at 1 MHz using the apparatus described in section 4.3.3. The C-V data (shown in Figure 5-2) was then analyzed to calculate the depletion widths and carrier profiles for the two structures. The net carrier concentration for the conventional APD is shown in Figure 5-3 as a function of the calculated depletion width. As the reverse bias is increased, the capacitance decreases to 0.8 pf, while the depletion width increases to about 2.6 μm prior to breakdown around 63V. Note that the carrier concentration increases sharply as the depletion edge is extended into the doped contact region. Figure 5-4 shows the corresponding plot for the doped-well MQW device which had a breakdown voltage of about 27 Volts. This plot clearly shows evidence of the depletion of all 10 stages in the MQW APD. The presence of the peaks in the carrier profile data is due to the unequal p and n doping concentrations

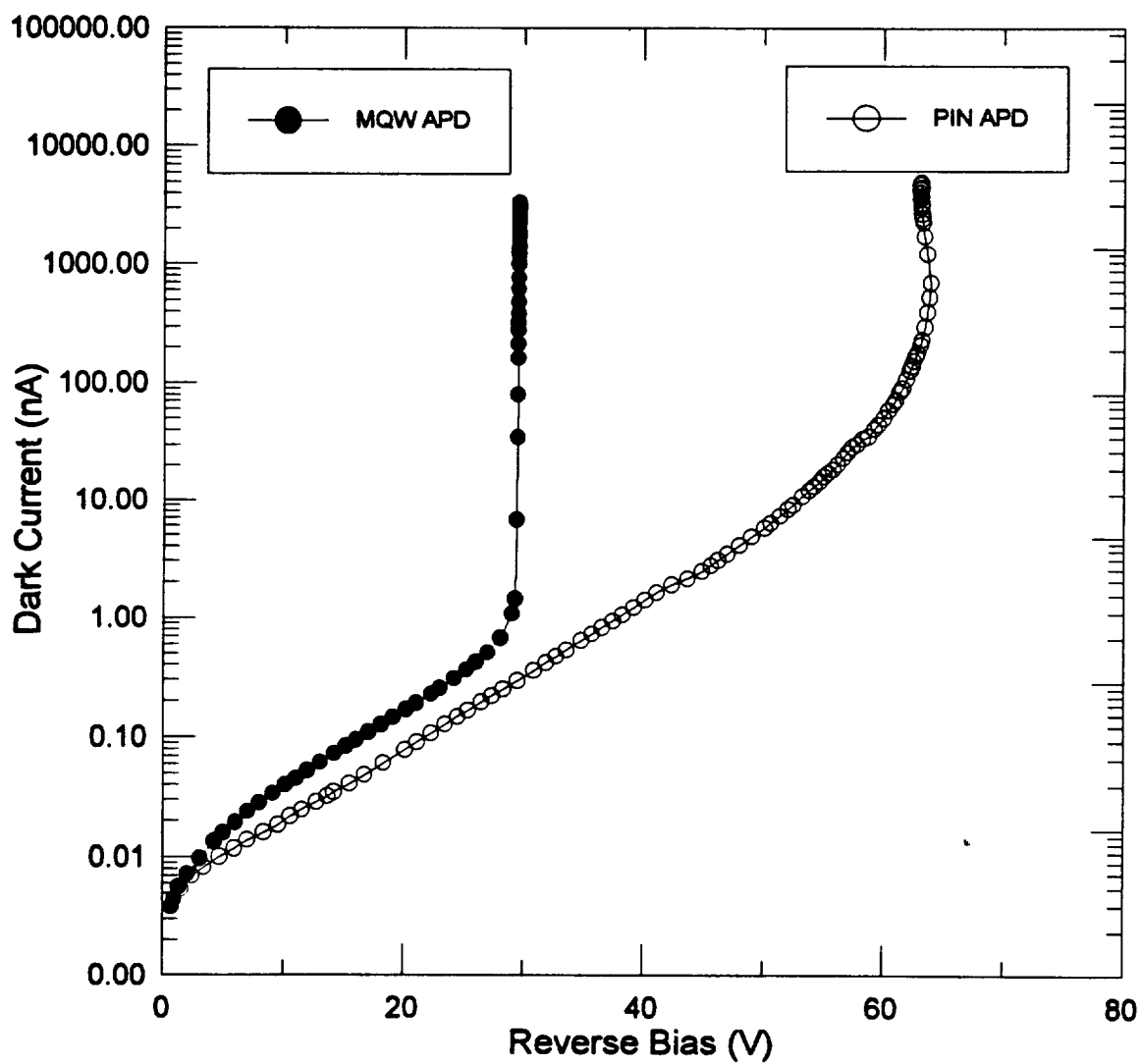


Figure 5-1: Dark IV plots for the PIN and the doped-well MQW APD

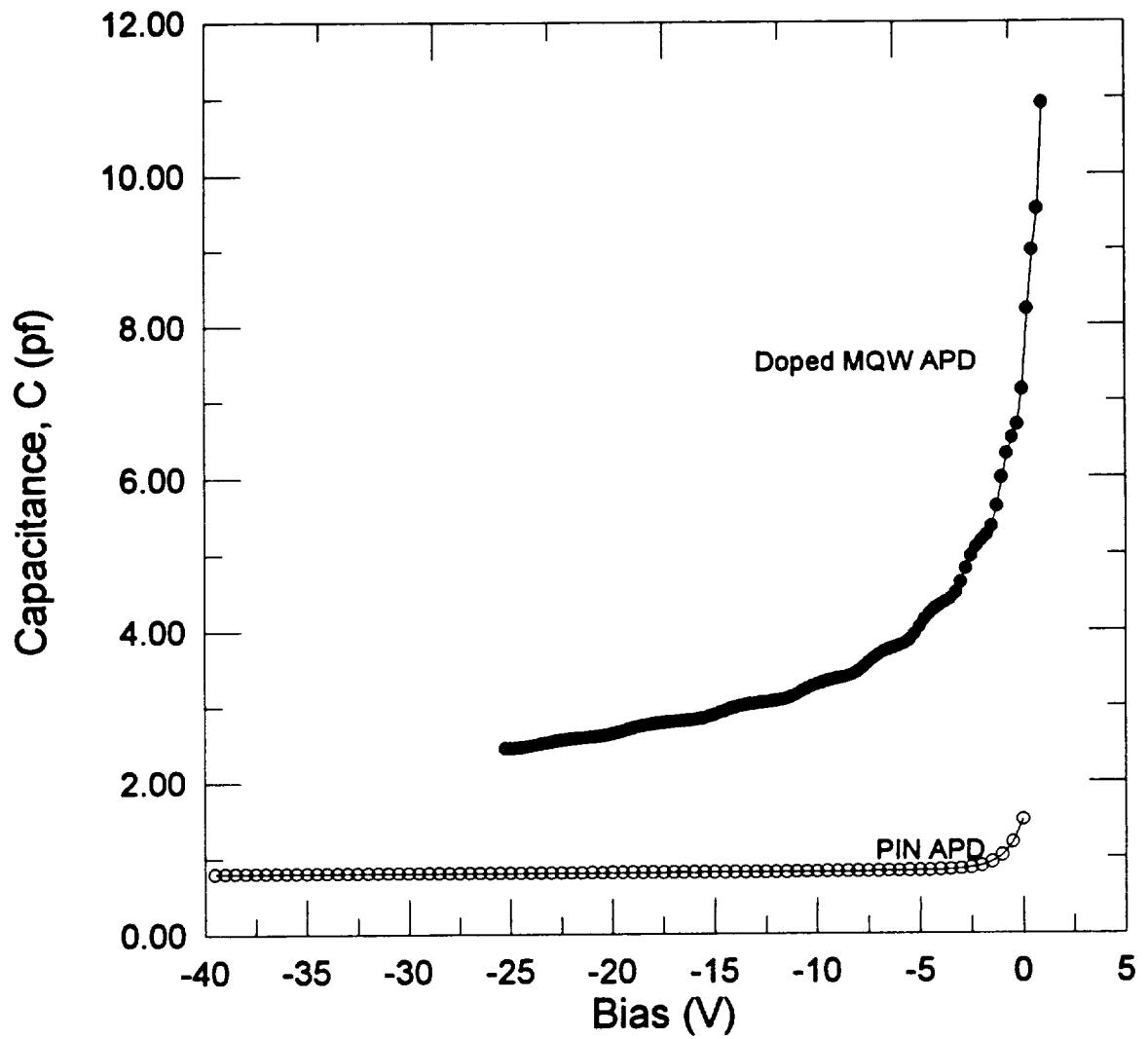


Figure 5-2: CV plots for PIN and a doped MQW APDs

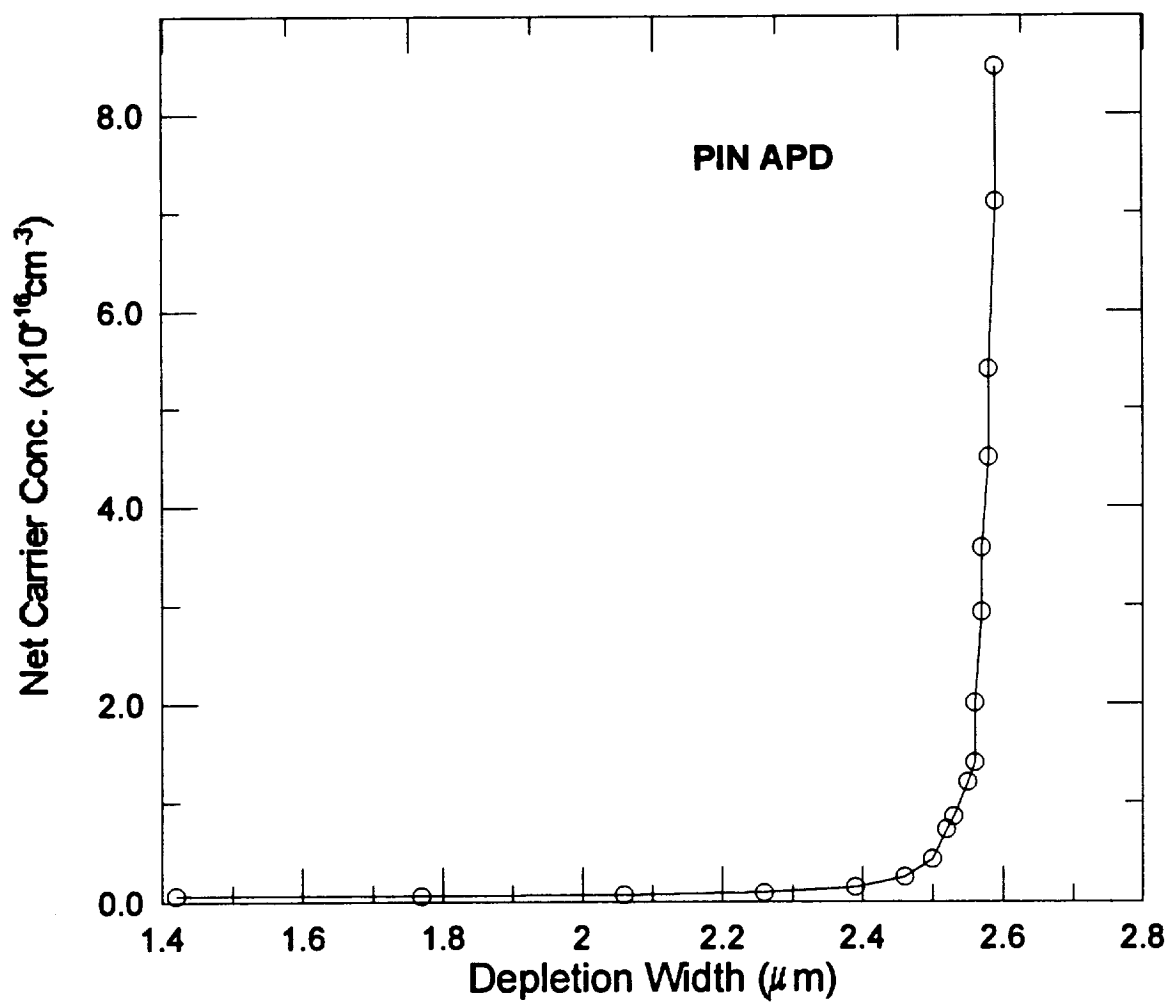


Figure 5-3: Carrier concentration profile vs depletion width for the PIN APD.

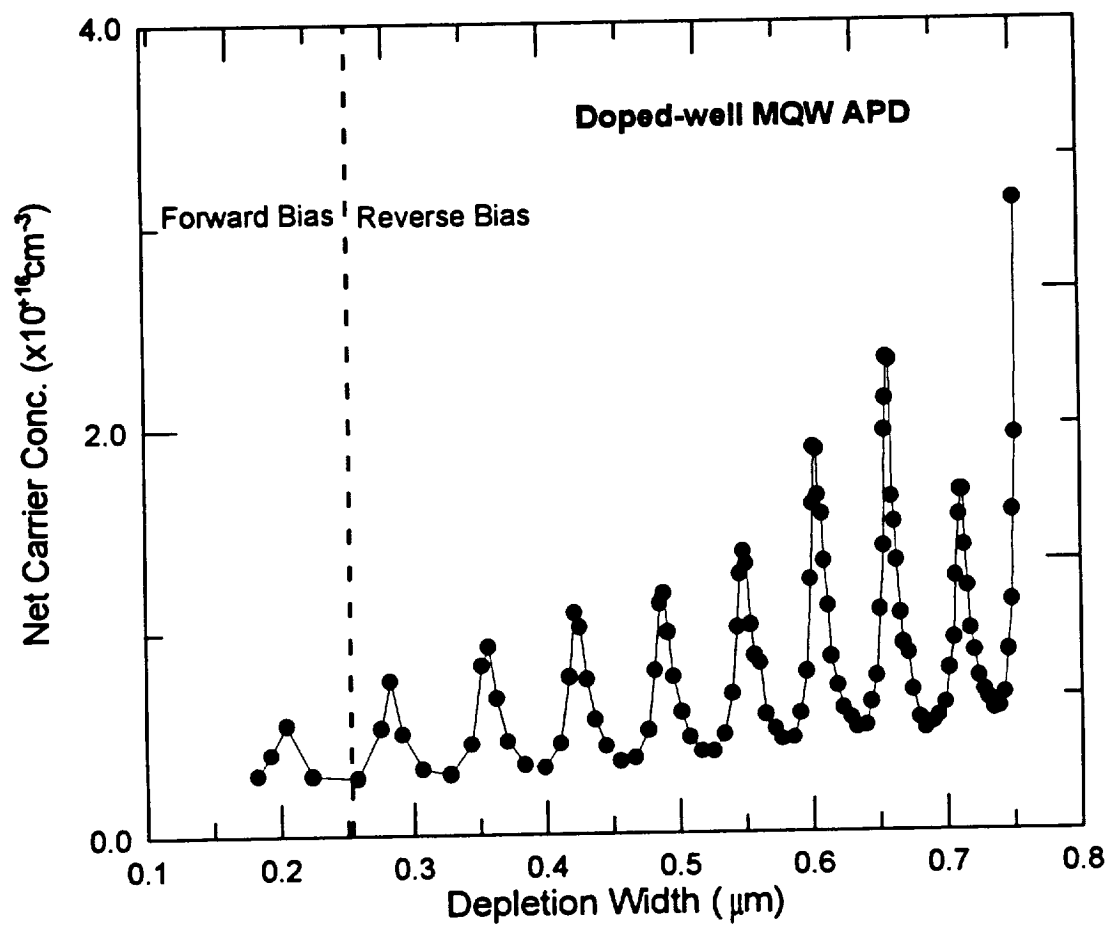


Figure 5-4: Carrier concentration profile vs depletion width for the doped MQW APD.

in the wells. This results in partial depletion of the junction as will be shown shortly. With applied bias, the depletion width increases, and additional quantum-well stages become depleted. This gives rise to ripples in the CV profile resulting from peaks in the carrier concentration. Note that the peak positions do not agree with the 1000 Å period of the MQW structure. This discrepancy is due to the fact that carrier concentration profiles were calculated assuming a one sided depletion.³¹ This is generally not the case in such structures unless there is a large doping imbalance in the junction preventing it from depleting both ways. In addition, the spatial resolution of the C-V measurements was limited by the Debye length given by³²,

$$L_D = \sqrt{(kT\epsilon_s / q^2 N)} \quad [5-2]$$

which is about 40 Å at room temperature for a doping level of $n=1.5 \times 10^{18} \text{ cm}^{-3}$. The Debye length is the distance over which the Coulomb (electrostatic) forces between charged layers are essentially screened out. Since the thickness of the doped layers in the wells was of the same order of magnitude (50 Å), abrupt changes in the doping concentration could not be accurately measured.

The gain curves, calculated from the I-V data, are shown in Figure 5-5 where the bias values were normalized by the breakdown voltage of each device to enable comparison. Figure 5-5(a) clearly shows the presence of gain in the doped MQW device in the low voltage region while the conventional p-i-n structure (Figure 5-5(b)) does not show any gain in this regime. This is an indication of a structure-induced carrier multiplication resulting from the band discontinuity and the doping in the MQW APD. In order to calculate the gain per period in the doped MQW, the carrier profile plot (Figure

5-4) was superimposed on the gain curve (Figure 5-5(a)) and the gain was estimated at each consecutive carrier concentration minimum as shown in Figure 5-6. The corresponding gain values per stage were found to increase from 1.03 at low bias (one depleted stage), to about 1.09 near breakdown (ten depleted stages). These results are in good agreement with theoretical predictions provided by Brennan²⁸ for similar derivatives of the doped MQW APD.

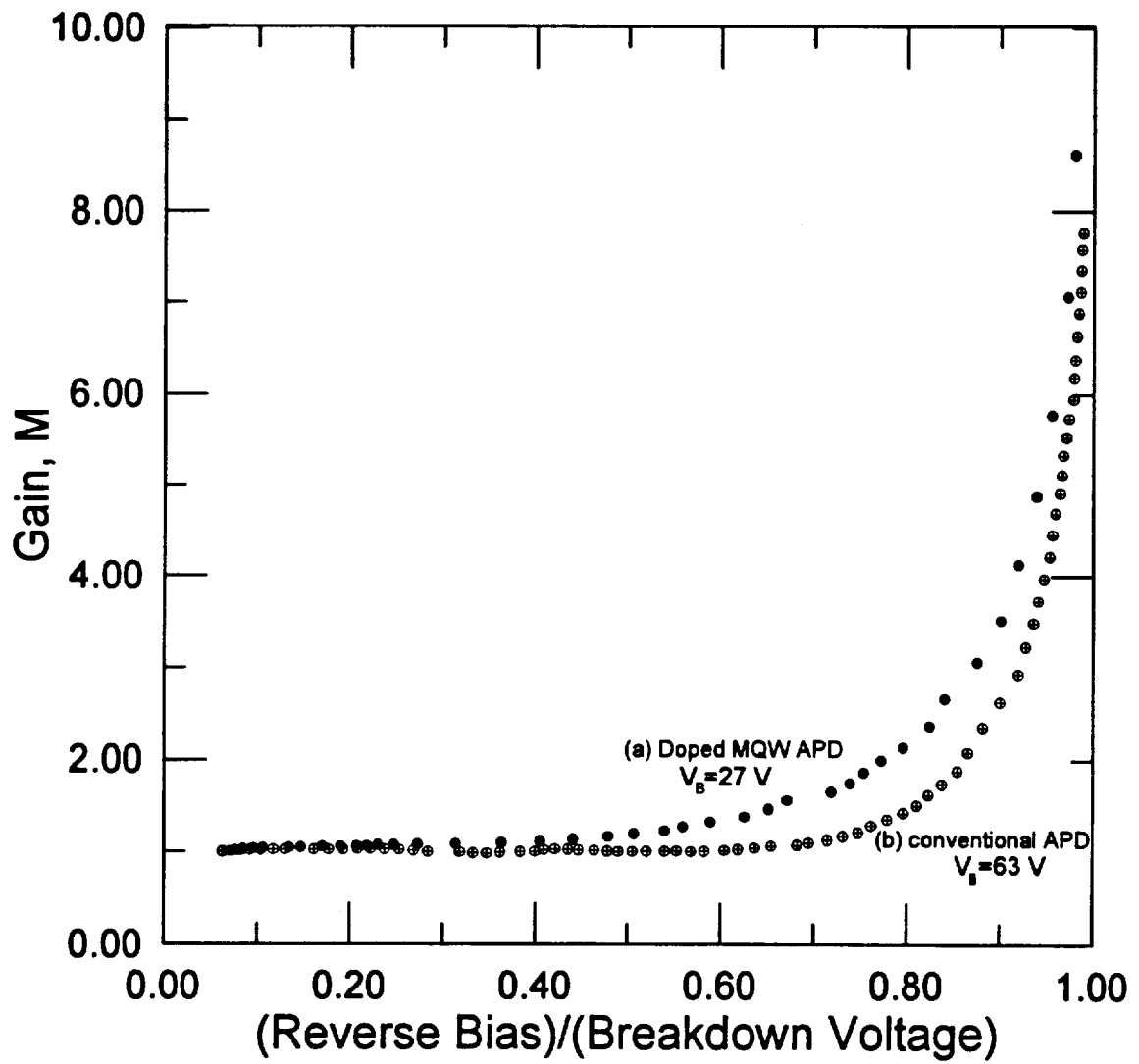


Figure 5-5: Gain vs. the ratio of reverse bias to breakdown voltage for the (a)MQW APD and (b)PIN APD.

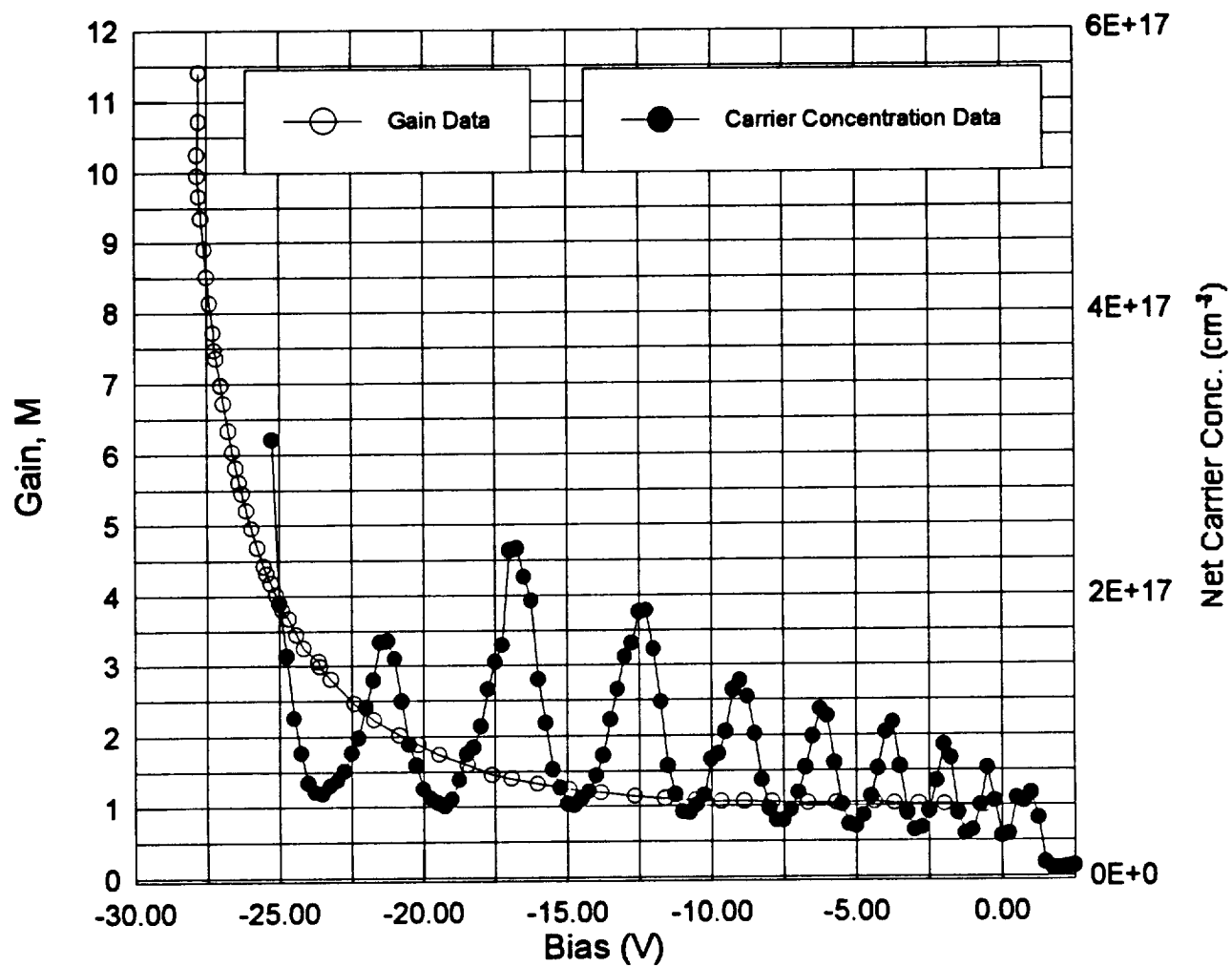


Figure 5-6: Plot used for determining gain per stage for a doped MQW APD

5.1.3 Dark Current Reduction

Dark current is one of the main parameters of concern in photodetectors. Dark current analysis and the reduction of dark current are very important for high sensitivity and low noise applications. Defect centers, heterojunction interface traps, as well as mesa surface leakage can generate high levels of excess dark current and reduce minority-carrier lifetime.³³

In a typical PN junction, the overall dark current is the sum of the bulk and surface components. The bulk component is usually made up of diffusion, generation-recombination, and tunneling currents. The surface component consists of generation-recombination, and leakage shunt currents usually formed at semiconductor and dielectric interfaces.³⁴ In a device structure with top p and n contacts such as the APDs used in our experiments, there are additional sources of dark current components. These are due to defect centers at the GaAs/AlGaAs interface and most importantly to surface leakage currents along the mesa edge which can contribute significantly to the dark current.

In this section, it will be shown how substantial the surface leakage component can be and how certain growth, processing and surface treatment techniques can be used to dramatically lower surface leakage currents by several orders of magnitude. The devices that were measured were volume- and delta-doped MQW. In the volume-doped MQW structures, the GaAs wells were doped with 50 Å ($3.0 \times 10^{18} \text{ cm}^{-3}$) adjacent p^+ and n^+ layers. In the delta-doped APDs, p^+ and n^+ layers with a sheet charge density of $1\text{--}5 \times 10^{12} \text{ cm}^{-2}$ were introduced separated by undoped spacer layers ranging from 50 to 150 Å. Through careful dopant calibration, the devices were grown such as to achieve full

depletion at low bias. After processing the devices into mesa diodes, various surface passivation treatments were investigated. These include both plasma ashing in an O_2 plasma and ammonium sulfide treatments. Through the application of such treatments, a decrease in the reverse bias dark current by as much as a factor of 1000 was achieved in the low bias region. This can be seen in Figure 5-7 where the dark current is plotted both before and after surface treatment by ammonium sulfide. The dark current approximately follows a square-root behavior at low to medium reverse bias while at high biases, avalanche currents dominate. The rapid increase in the dark current at low reverse bias and the large drop in its value achieved by surface treatment are indicative of surface leakage. The leakage in these heterojunction mesa diodes was dominated by generation/recombination current near the intersection of the mesa surface with the GaAs/AlGaAs depletion region.

As a result of surface treatment, dark currents as low as 1 pA were obtained under zero applied bias. In some APDs, the dark currents increased to only 12 pA at 20% of breakdown. In addition, these devices exhibited extremely high gains which exceeded 10,000 in some cases. In most traditional APDs, the presence of high dark currents usually presents a limiting factor preventing the further increase in a device's photocurrent gain beyond avalanche breakdown. By reducing the dark currents in these devices, it was possible to maintain it at levels well below that of the photocurrent. This made it possible to achieve and sustain high levels of gains well beyond breakdown.

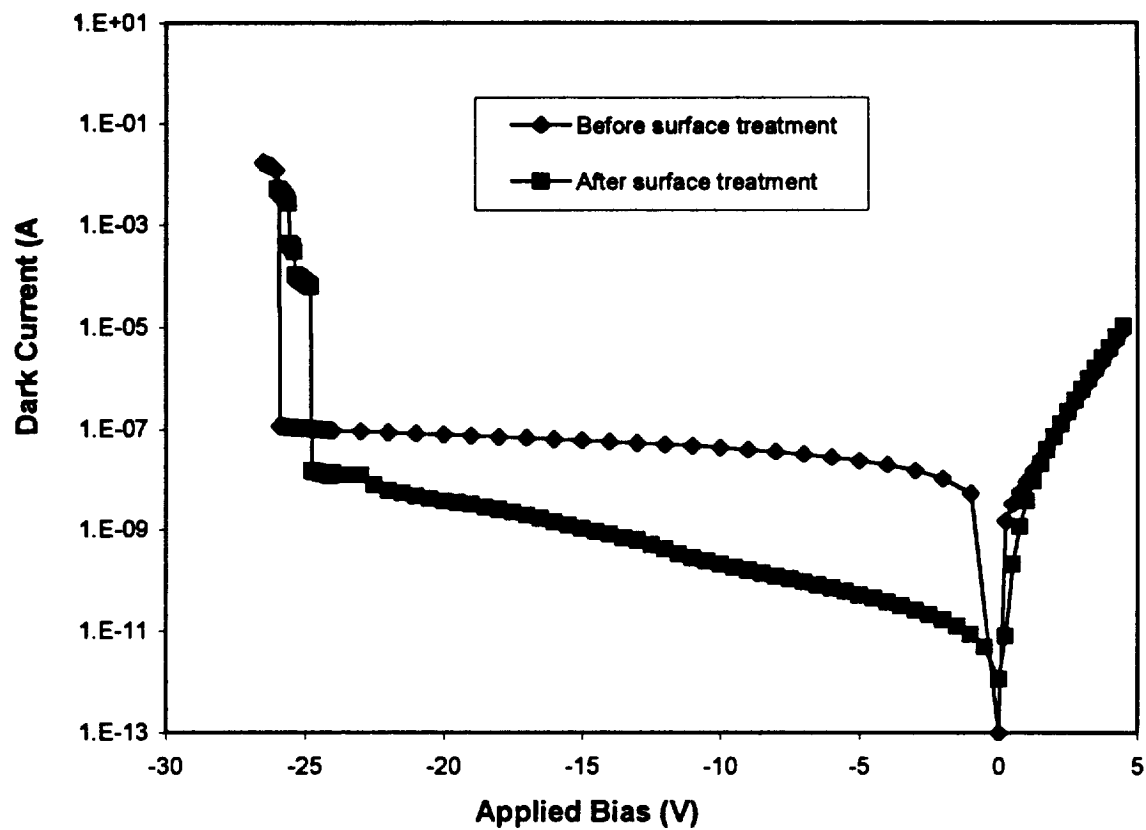


Figure 5-7: Dark current reduction as a result of surface treatment by ammonium sulfide

5.1.4 Excess Noise Reduction

There are many different types of noise that may be present in an electrical device. A brief discussion of the various types of noise mechanisms is presented below.

5.1.4.1 Johnson Noise

Johnson noise is caused by the random motion of thermally energetic electrons in resistive materials. Its instantaneous amplitude is not predictable, but the probability of its amplitude being within an interval of dV volts is equal to $p(V)dV$ where $p(V)$ is expressed by the familiar Gaussian probability function:

$$p(V) = \frac{1}{(2\sigma^2)^{1/2}} e^{-V^2/2\sigma^2} \quad [5-3]$$

where the parameter σ is the rms value of the fluctuations and the quantity universally accepted to describe the noise output from a resistor. σ is bandwidth dependent and is expressed as follows:

$$\sigma = (4kTR_s B)^{1/2} \quad (\text{volts}) \quad [5-4]$$

where k is Boltzmann's constant, T is the resistor temperature in K, R_s is the resistance in ohms, and B is the noise bandwidth in hertz. Johnson noise is "white noise", that is the rms value per unit bandwidth (rms density) is constant from DC to frequencies extending into the infrared region.

5.1.4.2 Shot Noise

Shot noise is the result of random current fluctuations in vacuum tubes and semiconductor junctions. It is caused by the random arrival of discrete electron charges at anodes, collectors, and drains. The rms value of shot noise is given by:

$$I_{shot} = (2eI_{dc}B)^{1/2} \quad (A) \quad [5-5]$$

where e is the electron charge, I_{dc} is the average DC current through the diode, and B is the noise bandwidth in hertz.

5.1.4.3 Flicker Noise

Flicker noise is characterized by its spectral composition and for most electronic devices, it dominates thermal and shot noise from DC to about 100 Hz. Although flicker noise can be detected in virtually all conducting materials with applied power, it seems to be most prominent where electron conduction occurs in granular or semiconductor devices. For most semiconductor devices, flicker noise is due to surface effects resulting in random carrier recombinations at interface traps. Flicker noise exhibits a $1/f^n$ power spectrum, with n typically ranging from 0.9 to 1.35.

5.1.4.4 Total Non-multiplication Noise

Because all the noise sources are considered to be random and uncorrelated, the noise power in a system is additive, and the total rms noise is the square root of the sum of the squares of each of the three noise sources previously described. The total non-multiplication noise output voltage is given by :

$$E_{tno} = [4kTR_sB + (I_{shot}R_s)^2 + e_f^2]^{1/2} \quad \text{volts rms} \quad [5-6]$$

5.1.4.5 Excess Noise

The excess noise factor is the component of total noise corresponding to fluctuations in the process of carrier multiplication in an avalanche photodiode. It is defined as the ratio of multiplication-related noise to that of the non-multiplication noise defined by equation [5-6]. Excess noise measurements are usually conducted at high frequencies where the shot noise is the most dominant non-multiplication term. Therefore, all other noise processes are commonly ignored in excess noise computations. McIntyre has shown³⁵ that the statistical nature of the multiplication process adds an additional component to the noise which can be included with the shot noise of the APD as an excess noise factor. The excess noise factor in the case of pure electron injection is given by:

$$F_e = \frac{M}{k} + (1 - \frac{1}{k})(2 - \frac{1}{M}) \quad [5-7]$$

where M is the multiplication factor, and k is the effective electron to hole ionization ratio of the APD. The root mean square noise current $\langle i_n^2 \rangle$ can be expressed as:

$$\langle i_n^2 \rangle = 2eI_{p0}M^2FB \quad [5-8]$$

where I_{p0} is the primary multiplied photocurrent. In other words, the actual photocurrent is given as:

$$I_{ph} = I_{p0} * M \quad \text{for } I_{ph} \gg I_D \text{ (dark current)} \quad [5-9]$$

A plot of $F(M)$ vs. M from McIntyre's theory is shown in Figure 5-8 for k' ($=1/k=\beta/\alpha$) ranging from 0.001 to 1000. The plots are approximately symmetric on a log-log scale about the axis $F(M)=M$ for k and 1/k. At any given gain, lower excess noise is obtained if

the carrier with the higher ionization coefficient is injected into the multiplication region. For low k' , if the correct carrier is injected, the excess noise can be quite low, with a limiting value of 2 for $k'=0$ at high gain. However, if the wrong carrier is injected, the excess noise becomes very high, with the penalty becoming increasingly more severe as the disparity between ionization coefficients decreases. Thus, it is important to inject the carrier with the higher ionization coefficient into the multiplication region. The lower the k' (or higher the k), the higher the relative difference between α and β , and the lower the excess noise. It is important to note that the McIntyre model is not well suited for describing the noise characteristics of MQW devices since it was intended mainly for conventional APDs. Better models have been developed by Teich et al.^{36,37} and are described in the literature. In addition, Marsland^{38,39} and Hayat⁴⁰ have recently considered the “dead space” between ionization events in their excess noise calculations. They concluded that McIntyre’s calculations overestimate the excess noise factor for a given k . McIntyre curves were used in our excess noise factor plot for comparison purposes in order to clearly illustrate the difference between the noise properties of conventional and MQW APDs. Multiplication noise measurements were conducted on both APDs using an HP8568B spectrum analyzer set at a 200 kHz center frequency with a 10 kHz resolution bandwidth.

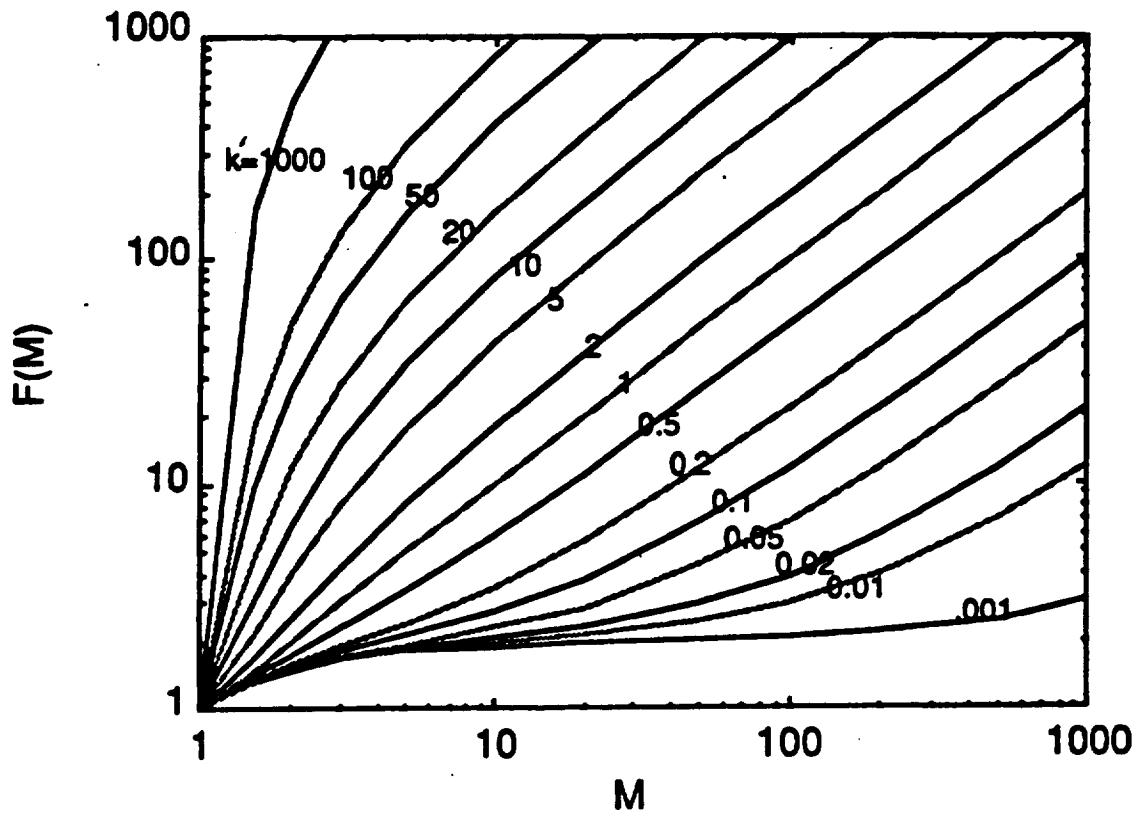


Figure 5-8: Excess noise factor $F(M)$ vs. M for constant k' , from McIntyre's equation.

Excess noise factor measurements were made with a HeNe laser using electron injection into the top p^+ layer. The experimental excess noise factor data is shown in Figure 5-9 where the dashed lines represent McIntyre's calculated theoretical curves. Figure 5-9(a) for the doped MQW APD clearly shows that for low gains ($M < 4$),

the ionization ratio is greatly enhanced ($k=10-50$) as compared to that in bulk GaAs ($k=1.67$). This fact is clear evidence of the validity of our previous results for the gain values per stage which assume single carrier multiplication at low voltages. At higher voltages, however, the value of k is reduced since the holes gain more energy from the applied electric field and are more likely to impact ionize⁴¹. The noise data for the conventional APD displayed in Figure 5-9(b) shows the high noise ($k \sim 1$) characteristics of the conventional APD even at low bias voltages. Excess noise factors at higher gain values were difficult to obtain since the dark current becomes large at high bias. Note that in Figure 5-9(a), the point where the excess noise data break away from the high k McIntyre curves corresponds to the breakdown voltage of the doped well APD. In addition, at high gains the k ratio for the doped well APD approaches the bulk GaAs value of 1.67. This is expected at high fields since the band bending resulting from the MQW structure becomes insignificant compared to that induced by the externally applied field.

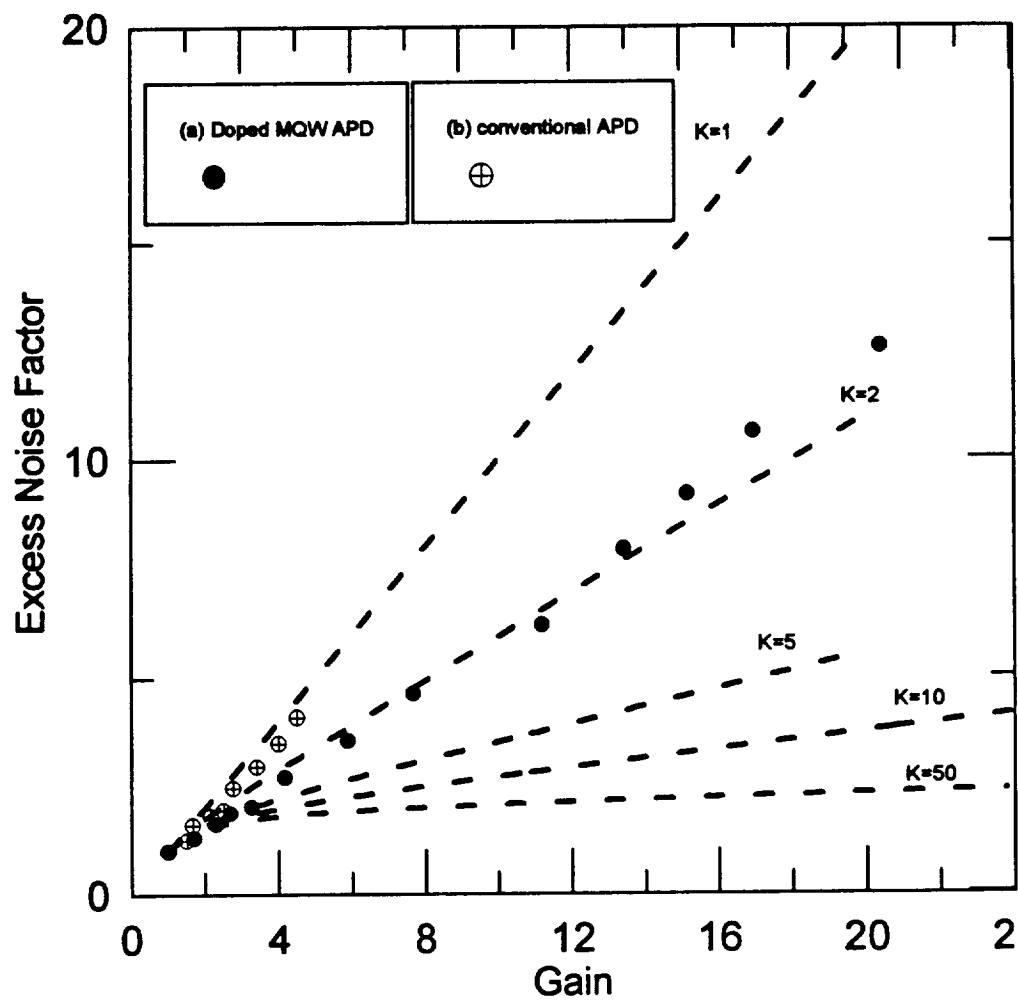


Figure 5-9: Excess noise factors for both (a) the doped MQW APD, and (b) the PIN APD. Dashed lines correspond to McIntyre theoretical curves for $k=1, 2, 5, 10$, and 50 .

-
- [28] K. Brennan, *IEEE J. Quantum Electron.*, QE-22, 1999 (1986)
- [29] F. Capasso, R. E. Nahory, M. A. Pollack, and T. P. Pearsall, *Phys. Rev. Lett.* 39, 723 (1977)
- [30] R. Chin, N. Holonyak, Jr., G. E. Stillman, J. Y. Tang, and K. Hess, *Electron. Lett.* 16, 467 (1980)
- [31] N. Yamamoto, K. Yokoyama, and M. Yamamoto, *Appl. Phys. Lett.* 62, 252 (1993).
- [32] S. M. Sze, *Physics of Semiconductor Devices*, 2nd ed. (Wiley, New York, 1981), Chap. 2, p. 77.
- [33] R. U. Martinelli, T. J. Zamerowski, and P. Longway, *Appl. Phys. Lett.*, vol. 53, no. 11, p. 989, 1988.
- [34] K. R. Linga, G. H. Olsen, V. S. Ban, A. M. Joshi, and W. F. Kosonocky, *Journal of Lightwave Technology*, Vol. 10, no. 8, August 1992.
- [35] R. J. McIntyre, *IEEE Trans. Electron Devices* 13, 164 (1966).
- [36] M. Teich, K. Matsuo, and B. Saleh, *IEEE J. Quantum Electron.*, QE-22, No 8, 1184 (1986)
- [37] N. Hakim, B. Saleh, M. Teich, *IEEE Trans. Electron Devices*, vol. 37, No. 3, 599 (1990)
- [38] J. S. Marsland, *J. Appl. Phys.* 67, 1929 (1990)
- [39] J. S. Marsland, R. C. Woods, and C. A. Brownhill, *IEEE Trans. Electron Devices*, ED-39, 1129 (1992)
- [40] M. M. Hayat, B. E. Saleh, M. C. Teich, *IEEE Trans. Electron Devices*, ED-39, 546 (1992)
- [41] P. Aristin, A. Torabi, A.K. Garrison, H.M. Harris, and C.J. Summers, *Appl. Phys. Letters* 60, 85 (1992).

5.2 Spectral Response Properties

5.2.1 APD Quantum Efficiency

The external quantum efficiency of a photodiode is defined as the number of electron-hole pairs generated at the output photocurrent per incident photon :

$$\eta_{ext} = (I_p / q) / (P_{opt} / h\nu) \quad [5-7]$$

where I_p is the photogenerated current as a result of the absorption of incident optical power P_{opt} at a given wavelength. Another related quantity is the responsivity which is defined as the ratio of the output photocurrent to the incident optical power:

$$\mathfrak{R} = \frac{I_p}{P_{opt}} = \frac{\eta q}{h\nu} = \frac{\eta \lambda (\mu m)}{1.24} \quad A/W \quad [5-8]$$

The quantum efficiency of a photodetector is primarily determined by the absorption coefficient α of the material. Figure 5-8 shows the measured intrinsic absorption coefficient for several materials used in photodetectors.¹ From that figure, we can see how the room temperature absorption for GaAs material drops sharply around 0.9 μm . This long-wavelength cutoff wavelength is determined by the GaAs energy gap which is about 1.43 eV (~ 867 nm) at room temperature. At short wavelengths, the values of α become very large, and the radiation gets absorbed very rapidly near the surface where the recombination time is short. This will cause the photocarriers to recombine before they are collected by the junction region in a photodiode.

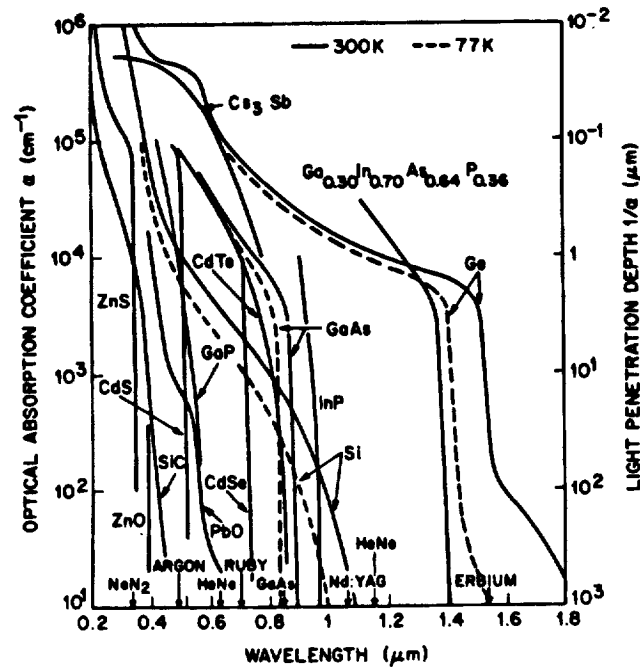


Figure 5-8 : Optical absorption coefficients for different materials at 77 K and 300 K.²

The internal quantum efficiency of a photodiode η_{int} depends on the wavelength of the light as well as the thickness and doping of the absorption material. The absorption follows Beer's law and the internal quantum efficiency can be expressed as $\eta_{int} = 1 - \exp(-\alpha x_{abs})$, where α is the wavelength dependent absorption coefficient as shown in Figure 5-8, and x_{abs} is the thickness of the absorbing material. The "absorption length", l_a , is defined as $1/\alpha$ and gives the amount of material needed so that $1/e$ of the light would be transmitted in the absence of reflections. The external quantum efficiency, η_{ext} , given by equation [5-7], includes the effect of reflection, and can be expressed as $(1 - R) \eta_{int}$, Where R is the wavelength-dependent reflectance of the photodetector.

5.2.2 Spectral Response Data

The long-wavelength behavior of the GaAs material was clearly demonstrated by spectral response measurements conducted on a doped PIN APD using the apparatus described in section 4.3.1. The spectral response output is shown in Figure 5-7. The experimental curve shown in Figure 5-7 was in good agreement with calculated spectral response data for similar devices. In order to calculate the experimental quantum efficiency, we measured the APD current output using a HeNe laser beam incident inside the p^+ ring with a total power of about 2 μW (inside a circular area with a 75 μm diameter). The experimentally calculated quantum efficiency at 632.8 nm was found to be about 19% for a doping level of $1 \times 10^{18} \text{ cm}^{-3}$. Table 5-1 shows the experimental external quantum efficiency as a function of the doping in the p^+ layer.

N_A in cm^{-3}	η_{ext} in %
1.0×10^{18}	18.9
2.0×10^{18}	9.0
3.5×10^{18}	7.7

Table 5-1: Measured quantum efficiencies as a function of doping for a GaAs PIN³

The simulated quantum efficiency curve (assuming zero reflection and no surface recombinations) is shown in Figure 5-8 for a 3 μm PIN photodiode at zero bias. The external source power density was maintained at 0.01 W/cm^2 . Using a 75 μm APD with an active area of $1.6 \times 10^{-4} \text{ cm}^2$, the total incident power on the top p surface calculates to

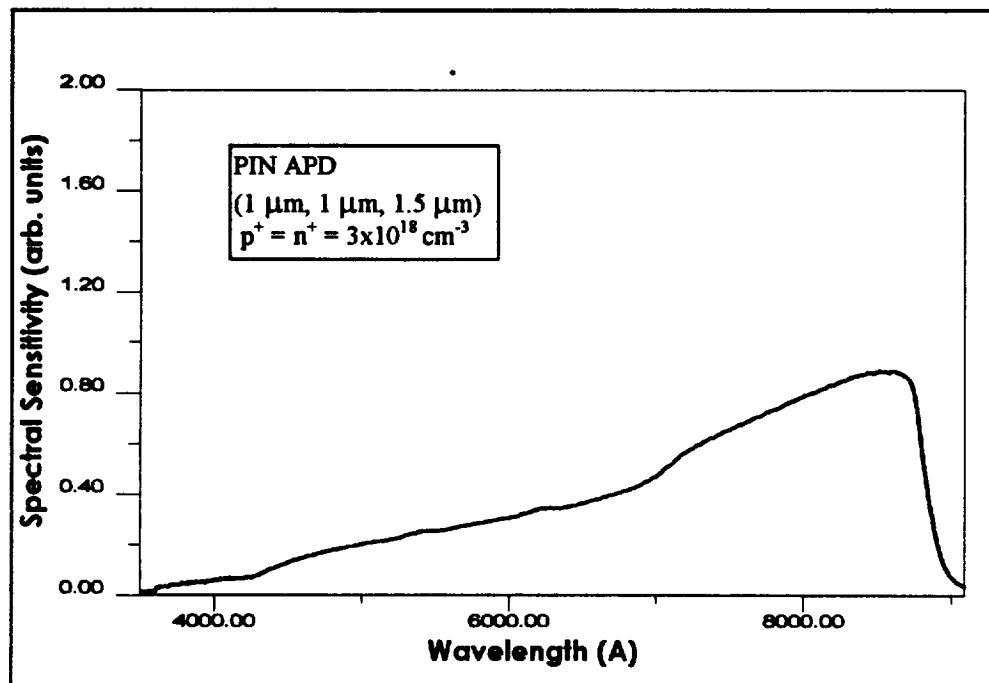


Figure 5-9: Spectral response measurement of an MBE grown PIN APD

be about 1.6 μW . This is comparable to the HeNe laser power incident on the surface which was used in our quantum efficiency experiment. Notice how the theoretical quantum efficiency at 633 is about 27% which is slightly higher than our experimental value. This is largely due to the loss of light due to surface reflection which was unaccounted for in our simulation. Even though reflection is neglected in the model, the maximum external quantum efficiency does not reach 100% due to the presence of various carrier recombination mechanisms (SRH, Auger, etc.) which were previously described.

It is possible to increase the quantum efficiency of the device through the introduction of a heavily doped p^{++} GaAs top layer which will help create a high-field region to enhance the diffusion of photogenerated electron-hole pairs toward the depletion region. Figure 5-9 shows the calculated improvements in quantum efficiency for various doping differences between the 0.1 μm p^{++} layer and the 1 μm p^+ layer. According to the model, it should be possible to increase the quantum efficiency by over a factor of 10 for the high energy part of the spectrum (0.2-0.4 μm). In addition, the response throughout the visible spectral region becomes more uniform as can be seen in Figure 5-9.

Note that the introduction of the thin layer does not make a significant difference to the quantum efficiency when the top absorption region is heavily doped ($3 \times 10^{18} \text{cm}^{-3}$). This is due to increased carrier recombination in the highly doped 1 μm region which tends to reduce the number of carriers diffusing toward the depletion region.

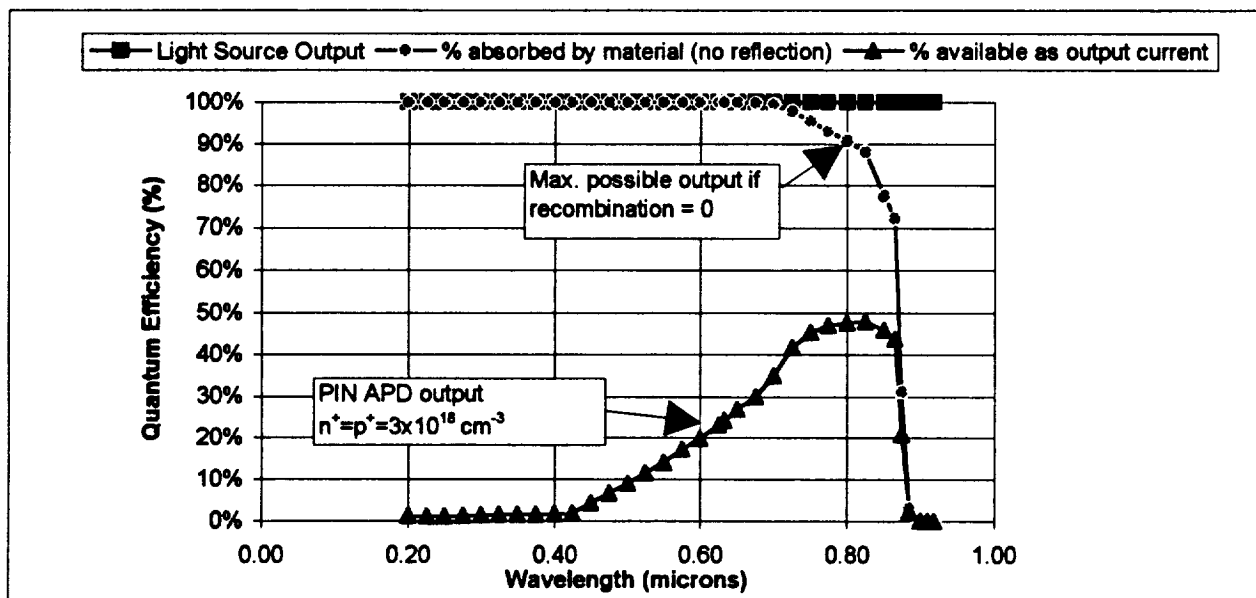


Figure 5-10: Theoretical quantum efficiency plot (zero reflection) for a 3 μm GaAs PIN (1 μm /1 μm /1 μm) APD where $p^+ = n^+ = 3 \times 10^{18} \text{ cm}^{-3}$

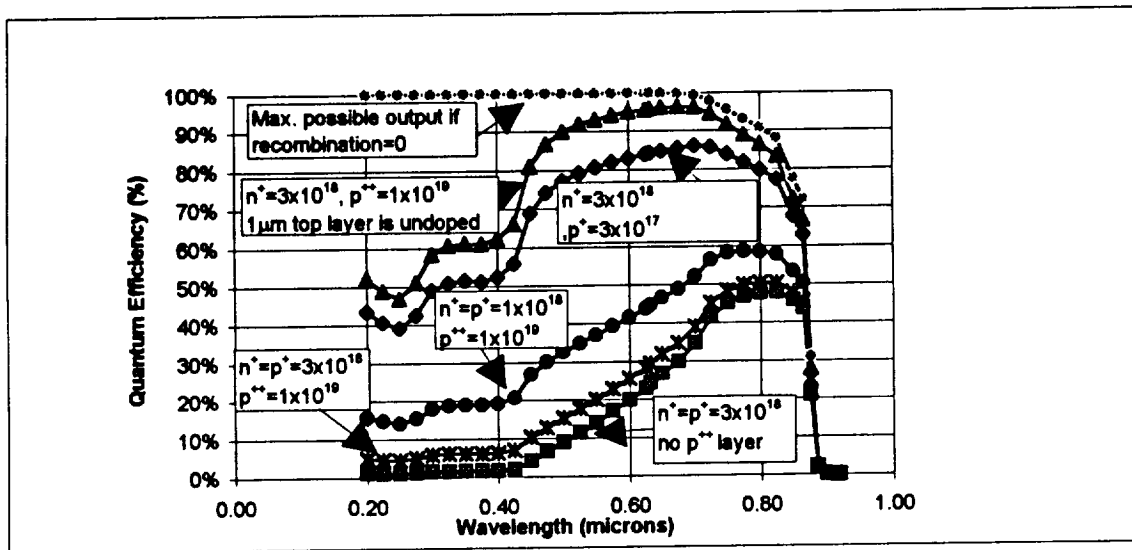


Figure 5-11: Theoretical plots showing possible improvement in quantum efficiency for a PIN APD through the introduction of a thin (0.02 mm) top p^{++} layer (all doping concentrations given are in cm^{-3})

5.3 Temperature Dependence

5.3.1 Impact Ionization vs. Tunneling

In most materials, the mechanisms of junction breakdown can be attributed to both impact ionization and tunneling. One way of determining the dominant process is by examining the temperature dependence of the junction's current-voltage or IV characteristics. Since the energy bandgap of GaAs decreases with increasing temperature, one would expect the breakdown voltage due to tunneling effect to have a negative temperature coefficient. In other word, the breakdown voltage would decrease with increasing temperature as shown in Figure 5-10. This is because a smaller applied field would be needed to reach the same current levels at higher temperatures.

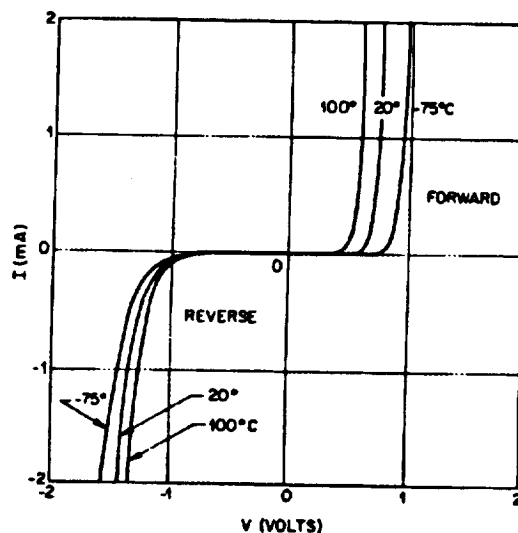


Figure 5-12: IV characteristics of tunneling breakdown⁴

On the other hand, avalanche breakdown has a positive temperature coefficient where the breakdown voltage increases with increasing temperature due to the shorter mean free path of carriers at higher temperatures. Increasing T increases the phonon vibrations of the

lattice, thereby increasing the probability of premature scattering and reducing the ionization coefficients for a given E-field. Other sources of leakage current, such as generation-recombination and diffusion also tend to increase with increasing T. The result of such an effect is shown in Figure 5-11 by the experimental data obtained for a doped MQW APD.

According to Tyagi⁵, the breakdown voltage is related to temperature through the following linear relationship:

$$V_B(T) = V_B(T_0)(1 + \beta(T - T_0)) \quad [5-5]$$

Where $\beta > 0$ in junctions where impact ionization dominate. Such linear dependency was shown experimentally to be valid by Forrest et al.⁶ in the case of p^+n junctions. However, our experimental measurements has shown that for doped MQW junctions, the data can be best fit using a third degree polynomial as shown in Figure 5-12.

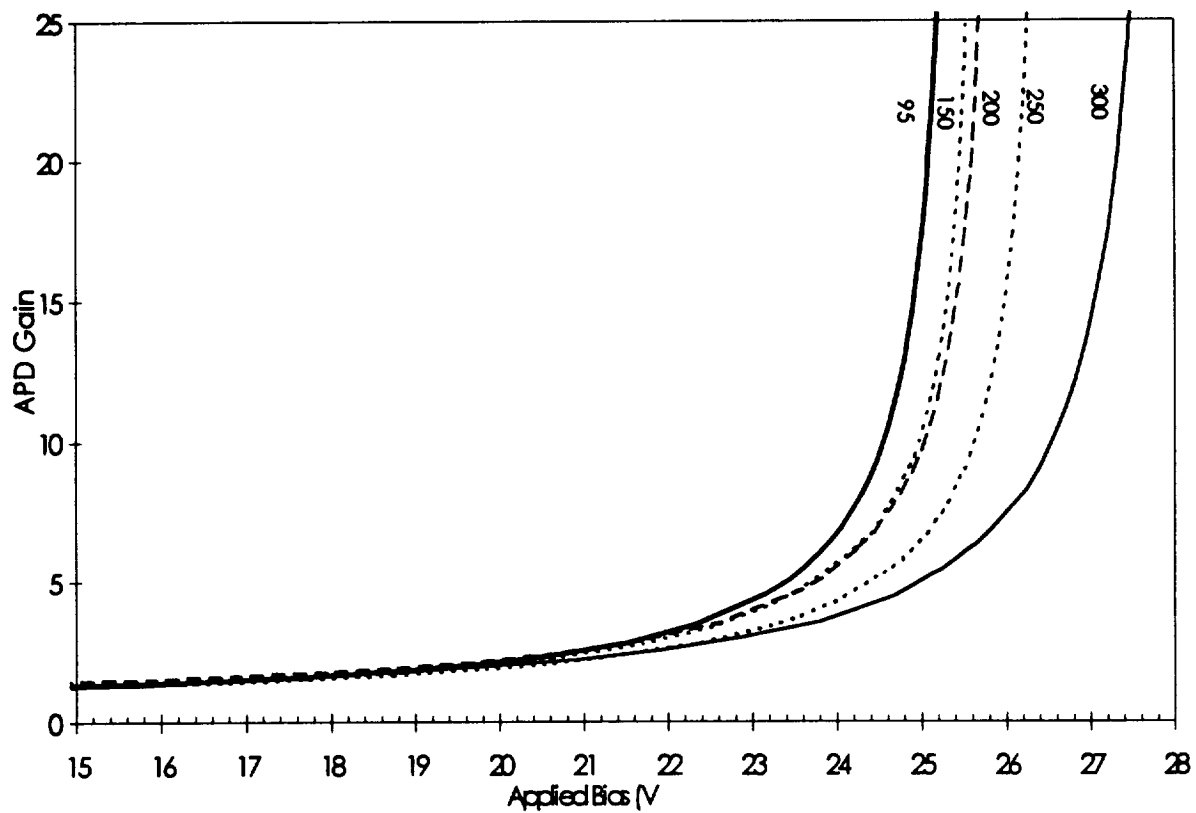


Figure 5-13: Measured gain as a function of temperature for a doped MQW APD

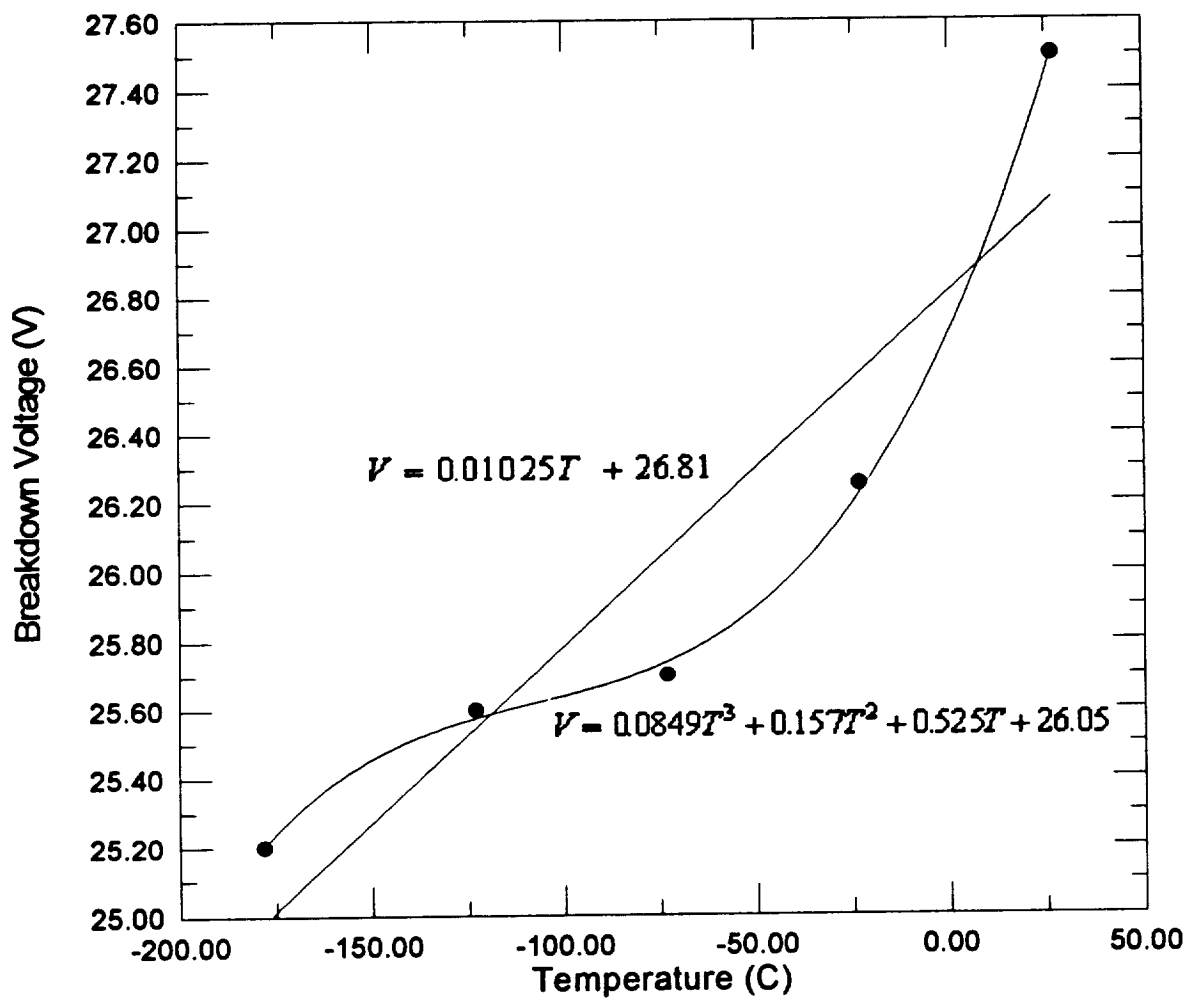


Figure 5-14: Experimental data and fits for a doped-well MQW APD

5.3.2 Junction Capacitance and Temperature

As was shown in equation [2-57], the pn junction capacitance is given by:

$$C_J = \frac{K_s \epsilon_0 A}{\left[\frac{2K_s \epsilon_0 (V_{bi} - V_A) (N_A + N_D)}{q N_A N_D} \right]^{1/2}} \quad [5-6]$$

which shows that C_J is proportional to $(V_{bi} - V_A)^{-1/2}$ where $V_{bi} = (kT/q) \ln(N_A N_D / n_i^2)$ and $n_i^2 = N_C N_V \exp(-E_g/kT)$. As was stated in equations [2-14] and [2-15], the effective density of states, N_C and N_V , are proportional to $T^{3/2}$. Therefore, n_i decreases with temperature as shown in Figure 5-13. The result is an overall positive dependency between V_{bi} and temperature. Therefore, V_{bi} increases with temperature which causes the capacitance to decrease with increasing temperature as shown in the experimental CV data in Figure 5-14. As the reverse bias is increased, V_A becomes the dominant term in equation [5-6], and the variation of capacitance with temperature becomes less significant. This explains the convergence toward a limiting capacitance value at high applied voltages. On the other hand, when the temperature is lowered, V_{bi} becomes more dominant, and the capacitance decreases at a slower rate with the applied bias (see Figure 5-14).

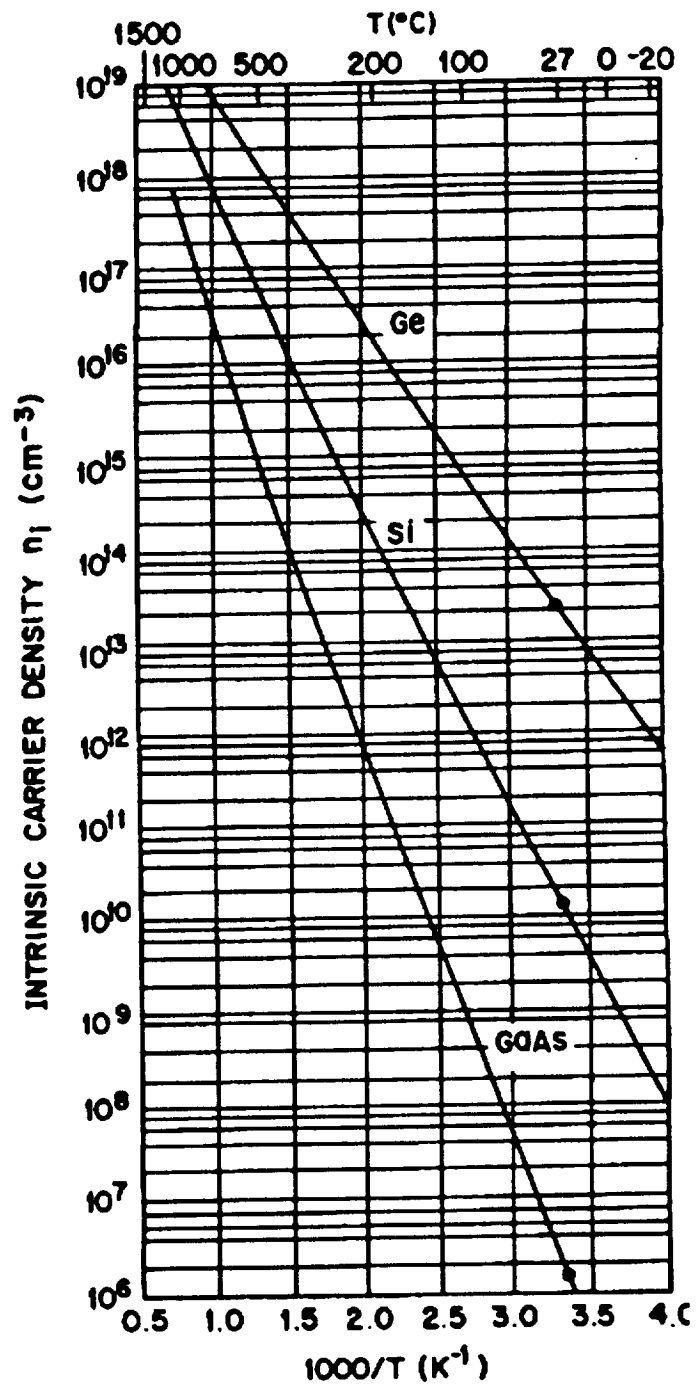


Figure 5-15: Intrinsic carrier densities of Ge, Si, and GaAs as a function of temperature

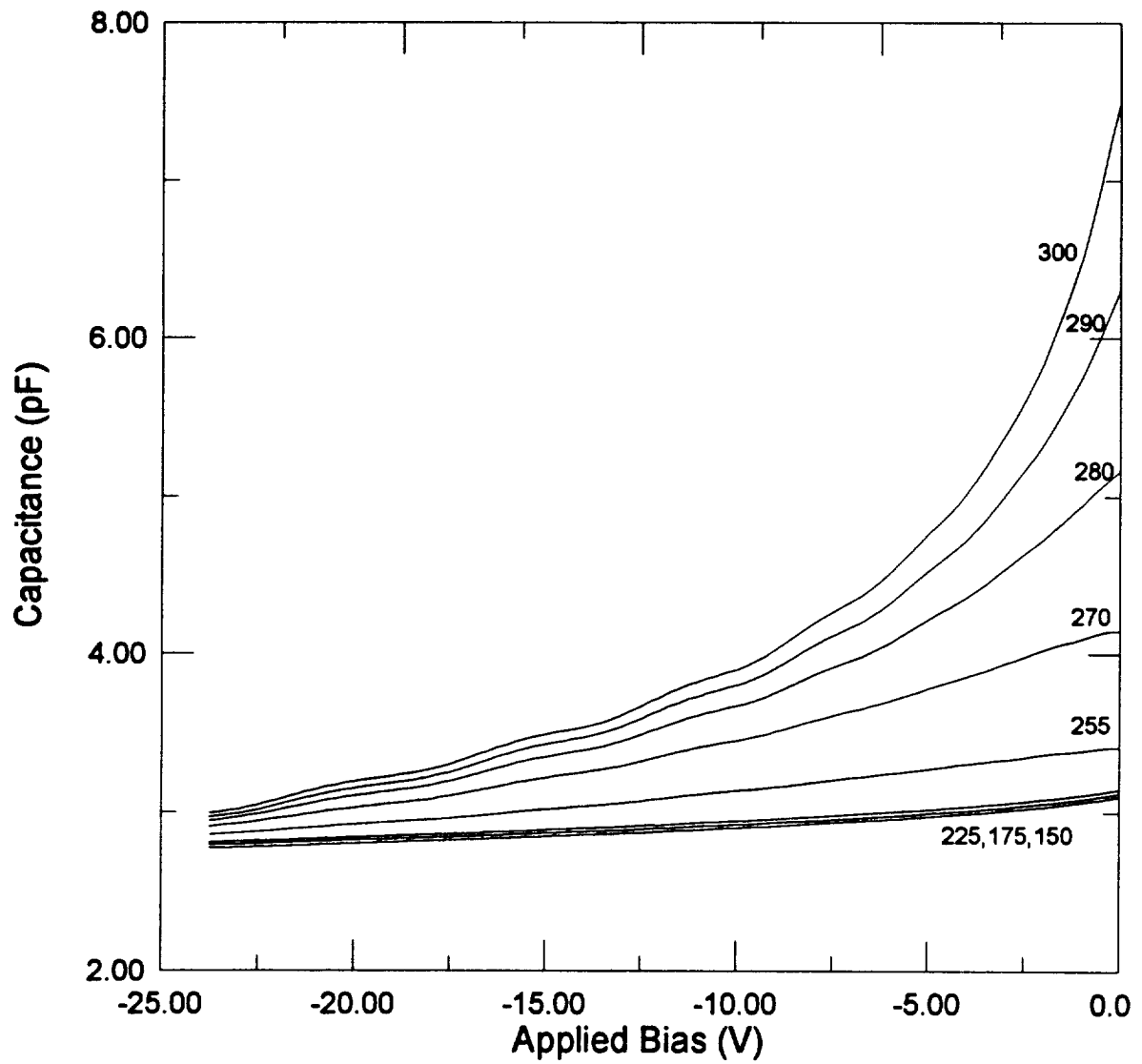


Figure 5-16: Experimental CV as a function of temperature for a doped-well MQW APD

-
- [1] D.C. Raynolds, G. Leies, L. Antes, and R.E. Marburger, "Photovoltaic Effect in Cadmium Sulfide," *Phys. Rev.*, **96**, 533 (1954)
 - [2] S.M. Sze, "Physics of Semiconductor Devices", Wiley, 1981.
 - [3] P. Aristin, "Fabrication et Caracterization de Photodiodes a Avalanche a Puits Quantiques Multiples", Ph.D. thesis, January 1992.
 - [4] M.J.O. Strutt, "Semiconductor Devices", Vol. 1, *Semiconductor and Semiconductor Diodes*, Academic, New York, 1966, Chap. 2.
 - [5] M.S. Tyagi, "Solid State Electronics", **11**, 99 (1968)
 - [6] S.R. Forrest, and O.K. Kim, "Solid State Electronics", **26**, 10, pp. 951-968 (1983)

<u>5.2 SPECTRAL RESPONSE PROPERTIES</u>	86
<u>5.2.1 APD QUANTUM EFFICIENCY</u>	86
<u>5.2.2 SPECTRAL RESPONSE DATA</u>	88
<u>5.3 TIME RESPONSE CHARACTERISTICS</u>	94
<u>5.3.1 BANDWIDTH LIMITATIONS OF PHOTODETECTORS</u>	95
<u>5.3.1 OVERALL PHOTODETECTOR BANDWIDTH</u>	97
<u>5.3.2 EXPERIMENTAL RESULTS</u>	98
<u>5.4 TEMPERATURE DEPENDENCE</u>	105
<u>5.4.1 IMPACT IONIZATION VS. TUNNELING</u>	105
<u>5.4.2 JUNCTION CAPACITANCE AND TEMPERATURE</u>	109

5.2 Spectral Response Properties

5.2.1 APD Quantum Efficiency

The external quantum efficiency of a photodiode is defined as the number of electron-hole pairs generated at the output photocurrent per incident photon :

$$\eta_{ext} = (I_p / q) / (P_{opt} / h\nu) \quad [5-10]$$

where I_p is the photogenerated current resulting from the absorption of incident optical power P_{opt} at a given wavelength. Another related quantity is the responsivity which is defined as the ratio of the output photocurrent to the incident optical power:

$$\mathfrak{R} = \frac{I_p}{P_{opt}} = \frac{\eta q}{h\nu} = \frac{\eta \lambda (\mu m)}{1.24} \quad A/W \quad [5-11]$$

The quantum efficiency of a photodetector is primarily determined by the absorption coefficient α of the material. Figure 5-11 shows the measured intrinsic absorption coefficient for several materials used in photodetectors.⁴² From this figure, we can see that the room temperature absorption for GaAs material drops sharply around 0.9 μm . This long-wavelength cutoff wavelength is determined by the GaAs energy gap which is about 1.43 eV (~ 867 nm) at room temperature. At short wavelengths, the values of α become very large, and the radiation gets absorbed very rapidly near the surface where the recombination time is short. This will cause the photocarriers to recombine before they are collected by the junction region in a photodiode.

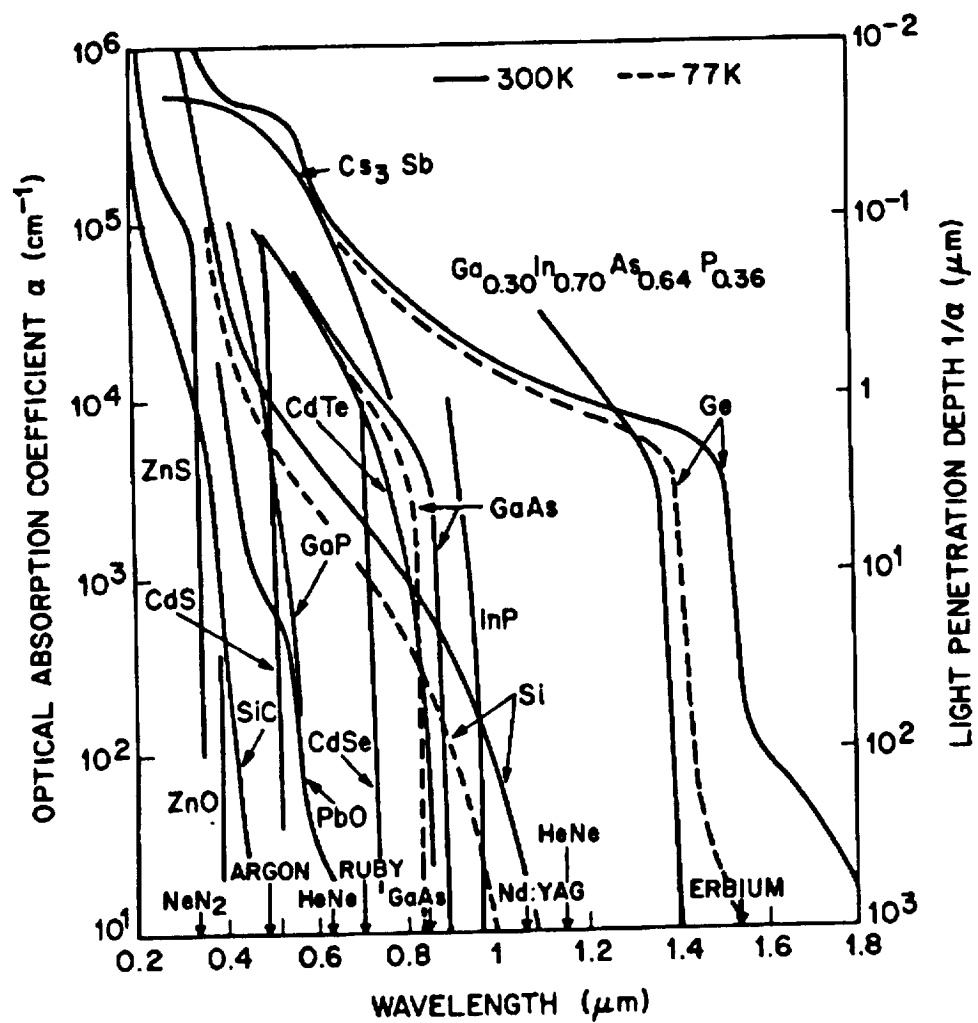


Figure 5-10: Optical absorption coefficients for different materials at 77 K and 300 K.⁴³

The internal quantum efficiency of a photodiode η_{int} depends on the wavelength of the light as well as the thickness and doping of the absorption material. The absorption follows Beer's law and the internal quantum efficiency can be expressed as $\eta_{int} = 1 - \exp(-\alpha x_{abs})$, where α is the wavelength dependent absorption coefficient as shown in Figure 5-10, and x_{abs} is the thickness of the absorbing material. The "absorption length", L_a , is defined as $1/\alpha$ and gives the amount of material needed so that 1/e of the light would be transmitted in the absence of reflections. The external quantum efficiency, η_{ext} , given by equation [5-10], includes the effect of reflection as well as the various carrier recombination mechanisms.

5.2.2 Spectral Response Data

The long-wavelength behavior of the GaAs material was clearly demonstrated by spectral response measurements conducted on a doped PIN APD using the apparatus described in section 4.3.3. The spectral response output is shown in Figure 5-11. The experimental curve shown in Figure 5-11 was in good agreement with calculated spectral response data for similar devices. In order to calculate the experimental quantum efficiency, we measured the APD current output using a HeNe laser beam incident inside the p^+ ring with a total power of about 2 μ W (inside a circular area with a 75 μ m diameter). The experimentally calculated quantum efficiency at 632.8 nm was found to be about 19% for a doping level of $1 \times 10^{18} \text{ cm}^{-3}$. Table 5-1 shows the experimental external quantum efficiency as a function of the doping in the p^+ layer.

Table 5-1: Measured quantum efficiencies (at 633 nm) as a function of doping for a GaAs PIN⁴⁴

N_A in cm^{-3}	η_{ext} in %
1.0×10^{18}	18.9
2.0×10^{18}	9.0
3.5×10^{18}	7.7

The simulated quantum efficiency curve (assuming zero reflection and no surface recombinations) is shown in Figure 5-12 for a 3 μm PIN photodiode at zero bias. The external source power density was maintained at 0.01 W/cm^2 . Using a 75 μm APD with an active area of $1.6 \times 10^{-4} \text{ cm}^2$, the total incident power on the top p surface is calculated to be about $1.6 \mu\text{W}$. This is comparable to the HeNe laser power incident on the surface during the quantum efficiency experiment. Notice how the theoretical quantum efficiency at 633 nm is about 27% which is considerably higher than our experimental value. This is largely due to the loss of light due to surface reflection and to surface recombination mechanisms which were unaccounted for in our simulation. Even though reflection is neglected in the model, the maximum external quantum efficiency does not reach 100% due to the presence of various carrier recombination mechanisms (SRH, Auger, etc.) which were previously described.

It is possible to increase the quantum efficiency of the device through the introduction of a heavily doped p^{++} GaAs top layer which will help create a high-field region to enhance the diffusion of photogenerated electrons toward the depletion region.

Figure 5-13 shows the calculated improvements in quantum efficiency for various doping differences between the $0.1\ \mu\text{m}\ p^{++}$ layer and the $1\ \mu\text{m}\ p^{+}$ layer. According to the model, it should be possible to increase the quantum efficiency by over a factor of 10 for the high energy part of the spectrum ($0.2\text{-}0.4\ \mu\text{m}$). In addition, the response throughout the visible spectral region becomes more uniform as can be seen in Figure 5-13.

Note that the introduction of the thin layer does not make a significant difference to the quantum efficiency when the top absorption region is heavily doped ($3\times 10^{18}\text{cm}^{-3}$). This is due to increased carrier recombination in the highly doped $1\ \mu\text{m}$ region which tends to reduce the number of carriers diffusing toward the depletion region.

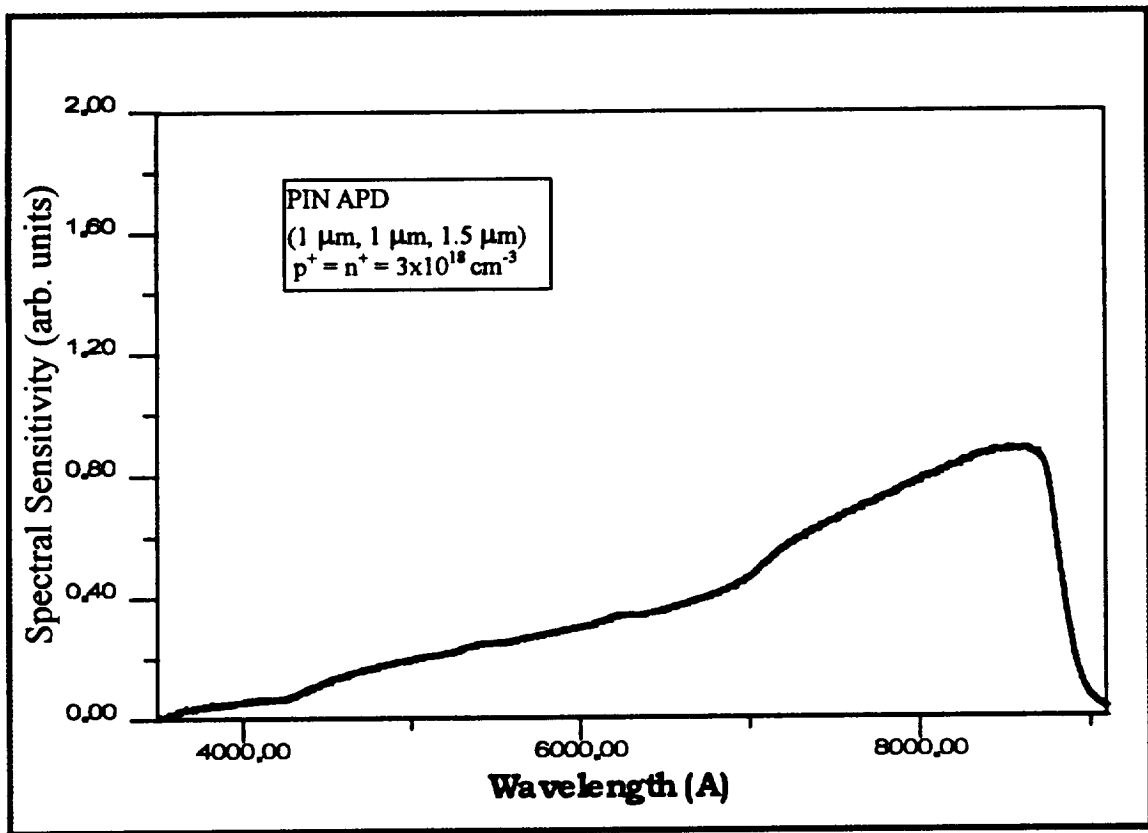


Figure 5-11: Spectral response measurement of an MBE grown PIN APD.

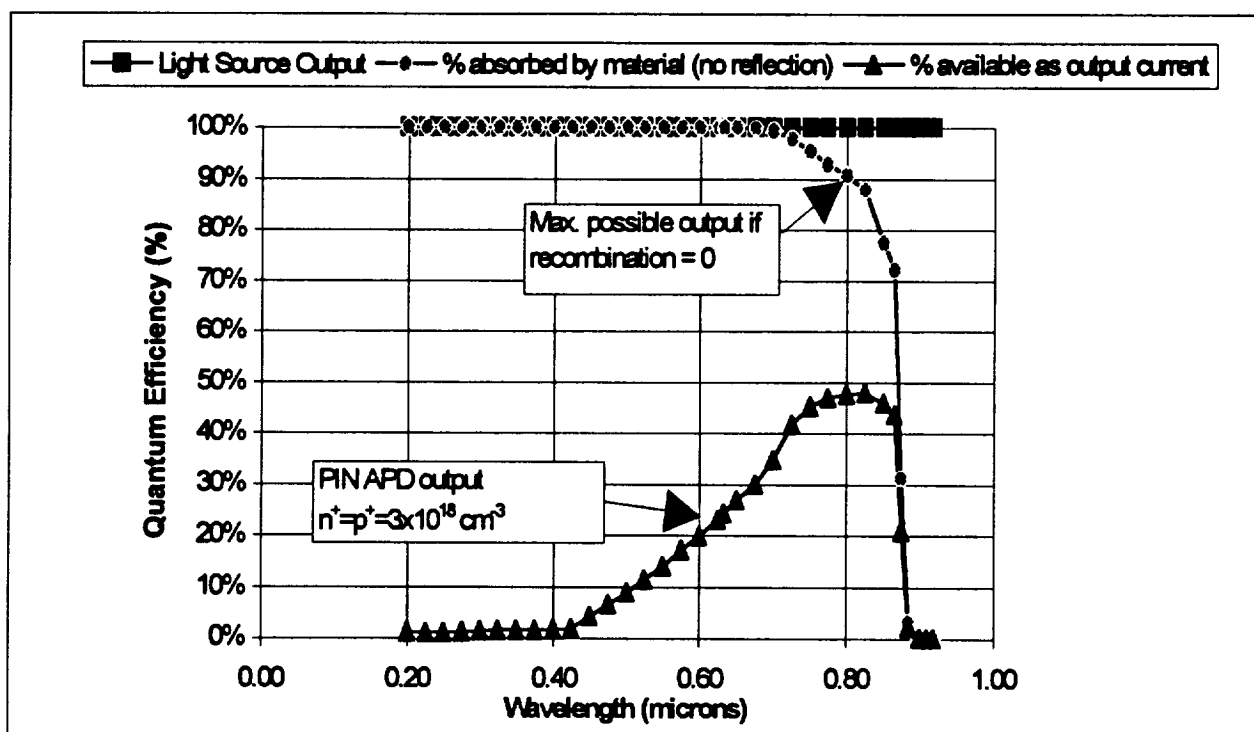


Figure 5-12: Theoretical quantum efficiency plot (zero reflection) for a 3 μm GaAs PIN (1 $\mu\text{m}/1 \mu\text{m}/1 \mu\text{m}$) APD where $p^+ = n^+ = 3 \times 10^{18} \text{ cm}^{-3}$.

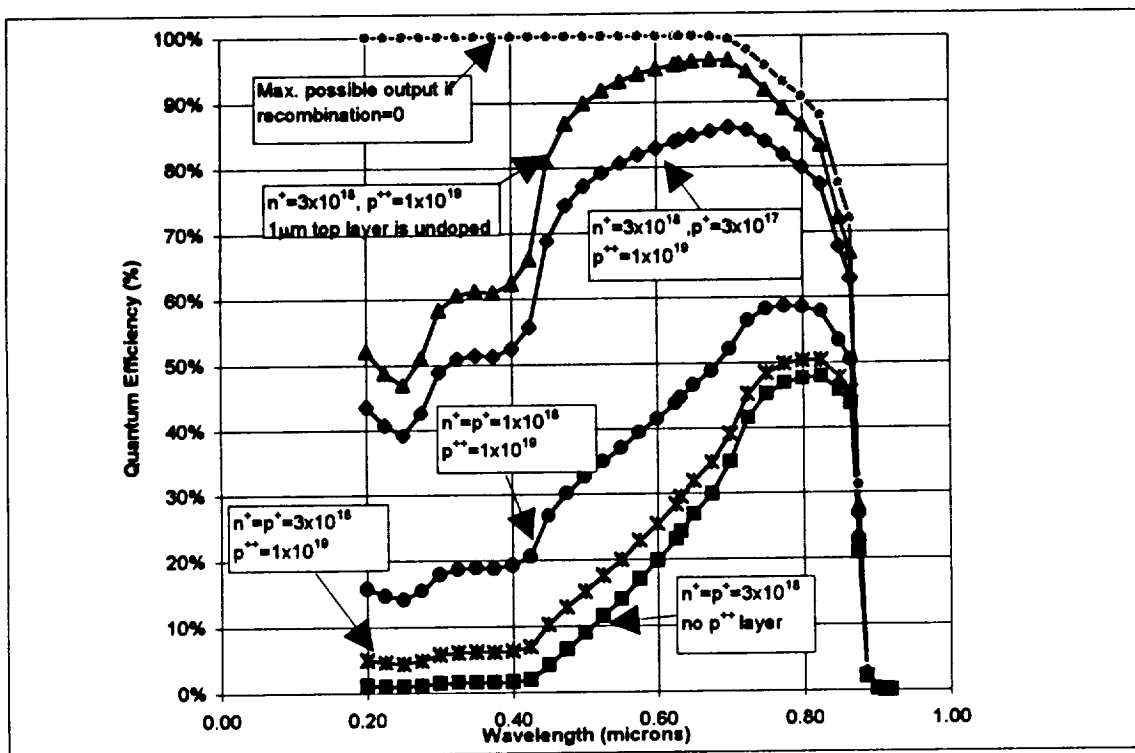


Figure 5-13: Theoretical plots showing possible improvement in quantum efficiency for a PIN APD through variations in the doping concentrations and the introduction of a thin (0.02 μm) top p^{++} layer (all doping concentrations given are in cm^{-3})

5.3 Time Response Characteristics

The requirements of high bit rate (> 4000 Mb/s) lightwave communication and image processing systems have necessitated the development of fast photodiodes that have higher sensitivity than the PIN detector. Improvement in sensitivity while maintaining wide bandwidths can only be provided using an amplification mechanism within the photodetector itself as is the case in avalanche photodiodes. For optimum operation, an APD must meet the following criteria⁴⁵: (1) the electric field in the multiplication region must be high enough to produce sufficient gain; (2) the electric field in the absorbing region must be low enough so that the tunneling component of the dark current is negligible; (3) the depletion region must extend far enough into the absorbing region so that diffusion effects are negligibly small. These requirements impose rather severe constraints on the doping concentrations and thickness of the epitaxial layers of the device. Transient response measurements can provide valuable information on the speed performance and the various factors that affect the bandwidth of APDs. Since carrier diffusion plays a major role in determining the time response of a photodetector, one would expect the speed to depend greatly on the depletion characteristics of the APD. The more depleted a structure is, the shorter the distance the carriers will have to diffuse, and the faster the response time will be. This will be shortly demonstrated with experimental time response data. But first, in order to better understand the results that were obtained, a brief discussion the various physical effects that limit the frequency response of a photodiode will be presented.

5.3.1 Bandwidth Limitations of Photodetectors

Considerable work has been done in the literature on the study of photodetector bandwidth limitations [1-4]. To summarize the results, the bandwidth of a Separate Absorption and Multiplication Regions (SAM) APD is determined by five physical effects:

1. *Transit Time*: This is the time it takes the generated carriers to travel through the depleted region under the effect of the electric field. There are two types of transit times in an APD. The primary carrier transit time corresponding to the photogenerated carriers, and the secondary carrier transit time required for the multiplied carriers of opposite type to retrace the steps of the primary ones. Transit times for electrons and holes (τ_e and τ_h) are usually calculated using the ratio of the distance traveled and the "saturation" velocity of the appropriate carrier.

2. *Carrier diffusion time*: In the undepleted regions of the device, carrier transport must take place by diffusion rather than drift. Because of the absence of electric field in the absorption layer of a PIN APD, the photogenerated carriers must diffuse in order to reach the avalanche region. This results in the slowing of the device's response. An oscilloscope trace of the transient output of such a device would show both a "fast" and a "slow" component. The fast component is due to carrier drift, and the slow one, referred to as the "diffusion tail", is due to diffusion from the undepleted regions of the device.

3. *RC time constant*: There is a fundamental limit on bandwidth due to the capacitive transient charging effects which arise from the depletion region capacitance of the device and the combined resistance R of the load and the device.

4. *Hole trapping*: In heterojunction APDs, there is a possibility of carrier delay caused by traps present at the heterojunction interface. This effect is related to the abruptness of the heterojunction, the barrier height, the temperature, and the effective mass of the carrier. Because the effective mass of holes is larger by an order of magnitude than that of electrons, trapping is more likely to occur for holes than electrons. This phenomena is known as "hole trapping" and it can be minimized through the use of graded composition layers instead of abrupt heterojunctions.

5. *Avalanche buildup time*: For single carrier ionization, one only needs to consider the transit time through the multiplication layer. For dual carrier ionization, however, there is a feedback process that introduces a time delay through the multiplication region. This is called the avalanche buildup time. In an APD, there is a buildup time τ_{aval} associated with the avalanche gain process which tends to limit the time response of the photodetector. The primary avalanche build-up time for electron initiated multiplication is :

$$\tau_{aval\ n} = \frac{K_{disp}}{v_n + v_p} \int_0^w \exp\left[-\int_0^x (\alpha - \beta) dx'\right] dx \quad [5-13]$$

where K_{disp} is a correction factor; v_n and v_p are the electron and hole velocities. The physical origin of K_{disp} is the electron/hole displacement current which arises from the space-charge induced E-field resulting from the motion of carriers.⁴⁶ The closer the value

of α is to that of β , the more secondary carriers are generated, and the higher the avalanche build-up time as can be seen from equation [5-13].

5.3.2 Overall Photodetector Bandwidth

In the case of a PIN photodetector where absorption takes place in the junction, the basic limitations to the response time are due to the RC and the transit times of the primary carriers. The overall PIN time constant is usually approximated by the square root of the sum of squares of the RC and transit time constants:

$$\tau_{pin}^2 = \text{Max}(\tau_h, \tau_e)^2 + \tau_{RC}^2 \quad [5-14]$$

As was previously mentioned, in an APD, there are two different transit times arising from the primary carriers traveling to, and secondary carriers traveling from, the multiplication region. In addition, there is the avalanche buildup time (proportional to gain) which is proportional to the multiplication process. The actual APD frequency response is a complicated function of all of these processes. Hollenhorst⁴⁷ and Roy⁴⁸ have developed complicated transfer functions and matrix expressions to estimate the time constants for arbitrary structures. For approximation purposes, the RC time constant is usually treated as being non-correlated with the rest of the time constants. In addition, the primary hole transit, hole trapping, avalanche buildup and secondary electron transit events can be assumed to occur in series, one following the other. In this case, the sum of squares can be used to approximate the total time constant as well.

In the following section, we will present some of the experimental data and attempt to provide the proper interpretations as they relate to the processes described above.

5.3.3 Experimental Results

Figure 5-14 shows the pulse response for an unbiased doped MQW device with a 2.5 μm MQW region. The APD was mounted on a 50 GHz Tektronix sampling scope and was excited with an 810 nm 50 ps laser pulse. As can be seen from the figure, the unbiased APD output pulse has a rise time of about 317 ps, a fall time of 2.5 ns and a full width at half max (FWHM) of about 1.4 ns. The oscilloscope trace is a convolution of the 50 ps gaussian laser pulse with the output response of the APD. The fast rise time component typically follows the relaxation oscillation of the laser pulse. The falling edge of the pulse shows a "fast" and a "slow" component. The slow component at the trailing edge is usually attributed to either charge trapping at interface states or diffusion of carriers in the undepleted regions of the structure.⁴⁹ Diffusion will limit the speed of the device as long as there are undepleted regions in the structure and a separate absorption layer is being used. At high bias, trapping is no longer an issue, and the device response is limited by the transit time and the RC time constant. In the following, it will be demonstrated that such a slow response is due largely to diffusion effects in the partially depleted APD structure.

Figure 5-15 shows the response of the above APD under bias (low gain). The fall time and the FWHM have now dropped to 819 and 952 ps, respectively, corresponding to about a 32% increase in the speed of the device. If the bias is increased further, as shown in Figure 5-16, those values drop to 570 and 593 ps, respectively, with a speed increase of about 58%. The large dependence of the pulse's width and tail on the applied bias is a clear indication of a diffusion-limited time response.

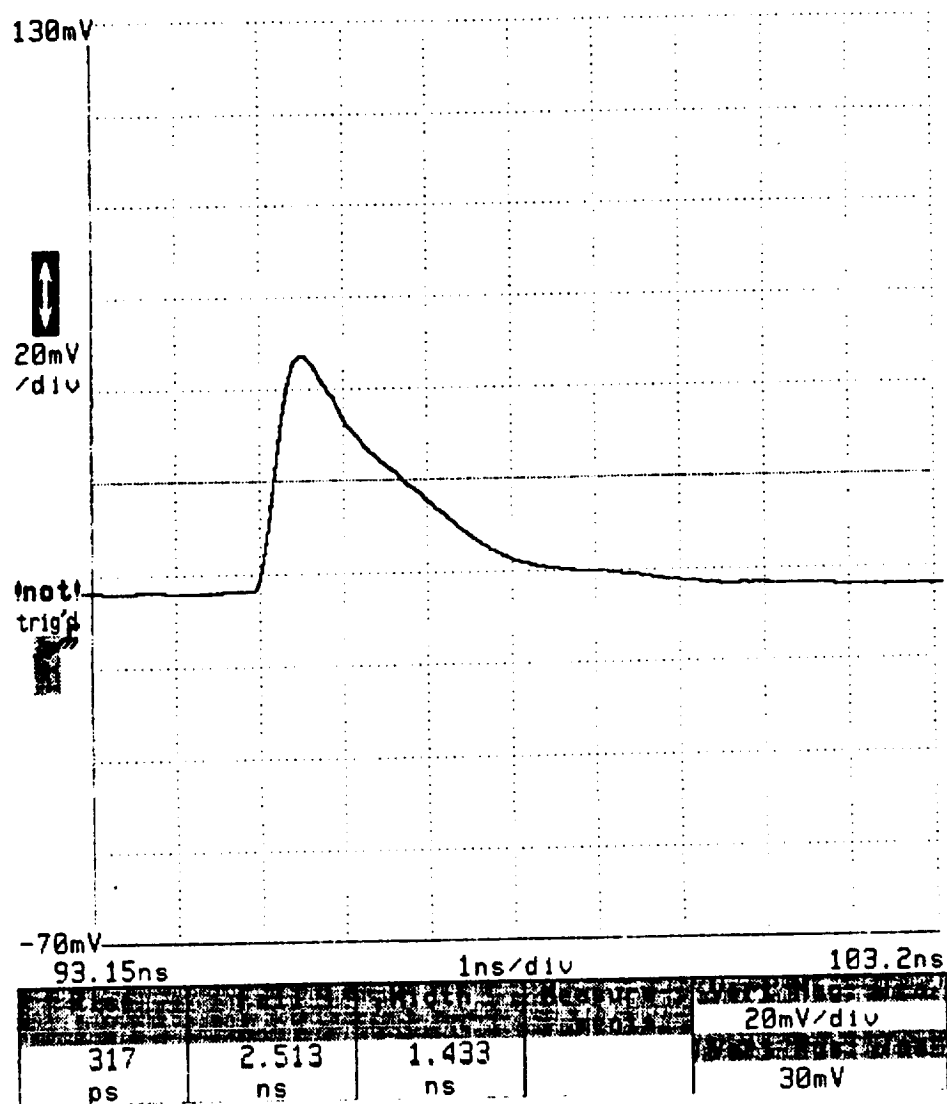


Figure 5-14: Oscilloscope trace of the pulse response of a doped 2.5 μm MQW APD under no bias

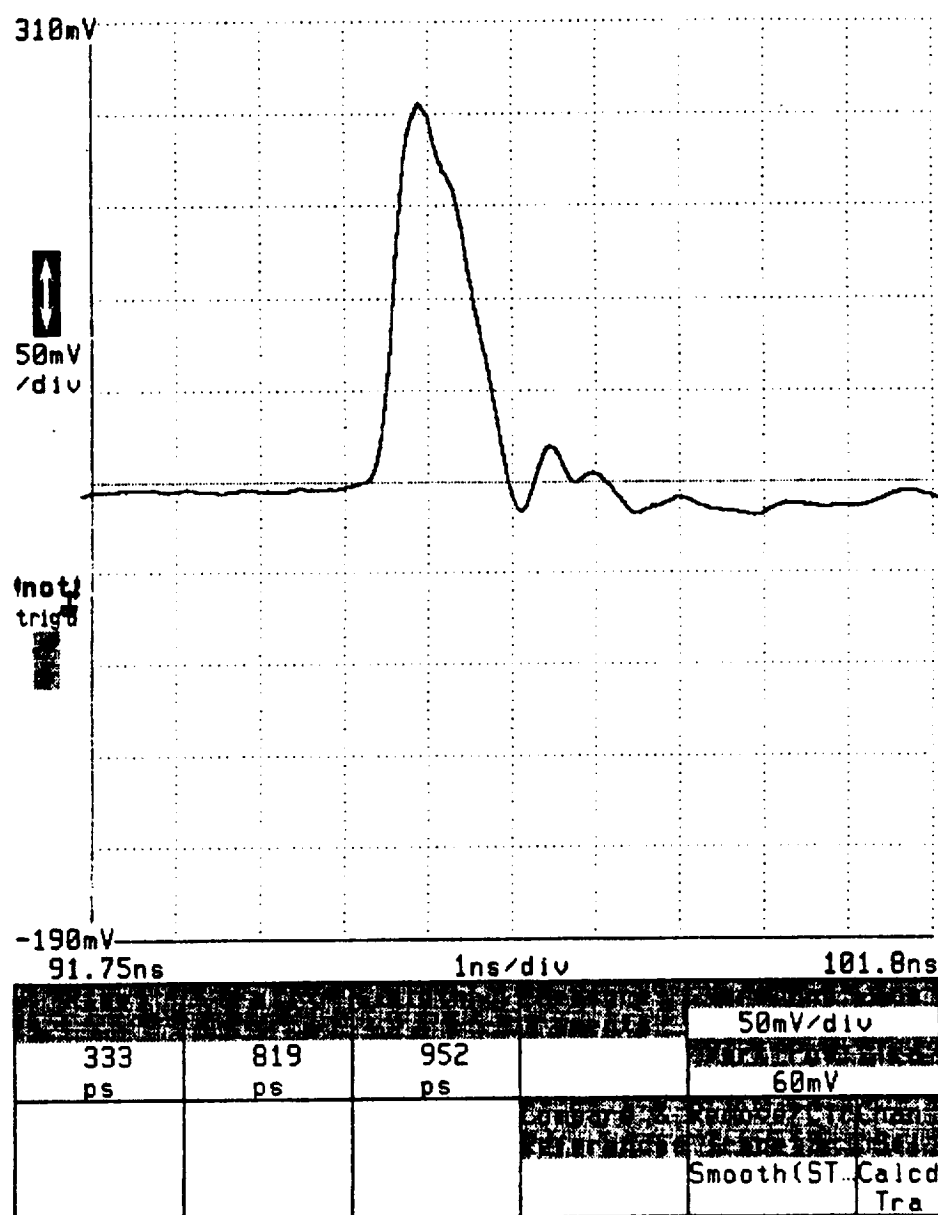


Figure 5-15: Oscilloscope trace of the pulse response of a doped 2.5 μm MQW APD under low bias

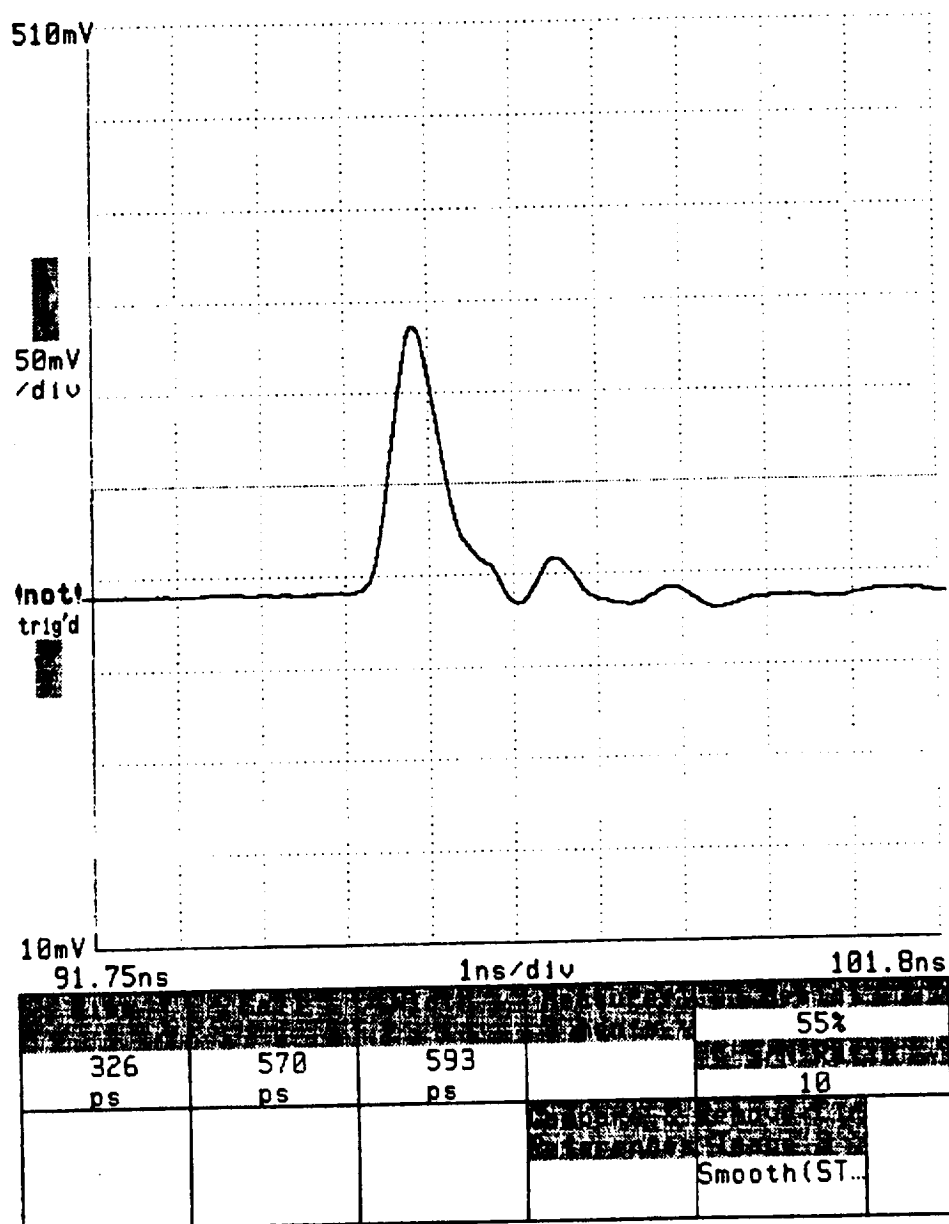


Figure 5-16: Oscilloscope trace of the pulse response of a doped 2.5 μm MQW APD near breakdown.

The diffusion-limited effect can be verified further by examining the depletion width characteristics of the structure obtained from CV measurements. This is shown in Figure 5-17 where the zero bias depletion width of the MQW and PIN structures are

about 0.1 μm and 1.4 μm respectively. These values can be used to estimate the drift time constants from $\tau_{\text{drift}} = W_{\text{depleted}} / v_{\text{sat}}$ where W_{depleted} is the width of the depleted region, and v_{sat} is the saturation velocity taken to be in the order of 10^7 cm/s. The drift time constants for the MQW and PIN structures were estimated to be 1 ps and 14 ps, respectively. Similarly, the ratio of the diffusion time constants between the MQW and the PIN structures is directly related to the ratio of the undepleted widths ($\tau_{\text{diff(MQW)}} / \tau_{\text{diff(PIN)}} = W_{\text{undep(MQW)}} / W_{\text{undep(PIN)}} = 2.2$). Using that ratio and the sums of squares approximation, the diffusion time constants for the MQW and PIN structures were calculated to be 1.5 ns and 0.7 ns, respectively. This result shows that the MQW structure is largely diffusion-limited due to the presence of a large undepleted region. As will be shown in Section 5.5, this behavior is largely due to a mismatch in the doping balance between the n and p doping layers in the MQW structure. On the other hand, the PIN APD shows a much faster time response (Figure 5-18) due to the fact that the structure is largely depleted even at zero applied bias (Figure 5-17). Therefore, the time response limitations for this structure are mainly due to 1) diffusion time in the top p^+ and bottom n^+ layers, and 2) transit time in the intrinsic field region of the structure. Diffusion time in the cap layers can be optimized by varying the thicknesses as well as the doping concentrations. The transit time can be shortened by increasing the field (applied bias) across the junction. This, however, begins to create an additional delay near breakdown due to the increase in the avalanche buildup time.

The "ringing effect" seen in the oscilloscope trace following the output pulse was due to the impedance mismatch between the APD circuit and that of the oscilloscope sampling head. With applied bias, the impedance of the APD changes due to the increased

conductivity of the structure. This increased the impedance mismatch in the circuit resulting in reflections of the output pulses as illustrated in Figures 5-15 and 5-16. Note that the relative magnitude of the pulses in the case of the MQW APD is not representative of the gain of the device since a variable resistor was used in an attempt to match circuit resistance and thus limited the voltage applied at the oscilloscope.

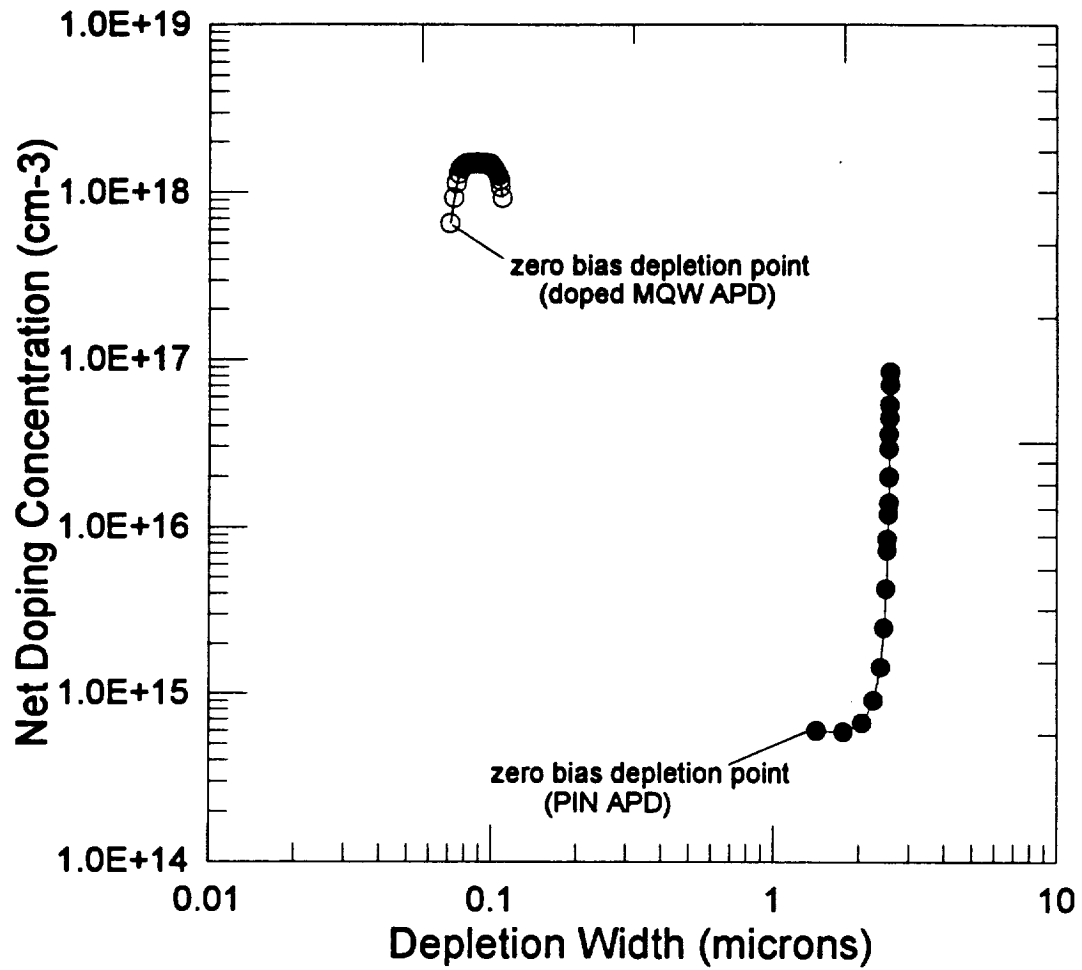


Figure 5-17: Depletion width plot showing the increase in the depletion region with applied bias for a largely undepleted doped (2.5 μm) MQW APD.

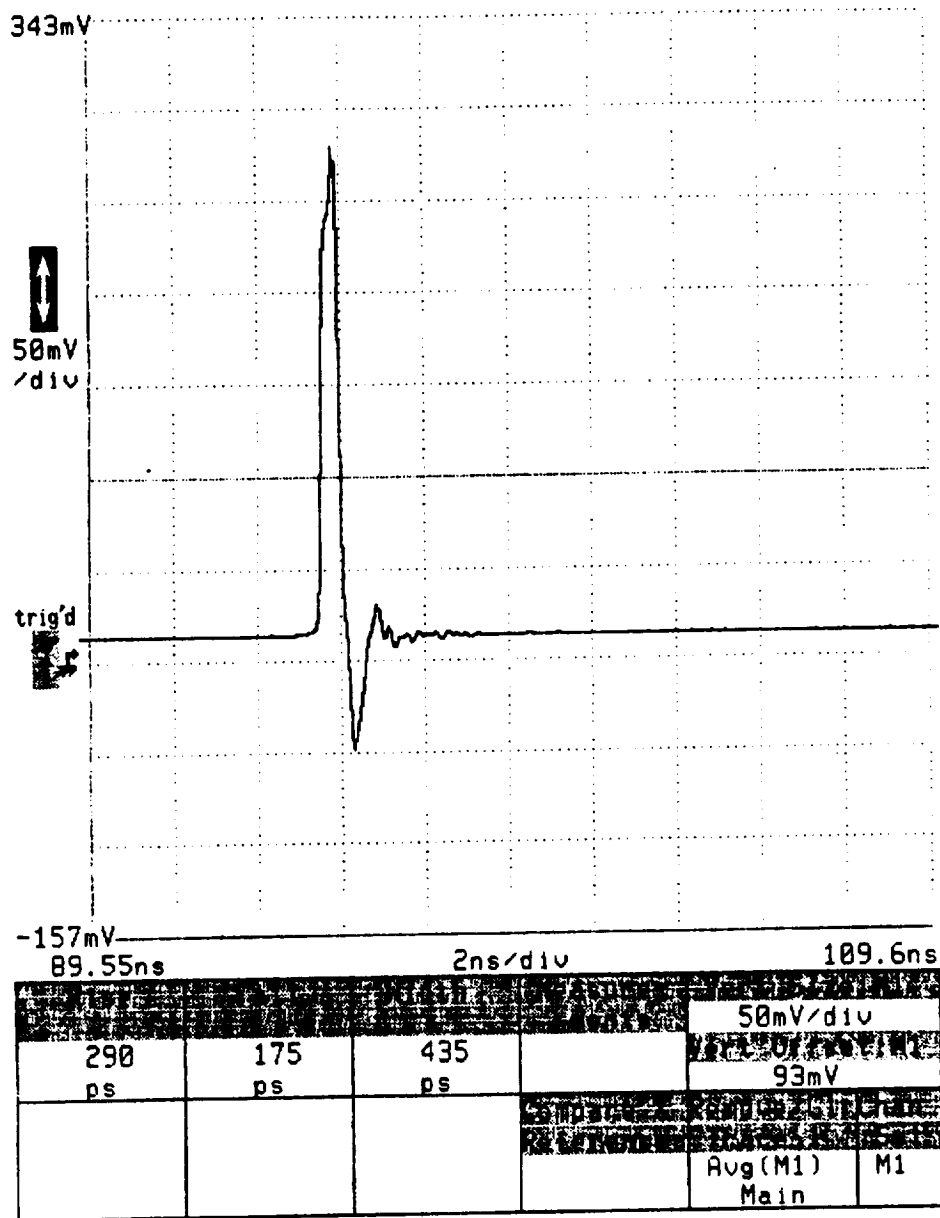


Figure 5-18: Oscilloscope trace of the pulse response of an undoped 2.5 μm PIN APD with no applied bias.

5.4 Temperature Dependence

5.4.1 Impact Ionization vs. Tunneling

In most materials, the mechanisms of junction breakdown can be attributed to both impact ionization and tunneling. One way of determining the dominant process is by examining the temperature dependence of the junction's IV characteristics. Since the energy bandgap of GaAs decreases with increasing temperature, one would expect the breakdown voltage due to the tunneling effect to have a negative temperature coefficient leading to a decrease in breakdown voltage with increasing temperature as shown in Figure 5-19. This is because a smaller applied field would be needed to reach the same current levels at higher temperatures. On the other hand, avalanche breakdown has a positive temperature coefficient where the breakdown voltage increases with increasing temperature due to the shorter mean free path of carriers at higher temperatures. Increasing T increases the phonon vibrations of the lattice, thereby increasing the probability of premature scattering and reducing the ionization coefficients for a given E-field. Other sources of leakage current, such as generation-recombination and diffusion also tend to increase with increasing T. The result of such an effect is shown in Figure 5-20 by the experimental gain data obtained from the IV curves of a doped MQW APD. According to Tyagi⁵⁰, the breakdown voltage is related to temperature through the following linear relationship:

$$V_B(T) = V_B(T_0)(1 + \beta(T - T_0)) \quad [5-5]$$

where $\beta > 0$ in junctions where impact ionization dominates. Such a linear dependence was shown experimentally to be valid by Forrest et al.⁵¹ in the case of p⁺n junctions. However,

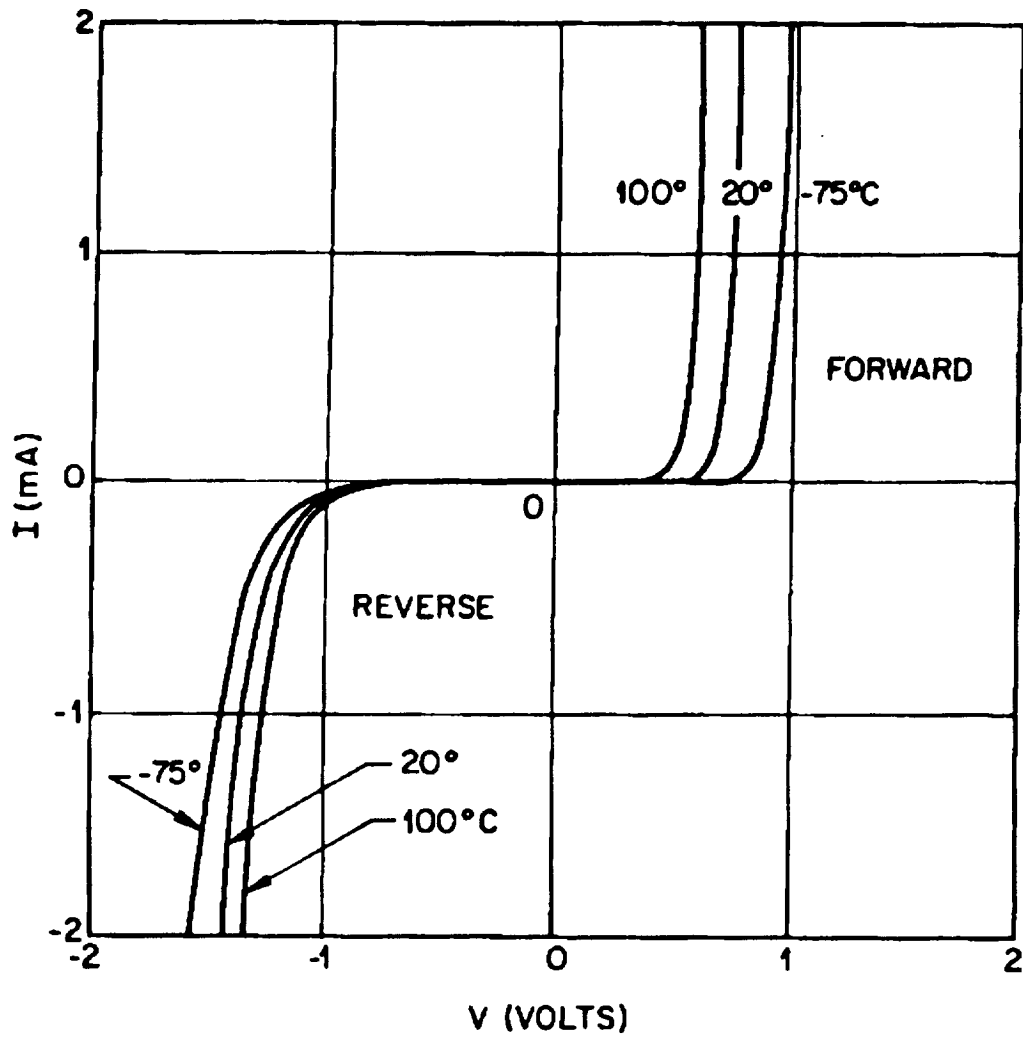


Figure 5-19: IV characteristics of tunneling breakdown⁵².

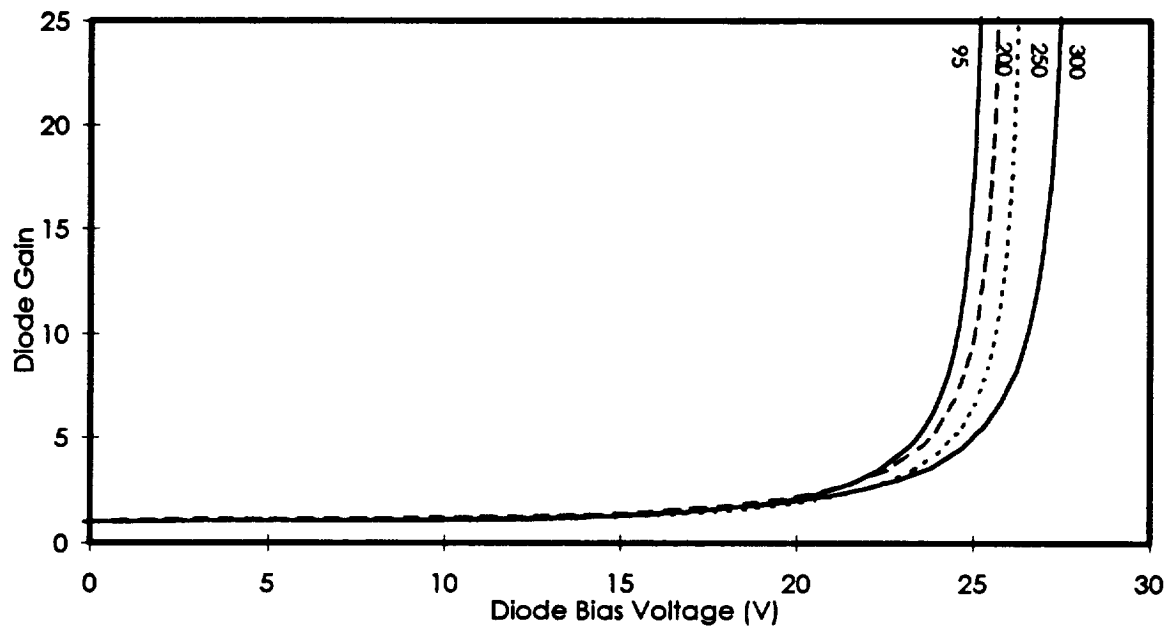


Figure 5-20: Measured gain as a function of temperature (in K) for a doped MQW APD.

our experimental measurements have shown that for doped MQW junctions, the data can be best fit using a third degree polynomial as shown in Figure 5-21.

5.4.2 Junction Capacitance and Temperature

As was shown in equation [2-57], the PN junction capacitance is given by:

$$C_J = \frac{K_s \epsilon_0 A}{\left[\frac{2K_s \epsilon_0 (V_{bi} - V_A)}{q} \frac{(N_A^- + N_D^+)}{N_A^- N_D^+} \right]^{1/2}} \quad [5-6]$$

which shows that C_J is directly proportional to $[N_A^- N_D^+ / (N_A^- + N_D^+)]^{1/2}$. The number of ionized donors and acceptors are given by:⁴³

$$N_D^+ = N_D \left[1 - \frac{1}{1 + \frac{1}{g_D} \exp\left(\frac{E_D - E_F}{kT}\right)} \right] \quad [5-7]$$

$$N_A^- = \frac{N_A}{1 + g_A \exp\left(\frac{E_A - E_F}{kT}\right)} \quad [5-8]$$

where g_D is the ground state degeneracy of the donor impurity level and is equal to 2 since a donor level can accept one electron with either spin or can have no electron. On the other hand, g_A is the ground-state degeneracy factor for acceptor levels and is equal to 4. This is because in GaAs as well as in Ge and Si, each acceptor impurity level can accept one hole of either spin and the impurity level is doubly degenerate as a result of the two degenerate valence bands at $k=0$.

Therefore, by examining equations [5-6]-[5-8], it is clear that the capacitance is expected to decrease exponentially with decreasing temperature following the decrease in

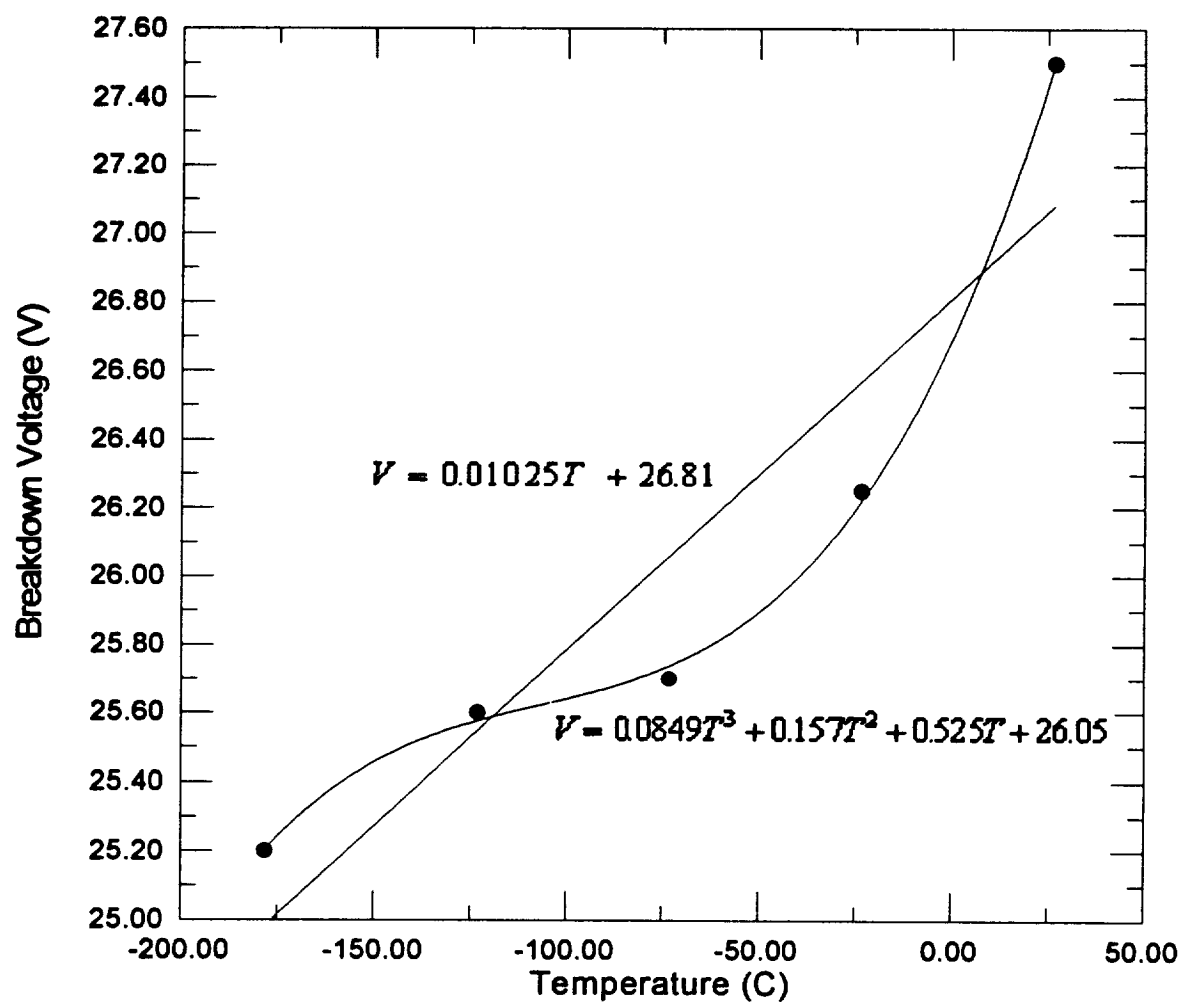


Figure 5-21: Experimental data and fits for a doped-well MQW APD.

the ionized donor and acceptor densities. This behavior is illustrated in the experimental CV data in Figure 5-22 where the capacitance at low bias decreases exponentially toward a limiting value of about 2.8 pF in the case of a doped-well MQW structure. As the reverse bias is increased at a given temperature, the depletion width increases causing the capacitance to drop toward 2.8 pF corresponding to the capacitance value for maximum depletion of the structure.

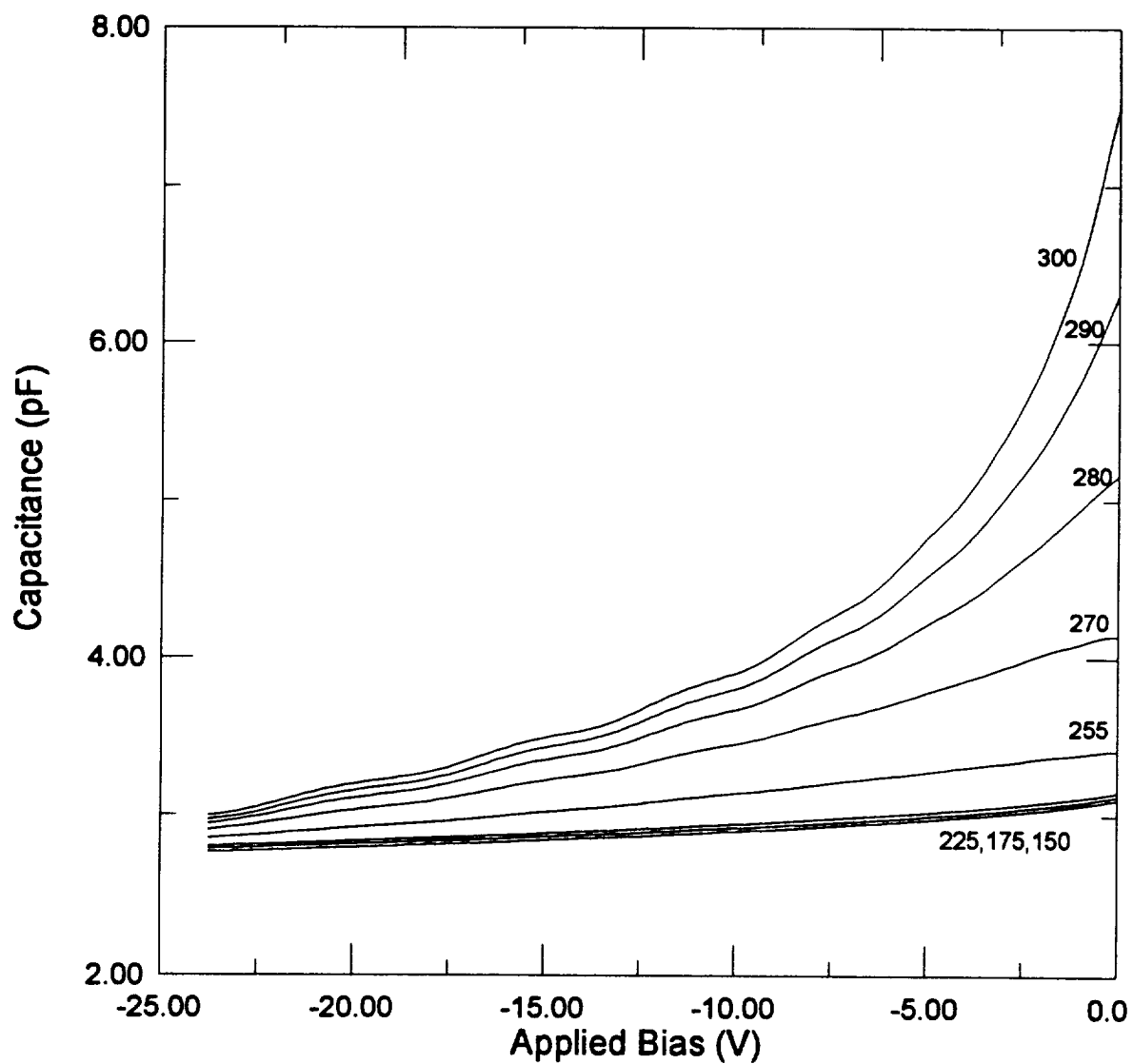


Figure 5-22: Experimental CV curves as a function of temperature for a doped-well MQW APD.

-
- [1] ~~R. B. Emmons, *J. Appl. Phys.* 38, 3705 (1967)~~
 - [2] ~~J.C. Campbell, W. T. Tsang, G. J. Qua and J. E. Bowers, *Appl. Phys. Lett.* 51, 1454 (1987).~~
 - [3] ~~J. N. Hollenhorst, *IEEE J. Lightwave Technology* LT-8, 531 (1990)~~
 - [4] ~~B.C. Roy and N.B. Chakrabarti, *IEEE J. Lightwave Technology* LT-10, 169 (1992).~~
 - [5] ~~R.D. Dupuis, J.C. Campbell and J.R. Velebir, *J. of Crystal Growth* 77, 598-605 (1986)~~
 - [6] ~~N. Yamamoto, K. Yokoyama and M. Yamamoto, *Appl. Phys. Lett.* 62, 253-254 (1993)~~
 - [42] D.C. Raynolds, G. Leies, L. Antes, and R.E. Marburger, "Photovoltaic Effect in Cadmium Sulfide," *Phys. Rev.*, 96, 533 (1954)
 - [43] S.M. Sze, "Physics of Semiconductor Devices", Wiley, 1981.
 - [44] P. Aristin, "Fabrication et Caracterization de Photodiodes a Avalanche a Puits Quantiques Multiples", Ph.D. thesis, January 1992.
 - [45] S.R. Forrest, R.G. Smith, and O.K. Kim, *IEEE J. Quantum Electron.* QE-18 (1982) 2040.
 - [46] R. Kuvas and C. A. Lee, *J. Appl. Phys.*, 41, 1743 (1970)
 - [47] J. N. Hollenhorst, *IEEE J. Lightwave Technology*, LT-8, 531 (1990)
 - [48] B. C. Roy, and N. N. Chakrabarti, *IEEE J. Lightwave Technology*, LT-10, 169 (1992)
 - [49] S.R. Forrest, and O.K. Kim, "Solid State Electronics", 26, 10, pp. 961-962 (1983)
 - [50] M.S. Tyagi, "Solid State Electronics", 11, 99 (1968)
 - [51] S.R. Forrest, and O.K. Kim, "Solid State Electronics", 26, 10, pp. 958-959 (1983)
 - [52] M.J.O. Strutt, "Semiconductor Devices", Vol. 1, *Semiconductor and Semiconductor Diodes*, Academic, New York, 1966, Chap. 2.

A COMPREHENSIVE ANALYSIS OF THE PHYSICAL PROPERTIES OF ADVANCED GaAs/AlGaAs JUNCTIONS

Hicham M. Menkara

Directed by Dr. Christopher J. Summers

In this work, a detailed experimental investigation and analysis were performed of the physical properties of advanced semiconductor junctions. The analysis includes a study of (1) the difference in the structure-induced multiplication gain between doped GaAs/AlGaAs MQW and PIN junctions, (2) the effect of variations in the doping profiles on the properties of doped MQW structures, (3) the effect of surface treatments on the dark current and gain characteristics, (4) the spectral and time response limitations of the structures, and (5) a complete modeling of the junction physics for the different structure types. All of these investigations were performed by conducting experimental measurements and theoretical simulations on new avalanche photodiode (APD) structures with built-in intrinsic (PIN), doped and undoped MQW structures.

In order to properly interpret the experimental data provided by the measurements, one needs to understand the correlation between such data and the physical parameters used in designing the structures. To accurately determine such a correlation usually requires the ability to grow and fabricate a large sample of structures produced under very similar conditions. Unfortunately, this is not very practical or even possible during material growth and fabrication. Therefore, developing theoretical models which accurately predict the relationships between the input and the output parameters is essential to understanding the physics behind the data.

Most of the experimental data will be presented and analyzed for the first time in the GaAs/AlGaAs material system. The experimental results were compared to theoretical models, and were used to demonstrate, for the first time, the impact of the doping imbalance throughout the structure on the optical and electrical characteristics of a doped MQW structure. These models accurately predicted most of the external behavior displayed by these structures during experimental testing. In addition, various surface treatment techniques which enabled a dramatic reduction in the reverse bias dark current by as much as a factor of 1000 will be discussed. Furthermore, a new technique will be presented for improving the quantum efficiencies of these structures, and its effectiveness was verified through theoretical models.

<u>5.5 EFFECT OF VARIATIONS IN THE DOPING PROFILES</u>	115
<u>5.5.1 INTRODUCTION</u>	116
<u>5.5.2 THEORETICAL RESULTS</u>	117
<u>5.5.3 EXPERIMENTAL RESULTS</u>	125
CHAPTER VI	130
CONCLUSIONS	130
PUBLICATIONS :	132
PRESENTATION :	133

5.5 Effect of Variations in the Doping Profiles

The purpose of the following analysis is to use both theoretical and experimental evidence to determine the impact of doping imbalance and symmetry on the physical and electrical characteristics of doped MQW APDs. Theoretical models have been developed to calculate the electric field, valence and conduction band profiles, CV profiles, as well as carrier concentration versus depth profiles. Our models showed a strong correlation between the p- and n-doping balance inside the GaAs wells and the number of depleted stages and breakdown voltage of the APD. A periodic doping imbalance in the wells has been shown to result in a gradual increase (or decrease) in the electric field profile throughout the device which gave rise to partially depleted devices at low bias. The MQW APD structures that were modeled consisted of the standard structure with a 1 μm doped-well MQW region. These simulation results showed that in an APD with nine doped wells, and where the 50 \AA p-doped layer is off by 10% compared to the n-doped layer ($p=1.65 \times 10^{18} \text{ cm}^{-3}$, $n=1.5 \times 10^{18} \text{ cm}^{-3}$), half the stages were shown to be undepleted at low bias which was a result of a reduction in the E-field near the p^+ cap layer by over 50% from its value in the balanced structure. Experimental CV and IV data on similar MBE grown MQW structures have shown very similar depletion and breakdown characteristics. The models have enabled a better interpretation of the experimental data and relate some of the observed peculiarities in the IV and CV curves directly to the doping profile in the MQW structure.

5.5.1 Introduction

As was described in Chapter IV, various characterization techniques have been devised to analyze and understand the optical and electrical properties of APDs⁵³. These include various experiments such as IV measurements which are used to determine the gain properties of the device, and CV measurements which are used to calculate carrier concentration versus depletion width profiles. However, the data obtained using such experimental techniques are not always easy to interpret and relate back to the physical processes taking place inside the structures. In addition, the practical limitations inherent in the growth and fabrication of large quantities of devices with different structural designs add even more complexity to the problem because of the large number of variables involved in the process.

In what follows, a more practical approach will be presented to analyzing the experimental data obtained using IV and CV experiments and specifically those relating the doping profile characteristics to device properties. Accurate theoretical models of MQW APD structures have been developed using AtlasII, Silvaco's two-dimensional device simulation framework. These models were used to provide graphical representations of the spatial variations of the electric field across the biased structure, as well as conduction and valence band diagrams of the GaAs/AlGaAs MQW structure before and after breakdown. In addition, avalanche breakdown simulations and small signal ac analysis were used to extract IV and CV curves in order to compare the data from the models to those obtained directly from our experimental devices. Both electron- and hole-injected photocurrent solutions were obtained by simulating a 632.8 nm

monochromatic light source with spot power of about 1 W/cm^2 incident on the devices' front and back surfaces. CV solutions were obtained using small signal analysis at a frequency of 1 MHz and with a signal magnitude of 0.03 V. All our analysis were conducted using Newton's two-carrier method⁵³ and the generation rate of electron-hole pairs due to impact ionization was modeled according to Selberherr⁵⁴.

5.5.2 Theoretical Results

The APD structure used in this model consisted of a top and bottom p^+ and n^+ doped ($3 \times 10^{18} \text{ cm}^{-3}$) GaAs layers with thicknesses of $1 \text{ }\mu\text{m}$. The middle region was made up of 10 periods of alternating layers of GaAs ($500 \text{ }\text{\AA}$) and $\text{Al}_{0.42}\text{Ga}_{0.58}\text{As}$ ($500 \text{ }\text{\AA}$). The GaAs wells were similarly doped with p-i-n layers whose thicknesses and doping concentrations were treated as variable parameters for the purpose of our study. When a reverse bias is applied, the combined effect of the applied electric field, the built-in field, and the conduction band offset enhances the ionization process of electrons in the GaAs. The holes, on the other hand, are subjected to a smaller valence band discontinuity and therefore gain less energy than the electrons.

In this study, the widths of the p and n doping layers were held constant at $50 \text{ }\text{\AA}$, and that of the intrinsic layer at $100 \text{ }\text{\AA}$. The doping imbalance ($\frac{|p|-|n|}{|n|}$) was varied between zero and 100 percent. Figure 5-23 shows the corresponding CV plots obtained

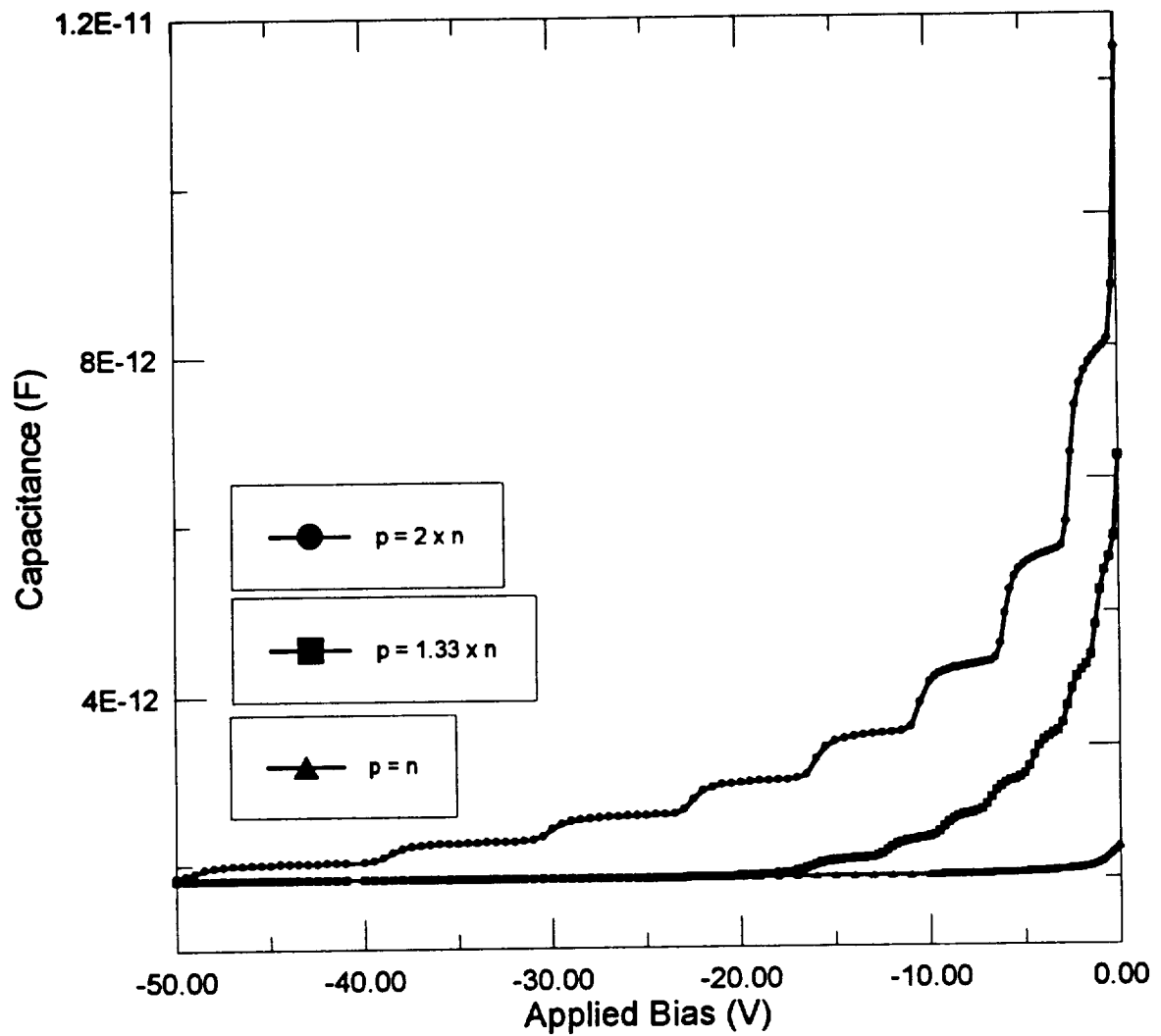


Figure 5-23: Comparison of theoretical CV data obtained for the same APD MQW structure where the doping mismatch in the wells was varied between 0% and 100%.

for similar devices with 0%, 33.3%, and 100% doping imbalance. As expected, the capacitance of the device is lowest when the p and n doping are perfectly matched since the net carrier concentration throughout the device is reduced to zero. However, the avalanche breakdown voltage as depicted by the IV curves in Figure 5-24, seems to be highest when p is equal to n. This is due to the fact that a doping mismatch would result in a gradual increase of the electric field throughout the device which would cause impact ionization to take place at a lower bias point (see E-field profile in Figure 5-25). Therefore, a large doping imbalance would actually lower the bias at which breakdown occurs. This, however, comes at the expense of a large undepleted region which could limit the quantum efficiency and severely hurt the time response characteristics of the photodiode.

Figure 5-26 shows the calculated carrier concentration versus depletion width profile for similar APD structures with 0%, 10%, 20%, 33.3%, and 100% doping mismatch. In the case where $p=n=1.5 \times 10^{18}$, it can be seen that the device is fully depleted at zero bias. The number of undepleted stages begins to increase when increasing the offset between p- and n-doping. In the case where the p-doping is twice that of n, only about 20% of the device is depleted at zero bias. In order to better understand the effect of the doping imbalance on the MQW structures, it is helpful to examine the valence and conduction band diagrams (Figure 5-27), as well as the electric field spatial profile shown in Figure 5-25. Devices corresponding to 0%, 33%, and 100% doping imbalances are modeled at a reverse bias of 20 V. As is seen from the two figures, the electric field is uniformly symmetric, and the MQW region is equally depleted in the case where $p=n$.

However, as p gradually increases, the electric field becomes progressively lower near the top p -layer which results in non-uniform depletion of the MQW structure. The effect of such non-uniform depletion on the device's photocurrent can be clearly seen in the IV plots shown in Figure 5-24. In the case of electron injection, the photocurrent at zero bias is about four orders of magnitude lower than that for hole injection. Gradually, the electron-injected photocurrent increases as the device is depleted until it reaches about 6×10^{-8} A corresponding to that of the hole-injected photocurrent. Therefore, a doping imbalance where $p > n$ can greatly reduce the device's external quantum efficiency in the case of electron injection. Such an effect is not as pronounced in the case where $n > p$ due to the smaller valence band discontinuity faced by the injected holes.

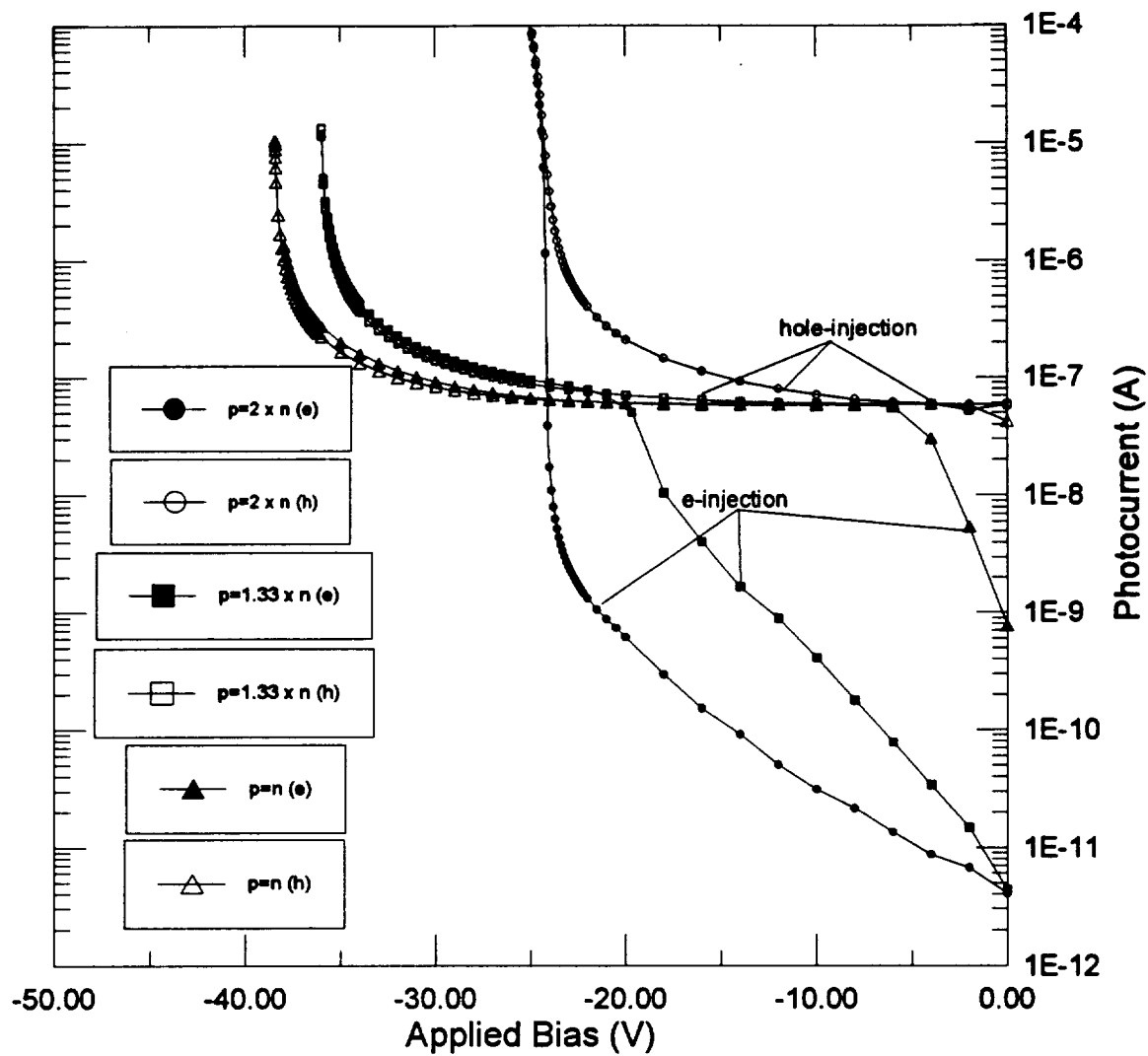


Figure 5-24: Comparison of theoretical light IV data obtained for the same APD MQW structure where the doping mismatch in the wells was varied between 0% and 100%

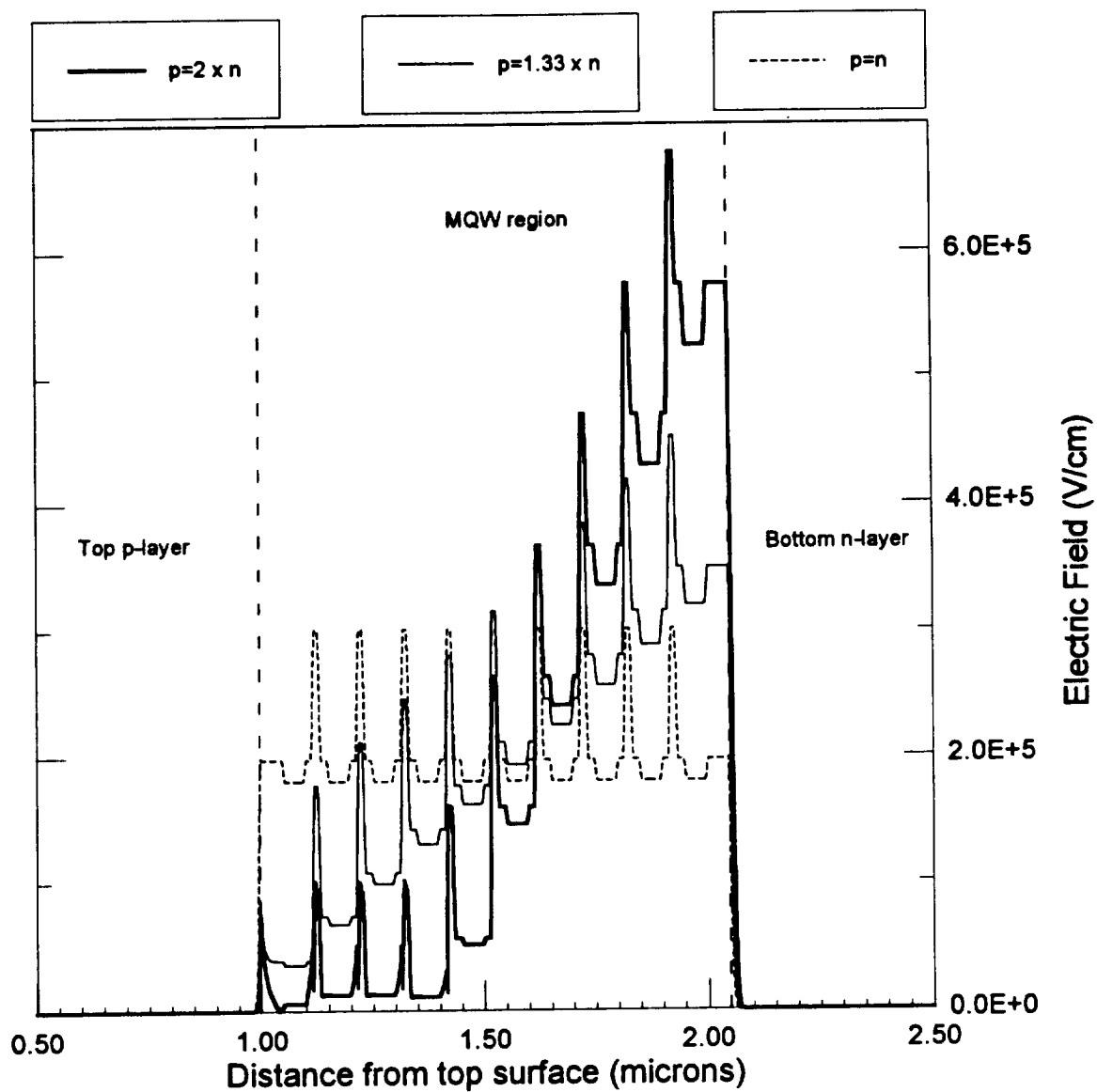


Figure 5-25: Theoretical electric field profiles of the same MQW APD structures with different doping imbalance in the wells ($V = -20$ V).

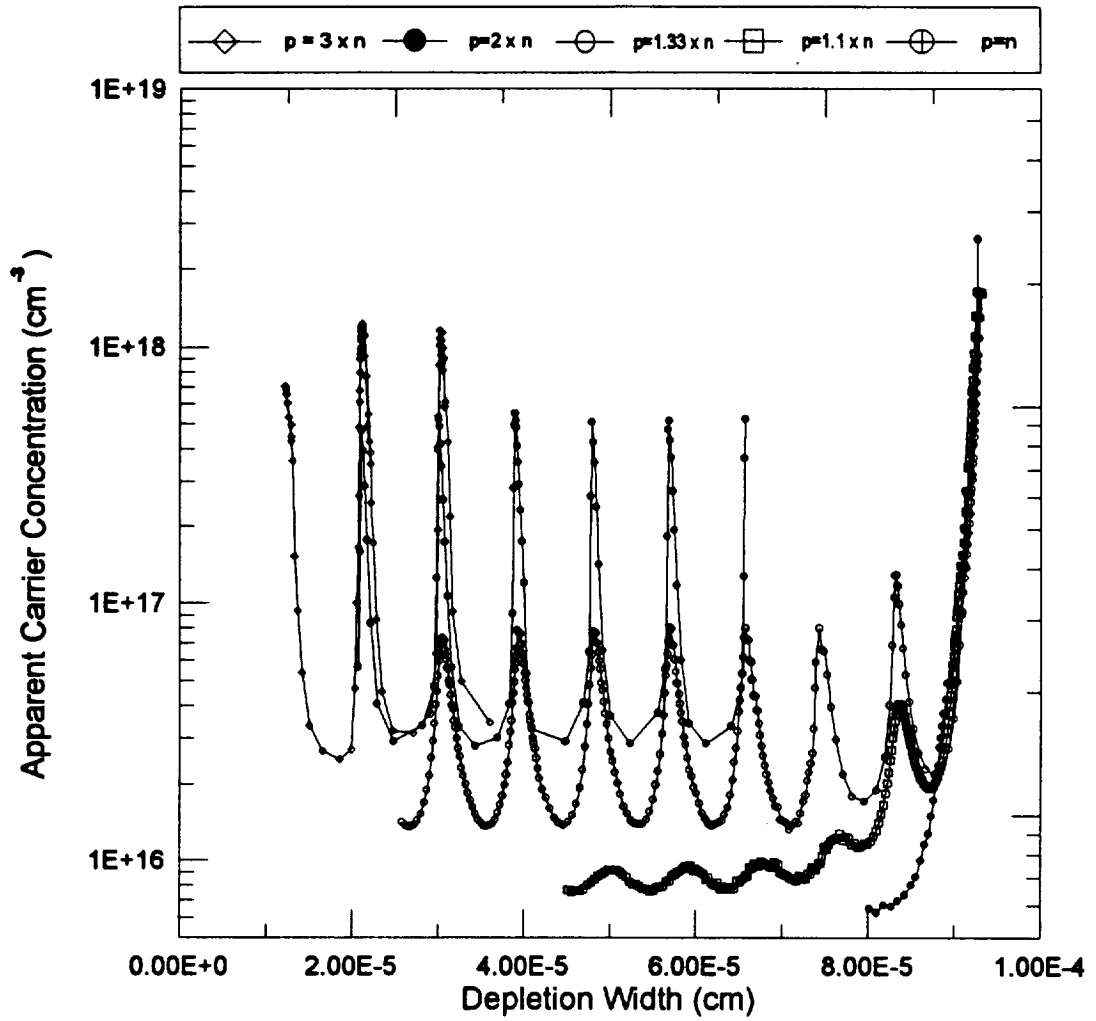


Figure 5-26: Calculated doping profiles versus depletion width using theoretical CV data obtained from AC analysis on similar MQW APDs with different doping imbalances in wells.

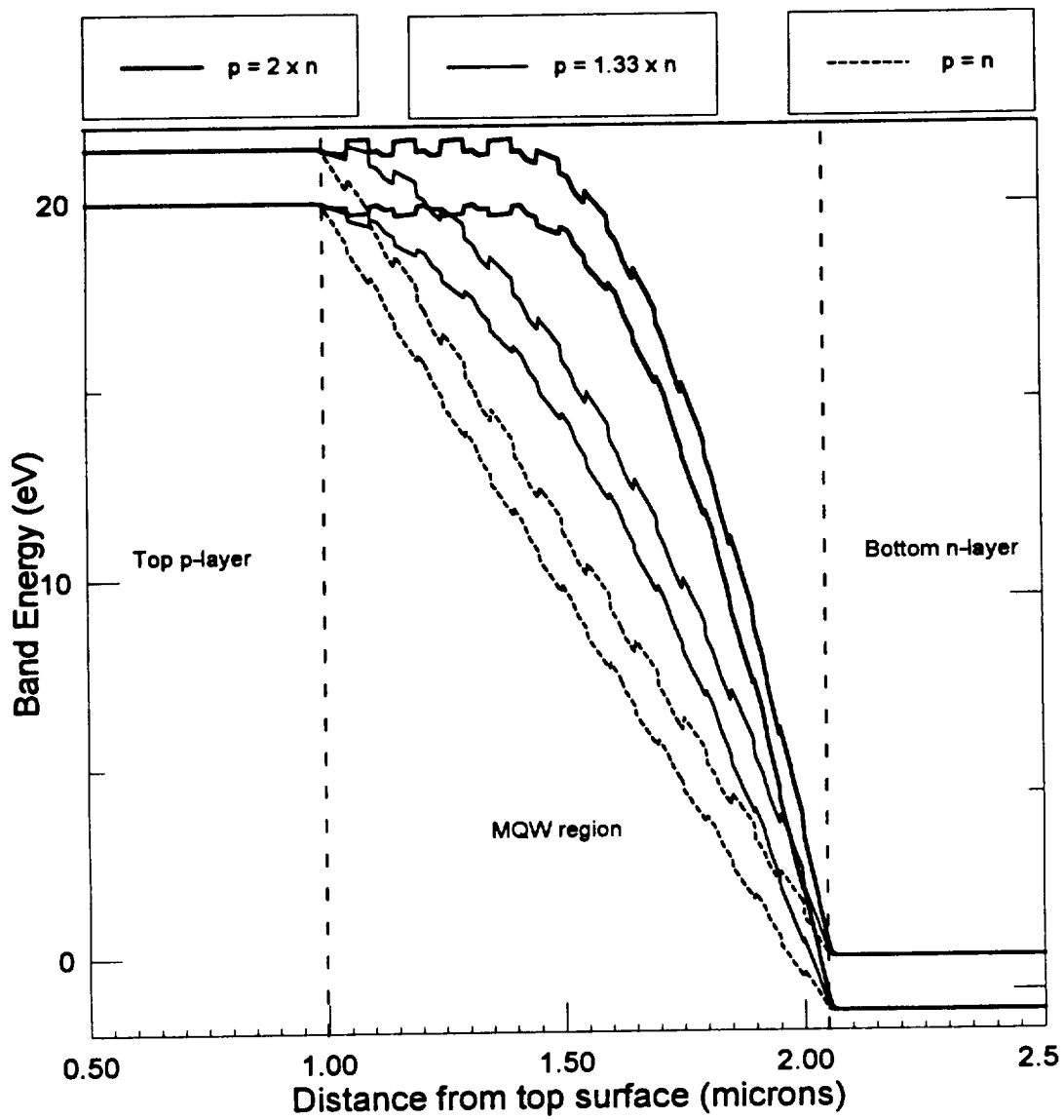


Figure 5-27: Theoretical band diagrams of the same MQW APD structures with different doping imbalance in the wells ($V = -20$ V)

5.5.3 Experimental Results

CV measurements were performed on all devices at 1 MHz using the previously described set-up. The CV data was then analyzed to calculate the depletion widths and carrier profiles for the structures. Figure 5-28 shows the net carrier concentration plots for four doped-well MQW devices labeled as APD1 through APD4. All devices have similar geometries except for the p- and n-doping in the wells which was varied between 0.5×10^{18} and $1.5 \times 10^{18} \text{ cm}^{-3}$. It is interesting to see that even though APD1 and APD2 were expected to have very similar properties, their CV and carrier concentration profiles were quite different. APD1 was almost fully depleted at zero bias, while APD2 was not and only reached full depletion right before breakdown. Note that the peak positions in the carrier profile of APD2 do not quite agree with the 1000 Å period in the MQW structure and with the doping profiles obtained using our models. This discrepancy is due to the fact that carrier concentration profiles calculated from the experimental CV data assumed a one sided depletion⁵⁵ which apparently does not hold true for the experimental devices. Other sources of error in the experimental data result from the inability to accurately account for parasitic capacitance between the devices and the metal contacts and bonding wires in the measurement system. In addition, note how the average net carrier concentration in the experimental doping profile gradually increases up to the top GaAs well where it then drops indicating that the doping imbalance is not the same throughout the structure.

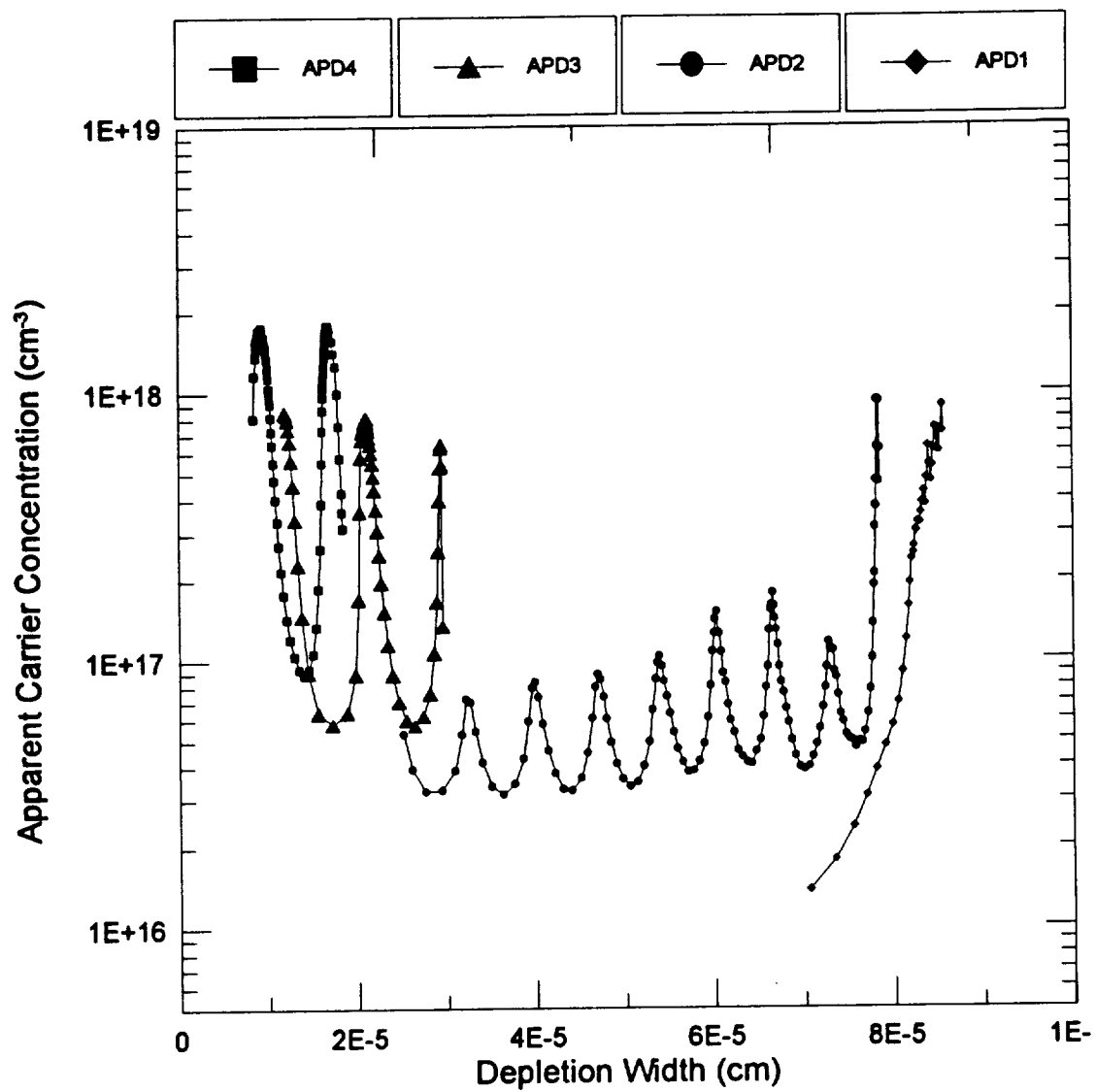


Figure 5-28: Calculated doping profile versus depletion width using experimental CV data from four 10-period doped-well MQW APDs.

The spatial resolution of the CV measurements (both experimental and theoretical) was limited by the Debye length (equation [5-1]) which is about 40 Å at room temperature for a doping level of $n=1.5 \times 10^{18} \text{ cm}^{-3}$. Since the thickness of the doped layers in the wells was of the same order of magnitude (50 Å), abrupt changes in the doping concentration could not be accurately measured. Therefore, it is generally difficult to relate the apparent carrier concentration obtained from the experimental devices to the actual doping imbalance in the wells. However, using our theoretical carrier profile data shown in Figure 5-26 where the actual doping imbalance is fully known, it is possible to estimate the actual doping mismatch in every doped layer in the experimental MQW device by superimposing both the experimental and theoretical data. By examining Figure 5-26 and Figure 5-28, we can roughly conclude that the average doping imbalance in APD1 is far less than 10% which resulted in full depletion at zero bias, while that in APD2 is between 30% and 40% where full depletion of the MQWs was achieved near breakdown around 27 V. In the case of APD3 and APD4, the situation was quite different. Apparently, the p- and n-doping mismatch was so large (~ 200 %) to the point where only partial depletion of two wells was accomplished before avalanche breakdown. By examining the electron injected photocurrent curves in Figure 5-29, we can easily conclude that for both APD1 and APD2, the doping mismatch is such that $n > p$, while in APD3 and APD4, the situation is reversed. This can be clearly understood by comparing the light IV data in Figure 5-29 to the theoretical curves shown in Figure 5-24. The gradual increase in the electron injected photocurrent in APD3 and APD4 is an indication

of trapping of injected electrons by the AlGaAs barriers near the p-layer where the device is undepleted. Therefore, according to the models shown in Figure 5-26, the average p-doping in the wells must be larger than that of n. In the case of APD1 and APD2, no trapping seems to take place since the low bias photocurrent is much higher and relatively flat. Therefore, these two devices have undepleted regions near the n-layer which indicates that $n > p$.

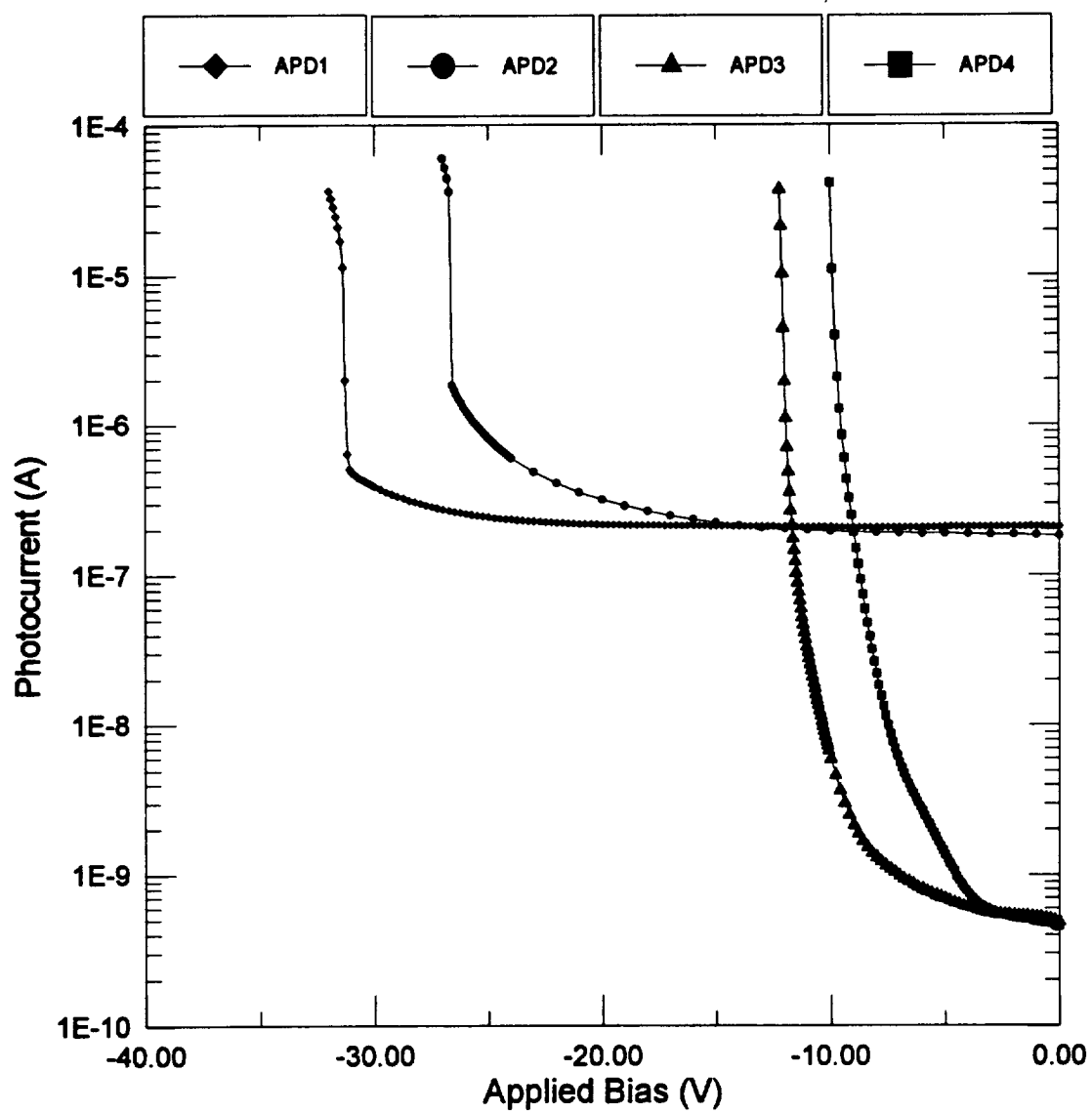


Figure 5-29: Experimental light IV curves obtained for all four 10-period doped-well MQW APDs for the same incident photon flux (electron injection)

CHAPTER VI

CONCLUSIONS

Throughout this work, a detailed comparison of the gain and noise characteristics of a conventional and a doped well MQW APD was presented. The data obtained demonstrated a direct experimental evidence of structure induced preferential multiplication of electrons over holes. For the doped MQW APDs, the average gain per stage was calculated by comparing gain data with carrier profile measurements, and was found to vary from 1.03 at low bias to 1.09 near avalanche breakdown. This is in contrast to conventional PIN structures which show no gain in this regime. It was also shown that, as the bias was increased, the effect of the structure became less pronounced, and the MQW device was reduced to a conventional PIN structure. Similar studies of the bias dependence of the excess noise characteristics show that the low-voltage gain is primarily due to electron ionization in the MQW APDs, and to both electron and hole ionization in the PIN APDs. Our measurements of the doped MQW APD clearly showed that for low gains ($M < 6$), the ionization ratio is greatly enhanced ($k = \alpha/\beta = 10 - 50$) as compared to that in bulk GaAs ($k = 1.67$). At higher voltages, however, the value of k is reduced since the holes gain more energy from the applied electric field and are more likely to impact ionize.

It was also observed that surface recombination has a significant on the dark current behavior of an APD. The resulting leakage currents can have dramatic

consequences on the sensitivities and attainable gain levels in a photodiode. As a result of surface treatment, dark currents at low bias were reduced to as low as 1 pA. The result of this reduction in dark current was manifested in the structures' high gain performance which exceeded 10,000 in some APDs. By being able to reduce the dark currents, it was possible to maintain dark current levels well below those of the photocurrents. This made it possible to achieve and sustain high levels of gains well beyond the onset of junction breakdown.

The spectral response and quantum efficiencies for some of the structures were also calculated and modeled. The experimental data were very consistent with the theoretical models. The quantum efficiencies of the fabricated structures were relatively low because of the loss of photogenerated carriers due to recombination mechanisms in the diffusion layer. It was shown how it was theoretically possible to significantly increase the quantum efficiency of the devices through the introduction of a heavily doped p^{++} GaAs top layer. Such layers help to create a high-field region that will enhance the diffusion of photogenerated electrons toward the depletion region.

An investigation was also made into the impact of doping imbalances in doped-well MQW APDs on device IV and CV characteristics and how such an imbalance would affect the depletion properties of the APDs. Our theoretical models were in full agreement with the observed experimental data and have provided a good understanding of the physical processes that take place inside a doped MQW APD. These models have been used to interpret experimental IV and CV data and to determine the extent of depletion in APD devices. How these parameters were affected by the p- and n-doping

imbalance in the structure was also determined. The model predicted that a doping mismatch as small as 10% could reduce the depletion layer by as much as 50%. It was also shown how a large doping imbalance would cause the device to quickly reach avalanche breakdown in the depleted layers and would prevent full depletion.

The presence of undepleted regions was also shown to be one of the major causes of the slow time response in avalanche photodiodes. Partial depletion gave rise to a diffusion-limited transient response in doped MQW structures. This was demonstrated experimentally to be the case by examining the change in diffusion tail of the output pulse response of the devices as a function of applied bias. Fully depleted PIN structures showed a fast time response even at zero applied bias. The relationships between the depleted (undepleted) widths and the drift (diffusion) time response were used in conjunction with the sums of squares approximation to get an estimate of the time constants which limit the overall response of both the PIN and the MQW structures. The diffusion time constant for the MQW structure ($\tau_{\text{diff}} \sim 1.5 \text{ ns}$) was found to be more than twice as large as that calculated for the PIN APD ($\tau_{\text{diff}} \sim 0.7 \text{ ns}$) and confirms that the undepleted MQW structure was diffusion-limited.

PUBLICATIONS :

- [1] Menkara, H. M., Wagner, B. K., Summers, C. J., "Gain properties of doped GaAs/AlGaAs multiple quantum well avalanche photodiode structures", *Appl. Phys. Lett.*, Vol. 66, no. 14, pp. 1764-1766 April 1995.
- [2] Yun, I., Menkara, H. M., Wang, Y., Oguzman, I. H., Kolnik, J., Brennan, K.F., May, G. S., Summers, C. J., Wagner, B. K., "Reliability assessment of multiple quantum well avalanche photodiodes", *1995 IEEE International Reliability Physics Proceedings*. 33rd Annual, p. 200-204.
- [3] Menkara, H. M., Wagner, B. K., Summers, C. J., "Effect of variations in the doping profiles on the properties of doped multiple quantum well avalanche photodiodes", to be published in *Optical Materials*.
- [4] Yun, I., Menkara, H. M., Wang, Y., Oguzman, I. H., Kolnik, J., Brennan, K.F., May, G. S., Summers, C. J., Wagner, B. K., "The effect of manufacturing process sequence on the reliability of GaAs multiple quantum well avalanche photodiodes", to be published.

PRESENTATION :

- [1] Menkara, H. M., Wagner, B. K., Summers, C. J.
Effect of variations in the doping profiles on the properties of doped multiple quantum well avalanche photodiodes. First International Workshop on Materials for Optoelectronics, Sheffield Hallam University, Sheffield, U.K, August 1995.

-
- [53] Silvaco International, "Atlas II User's Manual", 1st Edition, July 1, 1993.
- [54] S. Selberherr, "Analysis and Simulation of Semiconductor Devices", Springer-Verlag, Wien-New York. 1984.
- [55] N. Yamamoto, K. Yokoyama, and M. Yamamoto, *Appl. Phys. Lett.* 62, 252 (1993).

APPENDIX A

$\text{Al}_x\text{Ga}_{1-x}\text{As}$ MATERIAL SYSTEM PARAMETERS

GaAs/AlGaAs materials are frequently used in the fabrication of heterojunction devices. The parameters for GaAs can, in general, be derived from those for $\text{Al}_x\text{Ga}_{1-x}\text{As}$ by setting the value of x to zero. In the following few sections, the various optical and electrical parameters relevant to GaAs/AlGaAs structures modeling will be presented.

A.1 AlGaAs Band Parameters

The net material bandgap is chosen as the minimum value of the various default bandgap valleys in AlGaAs given by the following equations :

$$E_g(\text{G}) = E_{g0} + x(1.155 + 0.37 x) \quad [\text{A- 1}]$$

$$E_g(\text{L}) = 1.734 + x(0.574 + 0.055 x) \quad [\text{A- 2}]$$

$$E_g(\text{X}) = 1.911 + x(0.005 + 0.245 x) \quad [\text{A- 3}]$$

The temperature dependence of the bandgap is introduced through the E_{g0} parameter calculated from the following equation^{1,2}:

$$E_g(T) = E_g(0) - \frac{\alpha T^2}{T + \beta} = E_g(300) + \alpha \left[\frac{300^2}{300 + \beta} - \frac{T^2}{T + \beta} \right] \quad [\text{A- 4}]$$

where,

$$E_g(0) = 1.519 \text{ eV}$$

$$\alpha = 5.405 \times 10^{-4} \text{ eV/K}$$

$$\beta = 204.0 \text{ K}$$

The AlGaAs electron affinity for a given x value can be calculated from:

$$\chi = 4.07 - 0.85(E_g(G) - E_g(GaAs)) \quad [\text{A- 5}]$$

and the density of states mass of the valence band is given by:

$$m_v = (0.082^{3/2} + 0.45^{3/2})^{2/3} \quad [\text{A- 6}]$$

A.2 AlGaAs Dielectric Properties

The default value for the static dielectric constant for AlGaAs is given as a function of x by:

$$\epsilon' = 13.18 + 2.9 x \quad [\text{A- 7}]$$

In the case of GaAs, $x=0$, and $\epsilon' = \epsilon_{GaAs} / \epsilon_0 = 13.18$.

A.3 AlGaAs Bandgap Narrowing

Heavy doping of materials usually lead to bandgap narrowing which has an important effect on heterojunction characteristics. According to Lundstrom³, the bandgap narrowing effects are important only for p-type regions. The default bandgap narrowing parameters are shown in Table 1 for AlGaAs material:

Concentration cm^{-3}	Bandgap Narrowing meV
1.0E18	31.0
2.0E18	36.0
4.0E18	44.2
6.0E18	48.5
8.0E18	51.7
1.0E19	54.3
2.0E19	61.1
4.0E19	64.4
6.0E19	61.9
8.0E19	56.9
1.0E20	53.2
2.0E20	18.0

Table A-1: Default bandgap narrowing values

A.4 AlGaAs Recombination Parameters

The default parameters used for the various recombination mechanisms parameters are shown in Table A- 2 :

Parameter	Value	Equation
τ_{n0}	1.0×10^{-9}	[2-19]
τ_{p0}	2.0×10^{-8}	[2-20]
C_{opt}	1.5×10^{-10}	[2-18]
c_n	5.0×10^{-30}	[2-17]
c_p	1.0×10^{-31}	[2-17]

Table A- 2: Default Recombination Parameters for AlGaAs

A.5 GaAs Impact Ionization Coefficients

The coefficients used in the impact ionization model described by equations [2-21]-[2-23] are provided in Table A- 3.

Symbol	Value
α_n^∞	1.899×10^5
E_n^{crit}	5.75×10^5
β_n	1.82
α_p^∞	2.215×10^5
E_p^{crit}	6.57×10^5
β_p	1.75

Table A- 3: Impact Ionization Coefficients for GaAs

A.5 AlGaAs Mobility Parameters

The default low-field electron mobility for various ranges of $\text{Al}_x\text{Ga}_{1-x}\text{As}$ composition is given by the following set of equations :

$$\mu_n = 8000 - 1.818 \times 10^4 x \quad (0 < x < 0.429) \quad [\text{A- 8}]$$

$$\mu_n = 90 + 1.1435 \times 10^5 (x - 0.46)^2 \quad (0.429 < x < 0.46) \quad [\text{A- 9}]$$

$$\mu_n = 90 + 3.75 \times 10^4 (x - 0.46)^2 \quad (0.46 < x < 0.5) \quad [\text{A- 10}]$$

$$\mu_n = 200 - 2.0 / (x - 0.46) \quad (0.5 < x < 1.0) \quad [\text{A- 11}]$$

The default concentration-dependent mobility values for GaAs are given in Table A- 4.

The following expression is used to implement a field-dependent mobility which provides a smooth transition between low-field and high-field behavior:

$$\mu(E) = \mu_0 \left[\frac{1}{1 + \left(\frac{\mu_0 E}{v_{sat}} \right)^\beta} \right]^{1/\beta} \quad [\text{A- 12}]$$

Where β is a constant with a default value of 1.0 for both electrons and holes. The saturation velocities for AlGaAs are given by:

$$v_{satn} = 1.13 * 10^7 - 1.2 * 10^4 T \quad [A- 13]$$

$$v_{satp} = 1.12 * 10^7 - 1.2 * 10^4 T \quad [A- 14]$$

Concentration (cm ⁻³)	Mobility in GaAs (cm ² /V-s)	
	Electrons	Holes
1.0*10 ¹⁴	8000.0	390.0
2.0*10 ¹⁴	7718.0	380.0
4.0*10 ¹⁴	7445.0	375.0
6.0*10 ¹⁴	7290.0	360.0
8.0*10 ¹⁴	7182.0	350.0
1.0*10 ¹⁵	7300.0	340.0
2.0*10 ¹⁵	6847.0	335.0
4.0*10 ¹⁵	6422.0	320.0
6.0*10 ¹⁵	6185.0	315.0
8.0*10 ¹⁵	6023.0	305.0
1.0*10 ¹⁶	5900.0	302.0
2.0*10 ¹⁶	5474.0	300.0
4.0*10 ¹⁶	5079.0	285.0
6.0*10 ¹⁶	4861.0	270.0
8.0*10 ¹⁶	4712.0	245.0
1.0*10 ¹⁷	4600.0	240.0
2.0*10 ¹⁷	3874.0	210.0
4.0*10 ¹⁷	3263.0	205.0
6.0*10 ¹⁷	2950.0	200.0
8.0*10 ¹⁷	2747.0	186.9
1.0*10 ¹⁸	2600.0	170.0
2.0*10 ¹⁸	2060.0	130.0
4.0*10 ¹⁸	1632.0	90.0
6.0*10 ¹⁸	1424.0	74.5

Table A- 4: Default concentration-dependent mobilities for GaAs

APPENDIX B

SAMPLE SIMULATION ALGORITHMS

B.1 Light IV Simulation of a PIN Structure

```
$ GaAs pin Simulation under Light (p=i=n=1 micron)
$by: Hicham Menkara
$ input deck : pin_bias6_lite.in
$
$ SECTION 1: Mesh specification
$
mesh nx=3 ny=100 smooth=1 diag.flip space.mult=1.0 master.out
$
$mesh rect nx=3 ny=400 smooth=4 diag.flip
x.mesh n=1 loc=0 r=1
x.mesh n=3 loc=75.0 r=1

y.mesh n=1 loc=0.0
y.mesh n=8 loc=0.96
$y.mesh n=45 loc=1.2
y.mesh n=50 loc=1.5
$y.mesh n=255 loc=3.3
y.mesh n=92 loc=2.04
y.mesh n=100 loc=3

$ SECTION 2: Structure Specification
$
region num=1 GaAs y.max=1
region num=2 GaAs y.min=1 y.max=2
region num=3 GaAs y.min=2 y.max=3
$
elec num=1 x.min=0 x.max=75 y.max=0.0
elec num=2 bot
contact num=1 con.resist=1e4
contact num=2 con.resist=1e4

$
doping region=1 uniform p.type conc=3e18
doping region=3 uniform n.type conc=3e18
$
$ SECTION 3: Material model specification
$
material material=GaAs taup0=1.e-9 taun0=1.e-9
impact material=GaAs selb
models material=GaAs srh auger conmob fldmob print
$
$ SECTION 4: Optical source definition
$
beam num=1 x.origin=37.5 y.origin=-1.0 angle=90.0 wavelength=.6328 min.window=-9.0 max.window=9.0
$
```

\$ SECTION 5: Initial solution

```
$
symb newton carr=0
solve init
symb newton carr=2
method trap autonr climt=75000 ctolt.fact=500.0 maxtrap=6
solve prev
$plot.2d x.min=0 x.max=75 y.min=0 y.max=3 grid depl.edge
$plot.1d e.field a.x=37.5 b.x=37.5 a.y=0 b.y=5 points
solve bl=0.001
output e.field j.electron e.velocity e.mobility h.mobility qss e.temp h.temp val.band con.band qfn qfp impact
recomb tot.doping photogen flowlines u.auger u.radiative u.srh
save outf=pin_nobias_lite7.out
```

\$ SECTION 6: Voltage ramp

```
$
log outf=pin_IV_lite7.log master
solve prev v1=0.0 vstep=-2 vfinal=-10 elect=1
solve project v1=-12 vstep=-2 vfinal=-35 elect=1
plot.1d alphan a.x=37.5 b.x=37.5 a.y=0 b.y=5 points outfile=eionl35.dat ascii
plot.1d alphas a.x=37.5 b.x=37.5 a.y=0 b.y=5 points outfile=hionl35.dat ascii
save outf=pin_bias35_lite7.out
solve project v1=-35.2 vstep=-0.1 vfinal=-37.5 elect=1 master
solve project v1=-37.6 vstep=-0.1 vfinal=-45 elect=1 master
plot.1d alphan a.x=37.5 b.x=37.5 a.y=0 b.y=5 points outfile=eionl38.dat ascii
plot.1d alphas a.x=37.5 b.x=37.5 a.y=0 b.y=5 points outfile=hionl38.dat ascii

save outf=pin_bias38_lite6.out
tonyplot pin_IV_lite6.log
$
end
```

B.2 CV Simulation of a doped-well MQW Structure

\$ Doped MQW CV simulation example (10 barriers, 9 wells)

\$ by Hicham Menkara

\$ input deck : MQWCV7s2b.in

\$

\$ SECTION 1: Mesh Specification

\$

\$mesh space.mult=4.0

\$

mesh rect smooth=4 diag.flip

x.mesh loc=0 s=75

x.mesh loc=75.0 s=75

y.mesh loc=0.0 s=0.4

y.mesh loc=0.96 s=0.4

y.mesh loc=0.97 s=0.0024

y.mesh loc=1.525 s=0.0024

y.mesh loc=2.08 s=0.0024

y.mesh loc=2.09 s=0.4

y.mesh loc=3.05 s=0.4

\$

\$ SECTION 2: Structure Specification

```

$
region number=1 x.min=0 x.max=75 y.min=0 y.max=1.0 gaas
region number=2 x.min=0 x.max=75 y.min=1.0 y.max=1.05 gaas
region number=3 x.min=0 x.max=75 y.min=1.05 y.max=1.1 material=AlGaAs x.composition=0.42
region number=4 x.min=0 x.max=75 y.min=1.1 y.max=1.15 gaas
region number=5 x.min=0 x.max=75 y.min=1.15 y.max=1.2 material=AlGaAs x.composition=0.42
region number=6 x.min=0 x.max=75 y.min=1.2 y.max=1.25 gaas
region number=7 x.min=0 x.max=75 y.min=1.25 y.max=1.3 material=AlGaAs x.composition=0.42
region number=8 x.min=0 x.max=75 y.min=1.3 y.max=1.35 gaas
region number=9 x.min=0 x.max=75 y.min=1.35 y.max=1.4 material=AlGaAs x.composition=0.42
region number=10 x.min=0 x.max=75 y.min=1.4 y.max=1.45 gaas
region number=11 x.min=0 x.max=75 y.min=1.45 y.max=1.5 material=AlGaAs x.composition=0.42
region number=12 x.min=0 x.max=75 y.min=1.5 y.max=1.55 gaas
region number=13 x.min=0 x.max=75 y.min=1.55 y.max=1.6 material=AlGaAs x.composition=0.42
region number=14 x.min=0 x.max=75 y.min=1.6 y.max=1.65 gaas
region number=15 x.min=0 x.max=75 y.min=1.65 y.max=1.7 material=AlGaAs x.composition=0.42
region number=16 x.min=0 x.max=75 y.min=1.7 y.max=1.75 gaas
region number=17 x.min=0 x.max=75 y.min=1.75 y.max=1.8 material=AlGaAs x.composition=0.42
region number=18 x.min=0 x.max=75 y.min=1.8 y.max=1.85 gaas
region number=19 x.min=0 x.max=75 y.min=1.85 y.max=1.9 material=AlGaAs x.composition=0.42
region number=20 x.min=0 x.max=75 y.min=1.9 y.max=1.95 gaas
region number=21 x.min=0 x.max=75 y.min=1.95 y.max=2.0 material=AlGaAs x.composition=0.42
region number=22 x.min=0 x.max=75 y.min=2.0 y.max=2.05 gaas
region number=23 x.min=0 x.max=75 y.min=2.05 y.max=3.05 gaas
#
# #1=cathode #2=anode
electrode name=cathode number=1 top
electrode name=anode number=2 bottom
#
doping uniform conc=3e18 p.type direction=y regions=1
doping uniform conc=1.5e18 p.type direction=y y.min=1.115 y.max=1.120
doping uniform conc=1.5e18 n.type direction=y y.min=1.130 y.max=1.135
doping uniform conc=1.5e18 p.type direction=y y.min=1.215 y.max=1.220
doping uniform conc=1.5e18 n.type direction=y y.min=1.230 y.max=1.235
doping uniform conc=1.5e18 p.type direction=y y.min=1.315 y.max=1.320
doping uniform conc=1.5e18 n.type direction=y y.min=1.330 y.max=1.335
doping uniform conc=1.5e18 p.type direction=y y.min=1.415 y.max=1.420
doping uniform conc=1.5e18 n.type direction=y y.min=1.430 y.max=1.435
doping uniform conc=1.5e18 p.type direction=y y.min=1.515 y.max=1.520
doping uniform conc=1.5e18 n.type direction=y y.min=1.530 y.max=1.535
doping uniform conc=1.5e18 p.type direction=y y.min=1.615 y.max=1.620
doping uniform conc=1.5e18 n.type direction=y y.min=1.630 y.max=1.635
doping uniform conc=1.5e18 p.type direction=y y.min=1.715 y.max=1.720
doping uniform conc=1.5e18 n.type direction=y y.min=1.730 y.max=1.735
doping uniform conc=1.5e18 p.type direction=y y.min=1.815 y.max=1.820
doping uniform conc=1.5e18 n.type direction=y y.min=1.830 y.max=1.835
doping uniform conc=1.5e18 p.type direction=y y.min=1.915 y.max=1.920
doping uniform conc=1.5e18 n.type direction=y y.min=1.930 y.max=1.935
doping uniform conc=3e18 n.type direction=y regions=23

$
$ SECTION 3: Material Model Specification
$
material taup0=2.e-6 taun0=2.e-6
models srh auger conmob fldmob
impact selb

```

```

$
$ SECTION 4: Initial Solution
$
symb      Newton carr=2
method    comb trap autonr
solve     init
output    e.field j.electron e.velocity e.mobility h.mobility qss e.temp h.temp val.band con.band qfn qfp impact
recomb    tot.doping

save outf=nobiascent7s2b.out
log  outfile=MQWCV3j2b.log master
method itlimit=50 autonr nrcriterion=0.1 trap atrap=0.5 maxtrap=10

solve v1=0 v2=0 vstep=-0.1 vfinal=-10 elect=1 ac direct freq=1e6 vss=0.030 terminal=1
solve v1=-11 v2=0 vstep=-1 vfinal=-25 elect=1 ac direct freq=1e6 vss=0.030 terminal=1
save  outf=MQWcent725s2b.out
tonyplot MQWCV3j2b.log
end

```

B.3 Spectral Response Simulation of a PIN Structure

```

$Spectral response of PIN structure (p=i=n= 1 micron)
$ by Hicham Menkara
$input deck : PINspec2a.in
$
$ SECTION 1: Mesh Specification
$
$mesh space.mult=4.0
$
mesh rect smooth=4 diag.flip
x.mesh loc=0      s=75
x.mesh loc=75.0 s=75
y.mesh loc=0.0      s=0.01
y.mesh loc=0.96 s=0.01
y.mesh loc=0.97 s=0.004
y.mesh loc=1.05 s=0.01
y.mesh loc=2.08 s=0.004
y.mesh loc=2.09 s=0.4
y.mesh loc=3.05 s=0.4
$
$ SECTION 2: Structure Specification
$
region number=1 x.min=0 x.max=75 y.min=0 y.max=1.0 gaas
region number=2 x.min=0 x.max=75 y.min=1.0 y.max=2.05 gaas
region number=3 x.min=0 x.max=75 y.min=2.05 y.max=3.05 gaas

#
# #1=cathode #2=anode
electrode name=cathode number=1 top
electrode name=anode number=2 bottom

doping uniform conc=3e18 p.type direction=y regions=1
doping uniform conc=3e18 n.type direction=y regions=3
$
$ SECTION 3: Material Model Specification
$

```

```

material material=AlGaAs taup0=2.e-8 taun0=1.e-9 copt=1.5e-10 augn=5e-30 augp=1e-31
impact      selber an1=1.899e5 an2=1.899e5 bn1=5.75e5 bn2=5.75e5 ap1=221500 ap2=221500 bp1=657000
bp2=657000 betan=1.82 betap=1.75 egran=0

```

```

models      material=GaAs srh auger conmob fldmob print

```

```

$
$ SECTION 4: Optical source definition

```

```

$
beam      num=1 x.origin=37.5 y.origin=-1.0 angle=90.0 wavelength=.2 min.window=-9.0 max.window=9.0

```

```

$ SECTION 5: Initial solution

```

```

$
symb      newton carr=0
solve     init
symb      newton carr=2
method    trap autonr climitt=75000 ctolt.fact=500.0 maxtrap=10
solve     prev
output    e.field j.electron e.velocity e.mobility h.mobility qss e.temp h.temp val.band con.band qfn qfp impact
recomb    tot.doping photogen traps flowlines ey.velocity ex.velocity hx.velocity hy.velocity u.auger u.srh u.radiative
solve     prev b1=1
save      outf=PINspec2a0.out

```

```

$ SECTION 6: spectral response

```

```

$
log        outf=PINspec2a.log
solve      prev b1=1 lambda=0.2
solve      prev b1=1 lambda=0.225
solve      prev b1=1 lambda=0.25
solve      prev b1=1 lambda=0.275
solve      prev b1=1 lambda=0.3
solve      prev b1=1 lambda=0.325
solve      prev b1=1 lambda=0.35
solve      prev b1=1 lambda=0.375
solve      prev b1=1 lambda=0.4
save      outf=PINspec400.out
solve      prev b1=1 lambda=0.425
solve      prev b1=1 lambda=0.45
solve      prev b1=1 lambda=0.475
solve      prev b1=1 lambda=0.5
solve      prev b1=1 lambda=0.525
solve      prev b1=1 lambda=0.55
solve      prev b1=1 lambda=0.575
solve      prev b1=1 lambda=0.6
solve      prev b1=1 lambda=0.625
solve      prev b1=1 lambda=0.6325
save      outf=PINspec632.out
solve      prev b1=1 lambda=0.65
solve      prev b1=1 lambda=0.675
solve      prev b1=1 lambda=0.7
solve      prev b1=1 lambda=0.725
solve      prev b1=1 lambda=0.75
solve      prev b1=1 lambda=0.775
solve      prev b1=1 lambda=0.8
solve      prev b1=1 lambda=0.825
solve      prev b1=1 lambda=0.85
save      outf=PINspec850.out

```

```
solve    prev b1=1 lambda=0.865
solve    prev b1=1 lambda=0.875
solve    prev b1=1 lambda=0.885
solve    prev b1=1 lambda=0.9
solve    prev b1=1 lambda=0.91
solve    prev b1=1 lambda=0.9184
```

```
save outf=PINspec2a2.out
tonyplot PINspec2a.log
end
```

¹ G.A.M. Hurx, H.C. de Graaf, W.J. Klosterman, et. al., "A Novel Compact Model Description of Reverse Biase Diode Characteristics including Tunneling", ESSDERC, pp. 49-52, 1990.

² D.B.M. Klaassen, "Physical Modeling for Bipolar Device Simulation", In: Simulation of Semiconductor Devices and Processes, Edited by W. Fichtner and D. Aemmer, Harting-Gorre, 1991, Vol. 4, pp. 23-43.

³ M. Klausmeier-Brown, M. Lundstrom, M. Melloch, "The Effects of Heavy Impurity Doping on AlGaAs/GaAs Bipolar Transistors", IEEE Trans., ED-36, No. 10, pp. 2146-2155, 1989.

APPENDIX A

$\text{Al}_x\text{Ga}_{1-x}\text{As}$ MATERIAL SYSTEM PARAMETERS

GaAs/AlGaAs materials are frequently used in the fabrication of heterojunction devices. The parameters for GaAs can, in general, be derived from those for $\text{Al}_x\text{Ga}_{1-x}\text{As}$ by setting the value of x to zero. In the following few sections, the various optical and electrical parameters relevant to GaAs/AlGaAs structures modeling are presented.

A.1 AlGaAs Band Parameters

The net material bandgap is chosen as the minimum value of the various default bandgap valleys in AlGaAs given by the following equations :

$$E_g(\text{G}) = E_{g0} + x(1.155 + 0.37 x) \quad [\text{A- 1}]$$

$$E_g(\text{L}) = 1.734 + x(0.574 + 0.055 x) \quad [\text{A- 2}]$$

$$E_g(\text{X}) = 1.911 + x(0.005 + 0.245 x) \quad [\text{A- 3}]$$

The temperature dependence of the bandgap is introduced through the E_{g0} parameter calculated from the following equation^{56,57}:

$$E_g(T) = E_g(0) - \frac{\alpha T^2}{T + \beta} = E_g(300) + \alpha \left[\frac{300^2}{300 + \beta} - \frac{T^2}{T + \beta} \right] \quad [\text{A- 4}]$$

where,

$$E_g(0) = 1.519 \text{ eV}$$

$$\alpha = 5.405 \times 10^{-4} \text{ eV/K}$$

$$\beta = 204.0 \text{ K}$$

The AlGaAs electron affinity for a given x value can be calculated from:

$$\chi = 4.07 - 0.85(E_g(G) - E_g(GaAs)) \quad [\text{A- 5}]$$

and the density of states mass of the valence band is given by:

$$m_v = (0.082^{3/2} + 0.45^{3/2})^{2/3} \quad [\text{A- 6}]$$

A.2 AlGaAs Dielectric Properties

The default value for the static dielectric constant for AlGaAs is given as a function of x by:

$$\epsilon' = 13.18 + 2.9 x \quad [\text{A- 7}]$$

In the case of GaAs, x=0, and $\epsilon' = \epsilon_{GaAs} / \epsilon_0 = 13.18$.

A.3 AlGaAs Bandgap Narrowing

Heavy doping of materials usually lead to bandgap narrowing which has an important effect on heterojunction characteristics. According to Lundstrom³⁸, the bandgap narrowing effects are important only for p-type regions. The default bandgap narrowing parameters are shown in Table 1 for AlGaAs material:

Table A-1: Default bandgap narrowing values

Concentration cm^{-3}	Bandgap Narrowing meV
1.0E18	31.0
2.0E18	36.0
4.0E18	44.2
6.0E18	48.5
8.0E18	51.7
1.0E19	54.3
2.0E19	61.1
4.0E19	64.4
6.0E19	61.9
8.0E19	56.9
1.0E20	53.2
2.0E20	18.0

A.4 AlGaAs Recombination Parameters

The default parameters used for the various recombination mechanisms parameters are shown in Table A-2 :

Table A-2: Default Recombination Parameters for AlGaAs

Parameter	Value	Equation
τ_{n0}	1.0×10^{-9}	[2-19]
τ_{p0}	2.0×10^{-8}	[2-20]
C_{opt}	1.5×10^{-10}	[2-18]
c_n	5.0×10^{-30}	[2-17]
c_p	1.0×10^{-31}	[2-17]

A.5 GaAs Impact Ionization Coefficients

The coefficients used in the impact ionization model described by equations [2-21]-[2-23] are provided in Table A-3.

Table A-3: Impact Ionization Coefficients for GaAs

Symbol	Value
α_n^∞	1.899×10^5
E_n^{crit}	5.75×10^5
β_n	1.82
α_p^∞	2.215×10^5
E_p^{crit}	6.57×10^5
β_p	1.75

A.6 AlGaAs Mobility Parameters

The default low-field electron mobility for various ranges of $\text{Al}_x\text{Ga}_{1-x}\text{As}$ composition is given by the following set of equations :

$$\mu_n = 8000 - 1.818 \times 10^4 x \quad (0 < x < 0.429) \quad [\text{A- 8}]$$

$$\mu_n = 90 + 1.1435 \times 10^5 (x - 0.46)^2 \quad (0.429 < x < 0.46) \quad [\text{A- 9}]$$

$$\mu_n = 90 + 3.75 \times 10^4 (x - 0.46)^2 \quad (0.46 < x < 0.5) \quad [\text{A- 10}]$$

$$\mu_n = 200 - 2.0 / (x - 0.46) \quad (0.5 < x < 1.0) \quad [\text{A- 11}]$$

The default concentration-dependent mobility values for GaAs are given in Table A-4.

The following expression is used to implement a field-dependent mobility which provides a smooth transition between low-field and high-field behavior:

$$\mu(E) = \mu_0 \left[\frac{1}{1 + \left(\frac{\mu_0 E}{v_{sat}} \right)^\beta} \right]^{1/\beta} \quad [\text{A- 12}]$$

Where β is a constant with a default value of 1.0 for both electrons and holes. The saturation velocities for AlGaAs are given by:

$$v_{satn} = 1.13 * 10^7 - 1.2 * 10^4 T \quad [A- 13]$$

$$v_{satp} = 1.12 * 10^7 - 1.2 * 10^4 T \quad [A- 14]$$

Table A-4: Default concentration-dependent mobilities for GaAs

Concentration (cm-3)	Mobility in GaAs (cm ² /V-s)	
	Electrons	Holes
1.0*10 ¹⁴	8000.0	390.0
2.0*10 ¹⁴	7718.0	380.0
4.0*10 ¹⁴	7445.0	375.0
6.0*10 ¹⁴	7290.0	360.0
8.0*10 ¹⁴	7182.0	350.0
1.0*10 ¹⁵	7300.0	340.0
2.0*10 ¹⁵	6847.0	335.0
4.0*10 ¹⁵	6422.0	320.0
6.0*10 ¹⁵	6185.0	315.0
8.0*10 ¹⁵	6023.0	305.0
1.0*10 ¹⁶	5900.0	302.0
2.0*10 ¹⁶	5474.0	300.0
4.0*10 ¹⁶	5079.0	285.0
6.0*10 ¹⁶	4861.0	270.0
8.0*10 ¹⁶	4712.0	245.0
1.0*10 ¹⁷	4600.0	240.0
2.0*10 ¹⁷	3874.0	210.0
4.0*10 ¹⁷	3263.0	205.0
6.0*10 ¹⁷	2950.0	200.0
8.0*10 ¹⁷	2747.0	186.9
1.0*10 ¹⁸	2600.0	170.0
2.0*10 ¹⁸	2060.0	130.0
4.0*10 ¹⁸	1632.0	90.0
6.0*10 ¹⁸	1424.0	74.5

APPENDIX B

SAMPLE SIMULATION ALGORITHMS

B.1 Light IV Simulation of a PIN Structure

```
$ GaAs pin Simulation under Light (p=i=n=1 micron)
$by: Hicham Menkara
$ input deck : pin_bias6_lite.in
$
$ SECTION 1: Mesh specification
$
mesh nx=3 ny=100 smooth=1 diag.flip space.mult=1.0 master.out
$
$mesh rect nx=3 ny=400 smooth=4 diag.flip
x.mesh n=1 loc=0 r=1
x.mesh n=3 loc=75.0 r=1

y.mesh n=1 loc=0.0
y.mesh n=8 loc=0.96
$y.mesh n=45 loc=1.2
y.mesh n=50 loc=1.5
$y.mesh n=255 loc=3.3
y.mesh n=92 loc=2.04
y.mesh n=100 loc=3

$ SECTION 2: Structure Specification
$
region num=1 GaAs y.max=1
region num=2 GaAs y.min=1 y.max=2
region num=3 GaAs y.min=2 y.max=3
$
elec num=1 x.min=0 x.max=75 y.max=0.0
elec num=2 bot
contact num=1 con.resist=1e4
contact num=2 con.resist=1e4

$
doping region=1 uniform p.type conc=3e18
doping region=3 uniform n.type conc=3e18
$
$ SECTION 3: Material model specification
$
material material=GaAs taup0=1.e-9 taun0=1.e-9
impact material=GaAs selb
models material=GaAs srh auger conmob fldmob print
$
$ SECTION 4: Optical source definition
$
```

```

beam num=1 x.origin=37.5 y.origin=-1.0 angle=90.0 wavelength=.6328 min.window=-9.0 max.window=9.0
$
$ SECTION 5: Initial solution
$
sybm newton carr=0
solve init
sybm newton carr=2
method trap autonr climt=75000 ctolt.fact=500.0 maxtrap=6
solve prev
$plot.2d x.min=0 x.max=75 y.min=0 y.max=3 grid depl.edge
$plot.1d e.field a.x=37.5 b.x=37.5 a.y=0 b.y=5 points
solve bl=0.001
output e.field j.electron e.velocity e.mobility h.mobility qss e.temp h.temp val.band con.band qfn qfp impact
recomb tot.doping photogen flowlines u.auger u.radiative u.srh
save outf=pin_nobias_lite7.out
$
$ SECTION 6: Voltage ramp
$
log outf=pin_IV_lite7.log master
solve prev v1=0.0 vstep=-2 vfinal=-10 elect=1
solve project v1=-12 vstep=-2 vfinal=-35 elect=1
plot.1d alphan a.x=37.5 b.x=37.5 a.y=0 b.y=5 points outfile=eionl35.dat ascii
plot.1d alphap a.x=37.5 b.x=37.5 a.y=0 b.y=5 points outfile=hionl35.dat ascii
save outf=pin_bias35_lite7.out
solve project v1=-35.2 vstep=-0.1 vfinal=-37.5 elect=1 master
solve project v1=-37.6 vstep=-0.1 vfinal=-45 elect=1 master
plot.1d alphan a.x=37.5 b.x=37.5 a.y=0 b.y=5 points outfile=eionl38.dat ascii
plot.1d alphap a.x=37.5 b.x=37.5 a.y=0 b.y=5 points outfile=hionl38.dat ascii

save outf=pin_bias38_lite6.out
tonyplot pin_IV_lite6.log
$
end

```

B.2 CV Simulation of a doped-well MQW Structure

\$ Doped MQW CV simulation example (10 barriers, 9 wells)

\$ by Hicham Menkara

\$ input deck : MQWCV7s2b.in

\$

\$ SECTION 1: Mesh Specification

\$

\$mesh space.mult=4.0

\$

mesh rect smooth=4 diag.flip

x.mesh loc=0 s=75

x.mesh loc=75.0 s=75

y.mesh loc=0.0 s=0.4

y.mesh loc=0.96 s=0.4

y.mesh loc=0.97 s=0.0024

y.mesh loc=1.525 s=0.0024

y.mesh loc=2.08 s=0.0024

y.mesh loc=2.09 s=0.4

y.mesh loc=3.05 s=0.4

```

$
$ SECTION 2: Structure Specification
$
region number=1 x.min=0 x.max=75 y.min=0 y.max=1.0 gaas
region number=2 x.min=0 x.max=75 y.min=1.0 y.max=1.05 gaas
region number=3 x.min=0 x.max=75 y.min=1.05 y.max=1.1 material=AlGaAs x.composition=0.42
region number=4 x.min=0 x.max=75 y.min=1.1 y.max=1.15 gaas
region number=5 x.min=0 x.max=75 y.min=1.15 y.max=1.2 material=AlGaAs x.composition=0.42
region number=6 x.min=0 x.max=75 y.min=1.2 y.max=1.25 gaas
region number=7 x.min=0 x.max=75 y.min=1.25 y.max=1.3 material=AlGaAs x.composition=0.42
region number=8 x.min=0 x.max=75 y.min=1.3 y.max=1.35 gaas
region number=9 x.min=0 x.max=75 y.min=1.35 y.max=1.4 material=AlGaAs x.composition=0.42
region number=10 x.min=0 x.max=75 y.min=1.4 y.max=1.45 gaas
region number=11 x.min=0 x.max=75 y.min=1.45 y.max=1.5 material=AlGaAs x.composition=0.42
region number=12 x.min=0 x.max=75 y.min=1.5 y.max=1.55 gaas
region number=13 x.min=0 x.max=75 y.min=1.55 y.max=1.6 material=AlGaAs x.composition=0.42
region number=14 x.min=0 x.max=75 y.min=1.6 y.max=1.65 gaas
region number=15 x.min=0 x.max=75 y.min=1.65 y.max=1.7 material=AlGaAs x.composition=0.42
region number=16 x.min=0 x.max=75 y.min=1.7 y.max=1.75 gaas
region number=17 x.min=0 x.max=75 y.min=1.75 y.max=1.8 material=AlGaAs x.composition=0.42
region number=18 x.min=0 x.max=75 y.min=1.8 y.max=1.85 gaas
region number=19 x.min=0 x.max=75 y.min=1.85 y.max=1.9 material=AlGaAs x.composition=0.42
region number=20 x.min=0 x.max=75 y.min=1.9 y.max=1.95 gaas
region number=21 x.min=0 x.max=75 y.min=1.95 y.max=2.0 material=AlGaAs x.composition=0.42
region number=22 x.min=0 x.max=75 y.min=2.0 y.max=2.05 gaas
region number=23 x.min=0 x.max=75 y.min=2.05 y.max=3.05 gaas
#
# #1=cathode #2=anode
electrode name=cathode number=1 top
electrode name=anode number=2 bottom
#
doping uniform conc=3e18 p.type direction=y regions=1
doping uniform conc=1.5e18 p.type direction=y y.min=1.115 y.max=1.120
doping uniform conc=1.5e18 n.type direction=y y.min=1.130 y.max=1.135
doping uniform conc=1.5e18 p.type direction=y y.min=1.215 y.max=1.220
doping uniform conc=1.5e18 n.type direction=y y.min=1.230 y.max=1.235
doping uniform conc=1.5e18 p.type direction=y y.min=1.315 y.max=1.320
doping uniform conc=1.5e18 n.type direction=y y.min=1.330 y.max=1.335
doping uniform conc=1.5e18 p.type direction=y y.min=1.415 y.max=1.420
doping uniform conc=1.5e18 n.type direction=y y.min=1.430 y.max=1.435
doping uniform conc=1.5e18 p.type direction=y y.min=1.515 y.max=1.520
doping uniform conc=1.5e18 n.type direction=y y.min=1.530 y.max=1.535
doping uniform conc=1.5e18 p.type direction=y y.min=1.615 y.max=1.620
doping uniform conc=1.5e18 n.type direction=y y.min=1.630 y.max=1.635
doping uniform conc=1.5e18 p.type direction=y y.min=1.715 y.max=1.720
doping uniform conc=1.5e18 n.type direction=y y.min=1.730 y.max=1.735
doping uniform conc=1.5e18 p.type direction=y y.min=1.815 y.max=1.820
doping uniform conc=1.5e18 n.type direction=y y.min=1.830 y.max=1.835
doping uniform conc=1.5e18 p.type direction=y y.min=1.915 y.max=1.920
doping uniform conc=1.5e18 n.type direction=y y.min=1.930 y.max=1.935
doping uniform conc=3e18 n.type direction=y regions=23

$
$ SECTION 3: Material Model Specification
$
material taup0=2.e-6 taun0=2.e-6

```

```

models  srh auger conmob fldmob
impact selb
$
$ SECTION 4: Initial Solution
$
symb      Newton carr=2
method    comb trap autonr
solve     init
output    e.field j.electron e.velocity e.mobility h.mobility qss e.temp h.temp val.band con.band qfn qfp impact
recomb    tot.doping

save outf=nobiascent7s2b.out
log  outfile=MQWCV3j2b.log master
method itlimit=50 autonr nrcriterion=0.1 trap atrap=0.5 maxtrap=10

solve v1=0 v2=0 vstep=-0.1 vfinal=-10 elect=1 ac direct freq=1e6 vss=0.030 terminal=1
solve v1=-11 v2=0 vstep=-1 vfinal=-25 elect=1 ac direct freq=1e6 vss=0.030 terminal=1
save  outf=MQWcent725s2b.out
tonyplot MQWCV3j2b.log
end

```

B.3 Spectral Response Simulation of a PIN Structure

```

$Spectral response of PIN structure (p=i=n= 1 micron)
$ by Hicham Menkara
$input deck : PINspec2a.in
$
$ SECTION 1: Mesh Specification
$
$mesh space.mult=4.0
$
mesh rect smooth=4 diag.flip
x.mesh loc=0      s=75
x.mesh loc=75.0 s=75
y.mesh loc=0.0      s=0.01
y.mesh loc=0.96 s=0.01
y.mesh loc=0.97 s=0.004
y.mesh loc=1.05 s=0.01
y.mesh loc=2.08 s=0.004
y.mesh loc=2.09 s=0.4
y.mesh loc=3.05 s=0.4
$
$ SECTION 2: Structure Specification
$
region number=1 x.min=0 x.max=75 y.min=0 y.max=1.0 gaas
region number=2 x.min=0 x.max=75 y.min=1.0 y.max=2.05 gaas
region number=3 x.min=0 x.max=75 y.min=2.05 y.max=3.05 gaas

#
# #1=cathode #2=anode
electrode name=cathode number=1 top
electrode name=anode number=2 bottom

doping uniform conc=3e18 p.type direction=y regions=1
doping uniform conc=3e18 n.type direction=y regions=3
$

```

\$ SECTION 3: Material Model Specification

```
$
material material=AlGaAs taup0=2.e-8 taun0=1.e-9 copt=1.5e-10 augn=5e-30 augp=1e-31
impact      selber an1=1.899e5 an2=1.899e5 bn1=5.75e5 bn2=5.75e5 ap1=221500 ap2=221500 bp1=657000
bp2=657000 betan=1.82 betap=1.75 egran=0
```

```
models      material=GaAs srh auger conmob fldmob print
```

\$ SECTION 4: Optical source definition

```
$
beam        num=1 x.origin=37.5 y.origin=-1.0 angle=90.0 wavelength=.2 min.window=-9.0 max.window=9.0
```

\$ SECTION 5: Initial solution

```
$
symb        newton carr=0
solve       init
symb        newton carr=2
method      trap autonr climit=75000 ctolt.fact=500.0 maxtrap=10
solve       prev
output      e.field j.electron e.velocity e.mobility h.mobility qss e.temp h.temp val.band con.band qfn qfp impact
recomb tot.doping photogen traps flowlines ey.velocity ex.velocity hx.velocity hy.velocity u.auger u.srh u.radiative
solve       prev b1=1
save outf=PINspec2a0.out
```

\$ SECTION 6: spectral response

```
$
log          outf=PINspec2a.log
solve        prev b1=1 lambda=0.2
solve        prev b1=1 lambda=0.225
solve        prev b1=1 lambda=0.25
solve        prev b1=1 lambda=0.275
solve        prev b1=1 lambda=0.3
solve        prev b1=1 lambda=0.325
solve        prev b1=1 lambda=0.35
solve        prev b1=1 lambda=0.375
solve        prev b1=1 lambda=0.4
save outf=PINspec400.out
solve        prev b1=1 lambda=0.425
solve        prev b1=1 lambda=0.45
solve        prev b1=1 lambda=0.475
solve        prev b1=1 lambda=0.5
solve        prev b1=1 lambda=0.525
solve        prev b1=1 lambda=0.55
solve        prev b1=1 lambda=0.575
solve        prev b1=1 lambda=0.6
solve        prev b1=1 lambda=0.625
solve        prev b1=1 lambda=0.6325
save outf=PINspec632.out
solve        prev b1=1 lambda=0.65
solve        prev b1=1 lambda=0.675
solve        prev b1=1 lambda=0.7
solve        prev b1=1 lambda=0.725
solve        prev b1=1 lambda=0.75
solve        prev b1=1 lambda=0.775
solve        prev b1=1 lambda=0.8
solve        prev b1=1 lambda=0.825
```

```
solve    prev b1=1 lambda=0.85
save outf=PINspec850.out
solve    prev b1=1 lambda=0.865
solve    prev b1=1 lambda=0.875
solve    prev b1=1 lambda=0.885
solve    prev b1=1 lambda=0.9
solve    prev b1=1 lambda=0.91
solve    prev b1=1 lambda=0.9184
```

```
save outf=PINspec2a2.out
tonyplot PINspec2a.log
end
```

REFERENCES

- [1] F. Capasso, *Semiconductors and Semimetals*, edited by R. K. Willardson and A. C. Beer (Academic, New York, 1985), Vol. 22, part D, p.2
- [2] J. Gowar, *Optical Communication Systems*, Prentice/Hall, London, 1984
- [3] P. P. Webb, R.J. McIntyre, and J. Conradi, "Properties of avalanche photodiodes", *RCA Review* 35, 234 (1974).
- [4] S.M. Sze, *Physics of Semiconductor Devices*, 2nd ed., Wiley, 1981.
- [5] Y. Suematsu, K. Iga and K. Kishino, *GaInAsP Alloy Semiconductors*, Ch. 14, ed. T. Pearsall, Wiley, 1982.
- [6] W. T. Read, Jr., "A proposed high-frequency, negative resistance diode", *Bell System Technical Journal* 401, March, 1958.
- [7] J. C. Campbell, in "Optoelectronics Technology and Lightwave Communications Systems," edited by Chinlon Lin (1989), Ch. 14.
- [8] P. Aristin, "Fabrication et Caracterization de Photodiodes a Avalanche a Puits Quantiques Multiples", Ph.D. thesis, January 1992.
- [9] R. Chin, N. Holoniak, G. E. Stillman, J. Y. Tsang, and K. Hess, *Appl. Phys. Lett.* 16, 467 (1980).
- [10] F. Capasso, W. T. Tsang, A. L. Hutchinson, and P. G. Williams, *Appl. Phys. Lett.* 40, 38 (1982).
- [11] H. Blauvelt, S. Margalit, and A. Yariv, *Electron. Lett.* 18, 375 (1982).
- [12] J. D. Gordon, R. E. Nahory, M. A. Pollack, and J. M. Warlock, *Electron. Lett.* 15, 518 (1979).

- [13] F. Capasso, W. T. Tsang, A. L. Hutchinson, and P. W. Foy, Conf. Ser. - Inst. Phys., 63, 473 (1982).
- [14] R. Chin, N. Jr. Holonyak, G. E. Stillman, J. T. Tang, and K. Hess, Electron. Lett. 16, 467 (1980).
- [15] F. Capasso, W. T. Tsang, A. L. Hutchinson, and G. F. Williams, Tach. Dig.-Inst. Electron Devices Meet., 1981, Washington, DC, 284 (1981)
- [16] F. Capasso, W. T. Tsang, and G. F. Williams, IEEE Trans. Electron Dev. ED-30, 381 (1983)
- [17] H. Blauvelt, S. Margalit, and A. Yariv, Electron. Lett. 18, 375 (1982)
- [18] K. Brennan, IEEE Trans. Electron Dev. ED-34, 1658 (1987)
- [19] K. Brennan, K. Hess, F. Capasso, Appl. Phys. Lett. 50, 1897 (1987)
- [20] S.M. Sze, "Physics of Semiconductor Devices", Wiley, 1981.
- [21] D.J. Roulson, N.D. Arora, and S.G. Chamberlain, "Modeling and Measurement of Minority-Carrier Lifetime versus Doping in Diffused Layers of n^+ -p Silicon Diodes", IEEE Trans. on Electron Devices, ED-29, pp. 284-291. Feb., 1982.
- [22] S. Selberherr, "Analysis and Simulation of Semiconductor Devices", Springer-Verlag, Wien-New York. 1984.
- [23] L.J. Shiff, "Quantum Mechanics", 2nd ed., McGraw-Hill, New York, 1955.
- [24] J.L. Moll, "Physics of Semiconductors", McGraw-Hill, New York, 1964.
- [25] G.W. Neudeck, R.F. Pierret, "Modular Series on Solid State Devices: The PN Junction Diode", Vol.II, Addison-Wesley, 1983.
- [26] Silvaco International, ATLAS User's Manual, Device Simulation Software, version 4.0, June 1995.
- [27] J.W. Slotboom, "The PN Product in Silicon", Solid State Electronics 20, pp. 279-283. 1977.
- [28] K. Brennan, IEEE J. Quantum Electron., QE-22, 1999 (1986)
- [29] F. Capasso, R. E. Nahory, M. A. Pollack, and T. P. Pearsall, Phys. Rev. Lett. 39, 723 (1977)

- [30] R. Chin, N. Holonyak, Jr., G. E. Stillman, J. Y. Tang, and K. Hess, *Electron. Lett.* 16, 467 (1980)
- [31] N. Yamamoto, K. Yokoyama, and M. Yamamoto, *Appl. Phys. Lett.* 62, 252 (1993).
- [32] S. M. Sze, *Physics of Semiconductor Devices*, 2nd ed. (Wiley, New York, 1981), Chap. 2, p. 77.
- [33] R. U. Martinelli, T. J. Zamerowski, and P. Longway, *Appl. Phys. Lett.*, vol. 53, no. 11, p. 989, 1988.
- [34] K. R. Linga, G. H. Olsen, V. S. Ban, A. M. Joshi, and W. F. Kosonocky, *Journal of Lightwave Technology*, Vol. 10, no. 8, August 1992.
- [35] R. J. McIntyre, *IEEE Trans. Electron Devices* 13, 164 (1966).
- [36] M. Teich, K. Matsuo, and B. Saleh, *IEEE J. Quantum Electron.*, QE-22, No 8, 1184 (1986)
- [37] N. Hakim, B. Saleh, M. Teich, *IEEE Trans. Electron Devices*, vol. 37, No. 3, 599 (1990)
- [38] J. S. Marsland, *J. Appl. Phys.* 67, 1929 (1990)
- [39] J. S. Marsland, R. C. Woods, and C. A. Brownhill, *IEEE Trans. Electron Devices*, ED-39, 1129 (1992)
- [40] M. M. Hayat, B. E. Saleh, M. C. Teich, *IEEE Trans. Electron Devices*, ED-39, 546 (1992)
- [41] P. Aristin, A. Torabi, A.K. Garrison, H.M. Harris, and C.J. Summers, *Appl. Phys. Letters* 60, 85 (1992).
- [42] D.C. Reynolds, G. Leies, L. Antes, and R.E. Marburger, "Photovoltaic Effect in Cadmium Sulfide," *Phys. Rev.*, 96, 533 (1954)
- [43] S.M. Sze, "Physics of Semiconductor Devices", Wiley, 1981.
- [44] P. Aristin, "Fabrication et Caracterization de Photodiodes a Avalanche a Puits Quantiques Multiples", Ph.D. thesis, January 1992.
- [45] S.R. Forrest, R.G. Smith, and O.K. Kim, *IEEE J. Quantum Electron.* QE-18 (1982) 2040.

- [46] R. Kuvas and C. A. Lee, *J. Appl. Phys.*, 41, 1743 (1970)
- [47] J. N. Hollenhorst, *IEEE J. Lightwave Technology*, LT-8, 531 (1990)
- [48] B. C. Roy, and N. N. Chakrabarti, *IEEE J. Lightwave Technology*, LT-10, 169 (1992)
- [49] S.R. Forrest, and O.K. Kim, "Solid State Electronics", 26, 10, pp. 961-962 (1983)
- [50] M.S. Tyagi, "Solid State Electronics", 11, 99 (1968)
- [51] S.R. Forrest, and O.K. Kim, "Solid State Electronics", 26, 10, pp. 958-959 (1983)
- [52] M.J.O. Strutt, "Semiconductor Devices", Vol. 1, Semiconductor and Semiconductor Diodes, Academic, New York, 1966, Chap. 2.
- [53] Silvaco International, "Atlas II User's Manual", 1st Edition, July 1, 1993.
- [54] S. Selberherr, "Analysis and Simulation of Semiconductor Devices", Springer-Verlag, Wien-New York. 1984.
- [55] N. Yamamoto, K. Yokoyama, and M. Yamamoto, *Appl. Phys. Lett.* 62, 252 (1993).
- [56] G.A.M. Hurx, H.C. de Graaf, W.J. Klosterman, et. al., "A Novel Compact Model Description of Reverse Biase Diode Characteristics including Tunneling", ESSDERC, pp. 49-52, 1990.
- [57] D.B.M. Klaassen, "Physical Modeling for Bipolar Device Simulation", In: *Simulation of Semiconductor Devices and Processes*, Edited by W. Fichtner and D. Aemmer, Harting-Gorre, 1991, Vol. 4, pp. 23-43.
- [58] M. Klausmeier-Brown, M. Lundstrom, M. Melloch, "The Effects of Heavy Impurity Doping on AlGaAs/GaAs Bipolar Transistors", *IEEE Trans.*, ED-36, No. 10, pp. 2146-2155, 1989.

VITA

Hicham Menkara was born in Lebanon on August 31, 1968. He received his Bachelor degree (Magna Cum Laude) in Engineering Physics from the University of Toledo, Ohio in 1989. He then joined the Georgia Institute of Technology where he received an M.S. in Physics in 1990 and an M.S. in Electrical Engineering in 1993. He expects to receive an M.S. in Management from Georgia Tech in September 1996.

REFERENCES

-
- [1] F. Capasso, Semiconductors and Semimetals, edited by R. K. Willardson and A. C. Beer (Academic, New York, 1985), Vol. 22, part D, p.2
 - [2] J. Gowar, Optical Communication Systems, Prentice/Hall, London, 1984
 - [3] P. P. Webb, R.J. McIntyre, and J. Conradi, "Properties of avalanche photodiodes", RCA Review 35, 234 (1974).
 - [4] S.M. Sze, Physics of Semiconductor Devices, 2nd ed., Wiley, 1981.
 - [5] Y. Suematsu, K. Iga and K. Kishino, GaInAsP Alloy Semiconductors, Ch. 14, ed. T. Pearsall, Wiley, 1982.
 - [6] W. T. Read, Jr., "A proposed high-frequency, negative resistance diode", Bell System Technical Journal 401, March, 1958.
 - [7] J. C. Campbell, in "Optoelectronics Technology and Lightwave Communications Systems," edited by Chinlon Lin (1989), Ch. 14.
 - [8] P. Aristin, "Fabrication et Caracterization de Photodiodes a Avalanche a Puits Quantiques Multiples", Ph.D. thesis, January 1992.
 - [9] R. Chin, N. Holoniak, G. E. Stillman, J. Y. Tsang, and K. Hess, Appl. Phys. Lett. 16, 467 (1980).
 - [10] F. Capasso, W. T. Tsang, A. L. Hutchinson, and P. G. Williams, Appl. Phys. Lett. 40, 38 (1982).
 - [11] H. Blauvelt, S. Margalit, and A. Yariv, Electron. Lett. 18, 375 (1982).
 - [12] J. D. Gordon, R. E. Nahory, M. A. Pollack, and J. M. Warlock, Electron. Lett. 15, 518 (1979).
 - [13] F. Capasso, W. T. Tsang, A. L. Hutchinson, and P. W. Foy, Conf. Ser. - Inst. Phys., 63, 473 (1982).
 - [14] R. Chin, N. Jr. Holonyak, G. E. Stillman, J. T. Tang, and K. Hess, Electron. Lett. 16, 467 (1980).
 - [15] F. Capasso, W. T. Tsang, A. L. Hutchinson, and G. F. Williams, Tach. Dig.-Inst. Electron Devices Meet., 1981, Washington, DC, 284 (1981)

-
- [16] F. Capasso, W. T. Tsang, and G. F. Williams, IEEE Trans. Electron Dev. ED-30, 381 (1983)
- [17] H. Blauvelt, S. Margalit, and A. Yariv, Electron. Lett. 18, 375 (1982)
- [18] K. Brennan, IEEE Trans. Electron Dev. ED-34, 1658 (1987)
- [19] K. Brennan, K. Hess, F. Capasso, Appl. Phys. Lett. 50, 1897 (1987)
- [20] S.M. Sze, "Physics of Semiconductor Devices", Wiley, 1981.
- [21] D.J. Roulson, N.D. Arora, and S.G. Chamberlain, "Modeling and Measurement of Minority-Carrier Lifetime versus Doping in Diffused Layers of n^+ -p Silicon Diodes", IEEE Trans. on Electron Devices, ED-29, pp. 284-291. Feb., 1982.
- [22] S. Selberherr, "Analysis and Simulation of Semiconductor Devices", Springer-Verlag, Wien-New York. 1984.
- [23] L.J. Shiff, "Quantum Mechanics", 2nd ed., McGraw-Hill, New York, 1955.
- [24] J.L. Moll, "Physics of Semiconductors", McGraw-Hill, New York, 1964.
- [25] G.W. Neudeck, R.F. Pierret, "Modular Series on Solid State Devices: The PN Junction Diode", Vol.II, Addison-Wesley, 1983.
- [26] Silvaco International, ATLAS User's Manual, Device Simulation Software, version 4.0, June 1995.
- [27] J.W. Slotboom, "The PN Product in Silicon", Solid State Electronics 20, pp. 279-283. 1977.
- [28] K. Brennan, IEEE J. Quantum Electron., QE-22, 1999 (1986)
- [29] F. Capasso, R. E. Nahory, M. A. Pollack, and T. P. Pearsall, Phys. Rev. Lett. 39, 723 (1977)
- [30] R. Chin, N. Holonyak, Jr., G. E. Stillman, J. Y. Tang, and K. Hess, Electron. Lett. 16, 467 (1980)
- [31] N. Yamamoto, K. Yokoyama, and M. Yamamoto, Appl. Phys. Lett. 62, 252 (1993).

-
- [32] S. M. Sze, *Physics of Semiconductor Devices*, 2nd ed. (Wiley, New York, 1981), Chap. 2, p. 77.
- [33] R. U. Martinelli, T. J. Zamerowski, and P. Longway, *Appl. Phys. Lett.*, vol. 53, no. 11, p. 989, 1988.
- [34] K. R. Linga, G. H. Olsen, V. S. Ban, A. M. Joshi, and W. F. Kosonocky, *Journal of Lightwave Technology*, Vol. 10, no. 8, August 1992.
- [35] R. J. McIntyre, *IEEE Trans. Electron Devices* 13, 164 (1966).
- [36] M. Teich, K. Matsuo, and B. Saleh, *IEEE J. Quantum Electron.*, QE-22, No 8, 1184 (1986)
- [37] N. Hakim, B. Saleh, M. Teich, *IEEE Trans. Electron Devices*, vol. 37, No. 3, 599 (1990)
- [38] J. S. Marsland, *J. Appl. Phys.* 67, 1929 (1990)
- [39] J. S. Marsland, R. C. Woods, and C. A. Brownhill, *IEEE Trans. Electron Devices*, ED-39, 1129 (1992)
- [40] M. M. Hayat, B. E. Saleh, M. C. Teich, *IEEE Trans. Electron Devices*, ED-39, 546 (1992)
- [41] P. Aristin, A. Torabi, A.K. Garrison, H.M. Harris, and C.J. Summers, *Appl. Phys. Letters* 60, 85 (1992).
- [42] D.C. Raynolds, G. Leies, L. Antes, and R.E. Marburger, "Photovoltaic Effect in Cadmium Sulfide," *Phys. Rev.*, 96, 533 (1954)
- [43] S.M. Sze, *"Physics of Semiconductor Devices"*, Wiley, 1981.
- [44] P. Aristin, "Fabrication et Caracterization de Photodiodes a Avalanche a Puits Quantiques Multiples", Ph.D. thesis, January 1992.
- [45] S.R. Forrest, R.G. Smith, and O.K. Kim, *IEEE J. Quantum Electron.* QE-18 (1982) 2040.
- [46] R. Kuvas and C. A. Lee, *J. Appl. Phys.*, 41, 1743 (1970)

-
- [47] J. N. Hollenhorst, *IEEE J. Lightwave Technology*, LT-8, 531 (1990)
 - [48] B. C. Roy, and N. N. Chakrabarti, *IEEE J. Lightwave Technology*, LT-10, 169 (1992)
 - [49] S.R. Forrest, and O.K. Kim, "Solid State Electronics", 26, 10, pp. 961-962 (1983)
 - [50] M.S. Tyagi, "Solid State Electronics", 11, 99 (1968)
 - [51] S.R. Forrest, and O.K. Kim, "Solid State Electronics", 26, 10, pp. 958-959 (1983)
 - [52] M.J.O. Strutt, "Semiconductor Devices", Vol. 1, Semiconductor and Semiconductor Diodes, Academic, New York, 1966, Chap. 2.
 - [53] Silvaco International, "Atlas II User's Manual", 1st Edition, July 1, 1993.
 - [54] S. Selberherr, "Analysis and Simulation of Semiconductor Devices", Springer-Verlag, Wien-New York. 1984.
 - [55] N. Yamamoto, K. Yokoyama, and M. Yamamoto, *Appl. Phys. Lett.* 62, 252 (1993).
 - [56] G.A.M. Hurx, H.C. de Graaf, W.J. Klosterman, et. al., "A Novel Compact Model Description of Reverse Biase Diode Characteristics including Tunneling", ESSDERC, pp. 49-52, 1990.
 - [57] D.B.M. Klaassen, "Physical Modeling for Bipolar Device Simulation", In: *Simulation of Semiconductor Devices and Processes*, Edited by W. Fichtner and D. Aemmer, Harting-Gorre, 1991, Vol. 4, pp. 23-43.
 - [58] M. Klausmeier-Brown, M. Lundstrom, M. Melloch, "The Effects of Heavy Impurity Doping on AlGaAs/GaAs Bipolar Transistors", *IEEE Trans.*, ED-36, No. 10, pp. 2146-2155, 1989.

APPENDIX B

SAMPLE SIMULATION ALGORITHMS

B.1 Light IV Simulation of a PIN Structure

\$ GaAs pin Simulation under Light (p=i=n=1 micron)

\$by: Hicham Menkara

\$ input deck : pin_bias6_lite.in

\$

\$ SECTION 1: Mesh specification

\$

mesh nx=3 ny=100 smooth=1 diag.flip space.mult=1.0 master.out

\$

\$mesh rect nx=3 ny=400 smooth=4 diag.flip

x.mesh n=1 loc=0 r=1

x.mesh n=3 loc=75.0 r=1

y.mesh n=1 loc=0.0

y.mesh n=8 loc=0.96

\$y.mesh n=45 loc=1.2

y.mesh n=50 loc=1.5

\$y.mesh n=255 loc=3.3

y.mesh n=92 loc=2.04

y.mesh n=100 loc=3

\$ SECTION 2: Structure Specification

\$

region num=1 GaAs y.max=1

region num=2 GaAs y.min=1 y.max=2

region num=3 GaAs y.min=2 y.max=3

\$

elec num=1 x.min=0 x.max=75 y.max=0.0

elec num=2 bot

contact num=1 con.resist=1e4

contact num=2 con.resist=1e4

\$

doping region=1 uniform p.type conc=3e18

doping region=3 uniform n.type conc=3e18

\$

\$ SECTION 3: Material model specification

\$

material material=GaAs taup0=1.e-9 taun0=1.e-9

impact material=GaAs selb

models material=GaAs srh auger conmob fldmob print

\$

\$ SECTION 4: Optical source definition

\$

beam num=1 x.origin=37.5 y.origin=-1.0 angle=90.0 wavelength=.6328 min.window=-9.0 max.window=9.0

\$

\$ SECTION 5: Initial solution

\$

symb newton carr=0

solve init

symb newton carr=2

method trap autonr climitt=75000 ctolt.fact=500.0 maxtrap=6

solve prev

\$plot.2d x.min=0 x.max=75 y.min=0 y.max=3 grid depl.edge

\$plot.1d e.field a.x=37.5 b.x=37.5 a.y=0 b.y=5 points

solve b1=0.001

output e.field j.electron e.velocity e.mobility h.mobility qss e.temp h.temp val.band con.band qfn qfp impact

recomb tot.doping photogen flowlines u.auger u.radiative u.srh

save outf=pin_nobias_lite7.out

\$

\$ SECTION 6: Voltage ramp

\$

log outf=pin_IV_lite7.log master

solve prev v1=0.0 vstep=-2 vfinal=-10 elect=1

solve project v1=-12 vstep=-2 vfinal=-35 elect=1

plot.1d alphan a.x=37.5 b.x=37.5 a.y=0 b.y=5 points outfile=eionl35.dat ascii

plot.1d alphap a.x=37.5 b.x=37.5 a.y=0 b.y=5 points outfile=hionl35.dat ascii

save outf=pin_bias35_lite7.out

solve project v1=-35.2 vstep=-0.1 vfinal=-37.5 elect=1 master

solve project v1=-37.6 vstep=-0.1 vfinal=-45 elect=1 master

plot.1d alphan a.x=37.5 b.x=37.5 a.y=0 b.y=5 points outfile=eionl38.dat ascii

plot.1d alphap a.x=37.5 b.x=37.5 a.y=0 b.y=5 points outfile=hionl38.dat ascii

save outf=pin_bias38_lite6.out

tonyplot pin_IV_lite6.log

\$

end

B.2 CV Simulation of a doped-well MQW Structure

\$ Doped MQW CV simulation example (10 barriers, 9 wells)

\$ by Hicham Menkara

\$ input deck : MQWCV7s2b.in

\$

\$ SECTION 1: Mesh Specification

\$

\$mesh space.mult=4.0

\$

mesh rect smooth=4 diag.flip

x.mesh loc=0 s=75

x.mesh loc=75.0 s=75

y.mesh loc=0.0 s=0.4

y.mesh loc=0.96 s=0.4

y.mesh loc=0.97 s=0.0024

y.mesh loc=1.525 s=0.0024

y.mesh loc=2.08 s=0.0024

y.mesh loc=2.09 s=0.4

y.mesh loc=3.05 s=0.4

\$

\$ SECTION 2: Structure Specification

\$

region number=1 x.min=0 x.max=75 y.min=0 y.max=1.0 gaas
region number=2 x.min=0 x.max=75 y.min=1.0 y.max=1.05 gaas
region number=3 x.min=0 x.max=75 y.min=1.05 y.max=1.1 material=AlGaAs x.composition=0.42
region number=4 x.min=0 x.max=75 y.min=1.1 y.max=1.15 gaas
region number=5 x.min=0 x.max=75 y.min=1.15 y.max=1.2 material=AlGaAs x.composition=0.42
region number=6 x.min=0 x.max=75 y.min=1.2 y.max=1.25 gaas
region number=7 x.min=0 x.max=75 y.min=1.25 y.max=1.3 material=AlGaAs x.composition=0.42
region number=8 x.min=0 x.max=75 y.min=1.3 y.max=1.35 gaas
region number=9 x.min=0 x.max=75 y.min=1.35 y.max=1.4 material=AlGaAs x.composition=0.42
region number=10 x.min=0 x.max=75 y.min=1.4 y.max=1.45 gaas
region number=11 x.min=0 x.max=75 y.min=1.45 y.max=1.5 material=AlGaAs x.composition=0.42
region number=12 x.min=0 x.max=75 y.min=1.5 y.max=1.55 gaas
region number=13 x.min=0 x.max=75 y.min=1.55 y.max=1.6 material=AlGaAs x.composition=0.42
region number=14 x.min=0 x.max=75 y.min=1.6 y.max=1.65 gaas
region number=15 x.min=0 x.max=75 y.min=1.65 y.max=1.7 material=AlGaAs x.composition=0.42
region number=16 x.min=0 x.max=75 y.min=1.7 y.max=1.75 gaas
region number=17 x.min=0 x.max=75 y.min=1.75 y.max=1.8 material=AlGaAs x.composition=0.42
region number=18 x.min=0 x.max=75 y.min=1.8 y.max=1.85 gaas
region number=19 x.min=0 x.max=75 y.min=1.85 y.max=1.9 material=AlGaAs x.composition=0.42
region number=20 x.min=0 x.max=75 y.min=1.9 y.max=1.95 gaas
region number=21 x.min=0 x.max=75 y.min=1.95 y.max=2.0 material=AlGaAs x.composition=0.42
region number=22 x.min=0 x.max=75 y.min=2.0 y.max=2.05 gaas
region number=23 x.min=0 x.max=75 y.min=2.05 y.max=3.05 gaas

#

#1=cathode #2=anode

electrode name=cathode number=1 top

electrode name=anode number=2 bottom

#

doping uniform conc=3e18 p.type direction=y regions=1
doping uniform conc=1.5e18 p.type direction=y y.min=1.115 y.max=1.120
doping uniform conc=1.5e18 n.type direction=y y.min=1.130 y.max=1.135
doping uniform conc=1.5e18 p.type direction=y y.min=1.215 y.max=1.220
doping uniform conc=1.5e18 n.type direction=y y.min=1.230 y.max=1.235
doping uniform conc=1.5e18 p.type direction=y y.min=1.315 y.max=1.320
doping uniform conc=1.5e18 n.type direction=y y.min=1.330 y.max=1.335
doping uniform conc=1.5e18 p.type direction=y y.min=1.415 y.max=1.420
doping uniform conc=1.5e18 n.type direction=y y.min=1.430 y.max=1.435
doping uniform conc=1.5e18 p.type direction=y y.min=1.515 y.max=1.520
doping uniform conc=1.5e18 n.type direction=y y.min=1.530 y.max=1.535
doping uniform conc=1.5e18 p.type direction=y y.min=1.615 y.max=1.620
doping uniform conc=1.5e18 n.type direction=y y.min=1.630 y.max=1.635
doping uniform conc=1.5e18 p.type direction=y y.min=1.715 y.max=1.720
doping uniform conc=1.5e18 n.type direction=y y.min=1.730 y.max=1.735
doping uniform conc=1.5e18 p.type direction=y y.min=1.815 y.max=1.820
doping uniform conc=1.5e18 n.type direction=y y.min=1.830 y.max=1.835
doping uniform conc=1.5e18 p.type direction=y y.min=1.915 y.max=1.920
doping uniform conc=1.5e18 n.type direction=y y.min=1.930 y.max=1.935
doping uniform conc=3e18 n.type direction=y regions=23

```

$
$ SECTION 3: Material Model Specification
$
material taup0=2.e-6 taun0=2.e-6
models srh auger conmob fldmob
impact selb
$
$ SECTION 4: Initial Solution
$
symb      Newton carr=2
method    comb trap autonr
solve     init
output    e.field j.electron e.velocity e.mobility h.mobility qss e.temp h.temp val.band con.band qfn qfp impact
recomb    tot.doping

save outf=nobiascent7s2b.out
log  outfile=MQWCV3j2b.log master
method itlimit=50 autonr nrcriterion=0.1 trap atrap=0.5 maxtrap=10

solve v1=0 v2=0 vstep=-0.1 vfinal=-10 elect=1 ac direct freq=1e6 vss=0.030 terminal=1
solve v1=-11 v2=0 vstep=-1 vfinal=-25 elect=1 ac direct freq=1e6 vss=0.030 terminal=1
save  outf=MQWcent725s2b.out
tonyplot MQWCV3j2b.log
end

```

B.3 Spectral Response Simulation of a PIN Structure

```

$Spectral response of PIN structure (p=i=n= 1 micron)
$ by Hicham Menkara
$input deck : PINspec2a.in
$
$ SECTION 1: Mesh Specification
$
$mesh space.mult=4.0
$
mesh rect smooth=4 diag.flip
x.mesh loc=0      s=75
x.mesh loc=75.0 s=75
y.mesh loc=0.0      s=0.01
y.mesh loc=0.96 s=0.01
y.mesh loc=0.97 s=0.004
y.mesh loc=1.05 s=0.01
y.mesh loc=2.08 s=0.004
y.mesh loc=2.09 s=0.4
y.mesh loc=3.05 s=0.4
$
$ SECTION 2: Structure Specification
$
region number=1 x.min=0 x.max=75 y.min=0 y.max=1.0 gaas
region number=2 x.min=0 x.max=75 y.min=1.0 y.max=2.05 gaas
region number=3 x.min=0 x.max=75 y.min=2.05 y.max=3.05 gaas

#

```

```

# #1=cathode #2=anode
electrode name=cathode number=1 top
electrode name=anode number=2 bottom

doping uniform conc=3e18 p.type direction=y regions=1
doping uniform conc=3e18 n.type direction=y regions=3
$
$ SECTION 3: Material Model Specification
$
material material=AlGaAs taup0=2.e-8 taun0=1.e-9 copt=1.5e-10 augn=5e-30 augp=1e-31
impact selber an1=1.899e5 an2=1.899e5 bn1=5.75e5 bn2=5.75e5 ap1=221500 ap2=221500 bp1=657000
bp2=657000 betan=1.82 betap=1.75 egran=0

models material=GaAs srh auger conmob fldmob print
$
$ SECTION 4: Optical source definition
$
beam num=1 x.origin=37.5 y.origin=-1.0 angle=90.0 wavelength=.2 min.window=-9.0 max.window=9.0
$
$ SECTION 5: Initial solution
$
symb newton carr=0
solve init
symb newton carr=2
method trap autonr climt=75000 ctolt.fact=500.0 maxtrap=10
solve prev
output e.field j.electron e.velocity e.mobility h.mobility qss e.temp h.temp val.band con.band qfn qfp impact
recomb tot.doping photogen traps flowlines ey.velocity ex.velocity hx.velocity hy.velocity u.auger u.srh u.radiative
solve prev b1=1
save outf=PINspec2a0.out
$
$ SECTION 6: spectral response
$
log outf=PINspec2a.log
solve prev b1=1 lambda=0.2
solve prev b1=1 lambda=0.225
solve prev b1=1 lambda=0.25
solve prev b1=1 lambda=0.275
solve prev b1=1 lambda=0.3
solve prev b1=1 lambda=0.325
solve prev b1=1 lambda=0.35
solve prev b1=1 lambda=0.375
solve prev b1=1 lambda=0.4
save outf=PINspec400.out
solve prev b1=1 lambda=0.425
solve prev b1=1 lambda=0.45
solve prev b1=1 lambda=0.475
solve prev b1=1 lambda=0.5
solve prev b1=1 lambda=0.525
solve prev b1=1 lambda=0.55
solve prev b1=1 lambda=0.575
solve prev b1=1 lambda=0.6
solve prev b1=1 lambda=0.625

```

```
solve    prev b1=1 lambda=0.6325
save outf=PINspec632.out
solve    prev b1=1 lambda=0.65
solve    prev b1=1 lambda=0.675
solve    prev b1=1 lambda=0.7
solve    prev b1=1 lambda=0.725
solve    prev b1=1 lambda=0.75
solve    prev b1=1 lambda=0.775
solve    prev b1=1 lambda=0.8
solve    prev b1=1 lambda=0.825
solve    prev b1=1 lambda=0.85
save outf=PINspec850.out
solve    prev b1=1 lambda=0.865
solve    prev b1=1 lambda=0.875
solve    prev b1=1 lambda=0.885
solve    prev b1=1 lambda=0.9
solve    prev b1=1 lambda=0.91
solve    prev b1=1 lambda=0.9184

save outf=PINspec2a2.out
tonyplot PINspec2a.log
end
```

CHAPTER VI

CONCLUSIONS

Throughout this work, a detailed comparison of the gain and noise characteristics of a conventional and a doped well MQW APD was presented. The data obtained demonstrated a direct experimental evidence of structure induced preferential multiplication of electrons over holes. For the doped MQW APDs, the average gain per stage was calculated by comparing gain data with carrier profile measurements, and was found to vary from 1.03 at low bias to 1.09 near avalanche breakdown. This is in contrast to conventional p-i-n structures which show no gain in this regime. It was also shown that, as the bias was increased, the effect of the structure became less pronounced, and the MQW device was reduced to a conventional pin structure. Similar studies of the bias dependence of the excess noise characteristics show that the low-voltage gain is primarily due to electron ionization in the MQW APDs, and to both electron and hole ionization in the p-i-n APDs. Our measurements of the doped MQW APD clearly showed that for low gains ($M < 6$), the ionization ratio is greatly enhanced ($k = \alpha/\beta = 10 - 50$) as compared to that in bulk GaAs ($k = 1.67$). At higher voltages, however, the value of k is reduced since

the holes gain more energy from the applied electric field and are more likely to impact ionize.

We've also observed the significant effect of mesa surface recombination processes on the dark current behavior of an APD. The resulting leakage currents can have dramatic consequences on the sensitivities and attainable gain levels in a photodiode. As a result of surface treatment, dark currents at low bias were reduced to as low as 1 pA. The result of this reduction in dark current was manifested in the structures' high gain performance which exceeded 10,000 in some APDs. By being able to reduce the dark currents, it was possible to maintain dark current levels well below those of the photocurrents. This made it possible to achieve and sustain high levels of gains well beyond the onset of junction breakdown.

The spectral response and quantum efficiencies for some of the structures were also calculated and modeled. The experimental data were very consistent with the theoretical models. The quantum efficiencies of the fabricated structures were relatively low because of the losses of photogenerated carriers due to recombination mechanisms in the diffusion layer. It was shown how it was theoretically possible to significantly increase the quantum efficiency of the devices through the introduction of a heavily doped p^{++} GaAs top layer. Such layers help create a high-field region that will enhance the diffusion of photogenerated electrons toward the depletion region.

We have also made a full investigation of the impact of doping imbalance in doped-well MQW APDs on the devices' IV and CV characteristics and how such an imbalance would affect the depletion properties of the APDs. Our theoretical models were

in full agreement with the observed experimental data and have helped us develop a good understanding of some of the physical processes that take place inside a doped MQW APD. Our simplistic models have enabled us to easily interpret experimental IV and CV data and determine the extent of depletion in our APD devices. We've also determined how these parameters are affected by the p- and n-doping imbalance in the structure. The model predicted that a doping mismatch as small as 10% can reduce the depletion layer by as much as 50%. It was also shown how a large doping imbalance would cause the device to quickly reach avalanche breakdown in the depleted layers and would prevent full depletion.

The presence of undepleted regions was also shown to be one of the major causes of poor time response performance in avalanche photodiodes. Partial depletion gave rise to diffusion-limited transient response in doped MQW structures. This was demonstrated experimentally to be the case by examining the change in the "diffusion tails" of the output pulse response of the devices as a function of applied bias. Fully depleted PIN structures showed fast time response even at zero bias. Doped MQW APDs showed a decrease in the FWHM and fall time in direct proportion to the increase in the depletion region of the structure.

VITA

Hicham Menkara was born in Lebanon on August 31, 1968. He received his Bachelor degree (Magna Cum Laude) in Engineering Physics from the University of Toledo, Ohio in 1989. He then joined the Georgia Institute of Technology where he received an M.S. in

Physics in 1990 and an M.S. in Electrical Engineering in 1993. He expects to receive an M.S. in Management from Georgia Tech in September 1996.

PUBLICATIONS :

- [1] Menkara, H. M., Wagner, B. K., Summers, C. J., "Gain properties of doped GaAs/AlGaAs multiple quantum well avalanche photodiode structures", *Appl. Phys. Lett.*, Vol. 66, no. 14, pp. 1764-1766 April 1995.
- [2] Yun, I., Menkara, H. M., Wang, Y., Oguzman, I. H., Kolnik, J., Brennan, K.F., May, G. S., Summers, C. J., Wagner, B. K., "Reliability assessment of multiple quantum well avalanche photodiodes", *1995 IEEE International Reliability Physics Proceedings*. 33rd Annual, p. 200-204.

[3] Menkara, H. M., Wagner, B. K., Summers, C. J., "Effect of variations in the doping profiles on the properties of doped multiple quantum well avalanche photodiodes", to be published in *Optical Materials*.

[4] Yun, I., Menkara, H. M., Wang, Y., Oguzman, I. H., Kolnik, J., Brennan, K.F., May, G. S., Summers, C. J., Wagner, B. K., "The effect of manufacturing process sequence on the reliability of GaAs multiple quantum well avalanche photodiodes", to be published.

PRESENTATION :

[1] Menkara, H. M., Wagner, B. K., Summers, C. J.
Effect of variations in the doping profiles on the properties of doped multiple quantum well avalanche photodiodes. First International Workshop on Materials for Optoelectronics, Sheffield Hallam University, Sheffield, U.K, August 1995.

APPENDIX A

$\text{Al}_x\text{Ga}_{1-x}\text{As}$ Material System Parameters

GaAs/AlGaAs materials are frequently used in the fabrication of heterojunction devices. The parameters for GaAs can, in general, be derived from those for $\text{Al}_x\text{Ga}_{1-x}\text{As}$ by setting the value of x to zero. In the following few sections, the various optical and electrical parameters relevant to GaAs/AlGaAs structures modeling will be presented.

A.1 AlGaAs Band Parameters

The net material bandgap is chosen as the minimum value of the various default bandgap valleys in AlGaAs given by the following equations :

$$E_g(\text{G}) = E_{g0} + x(1.155 + 0.37 x) \quad [\text{A- 1}]$$

$$E_g(\text{L}) = 1.734 + x(0.574 + 0.055 x) \quad [\text{A- 2}]$$

$$E_g(\text{X}) = 1.911 + x(0.005 + 0.245 x) \quad [\text{A- 3}]$$

The temperature dependence of the bandgap is introduced through the E_{g0} parameter calculated from the following equation^{1,2}:

$$E_g(T) = E_g(0) - \frac{\alpha T^2}{T + \beta} = E_g(300) + \alpha \left[\frac{300^2}{300 + \beta} - \frac{T^2}{T + \beta} \right] \quad [\text{A- 4}]$$

where,

$$E_g(0) = 1.519 \text{ eV}$$

$$\alpha = 5.405 \times 10^{-4} \text{ eV/K}$$

$$\beta = 204.0 \text{ K}$$

The AlGaAs electron affinity for a given x value can be calculated from:

$$\chi = 4.07 - 0.85(E_g(G) - E_g(GaAs)) \quad [A- 5]$$

and the density of states mass of the valence band is given by:

$$m_v = (0.082^{3/2} + 0.45^{3/2})^{2/3} \quad [A- 6]$$

A.2 AlGaAs Dielectric Properties

The default value for the static dielectric constant for AlGaAs is given as a function of x by:

$$\epsilon' = 13.18 + 2.9 x \quad [A- 7]$$

In the case of GaAs, $x=0$, and $\epsilon' = \epsilon_{GaAs} / \epsilon_0 = 13.18$.

A.3 AlGaAs Bandgap Narrowing

Heavy doping of materials usually lead to bandgap narrowing which has an important effect on heterojunction characteristics. According to Lundstrom³, the bandgap narrowing effects are important only for p-type regions. The default bandgap narrowing parameters are shown in Table 1 for AlGaAs material:

Concentration cm ⁻³	Bandgap Narrowing meV
1.0E18	31.0
2.0E18	36.0
4.0E18	44.2
6.0E18	48.5
8.0E18	51.7
1.0E19	54.3
2.0E19	61.1
4.0E19	64.4
6.0E19	61.9
8.0E19	56.9
1.0E20	53.2
2.0E20	18.0

Table A-1: Default bandgap narrowing values

A.4 AlGaAs Recombination Parameters

The default parameters used for the various recombination mechanisms parameters are shown in Table A- 2 :

Parameter	Value	Equation
τ_{n0}	1.0×10^{-9}	[2-19]
τ_{p0}	2.0×10^{-8}	[2-20]
C_{opt}	1.5×10^{-10}	[2-18]
c_n	5.0×10^{-30}	[2-17]
c_p	1.0×10^{-31}	[2-17]

Table A- 2: Default Recombination Parameters for AlGaAs

A.5 GaAs Impact Ionization Coefficients

The coefficients used in the impact ionization model described by equations [2-21]-[2-23] are provided in Table A- 3.

Symbol	Value
α_n^∞	1.899×10^5
E_n^{crit}	5.75×10^5
β_n	1.82
α_p^∞	2.215×10^5
E_p^{crit}	6.57×10^5
β_p	1.75

Table A- 3: Impact Ionization Coefficients for GaAs

A.5 AlGaAs Mobility Parameters

The default low-field electron mobility for various ranges of $\text{Al}_x\text{Ga}_{1-x}\text{As}$ composition is given by the following set of equations :

$$\begin{aligned} \mu_n &= 8000 - 1.818 \times 10^4 x & (0 < x < 0.429) & \quad [\text{A- 8}] \\ \mu_n &= 90 + 1.1435 \times 10^5 (x-0.46)^2 & (0.429 < x < 0.46) & \quad [\text{A- 9}] \\ \mu_n &= 90 + 3.75 \times 10^4 (x-0.46)^2 & (0.46 < x < 0.5) & \quad [\text{A- 10}] \\ \mu_n &= 200 - 2.0/(x-0.46) & (0.5 < x < 1.0) & \quad [\text{A- 11}] \end{aligned}$$

The default concentration-dependent mobility values for GaAs are given in Table A- 4.

The following expression is used to implement a field-dependent mobility which provides a smooth transition between low-field and high-field behavior:

$$\mu(E) = \mu_0 \left[\frac{1}{1 + \left(\frac{\mu_0 E}{v_{sat}} \right)^\beta} \right]^{1/\beta} \quad [\text{A- 12}]$$

Where β is a constant with a default value of 1.0 for both electrons and holes. The saturation velocities for AlGaAs are given by:

$$v_{satn} = 1.13 * 10^7 - 1.2 * 10^4 T \quad [A- 13]$$

$$v_{satp} = 1.12 * 10^7 - 1.2 * 10^4 T \quad [A- 14]$$

Concentration (cm ⁻³)	Mobility in GaAs (cm ² /V-s)	
	Electrons	Holes
1.0*10 ¹⁴	8000.0	390.0
2.0*10 ¹⁴	7718.0	380.0
4.0*10 ¹⁴	7445.0	375.0
6.0*10 ¹⁴	7290.0	360.0
8.0*10 ¹⁴	7182.0	350.0
1.0*10 ¹⁵	7300.0	340.0
2.0*10 ¹⁵	6847.0	335.0
4.0*10 ¹⁵	6422.0	320.0
6.0*10 ¹⁵	6185.0	315.0
8.0*10 ¹⁵	6023.0	305.0
1.0*10 ¹⁶	5900.0	302.0
2.0*10 ¹⁶	5474.0	300.0
4.0*10 ¹⁶	5079.0	285.0
6.0*10 ¹⁶	4861.0	270.0
8.0*10 ¹⁶	4712.0	245.0
1.0*10 ¹⁷	4600.0	240.0
2.0*10 ¹⁷	3874.0	210.0
4.0*10 ¹⁷	3263.0	205.0
6.0*10 ¹⁷	2950.0	200.0
8.0*10 ¹⁷	2747.0	186.9
1.0*10 ¹⁸	2600.0	170.0
2.0*10 ¹⁸	2060.0	130.0
4.0*10 ¹⁸	1632.0	90.0
6.0*10 ¹⁸	1424.0	74.5

Table A- 4: Default concentration-dependent mobilities for GaAs

¹ G.A.M. Hurx, H.C. de Graaf, W.J. Klosterman, et. al., "A Novel Compact Model Description of Reverse Biase Diode Characteristics including Tunneling", ESSDERC, pp. 49-52, 1990.

² D.B.M. Klaassen, "Physical Modeling for Bipolar Device Simulation", In: Simulation of Semiconductor Devices and Processes, Edited by W. Fichtner and D. Aemmer, Harting-Gorre, 1991, Vol. 4, pp. 23-43.

³ M. Klausmeier-Brown, M. Lundstrom, M. Melloch, "The Effects of Heavy Impurity Doping on AlGaAs/GaAs Bipolar Transistors", IEEE Trans., ED-36, No. 10, pp. 2146-2155, 1989.

